An Acoustic Time-of-Flight Technique for Unsteady Temperature Measurements in Combustion Chambers: Characterization and Modeling of Entropy Waves

vorgelegt von
Dipl.-Ing.
Dominik Waßmer
geb. in Freiburg im Breisgau

Von der Fakultät V – Verkehrs- und Maschinensysteme
der Technischen Universität Berlin
zur Erlangung des akademischen Grades

Doktor der Ingenieurwissenschaften
– Dr.-Ing. –

genehmigte Dissertation

Promotionsausschuss:

Vorsitzende:	Prof. Dr. rer. nat. Stefanie Marker (TU Berlin)
Gutachter:	Prof. Dr.-Ing. Jonas P. Moeck (TU Berlin)
Gutachter:	Prof. Dr.-Ing. Christian Oliver Paschereit (TU Berlin)
Gutachter:	Prof. Dr.-Ing. Thomas Sattelmayer (TU München)
Gutachter:	Dr.-Ing. Mirko R. Bothien (Ansaldo Energia, Switzerland Ltd)

Tag der wissenschaftlichen Aussprache: 30. Oktober 2017

Berlin 2018

Vorwort

Die in dieser Zusammenschrift dargestellte Arbeit entstand im Rahmen meiner Tätigkeit als wissenschaftlicher Mitarbeiter am Fachgebiet Experimentelle Strömungsmechanik des Instituts für Strömungsmechanik und Technische Akustik an der Technischen Universität Berlin. Die Finanzierung erfolgte durch das AG Turbo 2020 Forschungsvorhaben 2.3.3. „Thermoakustisches Stabilitätsverhalten einer mager betriebenen Brennkammer“ des Bundesministeriums für Wirtschaft und Energie.

Bei dieser Arbeit durfte ich die Unterstützung vieler Menschen erfahren, durch die das Gelingen erst möglich wurde. Diesen möchte ich im Folgenden meinen Dank aussprechen.

Mein erster Dank gilt meinem Doktorvater, Herrn Prof. Dr.-Ing. Christian Oliver Paschereit, der mir mit seinem Fachgebiet und dessen herausragender experimenteller Infrastruktur die Chance zur Durchführung des Projekts auf solch professionellem Niveau gab. Die wissenschaftlichen Freiheiten und Möglichkeiten habe ich sehr geschätzt und sie sind in diesem Maße absolut keine Selbstverständlichkeit. Herzlichen Dank dafür!

Bei der Bearbeitung meines Projekts hatte ich zudem das große Glück am Institut von einem „zweiten Doktorvater“, Prof. Dr.-Ing. Jonas Moeck, betreut zu werden. Dir, Jonas, danke ich sehr für Deine fachliche Unterstützung, speziell bei sämtlichen mathematischen Fragestellungen, sowie für Deine große Geduld, wenn Du zum wiederholten Male versucht hast, mir mathematische Sachverhalte näherzubringen.

Für die hochkarätige Begutachtung meiner Arbeit bedanke ich mich herzlichst bei meinen externen Gutachtern Prof. Dr.-Ing. Thomas Sattelmayer und Dr.-Ing. Mirko Bothien, die trotz meiner kurzfristigen Anfrage nicht zögerten die Aufgabe zu übernehmen. Frau Prof. Dr. rer. nat. Stefanie Marker danke ich für die recht spontane und unkomplizierte Übernahme des Vorsitzes des Promotionsausschusses.

Ein ganz besonderer Dank geht an Dr. è sc. Bruno Schuermans, der das AG Turbo Projekt von Seiten des Kooperationspartners Alstom (bzw. GE Power) leitete. Bruno, ohne Deine spontanen sowie genialen Ideen, Dein überragendes mathematisches Verständnis und Deine Fähigkeit praktische und theoretische Sachverhalte optimal zu koppeln, wären einige Kapitel dieser Arbeit nicht entstanden. Aus unseren Telefonkonferenzen ging ich meist mit einer Fülle an neuen Ideen, Inspirationen und - auf teils ungeahnten mathematischen Pfaden - gelösten Problemen heraus. Die Zusammenarbeit mit Dir war stets eine große Motivation und ein Antrieb für mich!

Einen ebenfalls nicht unerheblichen Anteil am Gelingen dieser Arbeit haben meine beiden Studenten, Felix Pause und Julius Leglise. Vielen Dank für Euer großes Engagement, die unzähligen Stunden, die Ihr mit mir beim Experimentieren und Umbauen im Labor verbringen musstet und nicht zuletzt für den sehr freundschaftlichen und unkomplizierten Umgang mit Euch. Ganz speziell Dir, Felix, möchte ich für Deine ausgezeichneten und den üblichen Rahmen sprengenden Arbeiten im Zuge Deiner Masterarbeit danken. Du hast einen sehr wesentlichen Teil zu den tomographischen Untersuchungen in dieser Arbeit beigetragen.

An dieser Stelle sei auch ein großes Dankeschön an einen weiteren Studenten, Richard Blümner, gerichtet. Obwohl Du nicht „mein“ Student warst, hast Du sehr viel Zeit und Energie investiert, um die von Dir am Institut eingerichtete TDLAS-Messmethode für meine Versuche anwendbar zu machen. Umso mehr freute es mich, Dich später in unseren Reihen als Doktorand begrüßen zu dürfen.

Experimentelles Forschen und Arbeiten kann nur dann gut funktionieren, wenn die

Hardware genau das tut, was sie tun soll. Dies wiederum ist nur dann der Fall, wenn man als Doktorand auf ein erfahrenes und kompetentes Werkstattteam zurückgreifen kann. Vielen Dank an das gesamte Werkstattteam des HFI und auch des DLR für die Unterstützung bei jeglichen, meist sehr kurzfristigen und dringenden, Problemen. Ganz besonders Heiko Stolpe und Andy Göhrs sei für ihr Engagement und ihre pragmatischen wie qualitativ hochwertigen Lösungen getreu dem Motto „Geht nicht, gibt's nicht“ gedankt. Auch eine funktionierende Verwaltung ist für die geregelte und planmäßige Durchführung eines Projekts von Nöten. Mein Dank geht an Sandy Meinecke, Maria Lück, Kristin Halboth und Dr.-Ing. Navid Nayeri, die stets unkompliziert Mittel und Wege fanden, wenn irgendwo der Schuh drückte.

Neben all der fachlichen und praktischen Unterstützung, kann eine gute Arbeit auch nur dann zustande kommen, wenn die Arbeitsatmosphäre stimmt. Dies war auf Grund meiner ganzen Kolleginnen und Kollegen am Institut definitiv der Fall: ob beim Mittagessen in der Mensa, während des Joggens im Tiergarten in der Mittagspause oder bei hitzigen Duellen am Kickertisch. Die (viele) Zeit am Institut hat mir stets sehr viel Freude bereitet und war durchweg geprägt von freundschaftlichem und sehr kollegialem Umgang. Bei jeglichen fachlichen Problemen oder experimentellen Fragestellungen konnte ich stets auf die Erfahrung und Hilfe meiner Doktorandenkolleginnen und -kollegen vertrauen. Vielen herzlichen Dank Euch allen!
An dieser Stelle möchte ich nicht versäumen, die ganzen freiwilligen Helfer zu listen, die mir beim Korrekturlesen dieser Arbeit geholfen haben: Panos Stathopoulos, Myles Bohon, Sebastian Schimek, Joshua Gray, Bernhard Bobusch, Aditya Saurabh, Thoralf Reichel, Lisa Zander, Eric Bach, Georg Mensah Mohammad Rezay Haghdoost, Fabian Völzke, Richard Blümner, Niclas Hanraths, Tom Tanneberger, Holger Nawroth, Johann Vinkeloe, Sebastian Niether und Olaf Bölke.

Zuallerletzt, aber nicht minder herzlich, möchte ich mich bei meinen Eltern und Schwestern für die großartige und bedingungslose Unterstützung bedanken. Auch wenn ich die Arbeit leider oftmals als wichtiger erachtete als einen Heimatbesuch im Schwarzwald, wusste ich Euch immer hinter mir. Ohne Euch wäre ich nie bis zu diesem Punkt gekommen.

Abstract

In consideration of the manifold alternative electric energy sources, load flexibility in modern gas turbines is an essential requirement. To this end, the operational range of the engines must be extended. However, this is often impeded by low-frequency combustion instabilities that are associated with acoustics generated within the gas turbine combustor. These high-amplitude pressure oscillations (also referred to as indirect combustion noise) are primarily a result of accelerated entropy perturbations at the turbine inlet. Such entropy waves are generated by equivalence ratio fluctuations in the premixed fuel-air mixture upstream of the flame. Indirect combustion noise may also couple with other thermoacoustic mechanisms and provokes high noise emissions at the engine's exhaust.

Hence, monitoring and more importantly predicting and counteracting entropy waves in a combustion system is of high importance. As of yet, it has been difficult to realize monitoring or prediction due to the lack of appropriate measurement techniques. The present work contributes to the accomplishment of both needs.

A non-intrusive time-of-flight based technique for the measurement of entropy fluctuations is introduced, which is well-suited for the high-temperature and corrosive conditions of a combustor. The flight time of an acoustic pulse is equal to the line-integrated inverse speed of sound along its path, from which the line-integrated temperature is deduced. In this study presented here, the acoustic pulse is generated through an electric discharge, whose high-frequency content makes it detectable even in the presence of high-amplitude noise. The flight time along several acoustic paths is simultaneously measured by water-cooled microphones distributed over the circumference of the combustor. Mathematical means are derived that allow for the extraction of a cross-sectionally averaged temperature fluctuation crossing the measurement plane. Additionally, tomographic methods are adapted for the estimation of the corresponding radial temperature distribution. Their applicability to the measurement setup is verified via a phantom study, where flight times are numerically generated from known temperature fields.

The measurement technique is utilized in an atmospheric combustion test rig, where well-defined entropy waves are generated through the modulation of the fuel supply. Amplitude and phase of the advecting entropy spots are measured at various axial positions downstream of the flame. Furthermore, the fuel modulation frequency as well as the bulk velocity are varied. An additional measurement of the equivalence ratio in the mixing tube allows for the measurement of the transfer function between equivalence ratio fluctuations and entropy fluctuations. Based on reactor theory, a model for estimating the transfer function is derived and successfully validated with measured transfer functions. A clear low-pass behaviour of the frequency response is found and the Strouhal number is identified as the appropriate scaling parameter. To describe the transport of entropy fluctuations, a one-dimensional model is set up, which relates entropy fluctuations at two different axial positions in the combustor to each other. In agreement with various other models found in literature, the measured decay of the amplitude and the phase as function of a Strouhal number is well recovered. It is found that dispersion is the main driver for the dissipation of entropy waves.

Zusammenfassung

Die große Vielfalt an Energiequellen zur Stromerzeugung erfordert bei modernen Gasturbinen ein flexibles Lastverhalten. Um dies zu gewährleisten, ist eine Erweiterung des Betriebsbereichs erforderlich, was jedoch häufig von niederfrequenten Verbrennungsinstabilitäten begrenzt wird. Diese starken Druckfluktuationen, welche auch als indirekter Verbrennungslärm bezeichnet werden, resultieren größtenteils aus Entropieschwankungen, die am Turbineneintritt massiv beschleunigt werden. Entropiewellen werden durch Äquivalenzverhältnisschwankungen im Brennstoff-Luft Gemisch stromauf der Flamme erzeugt. Indirekter Verbrennungslärm kann weitere thermoakustische Instabilitäten auslösen und sorgt für erhöhte Lärmemissionen der gesamten Maschine.

Folglich ist das Messen von Entropiewellen und besonders deren Vorhersage und der Einsatz von Gegenmaßnahmen in Brennkammern von großer Bedeutung. Mangels geeigneter Messtechnik war die Messung und somit auch eine fundierte Vorhersage bislang jedoch sehr schwierig. Die vorliegende Arbeit trägt zur Lösung dieser Probleme bei.

In dieser Arbeit wird eine nicht-intrusive, Laufzeiten basierte Messtechnik zur Messung von Entropiewellen in Verbrennungssystemen vorgestellt, welche sowohl bei sehr hohen Temperaturen als auch in der korrosiven Umgebung einer Brennkammer eingesetzt werden kann. Die Laufzeit eines akustischen Pulses entspricht der linienintegrierten inversen Schallgeschwindigkeit entlang des akustischen Pfades, von welcher wiederum die linienintegrierte Temperatur abgeleitet werden kann. In der hier vorgestellten Arbeit wird der akustische Puls durch eine elektrische Entladung erzeugt, deren hochfrequente Anteile die Detektion des Pulses auch bei hohen Lärmamplituden erlaubt. Die Laufzeiten mehrerer akustischer Pfade werden mittels über den Umfang der Brennkammer verteilten wassergekühlten Mikrofone simultan gemessen. Mit Hilfe von weiterentwickelten mathematischen Methoden wird die Bestimmung der oberflächengemittelten Temperaturfluktuation an der axialen Messstelle möglich. Zudem kommen tomografische Verfahren zur Anwendung, an Hand derer die radiale Temperaturverteilung berechnet werden kann. Eine Validierung dieser Methoden findet mittels Phantomstudien basierend auf gemessenen statischen Temperaturfeldern statt.

Die Messtechnik wird an einem atmosphärischen Brennkammerprüfstand eingesetzt, an welchem mit Hilfe periodischer Modulation des Brennstoffs definierte Entropiewellen erzeugt wurden. Die Amplituden und Phasen der advektiv fortbewegten Entropiefluktuationen werden an mehreren axialen Positionen stromab der Flamme gemessen. Des weiteren wird die Modulationsfrequenz wie auch die Strömungsgeschwindigkeit im Brennkammerrohr variiert. Die zusätzliche Messung der Methankonzentration im Mischrohr des Brenners ermöglicht die Bestimmung der Transferfunktion zwischen Äquivalenzverhältnisschwankungen und Entropieschwankungen. Basierend auf diesen Messungen, wird ein Reaktormodell zur Vorhersage der Transferfunktion hergeleitet und validiert. Die Frequenzantworten der Entropiewellen weisen ein deutliches Tiefpass-Verhalten auf, wobei die Strouhalzahl als passender Skalierungsparameter dient. Um den Transport von Entropiewellen charakterisieren zu können, kommt ein eindimensionales Model zum Einsatz, welches Entropiewellen an verschiedenen axialen Positionen in Relation zueinander setzt. Dieses Modell wird experimentell validiert und zeigt, dass Dispersion der dominierende Faktor für die Dissipation von Entropiewellen darstellt.

Contents

Nomenclature

A few uniquely used variables are defined only at the location of their appearance.

Latin letters

A_{rec}	frequency response to a rectangular pulse (-)
c	(adiabatic) speed of sound (m/s)
c_e	effective speed of sound (m/s)
c_{h}	speed of sound in the microphone holder (m/s)
C_p	heat capacity at constant pressure (J/K)
c_p	specific heat capacity at constant pressure (J/kg/K)
C_v	heat capacity at constant volume (J/K)
c_v	specific heat capacity at constant volume (J/kg/K)
D	diameter (m)
d_e	distance between electrodes (m)
E	internal energy (J)
e	specific internal energy (J/kg)
f_s	sampling frequency (Hz)
f_{spark}	spark excitation frequency (Hz)
f_{v}	frequency of fuel modulation valve (Hz)
g	ratio between modulated fuel mass flow and total fuel mass flow (-)
H	enthalpy (J)
H_r	reactor transfer function (-)
H_t	transport transfer function (-)
h	specific enthalpy (J/kg)
h_f	specific reaction enthalpy (J/kg)
$\mathbf{I}$	unity matrix (-)
I_i	intensity of transmitted light ($\mathrm{W/m^2}$)
I_t	intensity of incident light ($\mathrm{W/m^2}$)
k	integer (-)
k_t	temperature correction factor (-)
k_h	humidity correction factor (-)
L	geometrical acoustic path length (m)
L_r	geometrical reactor length (m)
l	control variable along an acoustic path (-)
l_c	length of microphone holder's capillary (m)
m	model parameter (-)
N	number of particles in a system (mol)

N_g	number of one-dimensional discretization points (-)
N_L	number of acoustic paths (-)
N_ψ	number of phase angles within one period of oscillation (-)
N_s	number of spark events averaged for TOF measurement (-)
N_{spark}	number of total spark events per measurement (-)
$\mathbf{n}$	unit vector normal to wave front (-)
P	cycle period (s)
p_0	ambient pressure (Pa)
p	pressure (Pa)
Q	heat (J)
$\dot{Q}$	heat release rate (J/s)
q	specific heat (J/kg)
r	radial coordinate (m)
R	radius of combustion chamber (m)
R_u	universal gas constant ($R_u = 8.3144598$ J/mol/K)
R_g	specific gas constant (J/kg/K)
R_p	primary resistance (Ω)
S	entropy (J/K)
S	cross-section area (m^2)
S_{swirl}	swirl number (-)
s	specific entropy (J/K/kg)
s	penetration depth of electrodes' tips (m)
T	temperature (K)
T_0	ambient temperature (K)
u	velocity (m/s)
$u_\angle$	velocity obtained from measured phase angles (m/s)
U_b	breakdown voltage (V)
V	volume (m^3)
v	specific volume (m^3/kg)
v_g	group velocity (m/s)
v_p	phase velocity (m/s)
w	model parameter (-)

Greek letters

α	angle of asymmetry (deg)
α	diffusion coefficient (m^2/s)
β	angle between electrodes and radial symmetry axis (deg)
χ	duty cycle (%)
Δx	distance between burner inlet plane and TOF measurement plane (m)
ϵ_{sa}	deviation in cross-sectionally averaged temperature (K)
ϵ_{rms}	root mean square deviation between two temperature profiles (K)
γ	specific heat capacity ratio (-)
γ	Tikhonov regularization parameter (-)
ρ	density (kg/m^3)
$\mathbf{\Sigma}$	diagonal matrix (-)

λ_c	convective wavelength (m)
λ_k	relaxation parameter (-)
μ	chemical potential (J/mol)
μ	exponential factor of basis function for collocation (-)
ν	kinematic viscosity (m^2/s)
ω	angular frequency $\omega = 2\pi f$ (Hz)
ϕ	equivalence ratio (-)
ψ	phase angle (rad)
ψ_f	line shape function (-)
σ_i	i-th singular value (-)
ς	stoichiometric coefficient (-)
Θ	transmission coefficient (s)
τ	flight time (s)
τ_p	flight time extracted from phantom study (s)
τ_h	flight time in microphone holder (s)
Υ	constant ($V/(Pa{\cdot}m)^{-\frac{1}{2}}$)
Ξ	constant ($V/(Pa{\cdot}m)$)
ζ	optimization parameter used for collocation $\zeta = \mu/\gamma$ (-)

Subscripts

b	bulk flow
c	convective
e	electrodes
ed	eddy
eff	effective
f	fuel
ig	(auto-) ignition
md	molecular diffusion
mod	modulated
OP	onion peeling
opt	optimized
p	phantom
TC	thermocouple
td	turbulent diffusion
Tik	Tikhonov regularized
r	reactor
t	transport
v	valve

Superscripts

$(.)'$	fluctuation in time domain
$\hat{(.)}$	fluctuation in frequency domain
$\tilde{(.)}$	median value or cross-sectionally surface averaged value

$\check{(.)}$	inverse value ($\check{()} = 1/(.)$)
$\overline{(.)}$	mean value
$(.)^*$	non-dimensionalized value

Abbreviations

CFD	Computational Fluid Dynamics
CARS	Coherent Anti-Stokes Raman Spectroscopy
CPSC	Constant Pressure Sequential Combustion
CT	Computed Tomography
LES	Large Eddy Simulation
LS	Least Square
OP	Onion Peeling
PIV	Particle Image Velocimetry
RBF	Radial Basis Function
SVD	Singular Value Decomposition
TC	Thermocouple
TDLAS	Tunable Diode Laser Absorption Spectroscopy
TOF	Time of Flight
TSVD	Truncated Singular Value Decomposition

Non-dimensional characteristic numbers

Le	Lewis number ($\mathrm{Le} = \alpha/D$)
Pe	Peclet number ($\mathrm{Pe} = Lu/\alpha$)
Pr_t	turbulent Prandtl number ($\mathrm{Pr}_t = \nu_t/\alpha_{\mathrm{ed}}$)
Re	Reynolds number ($\mathrm{Re} = uD/\nu$)
St	Strouhal number ($\mathrm{St} = fL/u = L/\lambda_c$)
St_r	reactor Strouhal number ($\mathrm{St}_r = fL_r/u_r$)
St_t	transport Strouhal number ($\mathrm{St}_t = f\lvert\Delta x_1 - \Delta x_2\rvert/u$)

1 Introduction

This thesis deals with the experimental assessment and the analytical characterization of entropy waves in gas turbine combustors. The fact that both aspects, particularly the experimental investigations but also the analytical studies, break new ground to some extent, requires detailed and comprehensive discussions for each of them. This splits this study somewhat into two parts. One part explores the novel Time-of-Flight measurement technique, which has for the first time been adapted for the purpose of detecting entropy waves in a high-temperature environment. The other part deals with the modeling of the generation and the propagation mechanisms of entropy waves, which is, of course, only possible based on the measured entropy fluctuations.

The purpose of this introduction is to describe the motivation for the present study on entropy waves and to provide an overview of preceding studies related to this topic.

1.1 Motivation

There are three reasons why the measurement and the quantitative prediction of entropy waves in combustion systems are of interest. Each of them will be presented and discussed in the following subsections.

1.1.1 Indirect combustion noise

The main reason for all the past studies on entropy waves is the so-called *indirect combustion noise*. This phenomenon belongs to a class of phenomena that are attributed to the field of *thermoacoustics*. The latter describes the interaction between the unsteady heat release and the acoustic field in gas turbine combustion chambers and furnances. There, thermoacoustic effects are perceived as adverse and hazardous, as an unfavorable combination of the heat release fluctuations and the pressure oscillations might lead to significant and even devastating acoustic perturbations. This "unfavorable combination" between heat release and acoustics is well known as *Rayleigh criterion*, which states that a system can become unstable, if the maximum heat is released at the moment of highest pressure. In this context, unstable means that the growth of acoustic pressure oscillations in the combustion chamber is positive (in literature, "unstable" might sometimes falsely be used for a saturated stable system at high acoustic amplitudes). The name of the criterion recognizes the fundamental study of Rayleigh (1878), who laid the foundation for the understanding of thermoacoustic phenomena. Some time later, these combustion instabilities (this phrase is often used as an equivalent to thermoacoustic instabilities) became subject to research groups dealing with rocket engines (see, e.g.,

Tsien (1952); Crocco and Cheng (1956)). They discovered "combustion roughness" i.e. the unsteadiness of pressure, temperature, velocity, and gas composition, which causes either undesired noise emissions or might even prevent the safe operation of the engine and lead to serious damages due to massive vibrations. A comprehensive overview of the efforts undertaken to understand and tackle these problems is given by Culick and Yang (1995).

In case of industrial (gas turbine) combustors, which have a lower power density compared to rocket engines, thermoacoustic problems were encountered later, when lean premixed combustion systems were introduced. The replacement of diffusion-type burners was required to meet the ever stricter regulations regarding NO_x emissions (Döbbeling et al., 2005). The premixing of air and fuel enhances the susceptibility of typical combustors to thermoacoustic instabilities and motivated a lot of academic research groups as well as gas turbine manufacturers to gain more understanding of the respective phenomena (Keller, 1995; A. Dowling, 1995; Paschereit and Polifke, 1998; Schuermans, 2003; T. C. Lieuwen and Yang, 2005).

Indirect combustion noise represents one aspect of the various mechanisms that might lead to an unstable operation of a combustion system. First, it has to be differentiated between two different sources of noise: *Direct combustion noise* is emitted by the flame due to unsteady heat release rate, which causes unsteady local volumetric expansion and contraction in the reaction zone that in turn generate acoustic velocity fluctuations. In case of indirect combustion noise, the acoustic waves are triggered by non-isentropic temperature fluctuations, the so-called entropy waves, that are significantly accelerated at the turbine inlet or any other type of nozzle (Howe, 2010). Due to its generation mechanism, in literature, this noise is often referred to as "entropy noise" or "rumble" The latter term is attributed to the fact that indirect combustion noise, which is caused by entropy perturbations, occurs in the low-frequency regime in a range of $50 - 150\,\mathrm{Hz}$ (Eckstein, Freitag, et al., 2004). Note that indirect combustion noise is not merely attributed to entropy waves but can also be triggered by vorticity perturbations caused by temporal variation in combustion. The reason for the generation of acoustic waves at the nozzle is the local variation in mass flow that results in combination with the strong velocity gradients in the main flow field in acoustic velocity fluctuations. A simplified sketch of the interaction mechanism between equivalence ratio fluctuations, entropy waves, and pressure oscillations is given in Fig. 1.1. Indirect combustion noise can act disadvantageously in two ways. Firstly, the acoustic waves that are emitted back into the combustion chamber can interact with the unsteady heat release rate and cause a thermoacoustic feedback loop to close. On the other hand, the noise that propagates downstream might reach a harmful amplitude level. The latter can become a serious problem for aero-engines (A. P. Dowling and Mahmoudi, 2015).

Marble and Candel (1977) were the first who gave a full description of the interaction mechanism between unsteady density arriving at a nozzle and the associated pressure fluctuations that are consequently reflected back into the combustor. Their analytical model assumes a radially homogeneous distribution of the flow field as well as of the entropy field. Approaches that account for more realistic flow field conditions have been developed amongst others by Leyko et al. (2009), Huet and Giauque (2013), and Duran and Moreau (2013). The first who experimentally assessed and quantified the

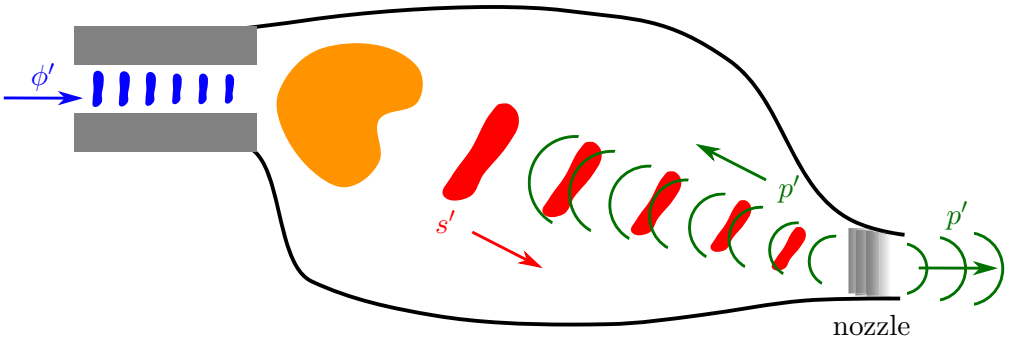

Figure 1.1: Simplified sketch of indirect combustion noise p' generation due to entropy waves s' that are triggered by equivalence ratio fluctuations ϕ' in the fuel-air mixture. Acoustic waves are partly reflected back into the combustion chamber and partly transmitted to the exhaust of the engine. Note that the entropy fluctuation is advected with the bulk flow velocity while the acoustic wave propagates with speed of sound.

transformation of entropy waves to acoustic waves were Bake et al. (2007); Bake (2008). Their entropy wave generator allows for the generation of a defined pulse in temperature within a duct flow that is accelerated through a convergent-divergent nozzle. For the realization of the temperature perturbation they employed an electric heating grid. The temperature pulse was detected by a bare wired thermocouple with a diameter of 25 μm. The transmitted pressure waves were assessed in the duct section downstream of the nozzle. They found that the acoustic amplitude scales linearly with the amplitude of the temperature fluctuation that advects into the nozzle. Based on a slightly different experimental setup, De Domenico et al. (2017) measured the pressure fluctuations between a pulsed heating grid (single pulse excitation) and a nozzle. With the help of temperature measurements at the nozzle, they were able to separate the indirect noise, emitted from the nozzle in upstream direction, from direct noise generated at the electric heating grid. A larger scale entropy wave generator, which employs a siren-type excitation for alternating hot and cold temperature spots has been presented by Gaetani et al. (2015). Comprehensive reviews on all aspects of indirect and direct combustion noise have recently been given by A. P. Dowling and Mahmoudi (2015) and Morgans and Duran (2016).

Two more considerations, that might play a stronger role in the future, need to be addressed here. Regarding ever stricter emission regulations in aviation, lean premixed combustion technologies, that have been developed for stationary gas turbines, might be adapted in aero-engines. Thus, associated thermoacoustic problems, that might not have occurred yet, will arise. Due to the more compact dimensions of the combustors, the probability of entropy waves surviving the advection process and reaching the turbine inlet increases. Another aspect that might lead to an increased relevance of entropy waves in the future is the augmented usage of (diluted) hydrogen or blends of natural gas and hydrogen in combustors. The significantly lower volumetric energy density might in general lead to higher bulk velocities in the combustion chambers. This, in turn, causes the entropy waves to be advected faster to the turbine inlet, which reduces the attenuation of its amplitude (this correlation will be derived in Sec. 6.2).

The cross-sectionally average amplitude of the entropy fluctuation, which is finally accelerated in the exit nozzle of the combustor, determines the strength of the indirect

combustion noise. Thus, in order to predict the probability of the occurrence of indirect combustion noise or to estimate the strength or the characteristics of the indirect combustion noise in terms of frequency and phase, the advection mechanisms of entropy waves need to be understood. In a recently published comprehensive review on (indirect) combustion noise, A. P. Dowling and Mahmoudi (2015) emphatically state that "*... most of the current understanding of the dispersion process* [of entropy waves] *is rather intuitive*" and that "*... entropy waves need to be measured*". Addressing these challenges is the major scope of this thesis.

1.1.2 Sequential combustion systems

Some gas turbines are equipped with a sequential combustion system. Typically, this means that the exhaust gases of a first combustion chamber are partly expanded via a (one stage) turbine and are completely combusted by injection of additional fuel in a second combustion chamber (Joos et al., 1996). One of the main advantages of such a combustion technology is a more beneficial thermodynamic gas turbine cycle, which allows to obtain more power at the same turbine inlet temperature compared to a conventional gas turbine cycle (Döbbeling et al., 2005). Additionally, these type of engines enable a more flexible operation in combined cycle power plants, as the exhaust temperature of the gas turbine can be controlled more independently from its load. In a very recent publication of Pennell et al. (2017), a novel sequential combustion system is presented, which does not utilize a high pressure turbine section between the two combustors (*Constant Pressure Sequential Combustion* (CPSC)). The exhaust gas of the primary combustor is diluted with air from the compressor, guided through vortex generators, and finally combusted with additional fuel in the secondary combustor. Here, the combustion in the downstream burner takes place at almost the same pressure as in the primary combustor. Beside an increased operational flexibility, this technology exhibits moderate temperatures in the second combustor (compared to the aforementioned system), which lowers the NO_x production (Pennell et al., 2017).

A sketch of a sequential combustion system is depicted in Fig. 1.2. In both gas turbine combustion systems described above, the flame in the second combustor is stabilized by auto-ignition. This brings the importance of entropy waves into play, which can here be considered as advected temperature spots (see Sec. 2.1). The auto-ignition delay time depends strongly on the gas temperature; for such high-temperatures, a difference of 100 K means a variation of the auto-ignition delay time of approximately one order of magnitude (Bounaceur et al., 2015). Consequently, a shift in auto-ignition delay time $\Delta\tau_{\mathrm{ig}}$ causes a spatial shift Δx of the axial flame position, which can be estimated with $\Delta x = \overline{u}\Delta\tau_{\mathrm{ig}}$, where $\overline{u}$ denotes the bulk flow velocity. For typical gas turbine operation parameters, a variation on the order of $T' = 50\,\mathrm{K}$ could lead to an axial variation in the flame position of several centimeters. Especially in case of the CPSC system, where the mixing quality of air-fuel for the secondary flame depends on the auto-ignition delay time, a shortening of the auto-ignition delay time due to high-temperature spots might be highly adverse. Apart from temperature fluctuations generated by the primary flame, in the CPSC system advective temperature spots can also be induced by a pulsed inflow of the cooling air in the dilution zone (triggered by acoustic perturbations).

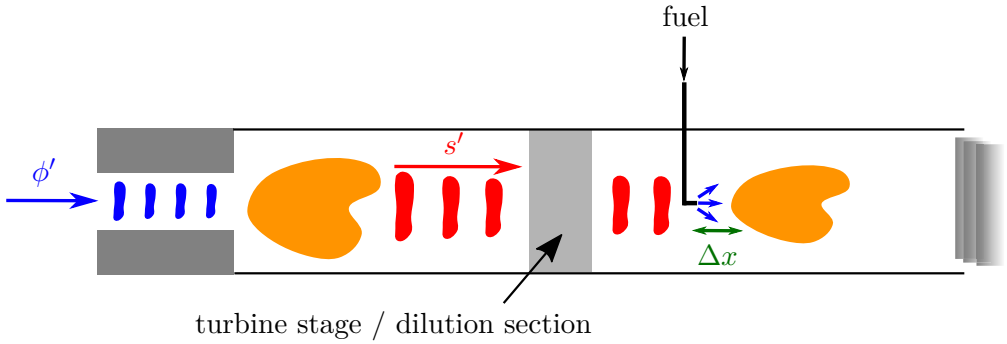

Figure 1.2: Simplified sketch of a sequential combustion system. The axial distance Δx between the fuel injection position and the second reaction zone depends on the varied auto-ignition delay time $\Delta\tau_{\mathrm{ig}}$ and the bulk flow velocity $\overline{u}$.

Axial oscillations of the heat release zone cause acoustic perturbations, which, in turn, might provoke thermoacoustic interactions to arise. It is therefore obvious that an up-front estimation of the probability and the strength of temperature fluctuations advecting between the two combustors is of utmost importance. Moreover, a non-stop, highly time resolved assessment of the temperature upstream of the secondary fuel injection would support appropriate countermeasures.

1.1.3 NO_x emissions

It is well known that the amount of NO_x molecules, which exit a combustor, mainly depend on the temperature field and on the residence time of the gas in the high-temperature areas of the combustor (Warnatz et al., 2009). The enhanced reaction rate of the formation of NO_x at elevated temperatures is the main reason why entropy waves (again, in this context it might be more convenient to use the term "advected temperature perturbations") have an unfavourable effect on NO_x emissions. Temporarily integrated, the gas molecules advected in a high temperature spot experience an elevated temperature in their residence time in the combustor. Consequently, more NO_x is generated. Due to the exponential growth of the NO_x formation with respect to the temperature, this effect is not compensated by the "cold spots" between the hot spots.

It might be debatable whether the impact of entropy waves on the NO_x emissions has to be considered or if it can be neglected. However, to estimate the surplus of NO_x formation due to entropy waves, a measurement technique is required that allows for an experimental assessment of temperature fluctuations in a gas turbine combustor. Alternatively, validated models have to exist that enable a prediction of the strength and the maximum "survival time" of the advected hot spots. The development of both of these means has been the scope of this study.

1.2 Introduction to the major scopes of the study

The three motivations presented in the preceding section clearly highlight two concerns whose solutions are strongly requested. These are

- the experimental assessment of entropy waves in realistic gas turbine combustors

  and

- analytic means to enable the estimation of the entropy waves' strength and phase.

Both of these aspects will be introduced in the following subsections; they have already partly been published in Wassmer, Schuermans, et al. (2016).

1.2.1 Measurement technique

The key part of this study constitutes the development of a measurement technique which allows for the quantitative assessment of temperature fluctuations in the reactive high-temperature environment of a gas turbine combustor. The goal was to develop an experimental setup that does not only serve for research purposes at (atmospheric) combustion test rigs but could be applied to real gas turbine engines. Thus, the applicability to high pressures and high temperatures has been considered as well as the reliability of the experimental hardware. Approaches for the measurement of entropy waves in model gas turbine combustors are scarce in literature. A noteworthy experimental study on low-frequency oscillations has been conducted by Eckstein (2004). He developed a double-thermocouple technique, where two bare-wired thermocouples (51 μm and 76 μm in diameter) enable a reconstruction of the temperature signal based on a Fourier analysis. Although this method served well in his investigations on the phase-relation to OH*-chemiluminescence measurements, quantitative values of the temperature amplitudes are difficult to extract. Furthermore, the temperature probe is limited in exposure time to the reactive high-temperature gases and provides only a point measurement.

Therefore, in this study, a non-intrusive time-of-flight (TOF) measurement technique has been developed, validated, and characterized. Key element of this approach is the relation between the flight time of an acoustic pulse, i.e., the line-integrated inverse speed of sound along its acoustic propagation path, and the temperature of the medium through which the propagation takes place. In case of an active acoustic pyrometer, which has been employed in this study, an acoustic pulse signal is actively triggered by a transmitter and its traveling time is detected by an acoustic receiver. This approach provides a highly time resolved measure of the cross-sectionally averaged temperature at an axial position in a combustion chamber. By employing multiple acoustic paths, one-dimensional radial temperature fields can be obtained.

The novelty of this active acoustic pyrometry approach in the present study is its application to a model gas turbine combustion chamber. The idea by itself has already been used for various technical purposes such as the temperature measurement in furnances (Green, 1985), boilers (Bramanti et al., 1996), gas turbine exhausts (DeSilva et al., 2013), or oceanography (Striggow, 1985). A more detailed introduction to the history and the different types of TOF measurement techniques is given in Sec. 2.2.

The use of a spark discharge as sender of the short acoustic pulse makes this technique to withstand the noisy and harsh conditions in a realistic combustor. The high-frequency content of such an acoustic pulse emitted by an electric discharge allows for an extraction of the arrival time even for significantly larger amplitudes of the combustion noise and the aerodynamic noise. This is done through a zero-phase high-pass filtering of the microphones' time signals. The adaption of a spark discharge for the usage in a combustion test rig, however, requires carefully designed hardware and proper understanding of the underlying physics (see Sec. 4).

Beside the design of the measurement hardware, the extraction of the cross-sectionally averaged temperature or the radial temperature field is an important aspect. Based on a singular value decomposition (SVD), an extraction method has been found, which provides a reliable quantitative measure of the cross-sectionally averaged temperature as a function of the entropy waves phase angle. Several tomographic methods have been employed to find a way for the assessment of the radial temperature field at a sufficiently high spatial resolution. There exist a lot of different tomographic methods and mathematical approaches to solve the associated inverse problems. Finding the most appropriate one for the particular spatial arrangement of the present experimental setup has been one of the main tasks. A comprehensive introduction to various extraction techniques that have been considered in this study, can be found in Sec. 2.3.1 and Sec. 2.3.2.

1.2.2 Characterization and low-order modeling of entropy waves

The purpose of the low-order models in the framework of this study has been to provide an analytical tool that allows for a quantitative estimation of the strength and the phase of an entropy wave in a combustor. The required input to the model should be reduced to a minimum in order to make the model applicable for an upfront estimation of the relevance of entropy waves in a given combustor geometry. On the other hand, the experimental analysis of entropy waves under variation of several parameters should lead to a better understanding of the underlying physics in terms of generation and advection of entropy waves.

The measurement technique, that has been developed in this study, allows for the very first time for an investigation of the generation and transport mechanisms of entropy waves under realistic combustor conditions. To do so, the TOF setup has been utilized at an atmospheric combustion test rig with a swirl stabilized flame fed by a lean mixture of natural gas and air. A fraction of the fuel flow rate has been modulated by a valve in order to generate well-defined equivalence ratio fluctuations that in turn cause entropy fluctuations to advect downstream from the reaction zone. Varying the relevant parameters, like the bulk flow velocity, the advection distance between flame and measurement plane, and the excitation frequency, enables a comprehensive investigation of the entropy wave's characteristics. Additionally, the equivalence ratio fluctuations in the mixing section of the burner have been assessed by means of a TDLAS approach and the global OH^*-chemiluminescence intensity has been measured in the reaction zone.

A well-stirred reactor model has been derived to obtain the frequency response of entropy fluctuations with respect to the corresponding equivalence ratio fluctuations. Such

models have also been developed by others on a theoretical basis as measurement data of entropy waves just downstream of a reaction zone did not exist so far (T. Lieuwen, Neumeier, et al., 1998). A detailed description and discussion can be found in Sec. 6.1.

To find a model that is capable to predict the attenuation of the entropy perturbation during its advection from the reaction zone to the combustor exit, the transport mechanisms need to be analyzed. The advection of passive scalars in ducts is experimentally as well as analytically studied since many decades (e.g., Taylor (1953); H. A. Becker et al. (1966)). In terms of entropy waves, the approaches have so far been of rather theoretical nature. In several studies, the dissipation has simply been neglected or a complete smearing out of the entropy wave on its way to the turbine inlet has been assumed. Sattelmayer (2002) was the first to take aerodynamic effects and dispersion into account. His approach has been taken up by Morgans, Goh, et al. (2013), who compared their theoretical considerations with numeric calculations. An experimental validation of these models has recently been conducted by Giusti et al. (2017). They generated temperature fluctuations in a pipe flow by periodic variation of the equivalence ratio, which causes the fuel-air mixture to be periodically ignited at the location of a glow plug at one axial position in the duct. The resulting alternating temperature is assessed by thin thermocouples at two axial locations. This study provides a comprehensive comparison and validation of the existing models, especially with regard to the influence of the mean flow field on the dissipation mechanisms. However, the measurement technique used in Giusti et al. (2017) is not applicable to realistic gas turbine combustors. This makes the experimental results in the present study a valuable addition to the model validations so far.

The existing models described above suffer from the requirement of at least one empirical constant. Thus, scope of this study was also to derive a one-dimensional model that ideally does not require detailed flow field information and delivers amplitude and phase of an entropy wave at an arbitrary axial location in the combustor. The required initial amplitude of the entropy wave due to equivalence ratio fluctuations is provided by the generation model (reactor model) introduced above. The derivation of the models and their comparison with the measurements is presented in Chapter 6.

2 Theory

This chapter is comprised of three sections. The first section deals with the term “entropy wave” and introduces the basic thermodynamic definitions required for an understanding of the interaction between equivalence ratio, heat release rate, and entropy.
⇒ Section 2.1

The subsequent section examines the idea of the time-of-flight method and the associated issues that have to be taken into account. An introduction is given to existing TOF methods and corresponding investigations in literature; formulations are presented for the flight times in the case of acoustic propagation in inhomogeneous media.
⇒ Section 2.2

Finally, methods are derived and presented, which allow for the extraction of temperature data based on the TOF measurements. Their particular advantages and disadvantages are discussed regarding their applicability to the experimental setup in this study. The most appropriate tomographic approaches, that have been chosen from the large number of methods that exist in literature, are presented in more detail. At the end, the mathematical methods that are required to solve the inverse problems associated with the tomographic algorithms are introduced.
⇒ Section 2.3

2.1 Entropy waves

The central term of this work is the *entropy wave*. This is a rather vague notion as it might easily be confused with a wave in the context of acoustics, associated with a plane wave propagation at the speed of sound. Alternative phrases that can be found in literature are "entropy fluctuations", "convected entropy spots", or "hot spots". However, Cumpsty and Marble (1974) were one of the first who introduced the term "entropy wave" and it became the common designation for advecting entropy perturbations.

In this section the thermodynamic idea and definition of *entropy* as such is summarized and its production term, which is crucial for the understanding of the phenomenon of entropy waves, is derived. One goal of this chapter is to give a justification for the use of a temperature fluctuation measurement as a sufficient means to investigate entropy fluctuations. This assumption is often used in literature (e.g., Morgans, Goh, et al. (2013), Giusti et al. (2017)) and will also be utilized in the present study. A large amount of literature exists on thermodynamics and there are slightly different formalisms applied by different authors; here, for the preparation of this section, the following books and articles have been consulted: Falk and Ruppel (1976), Alberty (2009), I. Müller and W. Müller (2009), Chu (1965), E. Becker (1968).

Definition of entropy

The quantity entropy has been introduced to express the second law of thermodynamics. It says that the natural heat flux is always directed from a high temperature reservoir to a colder reservoir; without any external force it is impossible to take place in opposite direction. Work that is performed by a heat engine, which makes use of the aforementioned natural heat transfer, could not completely convert the mechanical work into a heat transfer process that transfers the same amount of heat from the colder reservoir back to the reservoir of higher temperature. A part of it would be "lost" in the form of "wasted heat". This fact can also be expressed in terms of the reversibility of a process. If a thermodynamic process is considered as reversible, its initial thermodynamic state can be recovered without any intervention from outside the system. Entropy describes this fact via the following equality, as the change of entropy dS is defined as

$$dS = \frac{\delta Q}{T}. \tag{2.1}$$

For an ideally reversible and adiabatic process (= isentropic), the entropy in the homogeneous and closed system does not change ($dS = 0$ as $\delta Q = 0$), whereas for real processes, which are irreversible, entropy is generated ($dS > 0$). The irreversibility stems, e.g., from friction or chemical reactions. The temperature in Eq. 2.1 refers to the absolute temperature where the heat addition or the heat release occurs. The δ symbolizes that the heat Q is a process variable and depends on how it is created, so it is not a mathematical absolute differential as used for the state variable S. While the temperature is an intensive property which provides information about the thermodynamic balance of a system, entropy is an extensive quantity. Heat exchange does only exist in the presence of a temperature gradient, which causes the countable amount of entropy in the higher temperature system to decrease and the temperature in the lower temperature reservoir

to increase. Together, temperature and entropy are also considered as conjugate pair (TdS). This is analogous to the mechanical volume work δW performed by a system which is expressed by the conjugate pair of pressure and volume ($\delta W = -pdV$) or the energy released from a chemical reaction $\Gamma_{\text{chem.}}$ described by the number of molecules N and the chemical potential μ of the species as $\Gamma_{\text{chem.}} = \mu dN$ (Alberty, 2009).

Note that entropy is not a conserved quantity, it cannot be destroyed but it can increase. However, this should not be confused with the ability of entropy to diminish if entropy is transferred from one system to another.

Entropy can now be used to express the change of the internal energy dE of a system as

$$dE = TdS - pdV + \sum_{i=1}^{m} \mu_i dN_i, \tag{2.2}$$

where m denotes the number of different species within the system that might have different chemical potentials μ. The last term on the right side of Eq. 2.2 is added if the system is not a closed system but an open system or if a chemical reaction takes place within the system. The internal energy is altered if heat (TdS) is added or released, volume work (pdV) is performed on the system or performed by the system, or a chemical reaction (μdN) takes place. The internal energy does not comprise the gravitational energy or the kinetic energy of the system as a whole, it summarizes all energy that is contained within the systems boundary.

Another convenient way to express the energy of a system, especially when looking at energy transfer between systems or thermodynamic cycles, is the enthalpy. It is defined as the internal energy plus the work done to "create space" for the system:

$$H = E + pV \tag{2.3}$$

As the entropy S and the internal energy E, also the enthalpy H is an extensive quantity. Combining Eq. 2.2 and Eq. 2.3 and employing the identity $d(pV) = pdV + Vdp$, a change in enthalpy writes

$$dH = TdS + Vdp, \tag{2.4}$$

where in Eq. 2.4 it is assumed that the number of elements within the system does not change ($dN = 0$). For isobaric processes ($dp = 0$), the enthalpy change becomes a function of the entropy change at a certain temperature only. The latter is for example convenient when looking at the ideally isobaric combustion process in a Brayton cycle of a gas turbine.

For the investigation of the energy balance including chemical reactions, the definition of an additional kind of energy, *Gibbs free enthalpy* G, is introduced as

$$G = E + pv - TS = H - TS. \tag{2.5}$$

It will be seen in a subsequent section how this equation is utilized.

Another important correlation is obtained by the derivative of Eq. 2.2 with respect to

the independent variables V, T, and N:

$$T\frac{\partial S}{\partial T}dT + T\frac{\partial S}{\partial V}dV + T\frac{\partial S}{\partial N}dN = \frac{\partial E}{\partial T}dT + \left(\frac{\partial E}{\partial V} + p\right)dV + \left(\frac{\partial E}{\partial N} - \mu\right)dN. \tag{2.6}$$

If the volume as well the number of particles does not change, Eq. 2.6 reduces to

$$T\left(\frac{\partial S}{\partial T}\right)_{V,N} = \left(\frac{\partial E}{\partial T}\right)_{V,N} := C_v, \tag{2.7}$$

where C_v is defined as the heat capacity at constant volume (and constant number of particles). The heat capacity is considered as the heat that is added to a system per increase of temperature. Combining Eqs. 2.6 and 2.7 and applying the assumption that the number of particles of the system remains constant, the change in entropy reads:

$$dS = \frac{C_v}{T}dT + \frac{\partial p}{\partial T}dV \tag{2.8}$$

Analogous to the derivative of Eq. 2.2 with respect to all independent variables, the same can be applied on the enthalpy definition in Eq. 2.4. Here we assume constant pressure and again a constant number of particles which leads to the definition of the heat capacity C_p as

$$T\left(\frac{\partial S}{\partial T}\right)_{p,N} = \left(\frac{\partial H}{\partial T}\right)_{p,N} = \left(\frac{\partial E}{\partial T}\right)_{p,N} - p\left(\frac{\partial V}{\partial T}\right)_{p,N} := C_p. \tag{2.9}$$

So for a constant number of particles the change in entropy reads:

$$dS = \frac{C_p}{T}dT - \frac{\partial V}{\partial T}dp. \tag{2.10}$$

C_p as well as C_v can experimentally be determined for arbitrary substances and can be assumed to be constant for low temperatures. At temperatures that are relevant in combustion processes, however, the increase of the heat capacity with increasing temperature cannot be neglected anymore. It stems from the heat absorption of molecules as they significantly start to vibrate at high temperatures as well as from the dissociation process of molecules. This temperature dependence has been measured between 100 K and 6000 K and corresponding correlations can be found in McBride et al. (1993).

An important step is the introduction of specific quantities, so the quantities per number of particles N in the system. This could be the number of molecules in units mol or, for a closed system, where the number of molecules of each species remains constant, the mass of all particles in unit kg. The scaling of S, V, E, and H to Ns, Nv, Ne, and Nh is essential because it transforms the extensive quantities to intensive quantities. We will see later why this is of importance for the understanding of the generation of entropy waves. Note that the equations above (Eq. 2.1 to Eq. 2.10) can all be written with the extensive quantities replaced by its corresponding specific value because all variables within the equations depend on specific or intensive variables. Systems that allow the transformation of extensive quantities into specific quantities are referred to as *homogeneous systems*. However, this should not be confused with homogeneity in

the sense of a spatially homogeneous parameter field as it will be used in subsequent sections.

In this study we are purely interested in gaseous media. So, after we derived the principle idea of entropy and how it correlates with temperature, other forms of energy, pressure, volume, and heat capacity, we look on how the entropy of an ideal gas can be determined.

Ideal gas

Two requirements have to be fulfilled for a gaseous medium to be considered as an ideal gas. The product between the volume of the gas and the pressure has to correlate linearly with temperature

$$pV = NR_uT \tag{2.11}$$

and the internal energy of the gas must not depend on the volume of the gas

$$\frac{\partial E}{\partial V} = 0. \tag{2.12}$$

Equation 2.11 is known as the *thermodynamic state equation* or the *ideal gas law* and writes for intensive quantities $pv = R_gT$, where the universal gas constant R_u is replaced by the specific gas constant R_g and. This leads to the beneficial situation that the internal energy e, the enthalpy h as well as the specific heat capacities c_v and c_p of the ideal gas only depend on the temperature T. The lower the density of a gas, the better does it match the criteria of an ideal gas (Falk and Ruppel, 1976).

The change of the specific entropy Δs of an ideal gas from a state (0) to a state (1) can be expressed as a function of temperature T and specific volume v based on Eq. 2.8 as

$$\Delta s(T, v) = \int_{(0)}^{(1)} \left(\frac{c_v}{T} dT + \frac{\partial p}{\partial T} dv \right) \tag{2.13}$$

or based on Eq. 2.10 as a function of T and pressure p, which leads to

$$\Delta s(T, p) = \int_{(0)}^{(1)} \left(\frac{c_p}{T} dT + \frac{\partial v}{\partial T} dp \right). \tag{2.14}$$

We can now use Eq. 2.11 to replace the pressure p in Eq. 2.13 and the volume v in Eq. 2.14 and obtain by integration

$$\Delta s(T, v) = c_v \ln\left(\frac{T_1}{T_0}\right) + R_g \ln\left(\frac{v_1}{v_0}\right) \tag{2.15}$$

$$\Delta s(T, p) = c_p \ln\left(\frac{T_1}{T_0}\right) - R_g \ln\left(\frac{p_1}{p_0}\right). \tag{2.16}$$

Here, use has been made of $R_g = c_p - c_v$, which can be obtained from combining Eq. 2.3, Eq. 2.7, and Eq. 2.9. The change in specific entropy thus consists of one part that depends on temperature only and another part that depends on the change in volume or pressure for constant pressure or volume, respectively.

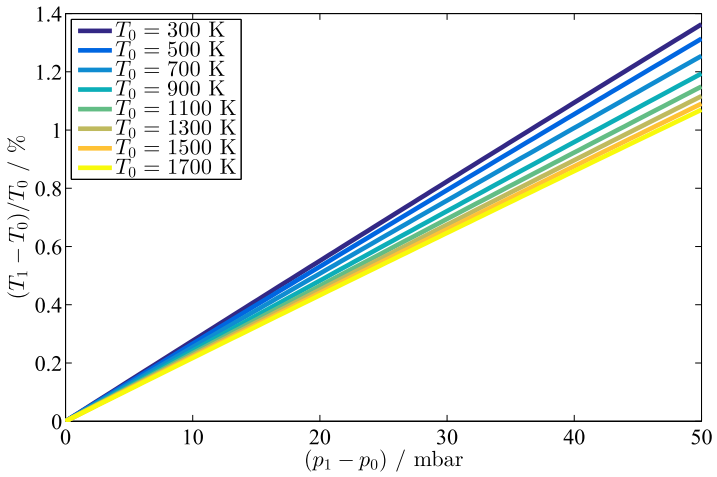

Figure 2.1: Isentropic state equation of pressure and temperature according to Eq. 2.17 for different temperatures T_0; $p_0 = 101325\,\mathrm{Pa}$; γ is evaluated by means of T_0 according to McBride et al. (1993).

For an isentropic change of state, so when $\Delta s = 0$, Eq. 2.15 and Eq. 2.16 lead to

$$\left(\frac{v_0}{v_1}\right)^{\gamma-1} = \left(\frac{p_1}{p_0}\right)^{\frac{\gamma-1}{\gamma}} = \frac{T_1}{T_0}, \tag{2.17}$$

where the isentropic exponent γ is defined as $\gamma = c_p/c_v$. A typical example where isentropic changes of states are assumed are acoustic waves, as their pressure amplitudes are usually very small compared to the mean pressure. In Fig. 2.1, the change in temperature is plotted for various temperatures T_0 as a function of the pressure deviation from the mean ambient pressure p_0. The range of the pressure deviation is chosen such that it corresponds to realistic values in the model gas turbine combustor investigated in this study. It can be seen that the temperature deviates by approximately 1 %.

In Eqs. 2.15-2.16, the difference in entropy between a state (0) and a state (1) is obtained. For sufficiently small changes we can make use of linearization, where each variable is represented by a steady term $\overline{(.)}$ and its fluctuating part $(.)'$. Applying linearization on Eq. 2.15 and Eq. 2.16 and introducing the density $\rho = 1/v$ yields the following three equations for s':

$$s' = c_v \frac{p'}{\overline{p}} - c_p \frac{\rho'}{\overline{\rho}} \tag{2.18}$$

$$s' = c_p \frac{T'}{\overline{T}} - R_g \frac{p'}{\overline{p}} \tag{2.19}$$

$$s' = c_v \frac{T'}{\overline{T}} - R_g \frac{\rho'}{\overline{\rho}}. \tag{2.20}$$

All these equations can be transformed into each other by using the equations obtained from linearization of the state equation for an ideal gas (Eq. 2.11). From Eq. 2.19 we can see that in case of zero or negligible pressure fluctuations, the entropy fluctuations are proportional to the temperature fluctuations. This assumption is often employed in literature (e.g., Morgans, Goh, et al. (2013); Strobio Chen et al. (2016)) and has also

been applied in the present study:

$$s' = c_p \frac{T'}{\overline{T}}. \tag{2.21}$$

Note, Eqs. 2.18-2.20 are only valid for small fluctuations of the quantities with respect to their mean value. The definition of "small" is not exactly quantified but as a rule of thumb it is approximated as $\approx 10\,\%$.

So far, we only considered a gaseous medium at rest that undergoes a change of its energy state due to heat addition (and, if not neglected, its pressure). We also derived an expression for a small fluctuation in entropy. In the following section, we apply these theoretical considerations to a model combustion chamber setup as investigated in this study.

Model combustion chamber

In this section, the chain of the generation of entropy waves in a model gas turbine combustor is described. A schematic of a combustor setup similar to the combustor used in the experimental part of this study is shown in Fig. 2.2.

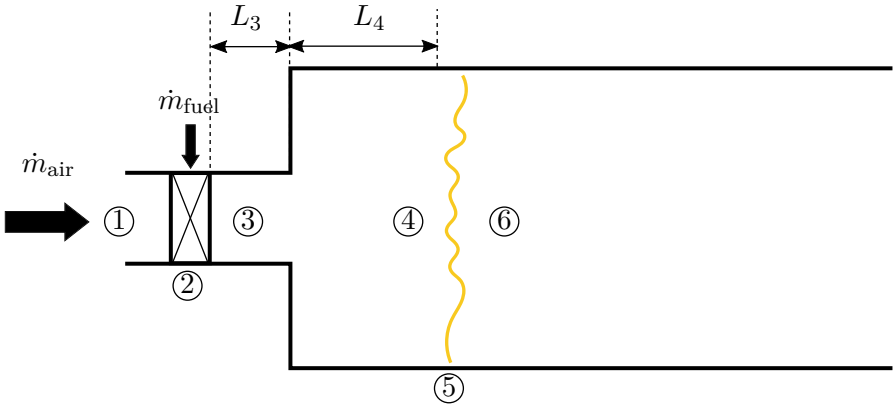

Figure 2.2: Scheme of burner with air entering from the left (①) followed by the fuel injection into the swirler (②), the mixing duct (③), and the combustion chamber where the air-fuel mixture (④) is oxidized in the flame front (⑤) and entropy waves might advect downstream of the flame (⑥).

Equivalence ratio fluctuations (①→④)

In the following, a formulation is derived to estimate the fluctuation of the equivalence ratio between the fuel injection upstream of the mixing tube and the flame front. The driving mechanisms have been investigated, inter alia, by Schuermans (2003) and T. Lieuwen, Torres, et al. (2000), whose derivations are used here. The (fuel-air) equivalence ratio ϕ indicates the stoichiometric regime of a mixture of a fuel mass flow $\dot{m}_{\mathrm{fuel}}$ and an air mass flow $\dot{m}_{\mathrm{air}}$. It is defined as

$$\phi = \frac{1}{\varsigma} \frac{\dot{m}_{\mathrm{fuel}}}{\dot{m}_{\mathrm{air}}}, \tag{2.22}$$

where ς represents the ratio $\dot{m}_{\mathrm{fuel}}/\dot{m}_{\mathrm{air}}$ required for stoichiometric combustion and hence depends on the composition of the fuel. Fluctuations of the equivalence ratio can either occur due to fluctuations of the fuel mass flow $\dot{m}'_{\mathrm{fuel}}$ or due to a fluctuation of the air mass flow $\dot{m}'_{\mathrm{air}}$. If we neglect any inhomogeneities of the fuel composition ($\varsigma = \mathrm{const.}$), linearization of Eq. 2.22 gives

$$\frac{\phi'}{\overline{\phi}} = \frac{\dot{m}'_{\mathrm{air}}}{\overline{\dot{m}}_{\mathrm{air}}} + \frac{\dot{m}'_{\mathrm{fuel}}}{\overline{\dot{m}}_{\mathrm{fuel}}} = -\frac{\rho'_{\mathrm{air}}}{\overline{\rho}_{\mathrm{air}}} - \frac{u'_{\mathrm{air}}}{\overline{u}_{\mathrm{air}}} + \frac{\rho'_{\mathrm{fuel}}}{\overline{\rho}_{\mathrm{fuel}}} + \frac{u'_{\mathrm{fuel}}}{\overline{u}_{\mathrm{fuel}}}. \tag{2.23}$$

The assumption of $\overline{\dot{m}}_{\mathrm{air}} \gg \overline{\dot{m}}_{\mathrm{fuel}}$ and of a high pressure loss from the fuel injection line to the mixing tube of the burner allows for simplification of Eq. 2.23. To do so, the incompressible Bernoulli equation (neglecting gravitational effects) is employed to derive an expression for the fuel mass flow:

$$\dot{m}_{\mathrm{fuel}} = \sqrt{2\rho_{\mathrm{fuel}} p} S_{\mathrm{f}}, \tag{2.24}$$

where S_{f} denotes the cross-sectional surface area of the fuel supply line. Linearization applied to Eq. 2.24 leads to

$$\frac{\dot{m}'_{\mathrm{fuel}}}{\overline{\dot{m}}_{\mathrm{fuel}}} = \frac{1}{2}\frac{\rho'_{\mathrm{fuel}}}{\overline{\rho}_{\mathrm{fuel}}} + \frac{1}{2}\frac{p'}{\overline{p}}. \tag{2.25}$$

It can now be seen that for a high pressure loss, which means high values of $\overline{\rho}_{\mathrm{fuel}}$ and $\overline{p}$, the fuel mass flow fluctuations become very small and can thus be neglected in Eq. 2.23. This gives

$$\frac{\phi'_2}{\overline{\phi}} = -\frac{\rho'_{\mathrm{air}}}{\overline{\rho}_{\mathrm{air}}} - \frac{u'_{\mathrm{air}}}{\overline{u}_{\mathrm{air}}}, \tag{2.26}$$

where ϕ'_2 denotes the equivalence ratio fluctuation at the outlet of the swirler. The average equivalence ratio $\overline{\phi}$ is constant from ② to ④: $\overline{\phi}_2 = \overline{\phi}_3 = \overline{\phi}_4 = \overline{\phi}$.

From Eq. 2.26 we can see that equivalence ratio fluctuations are generated whenever the mass flow of air passing the fuel injection section is disturbed, e.g., by acoustic perturbations. In technical applications the air flow is always perturbed and this can even be enhanced by a feedback loop that might be established between the equivalence ratio fluctuations, the heat release rate fluctuation, and the thereby generated acoustic waves (Huber, 2009; Peracchio and Proscia, 1999; T. Lieuwen and Zinn, 1998; Ćosić, Terhaar, et al., 2015). In addition, the assumption of a perfectly stiff fuel supply line does not hold in many applications and depends on its impedance (Schuermans, 2003; Huber, 2009).

As will be shown in more detail in Sec. 5, in the combustion test rig experiments conducted in this study, equivalence ratio fluctuations are forced via a periodic modulation of the fuel supply. In such a case, the very right term in Eq. 2.23 becomes dominant over the relative fluctuations of velocity and density in the air mass flow. For sufficiently large amplitudes of the fuel modulation, the first two terms on the r.h.s. of Eq. 2.23 could be neglected and Eq. 2.23 writes for the modulated equivalence ratio fluctuation ϕ'_{mod}:

$$\frac{\phi'_{\mathrm{mod}}}{\overline{\phi}} \approx \frac{u'_{\mathrm{fuel}}}{\overline{u}_{\mathrm{fuel}}}. \tag{2.27}$$

Generated at the axial location where the fuel is injected, the equivalence ratio fluctuation is advected downstream through the mixing duct into the combustion chamber and finally reaches the flame front. In literature, the transport from the injection plane to the flame has very often been assumed to happen without diffusion or dispersion (e.g. Polifke, Kopitz, et al. (2001), Hubbard and A. Dowling (1998)). If additionally the fuel injection is assumed to occur at one point in space, the equivalence ratio fluctuation at the flame front downstream of the injection plane can be estimated via a simple time lag τ_ϕ as $\phi'_4(t) = \phi'_2(t - \tau_\phi)$ with $\tau_\phi = L_3/\overline{u}_3 + L_4/\overline{u}_4$.

If the complex flow field in a combustor, especially between the swirl generator and the spatially distributed flame front, is considered, a simple time lag model does not longer reflect the transport of an equivalence ratio fluctuation. A distributed time lag model, as introduced by Sattelmayer (2002), allows to account for the dispersion of the equivalence ratio fluctuation when advected through mixing tube and combustion chamber inlet to the flame front. In the frequency domain with the angular frequency ω, his transfer function of the equivalence ratio fluctuation at the flame $\hat{\phi}_4$ and at the injection location $\hat{\phi}_2$ reads

$$\frac{\hat{\phi}_4(\omega)}{\hat{\phi}_2(\omega)} = -\frac{i\omega(1+k\Delta\tau)-k}{2\Delta\tau\omega^2}\left[e^{i\omega\Delta\tau\left(1-\frac{\tau_\phi}{\Delta\tau}\right)} - e^{-i\omega\Delta\tau\left(1+\frac{\tau_\phi}{\Delta\tau}\right)}\right]. \tag{2.28}$$

The variable $\Delta\tau$ denotes the temporal expansion of the arrival of the equivalence ratio pulse at the flame front. Hereby it is assumed that the equivalence ratio fluctuation generated at the fuel injection is a very short rectangular pulse which undergoes distortion due to dispersion and diffusion. While $\Delta\tau$ accounts for the spatio-temporal widening of the equivalence ratio pulse, the parameter k in Eq. 2.28 describes in a sense a distortion in shape with respect to a perfect rectangular pulse. The latter, however, does not significantly affect the result. This model for the transport of a scalar will appear in Sec. 6.2 for the characterization of the transport of entropy fluctuations from the flame through the combustion chamber.

Blümner et al. (2016) have shown for fluctuation frequencies between approximately 100 Hz and 500 Hz that the transfer function between the velocity fluctuation upstream of the fuel injection plane and the resulting equivalence ratio in the mixing section also strongly depends on the excitation frequency. To account for this effect, their measurement technique has been used in this study to assess the equivalence ratio fluctuations just upstream of the burner in the mixing tube, which makes a detailed modeling of the transport of the equivalence ratio fluctuation from the injection point to the flame redundant (see Sec. 5.4.1.1).

The flame as source of entropy waves (⑤→⑥)

We have so far found an estimation of how an equivalence ratio fluctuation is generated and a model is presented that describes the transport of the equivalence ratio fluctuation from its origin to the flame front. Now we are going to examine how the equivalence ratio fluctuations cause entropy fluctuations. Therefore, we first start with a very simple consideration of a thin flame front which can be assumed to be compact with respect to the wavelengths of the equivalence ratio fluctuations λ_ϕ. The latter is of the order

$\lambda_\phi = \overline{u}/f_\phi$, where f_ϕ denotes the frequency of the equivalence ratio fluctuation and $\overline{u}$ represents the bulk velocity.

To derive a relation between the equivalence ratio and the entropy that is generated within the reaction zone ⑤, we have to refer back to the definition of Gibbs free enthalpy in Eq. 2.5. A gas mixture is defined to be in its chemical equilibrium if the total differential of the Gibbs enthalpy equals zero, which gives by combining Eqs. 2.5 and 2.2:

$$dG = V\,dp - S\,dT + \sum_{i=1}^{m} \mu_i dN_i = 0. \tag{2.29}$$

The chemical potential μ_i is defined as the free energy that is added or substracted from a system when a number of N_i units of the i-th species is added or taken from the system. As an example we consider the oxidation reaction of methane:

$$\mathrm{CH_4} + 2\mathrm{O_2} \rightarrow 2\mathrm{H_2O} + \mathrm{CO_2}. \tag{2.30}$$

For this reaction, which is assumed to take place completely, so all educts are transformed to products, the sum of the chemical potentials μ^0 at standard conditions ($T_0 = 298.15\,\mathrm{K}$; $p_0 = 1\,\mathrm{bar}$) reads:

$$\sum_{i=1}^{m} \mu_i^0 dN_i = -1\mu^0_{\mathrm{CH_4}} - 2\mu^0_{\mathrm{O_2}} + 2\mu^0_{\mathrm{H_2O}} + 1\mu^0_{\mathrm{CO_2}} \tag{2.31}$$

For an ideal mixture of gases at a temperature $T \neq T_0$ and a pressure $p \neq p_0$ the chemical potential is defined as

$$\sum_{i=1}^{m} \mu_i dN_i = \sum_{i=1}^{m} \left[\mu_i^0 dN_i + R_g T dN_i \ln\left(\frac{p_i}{p_0}\right) \right], \tag{2.32}$$

where p_i denotes the partial pressure of the ith component of the number of m different species the mixture consists of (Warnatz et al., 2009; Alberty, 2009). For an ideal gas, the first term on the r.h.s. of Eq. 2.32 can be expressed by means of the standard reaction enthalpy $\Delta_r H^0$ and the standard reaction entropy $\Delta_r S^0$:

$$\sum_{i=1}^{m} \mu_i^0 dN_i = \Delta_r H^0 - T\Delta_r S^0. \tag{2.33}$$

The values for $\Delta_r H^0$ and $\Delta_r S^0$ in Eq. 2.33 have experimentally been determined for a large number of species and can be looked up in tables in literature. The definition of the standard reaction entropy is based on the third law of thermodynamics, which says that for a theoretical state of zero temperature $T = 0\,\mathrm{K}$ also the absolute entropy equals zero: $S(T = 0) = 0$. Thus, for a determined value of the total entropy $S^0(T_0)$ at a temperature T_0 and standard pressure, the standard reaction entropy at a temperature T_1 can be obtained via

$$\Delta_r S^0(T_1) = \sum_{i}^{m} dN_i \left[s_i^0(T_0) + \int_{T_0}^{T_1} \frac{c_{p,i}}{T} dT \right]. \tag{2.34}$$

For the combustion process in a model gas turbine combustor, the pressure remains

constant across the flame front. Furthermore, as we assume a complete combustion process over the flame front, we consider chemical equilibrium just downstream of the flame front after the reaction took place. Therefore, the first two terms on the r.h.s. of Eq. 2.29 equal zero as the pressure as well as the temperature do not change anymore. The combination of Eqs. 2.29, 2.32, and 2.33 finally results in

$$\Delta_r H^0(T) = T\Delta_r S^0(T), \tag{2.35}$$

where $\Delta_r H^0$ denotes the standard reaction enthalpy determined for standard pressure as

$$\Delta_r H^0(T) = \sum_i^m dN_i \left[h_i^0(T_0) + \int_{T_0}^{T} c_{p,i} dT \right]. \tag{2.36}$$

Finally, the growth in entropy due to the isobaric chemical reaction at atmospheric conditions can be expressed with specific quantities as

$$\Delta s = s_6 - s_5 = \frac{\Delta_r h^0(T_6)}{T_6} - \sum_i^m s_i^0(T_5). \tag{2.37}$$

Here, the sum of $s^0(T_5)$ over all species refers to the standard entropy of the unburned gas mixture. So the amount of entropy that is generated (or the heat $q = T_6 \Delta s$ that is released) depends on the reaction enthalpy. An equivalence ratio fluctuation with a convective wavelength that is much larger than the reaction zone would lead to an entropy wave of same frequency. Its amplitude can be deduced from the standard reaction enthalpies of the educts.

It is hereby also explained why entropy perturbations can only be generated by equivalence ratio fluctuations (either caused by fuel mass flow fluctuations, air mass flow fluctuations upstream of the injection, or by fluctuations of the fuel or air properties). Thus, in case of a perfectly premixed fuel-air mixture, no entropy waves could be generated. It is worth noting that heat release rate fluctuations in the flame zone do not necessarily coincide with entropy fluctuations. An acoustic perturbation may lead to a heat release rate fluctuation in a combustor fed with a perfect mixture of the reactants. However, in such a case, the gas composition and thus the right-hand side of Eq. 2.37 remains unchanged and consequently no entropy wave is generated. For a more comprehensive insight into this topic area, the reading of Strobio Chen et al. (2016) is recommended.

Summary on entropy waves

In this section, the thermodynamic definitions have been presented that are required to describe the formation process of entropy perturbations due to equivalence ratio fluctuations. Linearization of the equation that describes the change in entropy due to a change in pressure and temperature allows for the derivation of an expression for entropy fluctuations. If pressure perturbations are neglected, entropy waves can be considered to correlate linearly with temperature. The further investigations in this study rely highly on this hypothesis.

2.2 Measurement technique: the time-of-flight approach

The general idea of a TOF measurement method is the estimation of substance properties based on the detection of the traveling time of any kind of matter, particle, or wave. The measure of the propagation time leads back to other quantities, e.g., a path length between emitter and receiver, the (line averaged) traveling speed, or the mass of the particle in motion. The latter is for example used in mass spectroscopy, where the travel time is proportional to the square root of the ratio between the mass and the charge of an ion (Wiley and McLaren, 1955). This technique allows for the identification of specific atoms or molecules within a gas mixture. A very common and standard method for distance measurements are laser rangefinders, where by means of the analysis of the phase relation between a transmitted and the corresponding received light signal the distance between emitter and receiver is deduced.

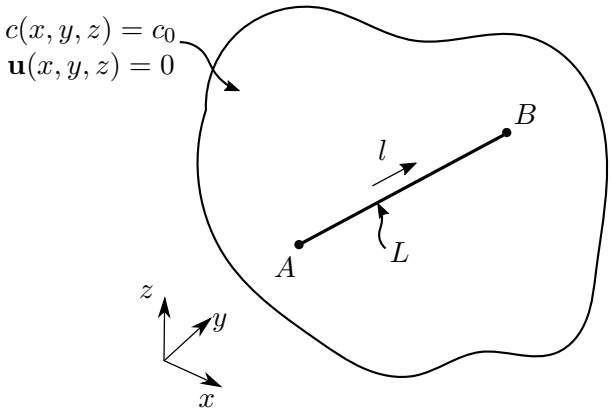

Figure 2.3: Schematic of the Time-of-Flight approach for a general case in an inhomogeneous three-dimensional space.

In this study, a special case of the TOF is employed, the so-called *acoustic pyrometry*. Here, the traveling time of an acoustic pulse is used as a measure of the integral speed of sound between an emitter and a receiver. In a very simplistic consideration, where a homogeneous medium with a constant speed of sound ($c(x,y,z) = c_0$) and no advection is assumed, the time of flight τ along a geometrical path of length L between an acoustic emitter and a receiver writes:

$$\tau = \int_L \frac{1}{c_0} dl, \tag{2.38}$$

where l denotes the spatial variable along the acoustic path. Equation 2.38 refers to the *forward problem*, where τ is determined by the speed of sound if L is known. In a TOF approach, however, we are interested in the speed of sound, and we thus have to solve the *inverse problem*. The simplest way to estimate the temperature from a τ-measurement for a homogeneous medium at rest writes

$$\tau \Longrightarrow c = \frac{L}{\tau} \Longrightarrow T = \frac{c^2}{\gamma R_g}, \tag{2.39}$$

with the gas constant R_g and the ratio of the specific heats γ. In Sections 2.2.2 and 2.2.3 it will be shown that the solution of the inverse problem becomes more complex if quiescence and homogeneity are not assumed anymore.

The first, who used the term *acoustic pyrometer* for the acoustical determination of

the temperature within a volume was Mayer (1873). He, however, did not measure the arrival time of an acoustic signal but "counted the wavelengths" that fit into the volume the temperature should be determined in. So he indeed made use of the relation between temperature and speed of sound but rather determined the resonance frequency of the volume, which is a function of the speed of sound and thus of temperature. Mayer (1873) was driven by the motivation of determining the temperature in a furnance, which has also been the scope of various other research groups later on that investigated acoustic pyrometry (Green, 1985; Sielschott and Derichs, 1995; Bramanti et al., 1996; J. A. Kleppe et al., 1996; Deduck and Suplicki, 2008). In contrast to Mayer (1873), they use the measurement of the traveling time of an acoustic signal as a means for calculating the gas temperature along an acoustic path.

The high temperature and the large scales of (blast) furnances or other tanks for industrial processes are problematic for classical intrusive temperature measurement probes, such as thermocouples or thermistors. Moreover, these measurement techniques provide a temperature measure at only one point in space. Here, acoustic pyrometry has significant advantages as it provides a temperature measurement along an acoustic path and in case of large distances, it becomes even less prone to errors due to increasing traveling times. There are also recent studies on acoustic pyrometry in boilers and other industrial applications by G. Q. Shen et al. (2006) and Jia et al. (2016) that particularly focus on the tomographic reconstruction of the temperature field that becomes possible due to acoustic pyrometry. A detailed review on tomographic methods and its application on the measurements conducted in this study is given in Section 2.3.2.

The advantage of the TOF approach with respect to large distances between emitter and receiver, which decreases the relative error of the measured arrival time, is also utilized by other fields of application, namely oceanography (Striggow, 1985; Munk, Worcester, et al., 1995; Cornuelle et al., 2008; Ashraf and Qayyum, 2011; Ostashev and D. K. Wilson, 2016; Bjørnø, 2017) and meteorology (Ziemann et al., 1999; Vecherin et al., 2008). There, temperature gradients are detected in oceans or in the atmosphere over distances of hundreds of meters up to 1000 km (Munk and Wunsch, 1979). Especially in meteorology, use is made of the acoustic pyrometry's capability, that not only the temperature field but also the velocity field can be reconstructed. The impact of the flow field on the acoustics will be further discussed in Sec.2.2.2.

Most of the TOF methods comprise an acoustic source which is actively triggered. There are various options to achieve sufficient acoustic excitation, a brief overview over these possibilities and a comprehensive discussion on the technique used in this study is given in Sec. 4.1. Some few applications rely on the so-called *passive acoustic pyrometry*, where, e.g., the combustion noise itself is used as acoustic source which is detected by two acoustic receivers placed at a known distance apart from each other (J. A. Kleppe et al., 1996; J. Kleppe et al., 2004). Sketches of principle setups for the active as well as the passive acoustic pyrometry are depicted in Fig. 2.4.

Depending on the characteristics of the acoustic excitation signal (e.g., short pulse, continuous harmonic signal, frequency-sweep, etc.), the measurement conditions (reflective boundaries or approximately open space), and the kind of pyrometry, different methods are used for the determination of the travel time. This could be an extrema detection, as used in this study, or the cross-correlation between two signals (either the correlation

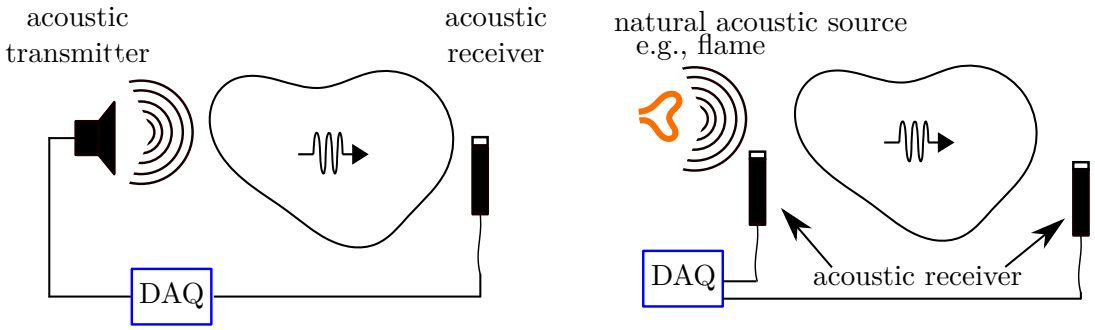

Figure 2.4: Exemplary sketches of active (left) and passive (right) acoustic pyrometry.

between the transmitted and the received signal (active pyrometry) or the correlation between two receivers (passive pyrometry)). In Sec. 4.2, the detection method used in this study is presented and discussed.

As can be seen in Eq. 2.38, the speed of sound is of central importance in this study, as its integral inverse is the quantity measured in the TOF method. It is worthwhile to look more into detail on how this scalar quantity is derived and which difficulties arise in case of an inhomogeneous temperature field. In the following sections, uncertainties and the corresponding assumptions that have to be made to obtain a measure of temperature from the TOF measurement will be discussed in detail.

2.2.1 Speed of sound in a quiescent medium

The speed of sound is defined as the propagation speed of an acoustic wave normal to its wave front. There exist two different definitions of acoustic velocities in literature, the *phase velocity* v_p and the *group velocity* v_g (e.g., Ostashev and D. K. Wilson (2016)). The phase velocity corresponds to the velocity of a certain phase of the wave (e.g. a crest of the wave) whereas the group velocity corresponds to the propagation velocity of the information of the wave as a whole (so to say the velocity of the envelope). For a homogeneous and non-dispersive medium at rest, the phase velocity can be considered in a first step to be equal to the group velocity. Consequently, in this case both match the speed of sound.

In the following, the speed of sound is first derived for isentropic conditions and in a second step, the influence of dispersion is discussed.

Adiabatic speed of sound

To obtain the propagation velocity of a sufficiently small pressure perturbation in a Newtonian fluid, we consider a homogeneous, compressible medium at rest within a duct of constant diameter. A pressure fluctuation is induced as a monopole at one point in space, whereas its amplitude is sufficiently small so that frictional losses due to viscosity can be neglected (A. Dowling and Williams, 1983). Furthermore, we assume an isentropic ideal gas, which is also named a barotropic flow, as the pressure depends on density only and vice versa. Isentropic conditions can be considered as it is assumed that

the change in pressure happens much faster compared to the heat transfer. Consequently, the mass and momentum conservation along a stream line in a duct write

$$\rho u = \text{const} \tag{2.40}$$

$$p + \rho u^2 = \text{const}, \tag{2.41}$$

where u represents the propagation velocity. We are interested in small perturbations of the mean quantities and therefore apply the total derivative on Eqs. 2.40 and 2.41, which yields

$$\rho du + u d\rho = 0 \tag{2.42}$$

$$dp + 2\rho u du + u^2 d\rho = 0. \tag{2.43}$$

Combining Eqs. 2.42 and 2.43 and solving for the propagation velocity u leads to

$$u = \sqrt{\frac{\partial p}{\partial \rho}} := c, \tag{2.44}$$

where c denotes the isentropic speed of sound (Rienstra and Hirschberg, 2004; Schade and Kunz, 1980). Hence, the propagation velocity of a pressure perturbation is a scalar state variable which is proportional to the change of pressure with respect to a density variation. This is not only valid for gases but also for solids and fluids. The result in Eq. 2.44 is quite intuitive, as for very stiff media, where a change in pressure causes only a very small change in the mediums density, a pressure information can propagate faster than in a rather compressible medium.

An expression for the partial derivative in Eq. 2.44 is derived from the caloric state equations. The specific internal energy u and the enthalpy h can be written in differential notation as

$$du = Tds - pdV \tag{2.45}$$

$$dh = Tds + \frac{1}{\rho} dp. \tag{2.46}$$

For an ideal gas, the ratio between the internal energy and the enthalpy is constant and well known as the isentropic exponent γ. With $ds = 0$ and $pdV = -(p/\rho^2)d\rho$, the formulation $\gamma = du/dh$ leads to the following expression:

$$\left(\frac{\partial p}{\partial \rho}\right)_s = \gamma \frac{p}{\rho}. \tag{2.47}$$

The isentropic exponent can also be written as $\gamma = c_p/c_v$, which is the ratio between the specific heat capacity at constant pressure ($c_p = dh/dT$) and the specific heat capacity at constant volume ($c_p = du/dT$) (Schade and Kunz, 1980). If the equation of state for an ideal gas $p/\rho = R_g T$ is applied to Eq. 2.47 and inserted into Eq. 2.44, the equation for the speed of sound is obtained as:

$$c = \sqrt{\gamma R_g T}. \tag{2.48}$$

The specific gas constant $R_g = c_p - c_v$ is defined as the difference between the specific heat

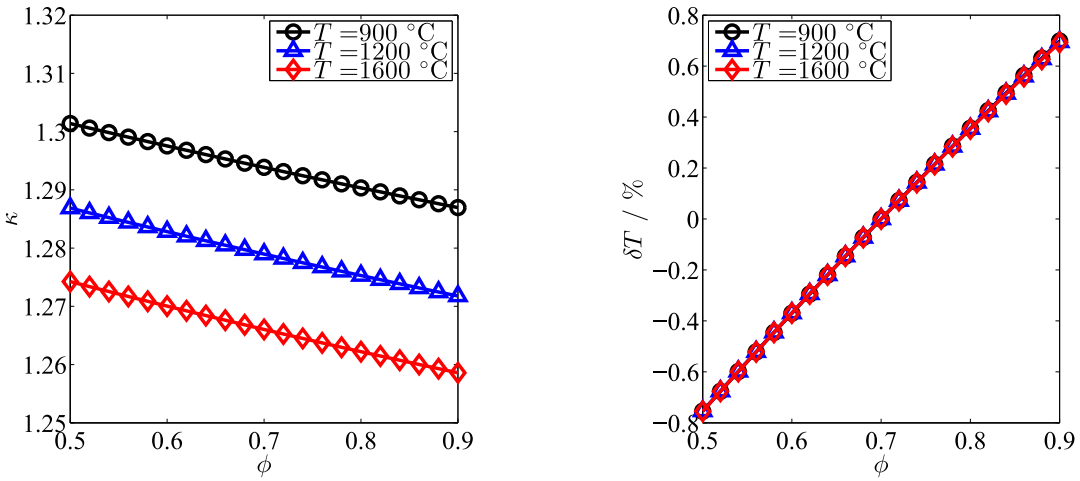

(a) **(b)**

Figure 2.5: **(a)**: Values for the ratio of the specific heats κ as a function of the equivalence ratio ϕ and for three gas temperatures; here, only the influence of the exhaust gas composition as shown in Eq. 2.49 is considered, temperature changes due to the ϕ-variation are not accounted. **(b)**: Percentage deviation of the evaluated gas temperature $\delta T = (T(\kappa(\phi)) - T_{\text{ref}})/T_{\text{ref}}$ around a reference temperature of $T_{\text{ref}} = T(\kappa(\phi = 0.7))$.

capacities. R_g is a function of the gas mixture and due to the temperature dependence of c_p also of temperature. The latter can be calculated by means of the NASA polynomials (McBride et al., 1993). Note, in some literature, the speed of sound in Eq. 2.48 is referred as the adiabatic speed of sound.

The accuracy of the determination of the adiabatic speed of sound strongly depends on the accuracy of the determination of the gas composition. In case of combustion experiments, where the TOF measurements are conducted in the exhaust gas, the gas mixture is affected by several phenomena. Apart from the fact that the gas composition is inhomogeneous in space, a temporal variation might be given due to fluctuations in the fuel or the air supply. The exhaust gas composition is approximated by the oxidation formula for methane:

$$\phi \mathrm{CH_4} + 2\mathrm{O_2} + \frac{158}{21}\mathrm{N_2} \Longrightarrow \phi 2\mathrm{H_2O} + \phi \mathrm{CO_2} + \frac{158}{21}\mathrm{N_2} + 2(1-\phi)\mathrm{O_2} \tag{2.49}$$

Apart from nitrogen, the concentrations of all molecules depend on the equivalence ratio ϕ. A change in the equivalence ratio causes, of course, a change in temperature which directly affects the speed of sound. But it also affects the gas composition and thus the ratio of the specific heats κ in Eq. 2.48. Therefore, in Fig. 2.5a, the κ-value of the exhaust gas is plotted as a function of the equivalence ratio only, not accounting for changes in temperature due to the variation in the equivalence ratio. As κ is a function of the temperature, the values for κ are shifted in Fig. 2.5a if different gas temperatures T are assumed.

In this study, the influence of the correct assessment of the exhaust gas composition on the speed of sound and thus on the temperature estimation is of interest. We define the percentage deviation between the temperature evaluated with $T = c^2/\kappa(\phi)/R_g$ and a reference temperature T_{ref} as $\delta T = (T(\kappa(\phi)) - T_{\text{ref}})/T_{\text{ref}}$ with $T_{\text{ref}} = T(\kappa(\phi = 0.7))$.

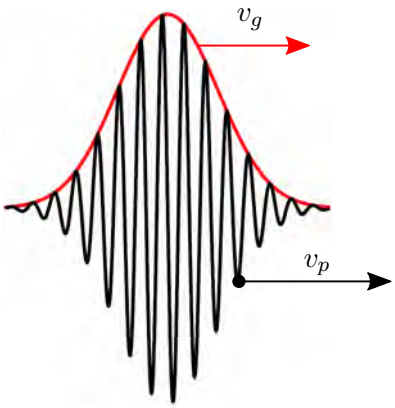

Figure 2.6: Sketch of an acoustic pulse signal, which is a superposition of multiple monofrequent signals, with the group velocity v_g and the phase velocity v_p.

The resulting temperature deviations are depicted in Fig. 2.5b for the same gas temperatures and in the same range of equivalence ratios as in Fig. 2.5a. Even for this wide range of ϕ, the deviation is well below 1 %. As the uncertainty of the gas composition would rather be of the order of $\phi = \pm 0.05$, an error in temperature of maximum 0.2 % needs to be considered.

Note, the preceding analysis assumes the oxidation of methane rather than natural gas, which has actually been used in the experiments in this study. However, as the exact composition of the natural gas and thus of the exhaust gas cannot be determined, methane is utilized as an approximation and we assume that the order of deviation in κ is comparable.

Dispersive effects

In the ultrasound regime, above approximately 20 kHz, molecular relaxation processes have to be considered (Borrell, 1967). Molecules can store energy in different states, e.g. translation, rotation, or vibration, whereas not all states are charged equally but certain states are preferred. So in case of an acoustic perturbation, the unsteady energy gain (or loss) is transformed between the different states. The time required for this energy absorption is called the *relaxation time* t_{relax}. For low frequencies, when $1/f \gg t_{\text{relax}}$, this time delay can be neglected, however, for $1/f \lessapprox t_{\text{relax}}$, this effect leads to an attenuation of the amplitude and the *phase velocity* becomes a function of frequency, which is defined as dispersion. As the different possible energy states of a molecule depend on its architecture, the relaxation times might differ significantly for various gases (Kuttruff, 1988).

In a dispersive medium, we have to differentiate between the group velocity v_g and the phase velocity v_p. This concept of analyzing the propagation behaviour will also be important in the upcoming sections. An illustration of the difference between group velocity and phase velocity is given in Fig. 2.6. The black signal is a superposition of various monofrequent signals. It will be shown in Section 4.1 that the order of frequencies between $10 - 100$ kHz is dominant in the acoustic pulse excitation applied in the TOF experiments in this study.

The determination of the attenuation and the dispersion is not trivial but requires some analysis. The propagation of a monofrequent wave can be described in the form $e^{i\tilde{k}x}$, where $\tilde{k}$ is defined as the complex wavenumber

$$\tilde{k} = k + i\alpha \tag{2.50}$$

with the wavenumber $k = \omega/v_p$ and the attenuation coefficient α. O'Donnell et al. (1978) use the compressibility $\mathcal{K}(\omega) = 1/(\rho v_p(\omega))$ as a complex value $\tilde{\mathcal{K}} = \mathcal{K}_R(\omega) + i\mathcal{K}_I(\omega)$ to derive $v_p(\omega)$ and α. The complex wavenumber, which they refer to as *ultrasonic wave vector*, and the complex compressibility are related by

$$\tilde{\mathcal{K}}(\omega) = \frac{\tilde{k}(\omega)^2}{\rho\omega^2}. \tag{2.51}$$

A way to estimate the dispersion from the complex value in Eq. 2.51 is the evaluation of the *Kramers-Kronig relation*. This relation allows to calculate the imaginary part of the response function of the system by means of the real part or vice versa. In terms of the dynamic compressibility Lee et al. (1990) obtain

$$\mathcal{K}_R(\omega) = \frac{2}{\pi} P \int_0^\infty \frac{\omega' \mathcal{K}_I(\omega')}{\omega'^2 - \omega^2} d\omega' \tag{2.52}$$

$$\mathcal{K}_I(\omega) = -\frac{2}{\pi} P \int_0^\infty \frac{\omega \mathcal{K}_R(\omega')}{\omega'^2 - \omega^2} d\omega', \tag{2.53}$$

where P denotes the Cauchy principal value. If we assume, that $k \gg \alpha$, so the propagation velocity is much larger than the attenuation coefficient, the frequency response of the system can completely be described in terms of the phase velocity $v_p(\omega)$ and the attenuation coefficient $\alpha(\omega)$ by

$$v_p(\omega) \cong \frac{1}{\sqrt{\rho \mathcal{K}_R(\omega)}} \tag{2.54}$$

$$\alpha(\omega) \cong \frac{\rho}{2} \omega v_p(\omega) \mathcal{K}_I(\omega). \tag{2.55}$$

The general problem of solving these equations is the highly non-local character of the integrals in Eqs. 2.52. To obtain the phase velocity, the attenuation in all frequencies is required. For sufficiently small values of v_p and α and assuming that both values do not change rapidly with respect to frequency, O'Donnell et al. (1978) and Lee et al. (1990) provide the following approximation for the phase velocity:

$$v_p(\omega) = \left[\frac{1}{v_p(\omega_0)} - \frac{2}{\pi} \int_{\omega_0}^{\omega} \frac{\alpha(\omega')}{\omega'^2} d\omega' \right]^{-1}, \tag{2.56}$$

where $v_p(\omega_0)$ corresponds to the speed of sound in Eq. 2.48 and the attenuation coefficient writes

$$\alpha(\omega) = \frac{\pi\omega^2}{2v_p(\omega)^2} \frac{dv_p(\omega)}{d\omega}. \tag{2.57}$$

In Alvarez and Kuc (2008), the dispersion is estimated based on the above derivation of $v_p(\omega)$ for air at different temperatures and relative humidities. The relaxation times are given in terms of relaxation frequencies $f_{\text{relax}} = 1/t_{\text{relax}}$. The relaxation frequencies of

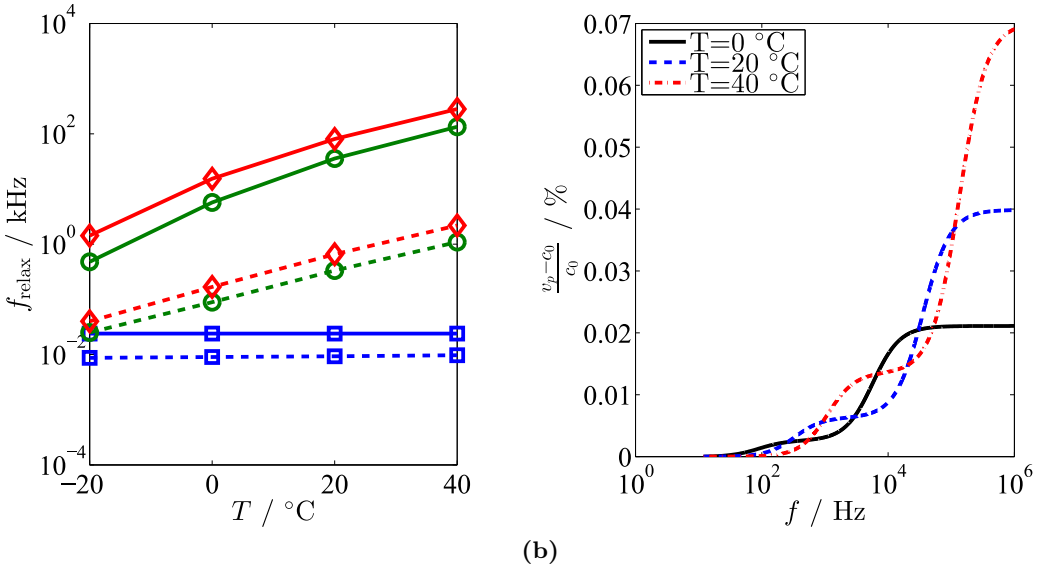

(a) **(b)**

Figure 2.7: (a): Relaxation frequencies of oxygen (solid) and nitrogen (dashed) as a function of the gas temperature for three different relative humidities: (□): 0 %, (◯): 50 %, (♢): 100 %. **(b)**: Relative deviation between the adiabatic speed of sound c_0 and the phase velocity v_p as a function of the acoustic frequency f for different gas temperatures according to Alvarez and Kuc (2008), $h = 50\,\%$.

nitrogen and oxygen provided by Alvarez and Kuc (2008) (referring to Bass et al. (1972)) are depicted in Fig. 2.7a for $-20°\mathrm{C} \leq T \leq 40°\mathrm{C}$ and three different humidities. The relaxation time depends strongly on temperature and humidity and becomes significantly smaller for increasing temperatures in case of non-zero humidity.

By means of Fig. 2.7a, Alvarez and Kuc (2008) provide a formula to obtain the difference between the inverse phase velocity and the inverse speed of sound (so the phase velocity for $c_0 = v_p(\omega = 0)$). These results are presented in terms of the relative error between v_p and c_0 in Fig. 2.7b for acoustic frequencies between 12 Hz and 1 MHz, three gas temperatures, and a humidity of 50 %. The phase velocity becomes larger than the speed of sound for increasing acoustic frequencies and in the ultrasound regime, an increase in gas temperature causes the phase velocity to deviate stronger from the speed of sound. However, for temperatures up to 40° C, this deviation can be neglected; the temperature estimation based on the overestimated speed of sound would differ by less than 0.5 K from the correct temperature.

For the measurements conducted in this study, a quantification of dispersion at about 1500°C would be relevant and of high importance. The distinct dependence of the phase velocity on temperature within the narrow range between −20°C and 40°C allows for the conclusion that the phase velocity might exceed the speed of sound even more significantly at high temperatures. Unfortunately, to the knowledge of the author, no usable information is available in literature.

CO_2, for example, exhibits dispersive features at $f \geq 25\,\mathrm{kHz}$, where higher frequencies travel faster than lower frequency contents (Bernhard, 2014).

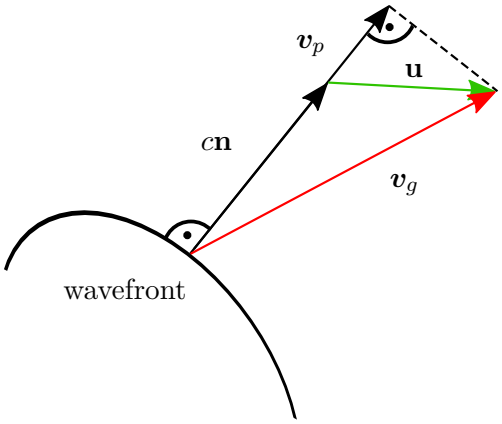

Figure 2.8: Sketch of an acoustic pulse signal, which is a superposition of multiple monofrequent signals, with the group velocity v_g and the phase velocity v_p.

2.2.2 Sound propagation velocity in a moving medium

In most technical applications, the acoustic wave is superposed by a flow velocity $\mathbf{u}$, where $\mathbf{u}(x, y, z)$ is a velocity vector in a 3-dimensional domain. To account for the effect of flow on the propagation of the acoustic wave, Ostashev and D. K. Wilson (2016) propose the following expressions for the phase and the group velocity vectors:

$$\boldsymbol{v}_p = v_p\mathbf{n} = (c + \mathbf{n} \cdot \mathbf{u})\mathbf{n} \tag{2.58}$$

$$\boldsymbol{v}_g = v_g\mathbf{s} = c\mathbf{n} + \mathbf{u}, \tag{2.59}$$

where $\mathbf{n}$ is the unit vector perpendicular to the wavefront and $\mathbf{s}$ denotes the vector of the consequential propagation velocity of the acoustic energy with

$$\mathbf{s} = \frac{c\mathbf{n} + \mathbf{u}}{|c\mathbf{n} + \mathbf{u}|} = \frac{\mathbf{n} + \mathbf{u}/c}{\sqrt{u^2/c^2 + 2\mathbf{n} \cdot \mathbf{u}/c + 1}}. \tag{2.60}$$

A 2-dimensional sketch of the vectors is shown in Fig. 2.8. The direction of the phase velocity and the group velocity does not coincide anymore, but differs depending on the direction of the flow velocity u. The derivation goes back to Rayleigh (1878), who postulated that the propagation of acoustic waves in a moving medium is the same as for a medium at rest, in which each point in space is advected with the same velocity in the same direction. In terms of a TOF measurement, however, not only the absolute value of the propagation velocity is of importance but also the spatial route of the acoustic energy. The acoustic path $\mathcal{L}$ is no longer the geometrically direct line between the emitter and the receiver and the traveling time becomes

$$\tau = \int_{\mathcal{L}} \frac{1}{(c\mathbf{n} + \mathbf{u})\mathbf{s}} dl. \tag{2.61}$$

This becomes essential in case of tomographic reconstruction, where the inverse problem is solved based on the knowledge of the acoustic path length and its course. A solution of this problem is presented in the following section, where the acoustic path refraction is addressed in terms of temperature inhomogeneities.

The effect of the flow velocity on the propagation velocity and the propagation direction

of the acoustic energy is utilized in several applications, where the acoustic pyrometry is not only used for the determination of the temperature field but of the velocity field (D. Wilson and Thomson, 1994; Ostashev and D. K. Wilson, 2016). A comprehensive study on this flow field reconstruction technique is provided by Jovanovic (2008).

The analytical compensation of the flow velocity effect requires detailed knowledge about the flow field. Its determination, however, is not trivial in many applications. For the TOF measurement in high-temperature gases, the speed of sound is sufficiently high, so that the influence of the flow velocity could often be neglected. This is also the case for the measurements conducted in this study. The speed of sound in the combustion chamber is typically of the order of 800 m/s, whereas a maximum bulk flow velocity, which impinges perpendicularly to the acoustic path, of approximately 10 m/s is detected. For the worst case scenario in the combustion rig setup, so for a maximum flight time of $\tau = L/c = (0.18\,\mathrm{m})/(800\,\mathrm{m/s}) = 22\,\mathrm{ms}$, the axial offset of the arriving acoustic wave at the receiver would be of the order of 2 mm.

2.2.3 Sound propagation through an inhomogeneous medium

In technical applications, where the TOF measurements are conducted, e.g, in reacting environments, the medium between acoustic emitter and receiver is highly inhomogeneous. The inhomogeneity is related to the velocity field, the temperature and density field as well as to the spatial gas composition. All these aspects significantly affect the propagation velocity and the shape of the acoustic path.

Approximation for a straight acoustic path

If we, in a first step, neglect the refraction of the acoustic path and assume a straight propagation direction from the acoustic emitter to the receiver (as shown in Fig. 2.3), we could write the travel time over the known length L as

$$\tau = \int_L \frac{1}{\boldsymbol{v}_g(\mathbf{R},t)\cdot\mathbf{n}}dl = \int_L \frac{1}{\sqrt{c(\mathbf{R},t)^2 + 2c(\mathbf{R},t)\mathbf{n}\cdot\mathbf{u}(\mathbf{R},t) + u(\mathbf{R},t)^2}}dl, \tag{2.62}$$

where $\mathbf{R}$ denotes the spatial coordinates $[x, y, z]$ and $\mathbf{n}$ the unity vector perpendicular to the wavefront (Ostashev and D. K. Wilson, 2016). We can now linearize Eq. 2.62 with respect to perturbations of the speed of sound and the convection velocity in space. The time and space dependent speed of sound $c(\mathbf{R},t)$ and the velocity $\mathbf{u}(\mathbf{R},t)$ are split into a spatially averaged part c_0 and $\mathbf{u}_0$ and a fluctuating part denoted as c' and $\mathbf{u}'$ to $c(\mathbf{R},t) = c_0(t) + c'(\mathbf{R},t)$ and $\mathbf{u}(\mathbf{R},t) = \mathbf{u}_0(t) + \mathbf{u}'(\mathbf{R},t)$. If higher order terms are omitted and $c_0 \gg c'$ and $\mathbf{u}_0 \gg \mathbf{u}'$ is assumed, Ostashev and D. K. Wilson (2016) derive the following expression from Eq. 2.62:

$$\tau = \frac{L}{c_0(t)}\left(1 - \frac{\mathbf{n}\cdot\mathbf{u}_0}{c_0(t)}\right) - \frac{1}{c_0(t)^2}\int_L \left(c'(\mathbf{R},t) + \mathbf{n}\cdot\mathbf{u}'(\mathbf{R},t)\right) dl. \tag{2.63}$$

In case of a quiescent medium and a stationary inhomogeneous temperature field, Eq. 2.63 reduces to

$$\tau = \frac{L}{c_0} - \frac{1}{c_0^2}\int_L c'(\mathbf{R})dl. \tag{2.64}$$

The forward problem, i.e. the estimation of the arrival time for a given velocity and temperature field and a known distance L, can be solved by means of Eq. 2.63. However, it would be an approximation, as we neglected the refraction of the acoustic path. For the solution of the inverse problem, i.e. the evaluation of the right-hand side of Eq. 2.63 or Eq. 2.64, it is essential to know the route of the acoustic energy, which in turn depends on the spatial temperature distribution. Due to the highly non-linear nature of Eq. 2.62, finding a solution is non-trivial and requires mathematical effort, which will be examined in the following.

Refraction of the acoustic path

The physics behind the bending phenomena of acoustic waves due to inhomogeneities can be understood by using the analogue from optics. The waveform character of light as well as sound causes the wavefront to be rotated, so-called refracted, when propagating from one medium into another medium of different density (e.g., from air into glass). The dispersion, i.e. the frequency dependence of the *refraction index*, causes the light to refract into its different frequency contents (say colors, e.g., refraction between air and water droplets cause a rainbow). According to *Snell's law*, the angle of the shift in direction depends on the difference between the refraction indices of the two media. The refraction index is defined as the relation between a reference velocity (e.g., the speed of sound) and the phase velocity in the medium:

$$\mu = \frac{c_0}{v_p}. \tag{2.65}$$

A sketch of a deflected acoustic path is shown in Fig. 2.9. Assuming the shaded area represents a higher temperature compared to the white area, the acoustic path is bent towards the hotter region. In the following, two approaches are presented that allow for

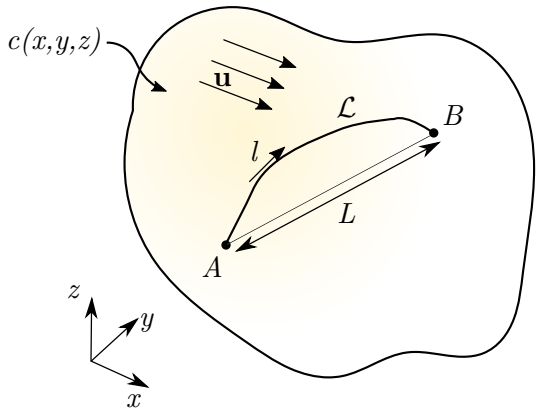

Figure 2.9: Schematic representation of the acoustic path refraction due to temperature inhomogeneities (indicated by shaded color) and a uniform flow field.

an estimation of the route of the acoustic wave based on the spatially inhomogeneous distribution of the speed of sound.

Eikonal equation and the Hamilton formalism

The following derivation is mainly based on the comprehensive study of Blokhintzev (1946), it has been adopted and further developed by others, e.g., Ostashev and D. K. Wilson (2016). For a time dependent inhomogeneous medium, the spatial and temporal propagation of a sound wave can be described by :

$$p(\mathbf{R},t) = \hat{p}(\mathbf{R})e^{i(-\omega t + k_0\Theta(\mathbf{R},t))}, \tag{2.66}$$

where $\hat{p}$ denotes the oscillation amplitude and $k_0\Theta$ expresses the phase of the wave with the wave number $k_0 = \omega/c_0$. For sufficiently low amplitudes and isentropic changes of state, the ansatz of Eq. 2.66 can be inserted into the linearized equations of fluid dynamics. This leads to the so-called *eikonal* equation which reads:

$$\frac{\partial\Theta(\mathbf{R},t)}{\partial n} = \frac{c_0}{c(\mathbf{R},t) + |\mathbf{u}(\mathbf{R},t)\cdot\mathbf{n}|}. \tag{2.67}$$

The left-hand side of Eq. 2.67 represents the differentiation of the phase along the direction normal to the wavefront (surface of constant phase). In case of zero flow velocity ($|\mathbf{u}| = 0$), the right-hand side of Eq. 2.67 equals the refraction index introduced in Eq. 2.65. So in order to solve the wave propagation in Eq. 2.66, the eikonal equation has to be solved. With respect to cartesian coordinates, the eikonal equation can be expressed as

$$|\nabla\Theta_t(\mathbf{R})| = \frac{c_0}{c} - \frac{\mathbf{u}\cdot\nabla\Theta_t(\mathbf{R})}{c}. \tag{2.68}$$

Here, we defined $\Theta_t(\mathbf{R}) = \Theta(\mathbf{R},t) + \omega t/k_0$, which makes Eq. 2.68 independent of time. The ∇-operator represents a vector which is defined as $\nabla = \frac{\partial}{\partial x} + \frac{\partial}{\partial y} + \frac{\partial}{\partial z}$. The goal is to find an expression for $\Theta_t(\mathbf{R})$, which would allow for the evaluation of the acoustic ray path as a function of the spatial distribution of the temperature (i.e. the speed of sound).

To solve this non-linear first order partial differential equation in Eq. 2.68 in order to determine the spatial route of the acoustic wave, the *Hamiltonian* formalism can be used (Chessell, 1973), which allows for the estimation of the shape of the acoustic path numerically. The Hamiltonian function $\mathcal{H}(\nabla\Theta_t, \mathbf{R})$ has to be solved for $\mathcal{H}(\nabla\Theta_t, \mathbf{R}) = 0$ which leads to the following ordinary differential equations:

$$\frac{d\mathbf{R}}{d\xi} = \frac{\partial\mathcal{H}}{\partial\mathbf{b}}, \tag{2.69}$$

$$\frac{d\mathbf{b}}{d\xi} = -\frac{\partial\mathcal{H}}{\partial\mathbf{R}}, \tag{2.70}$$

$$\frac{d\Theta_t}{d\xi} = \mathbf{b}\cdot\frac{\partial\mathcal{H}}{\partial\mathbf{b}}. \tag{2.71}$$

For the sake of simplicity, $\mathbf{b}$ denotes the spatial derivative of the phase function $\mathbf{b} = \nabla\Theta_t$ and ξ represents an independent variable along the acoustic path. The sound ray equation depends on the choice of how the Hamiltonian $\mathcal{H}(\mathbf{b},\mathbf{R})$ is defined. According to Eq. 2.68, the Hamiltonian yields

$$\mathcal{H}(\mathbf{b},\mathbf{R}) = b - \frac{c_0}{c} + \mathbf{b}\cdot\frac{\mathbf{u}}{c}, \tag{2.72}$$

where $b = |\mathbf{b}| = |\nabla \Theta_t|$ and $\mathbf{u}$ denotes the advective velocity vector. Inserting Eq. 2.72 into Eqs. 2.69-2.71 leads to

$$\frac{d\mathbf{R}}{d\xi} = \frac{\mathbf{b}}{b} + \frac{\mathbf{u}}{c}, \tag{2.73}$$

$$\frac{d\mathbf{b}}{d\xi} = -\frac{1}{c}\left[b\nabla c + \mathbf{b} \times (\nabla \times \mathbf{u}) + (\mathbf{b} \cdot \nabla)\mathbf{u}\right], \tag{2.74}$$

$$\frac{d\Theta_t}{d\xi} = b + \frac{\mathbf{b} \cdot \mathbf{u}}{c}. \tag{2.75}$$

The right-hand side of Eq. 2.73 equals the group velocity divided by the speed of sound $\boldsymbol{v}_g/c$ (see Eq. 2.59), which means, that the direction of the vector $\mathbf{R}(\xi)$ is the same as the direction of the group velocity.

For appropriate initial conditions for the vectors $\mathbf{R}(\xi)$ and $\mathbf{b}(\xi)$ at the origin of the acoustic ray or at the acoustic receiver, from Eqs. 2.73 and 2.74 the ray path can be obtained. Note, for a more descriptive representation, the independent variable ξ can be transformed to either the spatial coordinate along the acoustic path l or the time t via

$$d\xi = \frac{c}{u} dl, \tag{2.76}$$

$$d\xi = c dt. \tag{2.77}$$

So if the transformation in Eq. 2.76 is used and the ray path obtained from Eqs. 2.73 and 2.74 is applied to Eq. 2.75, and Eq. 2.75 is integrated, the eikonal in an inhomogeneous moving medium is obtained as

$$\Theta_t(l) = \Theta_{t,1} + \int_{l_1}^{l} \frac{c_0}{u} dl', \tag{2.78}$$

where l_1 is the initial point of the path in space, l is the final point, and $\Theta_{t,1} = \Theta_t(l_1)$. Using the definition of an incremental path length $dl = udt$, Eq. 2.78 yields the acoustic traveling time along the acoustic path:

$$\tau = \frac{\Theta_t(l) - \Theta_{t,1}}{c_0}. \tag{2.79}$$

This equation allows for ray tracing, where for a measured acoustic traveling time the matching ray path is evaluated numerically, e.g., by means of a shooting method. In that case, the boundary conditions, for example, the initial condition $\mathbf{b}(0)$, is altered until the ray path corresponds to the traveling time. Numerical procedures to solve the eikonal equation are investigated in Tucker and Karabasov (2009) for unstructured grids, and Waheed et al. (2015) present an algorithm which allows for an efficient and accurate numerical computation of the problem.

Fermat's principle and the calculus of variation

Another way to estimate the acoustic path through an inhomogeneous medium is based on *Fermat's principle* (Godin and Voronovich, 2004). Here, the impact of the advective flow velocity on the acoustic propagation time is neglected, which means that the group

velocity and the phase velocity are identical (if we consider a non-dispersive medium): $v_p = v_g = c$ (see Eqs. 2.58 and 2.59). It follows that the travel time along the path $\mathcal{L}$ can be evaluated via

$$\tau = \int_{\mathcal{L}} \frac{1}{c(\mathbf{R})} dl. \tag{2.80}$$

To further simplify the calculation, we consider a 2-dimensional domain with $c(x, y)$ and we define a path that starts at a point $p_1 = [x_1\ y_1]^\top$ and ends at a point $p_2 = [x_2\ y_2]^\top$ in space. A parameterization of the acoustic path $\mathcal{L}$ can be performed as

$$\mathcal{L}(x) = \begin{bmatrix} x \\ y(x) \end{bmatrix}, \tag{2.81}$$

where $x_1 \leq x \leq x_2$. If we assume linear dependence between x and $y(x)$ for incremental changes dx, the differential path length in Eq. 2.80 can be expressed as $dl = \sqrt{1 + (dy/dx)^2} dx$ and the arrival time can be expressed as:

$$\tau = \int_{p_1}^{p_2} \frac{\sqrt{1 + \left(\frac{dy}{dx}\right)^2}}{c(x, y)} dx. \tag{2.82}$$

According to Fermat's principle, which states that the wave takes the shortest way in time, i.e. the acoustic path with the smallest value of τ. This, in turn, means that we have to find the path where Eq. 2.82 becomes minimum or where its variation equals zero:

$$\delta\tau = \int_{p_1}^{p_2} \frac{\sqrt{1 + \delta\left(\frac{dy}{dx}\right)^2}}{c(x, y)} dx = 0. \tag{2.83}$$

We want to solve this equation for $y(x)$. Such a problem can be tackled via the calculus of variation, where a functional (a function whose input arguments are as well functions) is defined and its minimum is calculated (Gelfand and Fomin, 1964). In case of Fermat's principle, this leads to the *Euler-Lagrange equation*

$$\frac{\partial \mathcal{S}(x, y(x), y'(x))}{\partial y(x)} - \frac{d}{dx} \frac{\partial \mathcal{S}(x, y(x), y'(x))}{\partial y'(x)} = 0 \tag{2.84}$$

with $y' = dy/dx$ and the varied integral function

$$\mathcal{S}(x, y(x), y'(x)) = \frac{\sqrt{1 + y'(x)^2}}{c(x, y)}. \tag{2.85}$$

The solution of Eq. 2.84 leads to the following boundary value problem

$$\frac{\partial^2 y(x)}{\partial x^2} = c(1 + y'(x)^2) \left[\frac{\partial}{\partial y(x)} \frac{1}{c(x, y)} - y'(x) \frac{\partial}{\partial x} \frac{1}{c(x, y)} \right] \tag{2.86}$$

with the boundary conditions $y_1 = y(x_1)$ and $y_2 = y(x_2)$. The solution, which can be evaluated numerically, delivers the acoustic path $y(x)$ provided that the spatial distribution of the speed of sound $c(x, y)$ is known. This approach has been used by Lu et al. (2000), who compare tomographic temperature field reconstructions with and without considering the deflection of the acoustic path. It turns out that for large spatial gradients of the temperature field, the deviation between the two cases becomes significant.

In Sec. 5.3.4, we will apply the boundary value problem in Eq. 2.86 according to Lu et al. (2000) on the tomographic reconstruction approach used for determining the spatial distribution of the measured entropy waves. There, it will also be explained how the spatial distribution of the inhomogeneity can be obtained, as $c(\mathbf{R})$ is required as input for Eq. 2.67 or Eq. 2.86.

2.2.4 Error analysis of the flight time measurement

It has been discussed in the previous sections that the experimental estimation of the line integrated gas temperature depends on the accurate assessment of the arrival time τ. In realistic experimental applications, the latter is always erroneous to a certain degree; potential reasons will be discussed in Sec. 4.

It is therefore inherently important to project the error of the arrival time estimation on the resulting temperature. Based on Eq. 2.39, a second-order Taylor series expansion writes

$$T(\tau+\delta\tau) = T(\tau) + \frac{1}{1!}\frac{\partial T(\tau)}{\partial \tau}\delta\tau + \frac{1}{2!}\frac{1}{2}\frac{\partial^2 T(\tau)}{\partial \tau^2}(\delta\tau)^2. \tag{2.87}$$

The derivative of the temperature $T(\tau)$ with respect to τ yields

$$\frac{\partial T(\tau)}{\partial \tau} = \frac{\partial}{\partial \tau}\left(\frac{L^2}{\tau^2 \gamma R_g}\right) = -2\frac{L^2}{\tau^3 \gamma R_g} = -2\frac{c^2}{\tau \gamma R_g} = -2\frac{T}{\tau}, \tag{2.88}$$

and allows to approximate the error in temperature $\delta T = T(\tau+\delta\tau) - T(\tau)$ via the following equation:

$$\delta T = -2T\frac{\delta\tau}{\tau} + 3T\left(\frac{\delta\tau}{\tau}\right)^2. \tag{2.89}$$

Assuming that the error in the arrival time estimation $\delta\tau$ is much smaller than the flight time $\delta\tau \ll \tau$, the right-hand side term in Eq. 2.89 can be omitted and the relative error in temperature is obtained as proposed in Bernhard, 2014:

$$\frac{\delta T}{T} = -2\frac{\delta\tau}{\tau}. \tag{2.90}$$

Equation 2.89 reveals that the relative error in estimating the arrival time leads to an error in the temperature that is twice as high.

Analogously to the error analysis with respect to the flight time τ, the sensitivity of the temperature estimation regarding an error in the path length δL can be assessed. The procedure is the same as shown above, the resulting relative error writes:

$$\frac{\delta T}{T} = 2\frac{\delta L}{L}. \tag{2.91}$$

Especially the correlation given in Eq. 2.90 will be used for the error analysis in the result chapter (Sec. 5) of this study, as this is the quantity that is finally assessed.

2.3 Temperature reconstruction from arrival times

Looking at the expressions for the arrival time derived in the preceding section (e.g., Eq. 2.38), it is obvious that for the estimation of the inverse speed of sound, and with it the temperature, the acoustic path length must be known. If we assume that the acoustic signal propagates along the geometric distance L between emitter and receiver and if we further neglect the influence of the flow field and refraction, the line integrated temperature between emitter and receiver reads

$$T = \frac{L^2}{\tau^2 \kappa R_g}. \tag{2.92}$$

This resulting temperature, however, does not provide any information about how the temperature might vary along the acoustic path. This information might be crucial for applications with significant spatial inhomogeneities. Furthermore, obtaining the temperature from Eq. 2.92 requires an exact measure of the distance L. It will become clear in the section about the experimental setup that this is not necessarily given. In this Section, two approaches are presented. Each of them is capable to resolve one of the aforementioned constraints in estimating the temperature via Eq. 2.92.

The **zero-dimensional reconstruction approach** allows for the assessment of the dynamic cross-sectionally averaged temperature from the flight time measurement of multiple acoustic paths. Instead of the lengths of the acoustic paths, a measure of the steady temperature in the measurement plane proves to be sufficient. This method, however, aims only on the measurement of temperature fluctuations in terms of amplitude and phase.

For a spatially resolved temperature reconstruction, different **multi-dimensional approaches** are presented. One-dimensional reconstruction methods require the assumption of a rotational symmetric temperature field, whereas the two-dimensional methods, in turn, presuppose denser field information.

2.3.1 Zero-dimensional reconstruction: SVD approach

In realistic experimental setups, a correct estimate of the geometrical path length L may be affected by notable uncertainties and errors. As the arrival times are assessed along various paths in the measurement plane, each measure of the line integrated inverse speed of sound is biased differently. The diverse sources of these uncertainties are investigated and discussed in Sec. 5.

In contrast to classical tomography, which allows for a one-dimensional or two-dimensional reconstruction of the temperature field, we consider the method presented in this section a “zero-dimensional” approach.

In the following subsection, the use of a *singular value decomposition* (SVD) is presented. It allows for an extraction of the temperature fluctuation without demanding information about the acoustic path lengths. Merely the steady temperature measurement obtained from a thermocouple serves as an additional input parameter. In the following, it will be shown how this is possible.

To measure a temperature fluctuation of frequency f_v, a series of arrival times is recorded with a sampling rate $f_s = f_\mathrm{v} N_\psi$. Thus, for a number of N_ψ phase angles within one period of temperature oscillation and a number of N_m acoustic paths, the following matrix $\boldsymbol{\tau}$ of measured arrival times is obtained:

$$\boldsymbol{\tau} = \begin{pmatrix} \tau_{1,1} & \cdots & \tau_{1,N_m} \\ \vdots & \ddots & \vdots \\ \tau_{N_\psi,1} & \cdots & \tau_{N_\psi,N_m} \end{pmatrix}. \tag{2.93}$$

If we in a first step assume that the line integrated inverse speed of sound is the same along each of the acoustic paths at the same phase angle, a number of N_ψ sets of linear equations is obtained. For each phase angle, such a set of equations reads

$$\begin{aligned} \tau_{\psi,1} &= c_\psi^{-1} L_1 \\ &\vdots \\ \tau_{\psi,N_m} &= c_\psi^{-1} L_{N_m}. \end{aligned} \tag{2.94}$$

The subscript ψ assigns a parameter to a certain phase angle ψ. We are interested in the inverse speeds of sound $\boldsymbol{c}^{-1} = [c_1^{-1}, ..., c_{N_\psi}^{-1}]$; however, as stated above, we do not have information about the acoustic path lengths $\boldsymbol{L} \in \mathbb{R}^{N_m}$. A solution to this problem is found by application of the singular value decomposition. A SVD of $\boldsymbol{\tau}$ (Eq. 2.93) acts as a total least square estimation of these overdetermined linear systems of equations in Eq. 2.94 and takes the form (G. H. Golub and van Loan, 1996):

$$\mathrm{svd}(\boldsymbol{\tau}) := \mathbf{U}\boldsymbol{\Sigma}\mathbf{V}^\top = \begin{pmatrix} U_{1,1} & \cdots & U_{1,N_\psi} \\ \vdots & \ddots & \vdots \\ U_{N_\psi,1} & \cdots & U_{N_\psi,N_\psi} \end{pmatrix} \begin{pmatrix} \sigma_1 & \cdots & 0 \\ \vdots & \ddots & \vdots \\ 0 & \cdots & \sigma_{N_m} \\ \vdots & \ddots & \vdots \\ 0 & \cdots & 0 \end{pmatrix} \begin{pmatrix} V_{1,1} & \cdots & V_{1,N_m} \\ \vdots & \ddots & \vdots \\ V_{N_m,1} & \cdots & V_{N_m,N_m} \end{pmatrix}^\top. \tag{2.95}$$

The matrix $\mathbf{U}$ is a unitary matrix of size $N_\psi \times N_\psi$, matrix $\mathbf{V}$ is as well unitary and of size $N_m \times N_m$.

The entries of the $N_\psi \times N_m$ rectangular diagonal matrix $\boldsymbol{\Sigma}$ are the singular values of $\boldsymbol{\tau}$ with $\sigma_1 \geq \sigma_2 \geq ... \geq \sigma_r > 0$. The singular values are positive real numbers, whereas the number of non-zero singular values is defined as the rank r of the matrix $\boldsymbol{\tau}$ (see Eq. 2.96). The definition of the 2-norm provides the largest singular value, and the condition number β yields the ratio between the largest singular value and the sum of the remaining singular values:

$$r = \mathrm{rank}(\boldsymbol{\tau}) \tag{2.96}$$

$$\|\boldsymbol{\tau}\|_2 = \sigma_1 \tag{2.97}$$

$$\beta = \frac{\sigma_1}{\sum_{i=2}^{r} \sigma_i}. \tag{2.98}$$

Note that in literature, the condition number often refers to the ratio between the largest

singular value and the smallest singular value ($\beta = \sigma_1/\sigma_r$).

The columns of $\mathbf{U}$ are known as the left singular vectors and the columns of $\mathbf{V}$ are referred to as the right singular vectors of the matrix $\boldsymbol{\tau}$. Based on Eq. 2.95, $\boldsymbol{\tau}$ can be expressed as

$$\boldsymbol{\tau} = \sum_{j=1}^{r} \sigma_j [U_{1,j}, ..., U_{N_\psi,j}]^\top [V_{1,j}, ..., V_{1,N_m}]. \tag{2.99}$$

From Eq. 2.99 it is obvious that a unique solution for the inverse speed of sound for each phase angle can solely be obtained if the rank of $\boldsymbol{\tau}$ is reduced to $r = 1$. In, e.g., G. Golub and Kahan (1965) it is derived that the best approximation $\hat{\boldsymbol{\tau}}$ of a matrix $\boldsymbol{\tau}$ with $\hat{r} = \text{rank}(\hat{\boldsymbol{\tau}}) < r$ is obtained with

$$\hat{\boldsymbol{\tau}} = \mathbf{U}\hat{\boldsymbol{\Sigma}}\mathbf{V}^\top, \tag{2.100}$$

where $\hat{\boldsymbol{\Sigma}}$ is a rectangular diagonal matrix with $\hat{\sigma}_{N_m} \leq ... \leq \hat{\sigma}_{\hat{r}} \leq 0$ (Eckart and Young, 1936; G. Golub, Hoffman, et al., 1987). The error ϵ_{SVD} between the original measured matrix $\boldsymbol{\tau}$ and the rank-reduced reconstructed matrix $\hat{\boldsymbol{\tau}}$ can be assessed with the following definition:

$$\epsilon_{\text{SVD}} = \frac{\|\boldsymbol{\tau} - \hat{\boldsymbol{\tau}}\|}{\|\boldsymbol{\tau}\|}. \tag{2.101}$$

Here, $\|.\|$ refers to the *Frobenius norm* which is defined as $\|\boldsymbol{\tau}\| = \sqrt{\sum_i^{N_\psi} \sum_j^{N_m} |\tau_{i,j}|^2}$. This low-rank approximation is for example commonly used for the compression of data, where the reduction in rank reduces the size of a file. To a certain level of rank reduction, the loss of information might be tolerable. If the rank of $\hat{\boldsymbol{\tau}}$ is reduced to $\hat{r} = 1$, Eq. 2.99 reads

$$\hat{\boldsymbol{\tau}} = \sigma_1 [U_{1,1}, ..., U_{N_\psi,1}]^\top [V_{1,1}, ..., V_{1,N_m}]. \tag{2.102}$$

The unitary matrices $\mathbf{U}$ and $\mathbf{V}$ in Eq. 2.95 are in Eq. 2.102 reduced to vectors of length N_ψ and N_m, respectively. In our case that means that the left singular vector of length N_ψ corresponds to the inverse speed of sound and the right singular vector of length N_m refers to the acoustic path lengths. The inverse speed of sound for all phase angles is thus obtained as

$$\check{\boldsymbol{c}}_{\text{SVD}} = [c_1^{-1}, ..., c_{N_\psi}^{-1}]^\top = \frac{1}{N_\psi} \sum_{k=1}^{N_\psi} \frac{\check{c}_{\text{ref}}}{U_{k,1}} [U_{1,1}, ..., U_{N_\psi,1}]^\top, \tag{2.103}$$

where $\check{\boldsymbol{c}}_{\text{SVD}} \in \mathbb{R}^{N_\psi \times 1}$, and the inverse speed of sound $\check{c}_{\text{ref}}$ is a reference inverse speed of sound. The choice of $\check{c}_{\text{ref}}$ is quite important as it affects the absolute value of the oscillations amplitude. This is shown and discussed in terms of measured flight times in Sec. 5.4.2.1 (Fig. 5.36a therein). $\check{c}_{\text{ref}}$ can for example be obtained from temperature measurements via thermocouples $T_{\text{ref,SVD}}$, which leads to

$$\check{c}_{\text{ref}} = (\gamma R_g T_{\text{ref,SVD}})^{-\frac{1}{2}}. \tag{2.104}$$

Equation. 2.103 reveals that, apart from the left singular vector, the reference speed of sound $\check{c}_{\text{ref}}$ is the only input required to obtain the inverse speed of sound as a function of the phase angles. Consequently, the temperature as a function of the phase angle is

obtained from combining Eqs. 2.103 and 2.48 to

$$\boldsymbol{T}_{\mathrm{SVD}} = [T_1, ..., T_{N_\psi}]^\top = \frac{\check{\boldsymbol{c}}_{\mathrm{SVD}}^{-2}}{\gamma R_g}. \tag{2.105}$$

At a first glance it may seem somewhat unclear what the resulting temperature in Eq. 2.105 exactly means, as only a one-column array $\boldsymbol{T}_{\mathrm{SVD}} \in \mathbb{R}^{N_\psi \times 1}$ is obtained from the measurements of all arrival times over the various acoustic paths with $\boldsymbol{\tau} \in \mathbb{R}^{N_\psi \times N_m}$. Essentially, the SVD method provides a weighted average of the overall temperature fluctuations present along all acoustic paths. Thus, the physical meaning of the resulting temperature fluctuation strongly depends on the arrangement of the acoustic paths, their lengths, and the spatial mean temperature distribution of the field.

For the theoretical case of a temperature fluctuation that oscillates within the entire field around the same average temperature value but at each path with a different amplitude, the resulting inverse speed of sound is found to be the average over all line integrated inverse speeds of sound weighted by the square of the length of the paths. This is expressed as

$$\check{\boldsymbol{c}}_{\mathrm{SVD}} = \frac{\sum_{i=1}^{N_m} \left(\check{\mathbf{c}}_{\mathrm{path},i} L_i^2\right)}{\sum_{i=1}^{N_m} L_i^2}, \tag{2.106}$$

with the fluctuation of the inverse speed of sound at each individual path $\check{\mathbf{c}}_{\mathrm{path},i} \in \mathbb{R}^{1 \times N_\psi}$ and the lengths $L_i \in \mathbb{R}$ of the i-th acoustic path. Equation 2.106 is only valid if the applied reference inverse speed of sound $\check{c}_{\mathrm{ref}}$ equals the field's cross-sectionally averaged temperature.

The fluctuating temperature field investigated in the experimental part of this study (see Sec. 5.4.2.1) is not comparable to the theoretical case described above. To understand the meaning of the extracted temperature fluctuation, a study with artificially generated field data must be conducted. In Sec. 3.1, such a phantom study is presented based on the SVD approach as it has been presented in this section.

Nevertheless, the fact that this method allows for an extraction of the amplitude and phase of a temperature fluctuation without requiring the lengths of the acoustic paths as input makes it a valuable tool for the investigation of entropy waves based on TOF measurements.

2.3.2 Multi-dimensional reconstruction: acoustic tomography

Tomography denotes the determination of the distribution of a field based on line-integrated values, so-called projections, along paths that cross the field. This method is used in various applications, the most famous one might be the *CT* (computed tomography) in medicine (Cormack, 1963). There, the human body represents the investigated field and line-integrated radiodensities of electromagnetic waves that are sent through the body on different paths serve as projection. Since different tissues exhibit different abilities to attenuate electromagnetic waves, the distribution of various kinds of tissue is obtained from the reconstruction algorithm.

Other applications are the estimation of the heat release rate distribution in a flame by means of the measurement of OH* chemiluminescence (Anikin et al., 2010), the

reconstruction of density fields by means of the Schlieren method, which makes use of the change in the refraction index caused by density inhomogeneities (Décamp et al., 2008), or the estimation of a three-dimensional velocity field by means of particle image velocimetry (PIV) (Elsinga et al., 2008), where the propagation velocity and direction of particles carried by the flow is assessed from different angles. There are far more applications; in principle, tomography can be utilized whenever there is some continuous interaction (linear or non-linear) between a wave or matter that is propagating through a field and the property of the field that is examined.

The research groups who employed acoustic tomography have already been mentioned in the introduction part of the TOF method in Sec. 2.2. It is obvious that tomographic reconstruction is the optimal tool to extract information from TOF measurements. Consequently, provided that the distribution of the acoustic path is sufficiently dense, a one-dimensional or two-dimensional reconstruction is conducted.

In this section, different tomographic reconstruction methods are presented. First, a general overview of the most common approaches is given. Subsequently, the two tomographic methods that have been applied in this study will be introduced in more detail. At the end, the mathematical methods required for solving the inverse problem associated with the tomographic approaches will be discussed.

2.3.2.1 Overview of tomographic methods

There exist various different tomographic approaches in literature. Many of them lead to similar equations but employ different mathematical algorithms to solve the problem or are based on the same idea but might be named differently as they are used in a different field of research. All these methods can roughly be divided into two main groups, the *analytical* and the *algebraic* methods. In the following, both of them are briefly introduced and investigated regarding their application to the particular setup that is used in this study. A comprehensive overview of various tomographic methods and the solutions to the associated mathematical problems is given by Kak and Slaney (1988) and Natterer (2001b), which build the basis for the following subsections. Note that in this study only scalar tomography is considered. All formulations in the following are not necessarily valid for vector tomography. The latter is, for example, comprehensively described in Jovanovic (2008).

A mathematical description of tomography is given by the **Radon transform** $\mathcal{R}$. This integral transform between the field domain and a projection domain allows for calculating the spatial distribution of a field, in our case the inverse speed of sound $\check{c}(x, y)$, provided that the projection of the field, in our case the arrival times $\tau(\chi, \varphi)$, is known by measurement:

$$\mathcal{R}\{\check{c}(x,y)\}(\chi,\varphi) := \tau_\varphi(\chi) = \int_{L_{\chi,\varphi}} \check{c}(x,y)dl. \tag{2.107}$$

The acoustic paths $L(\chi, \varphi)$ are considered to be straight and rotated by an angle φ with respect to the field's coordinate system. The key idea is to find $\mathcal{R}$, i.e. the projection, which enables the calculation of the inverse Radon transform $\mathcal{R}^{-1}$. This provides the

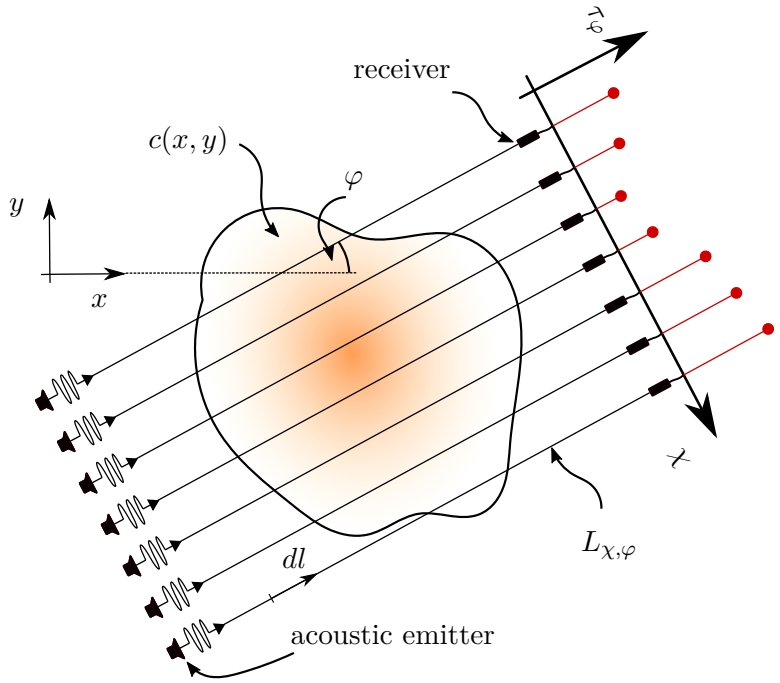

Figure 2.10: Schematic of the two-dimensional Radon transform by means of a TOF measurement setup; the shaded color represents a hotter area, where the speed of sound is larger than in the white area. φ is defined as the angle between the x-axis of the field coordinate system and the χ-axis of the projection's coordinate system.

field variable as a function of space based on the projection data:

$$\check{c}(x,y) = \mathcal{R}^{-1}\{\tau_\varphi(\chi)\}. \tag{2.108}$$

For the most typical case, where the lines of sight are parallel to each other, an illustration of the two-dimensional Radon transform is shown in Fig. 2.10. The spatial resolution of the resulting field increases with the number of acoustic paths and the number of angles φ that are employed throughout the measurement. It becomes also clear from Fig. 2.10 that the realization of such a measurement setup may be difficult for realistic technical applications. In case of a circular combustion chamber with all its constrains, an arrangement like this is practically impossible.

Analytic reconstruction methods

A method that is often used to analytically solve Eq. 2.108, is the *Fourier slice theorem*. It relates the Radon transform to the Fourier transform and eventually allows for the estimation of the inverse Radon transform by means of the inverse Fourier transform (Kak and Slaney, 1988). For a sufficiently high spatial resolution of the reconstructed field, however, the Fourier slice theorem requires a large number of projections, in terms of the number of parallel beams as well as projection angles φ. The most commonly used method, especially in CT applications, is the *filtered back-projection* algorithm, which

employs the Fourier slice theorem (W. Cai and Kaminski, 2017):

$$\check{c}(x,y) = \int_0^{\pi} \int_{-\infty}^{+\infty} \int_{-\infty}^{+\infty} \tau(\chi,\varphi) e^{-i2\pi w\chi} d\chi |w| e^{i2\pi w\chi} dw d\varphi. \tag{2.109}$$

The variable w denotes a ramp filter function to prevent the blurring of the reconstructed field; the inner integral in Eq. 2.109 corresponds to the Fourier transform of the projection. The disadvantage of the filtered back-projection is its demand for a high number of projections to deliver an accurate two-dimensional reconstruction of the field $\check{c}(x,y)$. Additionally, the projections need to be at regularly spaced angles to ensure the applicability of the Fourier transform (W. Cai and Kaminski, 2017). Due to the very restricted degrees of freedom in the arrangement of the projection paths in our experimental setup, this approach is not the method of choice in this study.

Algebraic reconstruction methods

More flexible reconstruction algorithms in terms of the ray path arrangement are provided by algebraic approaches. Here, the field is discretized and with it the ray paths along which the integration takes place. The discretization can be adjusted to the particular ray path arrangement and the field's geometry; in most applications, quadratic elements are employed. It is assumed that within such an element b_j, the field variable, again, in our case the inverse speed of sound $\check{c}(x,y)$, takes a constant value $\check{c}_j$: $\check{c}(x,y) \equiv \check{c}_j \, \forall \, \mathbb{R}^{x,y} \in b_j$. In contrast to the analytic approaches, this reconstruction method allows for taking into account the bending of the acoustic paths due to refraction effects. Therefore, we introduce the ray path $\mathcal{L}_i$ of the i-th path, which is not necessarily the same as the ideally straight path L_i. The part of $\mathcal{L}_i$ that passes the j-th element of the discretized field is denoted as $\mathcal{L}_{i,j}$.

For a number of N_j discretization elements, the projection of the field $\check{c}(x,y)$, which is in our case the travel time τ, can be written for the i-th path as

$$\tau_i = \sum_{j=1}^{N_j} \int_{\mathcal{L}_{i,j}} \check{c}_j dl = \sum_{j=1}^{N_j} l_{i,j} \check{c}_j, \tag{2.110}$$

where we additionally introduced $l_{i,j} := \int_{\mathcal{L}_{i,j}} dl$ for ease of notation. A schematic of an exemplary algebraic tomographic measurement setup, in this case with straight and parallel ray paths, is shown in Fig. 2.11.

For a number of N_i different ray paths, Eq. 2.110 leads to the following system of linear equations:

$$\underbrace{\begin{pmatrix} \tau_1 \\ \tau_2 \\ \vdots \\ \tau_{N_i} \end{pmatrix}}_{:=\boldsymbol{\tau}} = \underbrace{\begin{pmatrix} l_{1,1} & l_{1,2} & \cdots & l_{1,N_j} \\ l_{2,1} & l_{2,2} & \cdots & l_{2,N_j} \\ \vdots & \vdots & \ddots & \vdots \\ l_{N_i,1} & l_{N_i,2} & \cdots & l_{N_i,N_j} \end{pmatrix}}_{:=\mathbf{L}} \cdot \underbrace{\begin{pmatrix} \check{c}_1 \\ \check{c}_2 \\ \vdots \\ \check{c}_{N_j} \end{pmatrix}}_{:=\check{\boldsymbol{c}}}. \tag{2.111}$$

The projection vector is denoted as $\boldsymbol{\tau} \in \mathbb{R}^{N_i}$, the matrix $\mathbf{L} \in \mathbb{R}^{N_i \times N_j}$ is known as the geometry matrix, and $\check{\boldsymbol{c}} \in \mathbb{R}^{N_j}$ is the solution vector which comprises the inverse speeds of sound of all discretization elements. For given ray paths and a defined discretization

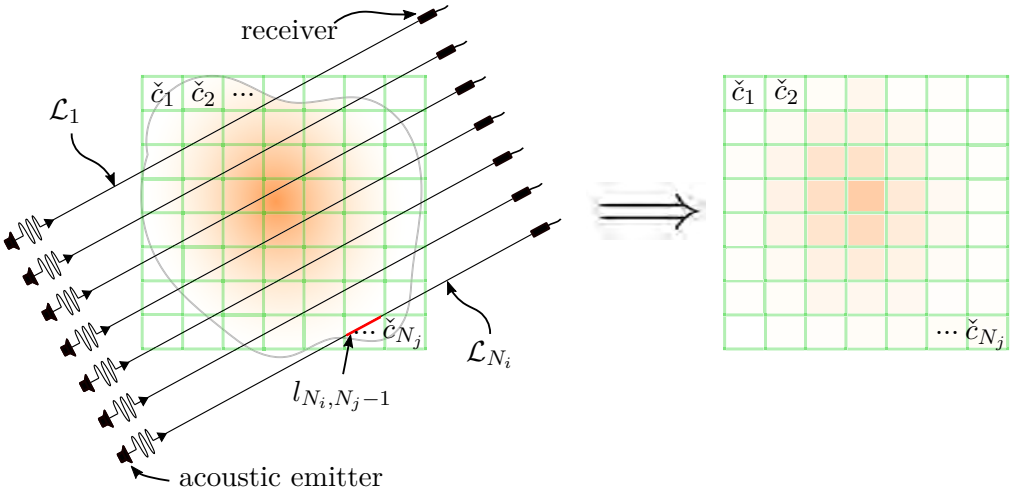

Figure 2.11: Left: Schematic of an algebraic tomography setup where the ray paths are straight and parallel (this is not a requirement), and the inhomogeneous field is discretized by rectangles; the shaded color represents different values of the inverse speed of sound. **Right**: Exemplary solution of the tomographic approach on the left with constant values $\check{\boldsymbol{c}}_j$ in each discretization element.

pattern, $\mathbf{L}$ is fully defined. With a measured projection vector, the solution vector can be estimated via inversion

$$\check{\boldsymbol{c}} = \mathbf{L}^{\dagger}\boldsymbol{\tau}, \tag{2.112}$$

where $\mathbf{L}^{\dagger}$ denotes the inversion of $\mathbf{L}$ by means of the *Moore-Penrose Pseudoinverse*. One way to calculate $\mathbf{L}^{\dagger}$ is by means of the singular value decomposition, which has already been introduced in Section 2.3.1. By following Eq. 2.99, the Moore-Penrose pseudoinverse writes

$$\mathbf{L}^{\dagger} = \sum_{i=1}^{r} V_i \sigma_i^{-1} U_i^{\top}, \tag{2.113}$$

where r denotes the rank of matrix $\mathbf{L}$ (see Eq. 2.96) and V_i and U_i are the left and the right singular vectors, respectively. The pseudoinverse can also be applied to singular matrices that are not invertible. The solution shown in Eq. 2.112 could then be found by

$$\check{\boldsymbol{c}}^{*} = \mathbf{L}^{\dagger}\boldsymbol{\tau} = \sum_{i=1}^{r} \sigma_i^{-1}(U_i^{\top}\boldsymbol{\tau})V_i. \tag{2.114}$$

In case of a singular system matrix, the solution vector $\check{\boldsymbol{c}}^{*}$ represents a least square solution.

Ideally, $\mathbf{L}$ has full rank, which means that all equations are linearly independent of each other. However, in most of the tomographic applications, this is not the case and the system is either over-determined or under-determined. Additionally, it can happen that not all discretization elements are penetrated by a ray path or there are too many rays compared to the number of discretization elements. This all leads in practical tomographic applications often to ill-conditioned system matrices, for which finding a solution becomes more challenging.

In the case of large numbers of unknowns, e.g., in CT applications, the algebraic reconstruction approaches are numerically more expensive than analytical methods. However, they provide better and more robust results if the projection data is noisy or the ray

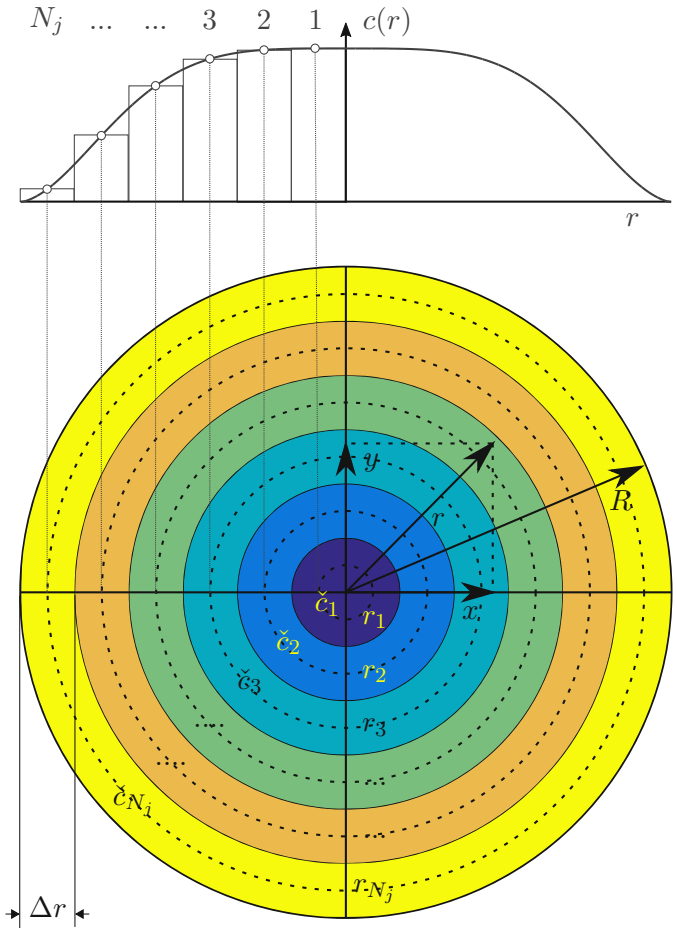

Figure 2.12: Schematic of the onion peeling approach for a typical radial field of the speed of sound in a circular combustor; in this example, the concentric rings are of the same thickness $\Delta r = R/N_j$. The field profile $c(r)$ shown in the upper graph depicts an interpolation between the ring elements.

paths are irregular (Verhoeven, 1993; Kak and Slaney, 1988). There comes an important advantage of the algebraic reconstruction into play: due to the selectable arrangement of the discretization elements, information about the field distribution can a-priori be incorporated.

Algebraic reconstruction methods that are utilized in this study are introduced in the following sections. Subsequently, methods for solving Eq. 2.112 in the case of ill-conditioned systems are presented and discussed. More comprehensive overviews and detailed insights to the various tomographic methods are given by Kak and Slaney (1988); Natterer (2001a); Herman (2009); W. Cai and Kaminski (2017).

2.3.2.2 Onion peeling

The most common tomographic reconstruction method for a rotationally symmetric field, which to a certain extend has been assumed in this study, is the *onion peeling* approach. Here, the field is, similar to an onion, divided into concentric rings. For each of these ring-shaped discretization elements, the field variable is considered to be constant. A schematic of the onion-peeling approach is depicted in Fig. 2.12.

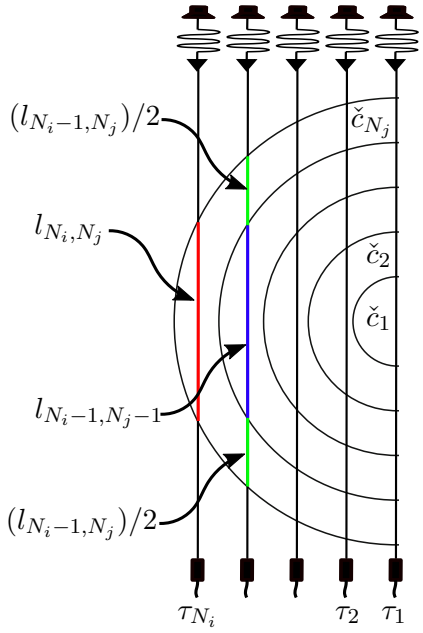

Figure 2.13: Schematic of the definition of the elements in the system matrix **L** shown in Eq. 2.115.

In case of a number of N_j parallel ray paths, a number of N_j ring elements must be defined to obtain a square system matrix. The thickness Δr of the ring elements would be chosen such that the outmost ring is hit by the outmost path, the neighboring ring is hit by the same path and the neighboring path and so on. This leads to an upper triangular system matrix **L**:

$$\begin{pmatrix} \tau_1 \\ \tau_2 \\ \vdots \\ \tau_{N_i} \end{pmatrix} = \begin{pmatrix} l_{1,1} & l_{1,2} & \cdots & l_{1,N_j} \\ 0 & l_{2,2} & \cdots & l_{2,N_j} \\ \vdots & \vdots & \ddots & \vdots \\ 0 & 0 & \cdots & l_{N_i,N_j} \end{pmatrix} \cdot \begin{pmatrix} \check{c}_1 \\ \check{c}_2 \\ \vdots \\ \check{c}_{N_j} \end{pmatrix}. \tag{2.115}$$

The definition of the element lengths l in Eq. 2.115 is illustrated in Fig. 2.13 for half of the rotationally symmetric field. This allows for solving the system of equations in a sequential manner. First, the field variable is evaluated in the outmost ring element, as there is one equation with one unknown available. In a second step, the field variable of the neighboring ring element is calculated by means of subtracting the information about the field variable obtained in the preceding step:

$$\begin{aligned} \check{c}_{N_j} &= \frac{l_{N_i,N_j}}{\tau_{N_i}} \\ \check{c}_{N_j-r} &= \frac{l_{N_i-r,N_j-r}}{\tau_{N_i-r} - \sum_{k=0}^{r-1} \frac{l_{N_i-k}}{\check{c}_{N_j-k}}} \qquad \text{for } N_i = N_j \text{ and } r \in \mathbb{N}^{N_j-1}. \end{aligned} \tag{2.116}$$

The potential problem of this method becomes obvious when looking at the bottom equation in Eq. 2.116. Each evaluation step from the outmost ring element to the center ring element comprises information about the field variable $\check{c}$ from all preceding steps.

This means that errors arising in the evaluation of the outer elements are propagated and multiplied to the evaluation of the inner ring elements.

Due to technical constraints, however, such a parallel ray path arrangement, as it is shown in Fig.2.12, cannot be realized in the experimental setup in this study. The rays are neither parallel nor symmetric in any way. Thus, the system matrix becomes dense and might be ill-conditioned. Note that in this study onion peeling refers to an algebraic algorithm where the field is discretized according to the classic onion peeling approach but where the solution of the problem does not follow the typical steps described above in Eqs. 2.115 and 2.116.

In the studies of Dasch (1992) and K. J. Daun et al. (2006) it is pointed out that mathematical means are crucial to obtain stable and accurate results from noisy projection data and ill-conditioned problems. These regularization methods, in particular the *Tikhonov regularization*, will be introduced in the subsequent sections.

The application of the onion peeling method on the measured flight times in the combustion test rig reveals what happens if the assumption of rotational symmetry does not hold true. A detailed investigation on this issue is conducted in Sec. 5.4.2.2.

2.3.2.3 Collocation

The term *collocation methods* in the context of tomography has been introduced by Sielschott and Derichs (1995). They investigated the reconstruction of the temperature field in a combustion chamber of a coal fired power plant by means of acoustic pyrometry.

The idea of the collocation method is to approximate the scalar field $\check{c}(\boldsymbol{R})$ with $\boldsymbol{R} \in \mathbb{R}^2$ by a linear combination of a number of N_j basis functions φ_j with $j = 1, ..., N_j$. These basis functions are centered at the discrete locations $\boldsymbol{R}_j$, which can be defined according to a-priori information about the field distribution:

$$\check{c}(\boldsymbol{R}) \approx \sum_{j=1}^{N_j} \xi_j \varphi_j(\boldsymbol{R}). \tag{2.117}$$

The parametrization of the solution is done by introducing the coefficients ξ_j, which scale the different basis functions to fit them to the field $\check{c}(\boldsymbol{R})$.

Bramanti et al. (1996), who also studied the experimental mapping of the temperature field in a boiler of a coal fired power plant, used in their collocation approach (which they did not name *collocation* but *regularization*) trigonometric basis functions. Although their results look promising, Sielschott and Derichs (1995) proposed an alternative basis function, which is more appropriate for the field approximation with acoustic pyrometry. Based on a covariance analysis, they found that Gaussian functions provide superior results:

$$\varphi_j(\boldsymbol{R}) = e^{-\mu \|\boldsymbol{R} - \boldsymbol{R}_j\|_2^2}, \tag{2.118}$$

where the parameter μ expands or compresses the Gaussian curve and has to be selected empirically according to the actual problem. The collocation method comprising

exponential basis functions has successfully been applied to the temperature field reconstruction in furnances, e.g., by Sielschott and Derichs (1996),Y.-Q. Li and Zhou (2006), and X. Shen et al. (2015).

If Eq. 2.117 and Eq. 2.110 are combined, an expression for the summation of the scaled line-integrals of the i-th ray across the j-th basis function is obtained:

$$\tau_i = \sum_{j=1}^{N_j} \xi_j \int_{\mathcal{L}_i} \varphi_j(\boldsymbol{R}(l) - \boldsymbol{R}_j) dl. \tag{2.119}$$

The integral in Eq. 2.119 can numerically be evaluated and, thus, will be substituted in the following by $g_{ij} = \int_{\mathcal{L}_i} \varphi_j(\boldsymbol{R}(l) - \boldsymbol{R}_j) dl$, which leads to

$$\tau_i = \sum_{j=1}^{N_j} \xi_j g_{ij}. \tag{2.120}$$

The similarity between this equation and Eq. 2.110 is obvious and the resulting set of linear equations can consequently be written as

$$\underbrace{\begin{pmatrix} \tau_1 \\ \tau_2 \\ \vdots \\ \tau_{N_i} \end{pmatrix}}_{:=\boldsymbol{\tau}} = \underbrace{\begin{pmatrix} g_{1,1} & g_{1,2} & \cdots & g_{1,N_j} \\ g_{2,1} & g_{2,2} & \cdots & g_{2,N_j} \\ \vdots & \vdots & \ddots & \vdots \\ g_{N_i,1} & g_{N_i,2} & \cdots & g_{N_i,N_j} \end{pmatrix}}_{:=\mathbf{G}} \cdot \underbrace{\begin{pmatrix} \xi_1 \\ \xi_2 \\ \vdots \\ \xi_{N_j} \end{pmatrix}}_{:=\boldsymbol{\xi}}. \tag{2.121}$$

The coefficient vector $\boldsymbol{\xi}$ is calculated from the inversion of matrix $\mathbf{G}$ and finally allows to approximate the field:

$$\boldsymbol{\xi} = \mathbf{G}^{\dagger}\boldsymbol{\tau} \implies \sum_{j=1}^{N_j} \xi_j \varphi_j(\boldsymbol{R}) \approx \check{c}(\boldsymbol{R}). \tag{2.122}$$

Collocation methods offer important advantages compared to methods that are based on discretization elements that contain a constant field value (=pixels). The latter generate a discontinuity between the elements which cause problems when solving the boundary value problem that arises due to ray path refraction (see Eq. 2.86). Especially when dealing with problems that suffer from a low number of available data, e.g., only few projections, collocation is the more powerful tool. Here, each basis function contains information about all rays that penetrate the field, which leads to a more stable and less noisy solution of the tomographic reconstruction. In case of pixel based methods, sparse data often give rise to the problem that some pixels might not be penetrated by any ray or, in order to prevent this issue, the discretization scheme has to be modified accordingly. Both conditions provoke either an unstable solution or a poor spatial resolution of the reconstructed field.

If rotational symmetry of the field distribution can be assumed, which is strictly required for the onion peeling approach in Sec. 2.3.2.2, the above described collocation algorithm can analogously be expressed in a one-dimensional fashion. The only difference is that the field coordinate variable $\boldsymbol{R}$ is no longer a function of the x and y coordinates but merely

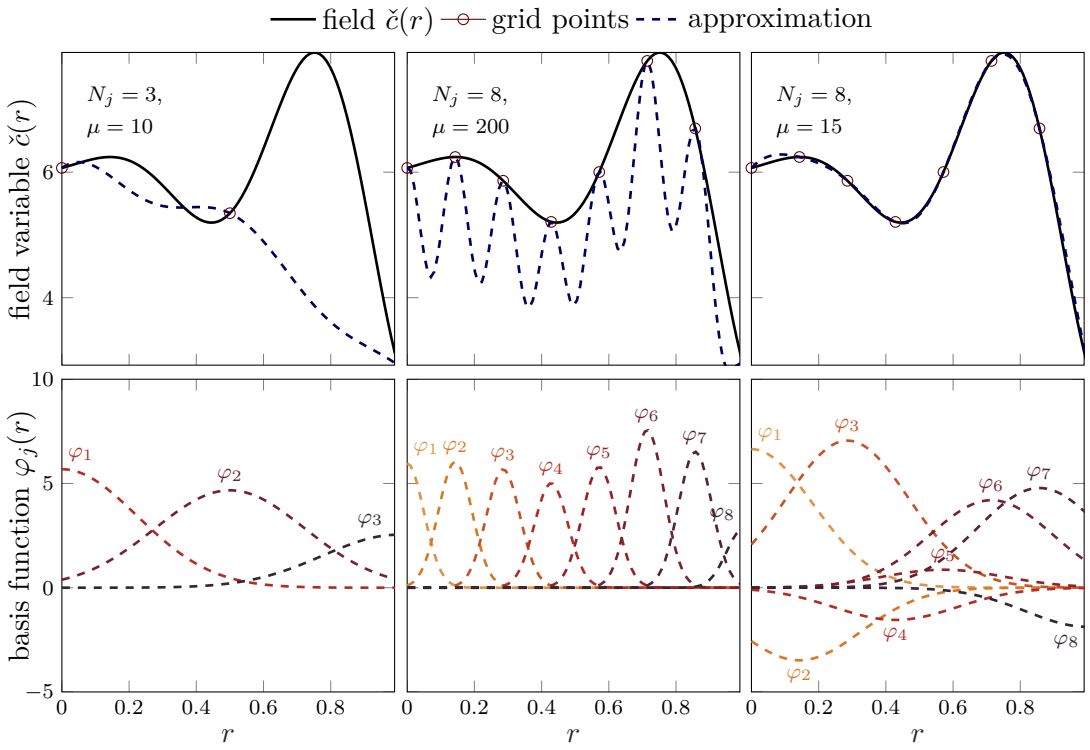

Figure 2.14: Approximation of the field function $\check{c}(r)$ by means of collocation; Gaussian functions (see Eq. 2.118) are used for the RBF. In the top plots, the approximation is shown for different numbers N_j of grid points and different values of the design parameter μ; the lower graphs depict the basis functions that by summing up lead to the corresponding upper approximation. This plot is taken from Pause (2017).

depends on the radial coordinate r. For such a one-dimensional collocation approach, an illustration of the working principle of collocation with Gaussians as radial basis functions (RBF) is depicted in Fig. 2.14. From the very left-hand side plots it is derived that a too small number of grid points is not capable of reproducing the characteristics of the field. If the number of grid points increases, the approximation might become more accurate as depicted in the very right-hand side plots. However, the design parameter μ has to be chosen correctly. The centered graphs demonstrate that an unfavourable choice of μ leads to an approximation which strongly exhibits the characteristics of the basis functions. This illustrates the major disadvantage of the collocation method. With the number of grid nodes and the design parameter μ, two parameters have to be adjusted empirically, where both of them can have significant impact on the approximation of the field.

2.3.2.4 Solution to ill-conditioned problems

In case of the CT, where the system matrix becomes very large due to the very large number of ray paths and discretization elements, an inversion is not feasible, and iterative methods have been developed to cope with the very large system matrix.

However, in many tomographic applications, the main problem is the ill-condition of the system matrix due to experimental constraints. If a system matrix is considered as *well-conditioned*, it fulfills the following three conditions: (i) there exists a solution, (ii)

the solution is unique, and (iii) the solution changes continuously with a change of the input. As soon as one of these requirements is violated, the system matrix is considered as ill-conditioned.

Basically, there are two types of ill-conditioned problems (Hansen, 1998):

- rank deficiency
- ill-posedness.

In the case of a **rank deficient** matrix, the number of unknowns, i.e. the number of discretization elements, is larger than the number of projections. This means that the system of equations is under-determined and there exists an infinite number of solutions, which violates requirement (ii). This is also the case for matrices that might have more equations than unknowns but with equations that linearly depend on each other and thus do not contribute to the information comprised in the system.

Opposite to rank deficient problems, the matrices of **ill-posed problems** are either square or over-determined (Hansen, 1998). Here, the uniqueness of the solution is met, however, requirement (iii) is violated, the solution becomes unstable. This instability means that a small error in the input vector $\boldsymbol{\tau}$ could cause a significant error in the solution vector $\check{\mathbf{c}}$.

There exist many different approaches to solve ill-conditioned problems. In the following, two iterative methods, that have been used in this study, are briefly introduced. Furthermore, it will be shown which other mathematical tools, in particular regularization, can be utilized to solve strongly ill-conditioned systems.

Kaczmarz method The so-called *Kaczmarz method* has been postulated by Kaczmarz (1937). It is based on a sequential column by column and row by row evaluation of the system matrix. It is an iterative algorithm, where the next solution vector of the k-th iteration reads

$$\check{\boldsymbol{c}}^{(k+1)} = \check{\boldsymbol{c}}^{(k)} + \lambda_k \boldsymbol{l}_i \frac{\tau_i - \langle \boldsymbol{l}_i, \check{\boldsymbol{c}}^{(k)} \rangle}{\|\boldsymbol{l}_i\|_2^2}. \tag{2.123}$$

Here, λ_k denotes a relaxation parameter, $\langle ., . \rangle$ denotes the inner product, and $\|.\|$ the Euclidean norm; vectors are indicated with bold symbols. In case of the randomized version of the *Kaczmarz* method, which has been employed in this study, the i-th row is randomly selected from the number of N_i rows of the system matrix $\mathbf{L}$ (Strohmer and Vershynin, 2009). The probability is proportional to $\|l_i\|_2^2$, which means that rays, which pass more discretization elements, are automatically taken more into account.

SIRT Another iterative method to solve the system of linear equations that has been used in this study is one of the group of *simultaneous iterative reconstruction techniques* (SIRT). One of these methods is the *Landweber* algorithm (Landweber, 1951), which can be expressed as

$$\check{\boldsymbol{c}}^{(k+1)} = \check{\boldsymbol{c}}^{(k)} + \lambda_k \mathbf{I}\mathbf{L}^\top \mathbf{I} \left(\boldsymbol{\tau} - \mathbf{L}\check{\boldsymbol{c}}^{(k)} \right). \tag{2.124}$$

Again, λ_k denotes a relaxation parameter and $\mathbf{I}$ represents the unity matrix. This method is recommended by W. Cai and Kaminski (2017) for the evaluation of a system of linear equations if only a small number of projections is available.

Regularization of ill-posed problems Ill-posed problems are characterized by an over-determined system of equations, where the solution is not stable but very sensitive to errors in the projection vector. The ill-posedness is indicated by a continuous decrease of the systems singular values. This causes an enhancement of the sensitivity of the solution vector towards errors in the projection vector. It can be seen by rewriting Eq. 2.114 for the case that $\mathbf{L}$ is over-determined. In a least square sense, the solution writes

$$\check{\boldsymbol{c}}^{\mathrm{LS}} = \min\left\{\|\mathbf{L}\check{\boldsymbol{c}} - \boldsymbol{\tau}\|_2^2\right\} = \underbrace{\sum_{i=1}^{r} \sigma_i^{-1}(U_i^\top \boldsymbol{\tau}^{\mathrm{exact}})V_i}_{\check{\boldsymbol{c}}^{\mathrm{exact}}} + \underbrace{\sum_{i=1}^{r} \sigma_i^{-1}(U_i^\top \delta\boldsymbol{\tau})V_i}_{\check{\boldsymbol{c}}^{\mathrm{error}}}. \tag{2.125}$$

The measurement error is represented by $\delta\boldsymbol{\tau}$. As $\check{\boldsymbol{c}}^{\mathrm{error}}$ depends inversely on the singular values σ_i, it is obvious that especially the small singular values contribute most to the error in the least square solution $\check{\boldsymbol{c}}^{\mathrm{LS}}$.

One commonly used approach to prevent error components of higher frequency to contribute to the solution vector is the *truncated singular value decomposition* (TSVD). Here, the solution is estimated similar to Eq. 2.114, but the evaluation is truncated after a certain number q of singular values:

$$\check{\boldsymbol{c}}^{\mathrm{TSVD}} = \sum_{i=1}^{q<r} \sigma_i^{-1}(U_i^\top \boldsymbol{\tau})V_i. \tag{2.126}$$

The selection of an appropriate truncation value q is of course the critical step and tackled by another very common method, the *Tikhonov regularization* (Tikhonov, 1963; Phillips, 1962). It can be expressed in a general form by the following minimization problem:

$$\check{\boldsymbol{c}}^{\mathrm{Tik}} = \min\left\{\|\mathbf{L}\check{\boldsymbol{c}} - \boldsymbol{\tau}\|_2^2 + \gamma^2\|\mathbf{M}\check{\boldsymbol{c}}\|_2^2\right\}, \tag{2.127}$$

where γ denotes the regularization parameter which weights the regularization term on the right-hand side within the brackets. In case of ill-posed problems, the regularization matrix $\mathbf{M}$ is defined as an identity matrix with $\mathbf{M} \in \mathbb{R}^{N_i \times N_i}$. To better understand the mode of action of the Tikhonov regularization, a more illustrative notation is given by Hansen (1998):

$$\check{\boldsymbol{c}}^{\mathrm{Tik}} = \min\left\{\left\|\begin{bmatrix}\mathbf{L}\\ \gamma\mathbf{M}\end{bmatrix}\check{\boldsymbol{c}} - \begin{bmatrix}\boldsymbol{\tau}\\ 0\end{bmatrix}\right\|_2^2\right\}. \tag{2.128}$$

The original system matrix is extended in order to transform this ill-posed problem to a well-conditioned one. The crucial step is to find a value for γ that leads to the optimal solution. The regularization acts like a filter, and according to Hansen (1998), "*[...] regularization of a discrete ill-posed problem is a matter of finding out which erroneous SVD components to filter out, and how to filter them out*". Additionally, he also points out that the amount of filtering plays an important role. The filtering character of the Tikhonov regularization becomes obvious when looking at the relation between the Tikhonov regularization and the TSVD. Effectively, Eq. 2.126 is extended by a filter factor f_i to

$$\check{\boldsymbol{c}}^{\mathrm{Tik}} = \sum_{i=1}^{q} f_i\sigma_i^{-1}(U_i^\top \boldsymbol{\tau})V_i, \tag{2.129}$$

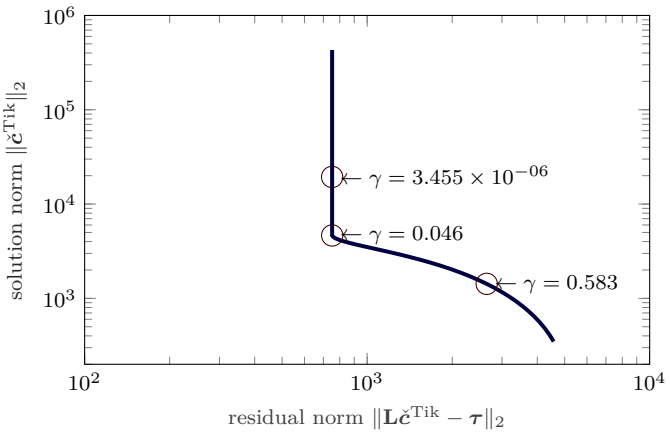

Figure 2.15: Example of a L-curve to determine the optimal regularization value γ. It results from plotting the regularized solution norm versus the residual norm for different regularization parameters γ, whereas the γ-value at the strongest curvature is selected (in this case $\gamma = 0.046$).

where f_i is defined as

$$f_i = \frac{\sigma_i^2}{\sigma_i^2 + \gamma^2}. \tag{2.130}$$

σ_i denotes the i-th singular value of $\mathbf{L}$. From Eq. 2.130 it can be seen that the filter effectively sets in at singular values that are of the order of γ. For high γ-values, the filter converges to unity and thus does not affect the solution in Eq. 2.129.

The choice of the regularization parameter γ determines whether the solution becomes accurate but unstable or whether it is stable, i.e. the solution vector is not superimposed by higher frequency content, but the solution is not very accurate, as a lot of information is filtered out (Hansen and O'Leary, 1993).

There exist different ways to estimate the optimal value for γ. One, which is commonly used, is the *L-curve criterion*. Here, the norm of the residual $\|\mathbf{L}\check{\boldsymbol{c}}^{\mathrm{Tik}} - \boldsymbol{\tau}\|_2$ and the norm of the Tikhonov regularized solution $\|\check{\boldsymbol{c}}^{\mathrm{Tik}}\|_2$ are plotted for various values of γ. An exemplary curve of this kind is depicted in Fig. 2.15. For small values of γ, the residual norm decreases, which means that the solution becomes very accurate. However, the vector norm of the regularized solution vector increases at the same time, which in turn means that the solution becomes very noisy and unstable, respectively. It is elaborately derived and discussed in Hansen and O'Leary (1993) that the location in the L-curve with the highest curvature can be considered as the optimal regularization parameter γ. An illustrative application of the *L-curve criterion* is given by K. J. Daun et al. (2006), where they apply Tikhonov regularization and investigate the influence of the regularization level.

Regularization of rank-deficient problems In case of a rank-deficient problem, the regularization algorithm is related to the one introduced above but with some changes. The Tikhonov regularization can be applied similar to Eq. 2.127:

$$\check{\boldsymbol{c}}^{\mathrm{Tik}} = \min \left\{ \|\mathbf{L}\check{\boldsymbol{c}} - \boldsymbol{\tau}\|_2^2 + \gamma^2 \|\mathbf{S}\check{\boldsymbol{c}}\|_2^2 \right\}, \tag{2.131}$$

whereas the square matrix $\mathbf{S} \in \mathbb{R}^{N_j \times N_j}$ is not defined as a unity matrix but as a Laplacian:

$$S_{m,n} = \begin{cases} 1, & \text{if } m = n \\ -1/k_m, & \text{if } m \neq n \text{ and element } n \text{ is adjacent to element } m \\ 0, & \text{elsewhere.} \end{cases} \tag{2.132}$$

k_m denotes the number of adjacent elements to the m-th discretization element. This kind of regularization is also referred to as a *first-order Tikhonov regularization* (in opposition to the *zeroth-order Tikhonov regularization* in Eq. 2.127). It is recommended by K. Daun et al. (2016) that the determination of γ in case of a rank-deficient problem should not be performed via the L-curve theorem. They suggest a SVD of an extended system matrix $[\mathbf{L}; \gamma\mathbf{S}]$. By doing so, the number of singular values increases, whereas the correct regularization parameter γ is found, when the singular values of the unextended matrix are not overwritten by the additional singular values. An example of this method can be found in Pause (2017).

3 Phantom Study

To verify and investigate the temperature extraction approaches proposed in Sections 2.3.1 and 2.3.2, a phantom study is conducted. This means that the circular measurement plane, as it exists in the experimental setup at the combustion test rig, is numerically simulated. The resulting discretized two-dimensional field is superimposed by a generic temperature field. Virtual acoustic paths are implemented, which are similarly arranged as in the "real" experimental setup. Integration along those virtual acoustic paths allows for the evaluation of the line-integrated inverse speeds of sound, which, in turn, can be used to calculate the virtual flight times (see Eq. 2.38). Finally, the zero- and one-dimensional methods derived in Sec. 2.3 can be applied to these artificial data. Ideally, their reconstructed temperature field should, of course, be equal to the generic temperature field that has been used to evaluate the artificial flight times.

Thus, such a phantom study allows for the assessment of different configurations and arrangements of receivers and emitter regarding their ability to reproduce the cross-sectionally averaged temperature. Furthermore, by adding artificial noise to the artificial flight times, the sensitivity of the temperature extraction methods towards perturbations of the arrival times can be estimated. Systematical errors of the experimental setup can so be separated from errors due to noisy measurement data.

Two different artificial temperature fields are considered in this study. In a rather generic plane wave configuration we assume a radially homogeneous temperature distribution. This allows for investigations on the impact of noise on the measurement data on the reconstructed temperature field. In a second case a more realistic one-dimensional temperature field is deployed. This has been derived from temperature measurements of type-S thermocouples that have been radially traversed through the measurement plane. This experimentally obtained steady-state radial temperature distribution is depicted in Fig. 3.1a with respect to the normalized radius. The thermocouple measurements revealed that the assumption of rotational symmetry of the steady-state temperature field, which is presupposed throughout this work, is reasonable. More detailed investigations on the measured radial steady-state temperature can be found in Sec. 5.3.1. A contour plot of the artificial temperature field derived from the measurements shown in Fig. 3.1a is depicted in Fig. 3.1b.

In the following sections, phantom studies will be conducted to validate the zero-dimensional method (Sec. 3.1) as well as the one-dimensional approaches (Sec. 3.2).

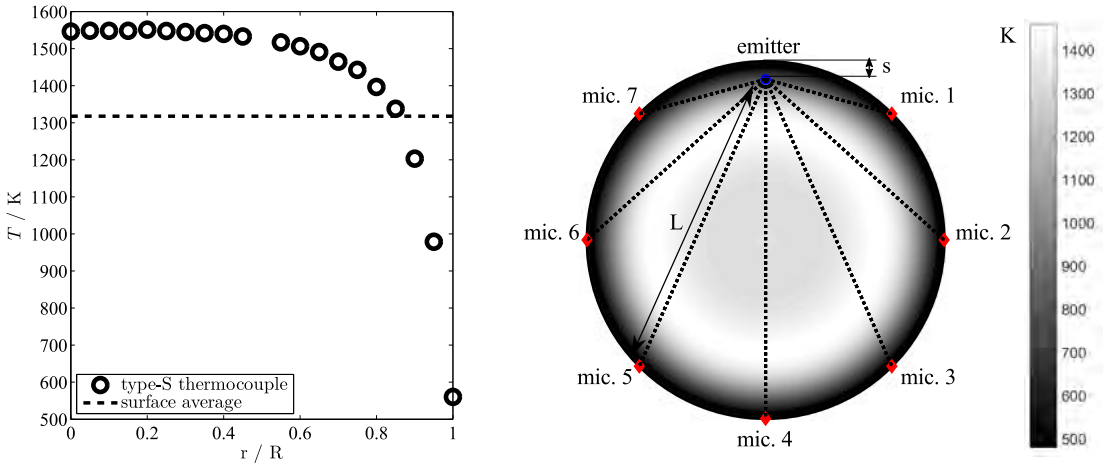

(a) **(b)**

Figure 3.1: **(a)**: **Markers**: Steady-state radial temperature profile measured by a thermocouple that has been radially traversed through the measurement plane at one axial location in the combustion test rig downstream of the flame. **Dashed line**: Cross-sectionally averaged temperature. **(b)**: Contour plot of the artificial rotationally symmetric temperature field based on the measured radial temperature distribution shown in (a). The virtual acoustic paths correspond to the symmetric TOF setup (see Fig. 4.23).

3.1 Phantom study of the SVD approach

In this section, the zero-dimensional SVD approach for the extraction of the cross-sectionally averaged temperature perturbation from flight times is validated by means of the phantom study. The arrangement of the virtual acoustic paths follows the experimental setup shown in Fig. 3.1b and described in Sec. 4.3. This setup is also referred to as "symmetric" setup.

3.1.1 Phantom study of the SVD approach without noise

In this study, the fluctuation of the cross-sectionally surface averaged temperature $\tilde{T}$, indicated as dashed line in Fig. 3.1a, is of interest. If an entropy wave is considered, the cross-sectionally surface averaged temperature becomes a function of the phase angle ψ, where $\psi = 0...2\pi$ describes one period of the temperature fluctuation. To artificially generate the measurement matrix $\boldsymbol{\tau}_p$, whose number of rows corresponds to the number of phase angles (see Eq. 2.93), a sinusoidal variation of the cross-sectionally surface averaged temperature is superposed on the radial temperature field in the phantom study. The amplitude of this artificial temperature fluctuation is defined to be a function of the radial locations. It becomes smaller for regions closer to the wall. This is done because the temperature close to the wall is strongly dominated by the wall temperature rather than by the temperature of the bulk flow. Thus, fluctuations of the gas temperature are more present in the center region of the duct. This phenomenon has also been observed in the tomographic analysis in Sec. 2.3.2. The artificial temperatures for an amplitude of the cross-sectionally surface averaged temperature of $\tilde{T}' \approx 100\,\mathrm{K}$ are shown in Fig. 3.2a as linearly interpolated values in a contour plot. In the center region ($r/R \lesssim 0.6$) the amplitude reaches much higher values. To properly reflect the experimental conditions,

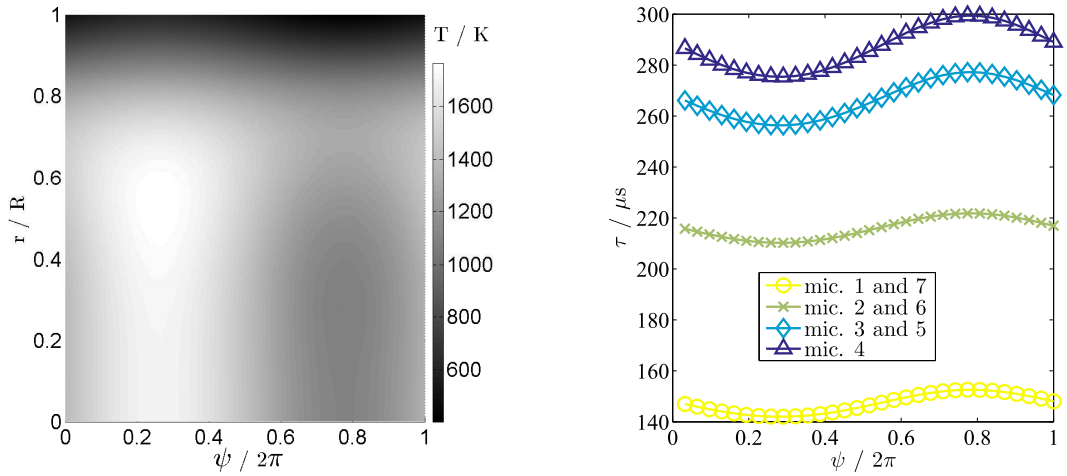

(a) **(b)**

Figure 3.2: **(a)**: Artificial radial temperature field as function of the wave phase angle ψ for an amplitude $\tilde{T}' \approx 100\,\mathrm{K}$. **(b)**: Values of the virtual flight times $\boldsymbol{\tau}_p$ for an imposed temperature amplitude $\tilde{T}' \approx 100\,\mathrm{K}$. The legend entries refer to the designation of the receivers according to Fig. 4.23.

one period of the artificial temperature fluctuation is resolved by 31 phase angles (see Sec. 4.1).

The values of the corresponding virtual flight times $\boldsymbol{\tau}_p$, i.e. the virtual arrival times for all microphones at all phase angles, are shown in Fig. 3.2b. As it has been introduced before, these arrival times are gained by transforming the artificial temperature field in Fig. 3.2a into a field of the inverse speed of sound. The length L of each path multiplied by the line-averaged inverse speed of sound finally yields the traveling time. For microphones 3, 5, and 4, the fluctuation of the arrival times reveals a larger amplitude compared to the other microphones (the microphones' positions can be found in Fig. 4.23). This is because their paths are directed through more central regions of the duct.

Now we apply the SVD approach to the virtual flight times shown in Fig. 3.2b. An indication of how well the SVD method works is given by the error measure ϵ_{SVD}. According to Eq. 2.101, the matrix $\boldsymbol{\tau}_p$ is compared to the single-rank approximated matrix $\hat{\boldsymbol{\tau}}_p$ obtained from the SVD approach. The values of ϵ_{SVD} with respect to the applied artificial temperature amplitude are shown in Fig. 3.3a.

The error increases linearly with increasing amplitude of the temperature fluctuation. However, it stays below 1 % range of temperature amplitudes that are relevant in this study. This observation holds true for all different penetration depths s of the acoustic source that have been realized in the experimental setup (see also Fig. 4.23). Note that the configuration with the acoustic emitter placed directly at the wall is the one with the lowest error.

Based on the small errors that occur when reconstructing the matrix of the virtual arrival times in Fig. 3.3a, the reconstructed temperature amplitudes also match well with the amplitudes imposed to the artificial temperature field of the phantom study. This is depicted in Fig. 3.3b. The amplitudes of the temperature fluctuations are estimated

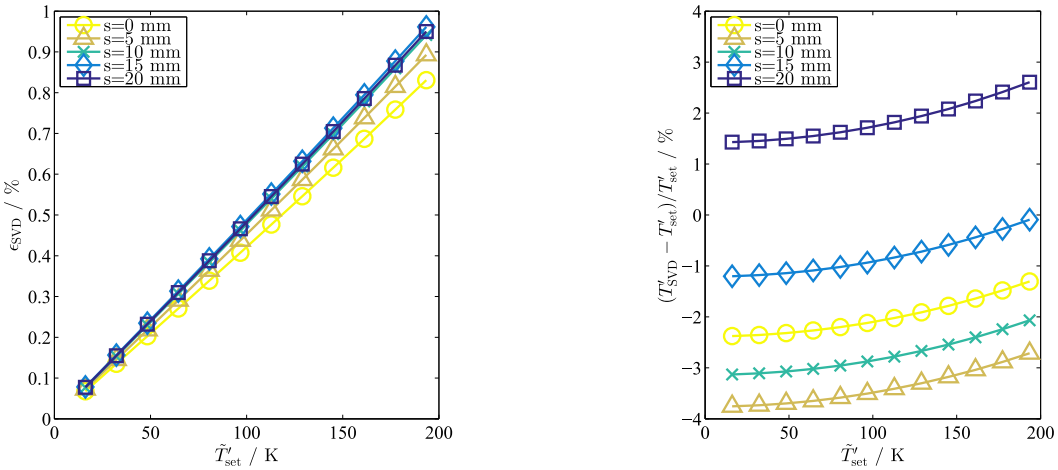

(a) **(b)**

Figure 3.3: **(a)**: Error measure ϵ_{SVD} for various artificial amplitudes $\tilde{T}'$ of the cross-sectionally averaged temperature oscillation; the different colors denote different penetration depths s of the acoustic source. **(b)**: Relative deviation between the cross-sectionally averaged temperature fluctuation amplitude for various penetration depths.

by means of a Fourier transform of the temperature vector derived from Eq. 2.103 (see Eq. 5.12). The relative error between the temperature amplitude specified in the phantom study and the corresponding amplitude extracted by the SVD method is well below 4 % and remains on the approximately same level for different imposed temperature amplitudes.

This result is not intuitive at a first glance as the radial temperature profile defined in the phantom study is strongly inhomogeneous and the different acoustic paths provide a rather poor coverage of the total measurement plane. To gain a better understanding of why the cross-sectionally averaged temperature amplitude is nevertheless obtained with a good accuracy, the interdependency between the temperature profile and the arrangement of the acoustic paths needs to be considered. Obviously, for the estimation of the cross-sectionally averaged temperature, regions at higher radii are weighted stronger (quadratically) than regions closer to the center of the duct.

By way of illustration, the acoustic paths are plotted in Fig. 3.4a for a penetration depth $s = 5\,\mathrm{mm}$ in polar coordinates. Obviously, the regions closer to the duct's wall are covered more densely by the acoustic paths than the inner region. To quantify this, a probability density estimate of the radial density of the acoustic paths is shown in Fig. 3.4b. The thin lines represent the density estimates of the different paths, the bold black line denotes the sum of the estimates of all seven paths. A clear peak is observed at about $r = 0.9R$, which mainly stems from the two microphones 1 and 7 that are located very close to the emitter. To relate the paths density to the cross-sectional average of a circle, the normalized squared radius r^2 is plotted as dashed red line. It represents the weighting of the radii for the cross-sectional average. It can clearly be seen that the sum of the probability density estimates of the paths (solid black line) exhibits a very similar characteristic with respect to the radius.

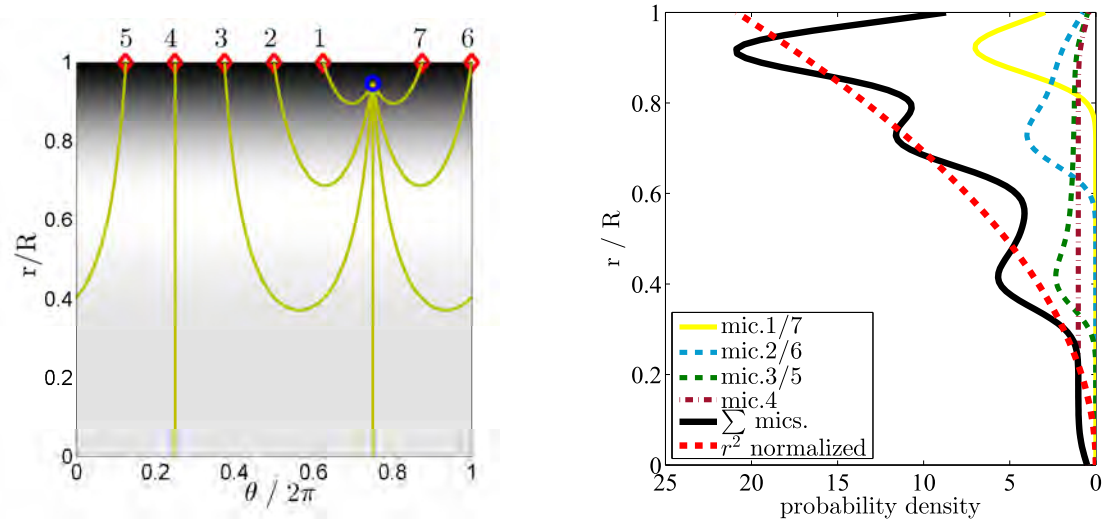

(a) **(b)**

Figure 3.4: **(a)**: Acoustic paths in polar coordinates for a penetration depth of the acoustic emitter of $s = 5\,\mathrm{mm}$. **(b)**: Probability density estimate (percentage) of the acoustic paths with respect to the normalized radius r/R; normalized square of the radius (bold dashed).

This is a rather qualitative than quantitative justification of the favourable performance of the SVD method to reconstruct the cross-sectionally averaged temperature fluctuation amplitude, but it seems reasonable. Phantom studies with various placements of the sound emitter and the microphones verify this outcome. These results can be found in Appendix A.1.

With regard to the experiments, however, it is important to also consider the corruption of the arrival time data by noise. The influence of this additional parameter is discussed in the following section.

3.1.2 Effect of noise on the SVD approach

In the previous section it has been shown that the SVD approach serves as a useful tool to estimate the amplitude of the cross-sectionally averaged temperature fluctuation. The measurement of the arrival times in a model gas turbine combustor, however, is strongly affected by noise, which stems from several uncertainties of different nature. The reasons for these uncertainties are discussed and quantified in Sec. 4. In the following, the effect of noise on the reconstructed amplitude of the cross-sectionally averaged temperature is investigated.

For the combustion chamber measurements, a maximum zero-to-peak noise level of $3\,\mu\mathrm{s}$ is observed for the arrival times (see Sec. 4.2.2.2). In Sec. 3.2.2, the implementation of noise is further explained. The resulting values of $\boldsymbol{\tau}_p$ are depicted in Fig. 3.5a as solid lines. The single-rank approximated matrix $\hat{\boldsymbol{\tau}}_p$ is represented in the same plot by dashed lines. The reconstructed arrival times are found to be less noisy than the input arrival times. The error that arises from the low-rank approximation does not strongly increase compared to the case without noise. In Fig. 3.5b, the relative error ϵ_{SVD} is plotted for various amplitudes of the cross-sectionally averaged temperature fluctuations $\tilde{T}'_{\mathrm{set}}$ and

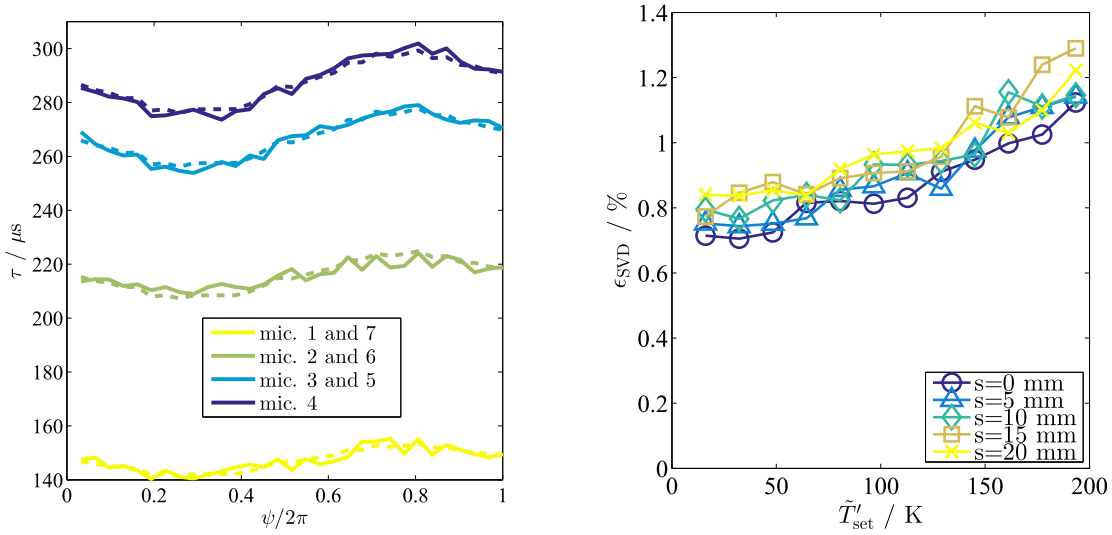

(a) **(b)**

Figure 3.5: **(a)**: **Solid lines**: $\boldsymbol{\tau}_p$ for $\tilde{T}' \approx 100\,\mathrm{K}$ and with $3\,\mu\mathrm{s}$ noise added to the flight times. **Dashed lines**: Corresponding single-rank approximation $\hat{\boldsymbol{\tau}}_p$. **(b)**: ϵ_{SVD} for various amplitudes $\tilde{T}'$ of the cross-sectionally averaged temperature oscillation and for different penetration depths s of the acoustic source; noise with an amplitude of $3\,\mu\mathrm{s}$ has been added to the flight times.

for different penetration depths of the acoustic emitter. When compared to Fig. 3.3a, it is evident that the error is only slightly shifted up to values of approximately 1 % and that the dependence of ϵ_{SVD} on the temperature amplitude is not strong anymore.

Regarding the reconstruction of the cross-sectionally averaged temperature amplitude, noise on the flight times exerts significant influence in the case of low temperature amplitudes. This can be seen in terms of the relative error between the imposed and the reconstructed cross-sectionally averaged temperature amplitude in Fig. 3.6a. Here, the noise on the arrival time fluctuations causes temperature perturbations in the order of the cross-sectionally averaged temperature amplitude specified in the phantom study. This is depicted in Fig. 3.6b for different penetration depths. Opposite to Fig. 3.3b, a clear trend between the different penetration depths s is observed. The relative error of the amplitude prediction decreases for positions of the acoustic emitter closer to the duct's wall. This is because the overall paths lengths become smaller when the acoustic emitter is located further inside the duct. This coincides with a decrease of the flight times. Consequently, the relative deviation due to noise increases. This trend can also slightly be seen in Fig. 3.5b, where ϵ_{SVD} is found to be larger for increasing penetration depths s. However, for cross-sectionally averaged temperature amplitudes larger than 60 K, the error of the amplitude estimated using the SVD approach remains below 5 %, which is an acceptable uncertainty. The noise level of $3\,\mu\mathrm{s}$ is rather a worst case scenario; in most of the measurements the level of noise is significantly lower.

In the framework of this phantom study, the SVD approach has proven to be a robust and accurate tool for the estimation of the fluctuation amplitude of the cross-sectionally averaged temperature. The amplitudes that are defined in the phantom study are reconstructed with an uncertainty of less than 5 %, this is also valid for very noisy flight times. The investigation also included various spatial positions of the acoustic emitter

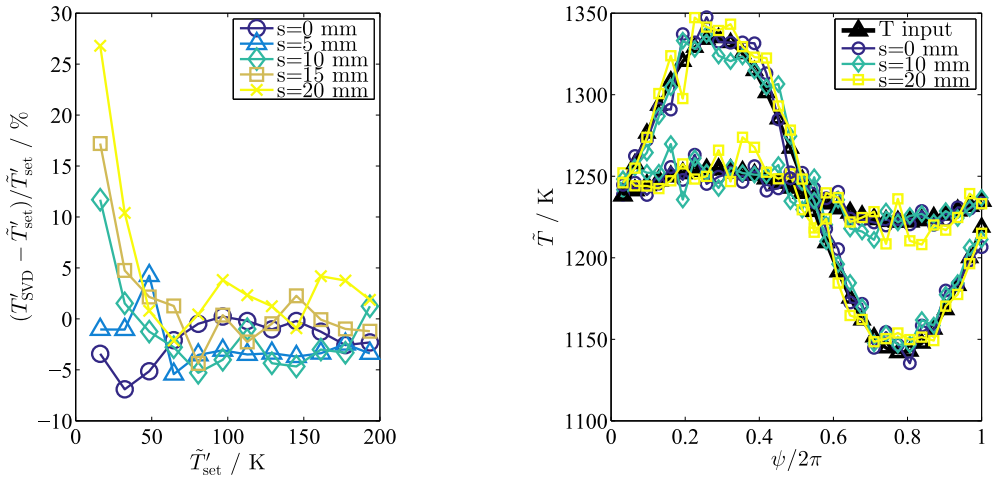

(a) **(b)**

Figure 3.6: **(a)**: Relative deviation between $\tilde{T}'_{\text{set}}$ and T'_{SVD} for various penetration depths and noise added to the arrival times (3 μs). **(b)**: One period of the temperature fluctuation with an amplitude of the cross-sectionally averaged temperature of approximately 100 K and 20 K.

that might occur in the measurement setup. Note that for different arrangements of the microphones and/or the acoustic emitter, the temperature amplitude obtained from the SVD method does not necessarily represent the oscillation of the cross-sectionally surface averaged temperature. In such cases, the path density shown in Fig. 3.4b looks very different, which is shown in Appendix A.1.

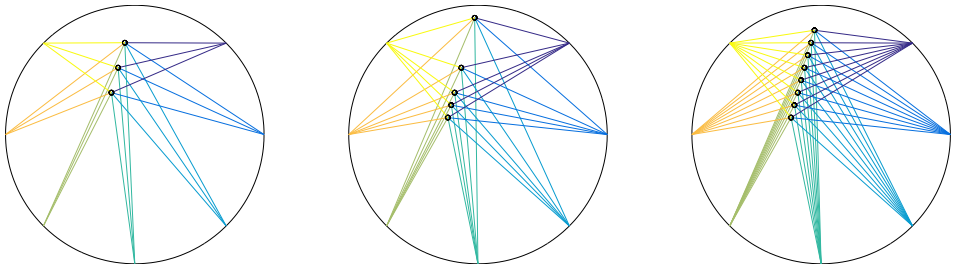

(a) $N_L = 21$ **(b)** $N_L = 35$ **(c)** $N_L = 56$

Figure 3.7: Arrangement of the acoustic paths used for the phantom study, this setup corresponds to the experimental setup used in the combustor test rig (see Section 4.3). **(a)**: Three spark positions at penetration depths $s = [30, 50, 70]$ mm which lead to a total number of $N_L = 21$ acoustic paths. **(b)**: Five spark positions at penetration depths $s = [10, 50, 70, 80, 90]$ mm which lead to a total number of $N_L = 35$ acoustic paths. **(c)**: Eight spark positions at penetration depths $s = [20, 30, 40, 50, 60, 70, 80, 90]$ mm which lead to a total number of $N_L = 56$ acoustic paths.

3.2 Validation of the asymmetric TOF setup

In this section, the onion peeling and collocation approaches introduced in Sec. 2.3.2 are validated by artificial sets of flight times.

In contrast to the phantom study in Sec. 3.1, where the target value was the amplitude of the reconstructed entropy wave, in this analysis, a one-dimensional spatial profile is reconstructed. Therefore, two additional error measures must be introduced. For the investigation of entropy waves, the cross-sectionally averaged temperature $\widetilde{T}$ is of interest. The corresponding error measure is defined as

$$\epsilon_{\mathrm{sa}} = \widetilde{T}_{\mathrm{reconstructed}} - \widetilde{T}_{\mathrm{input}}, \tag{3.1}$$

where $\widetilde{T}_{\mathrm{reconstructed}}$ is the cross-sectionally average of the reconstructed temperature field and $\widetilde{T}_{\mathrm{input}}$ is the cross-sectionally averaged temperature of the temperature field that has been used as input to generate the artificial flight time data. This error measure allows for the estimation of the accuracy of the temperature fluctuation reconstruction; however, it does not provide information on the shape of the reconstructed profile. Therefore, a *rms* error is defined as

$$\epsilon_{\mathrm{rms}} = \sqrt{\frac{1}{N_g} \sum_{i=1}^{N_g} \left(T_{i,\mathrm{reconstructed}} - T_{i,\mathrm{input}}\right)^2}, \tag{3.2}$$

where N_g denotes the number of discrete grid points the field is evaluated on. In the case of onion peeling, N_g refers to the number of discretization rings, and in the case of the collocation approach, N_g represents the number of discrete positions the basis functions are located at.

Three different experimental arrangements are considered (see Fig. 3.7). All of them refer to the asymmetric measurement setup presented in Sec. 4.3. The acoustic pulse

source location is asymmetrically traversed through the measurement plane; in case (a), the tomographic reconstruction algorithm is performed by means of $N_L = 21$ acoustic paths, for case (b), $N_L = 35$ acoustic paths are employed, and in the experimental setup (c) $N_L = 56$ ray paths are used for tomography. The asymmetric arrangement has been chosen in order to obtain more (linearly independent) information from one set of measured flight times (Sec. 4.3).

Similar to the phantom study in Sec. 3.1, the steady temperature profile obtained from thermocouple measurements serves as input temperature field (see Fig. 3.1a). Also in this study, a rotationally symmetric temperature field is assumed, which is a prerequisite for the application of an onion peeling approach and the one-dimensional collocation.

A phantom study is well suited to investigate the effect of measurement errors, i.e. errors in the projection, on the reconstructed field. However, before applying noise on the artificial measurement data, the setups are analyzed based on ideal data. The reason for this is the estimation of the error that may occur due to the unusual arrangement of the acoustic paths compared to the typical parallel path arrangement (see Fig. 2.11). In most applications found in literature, the ray paths penetrate the field as whole, their origin is not located within the field.

3.2.1 Onion peeling in the absence of noise

The irregular and asymmetric arrangement of the acoustic paths turns out to be challenging for the onion peeling algorithm. Even without noisy but ideal projection data, a (weak) regularization of the system matrix is required to obtain a sufficiently stable reconstructed field. This is shown in Fig. 3.8, where the reconstructed temperature field obtained from the onion peeling is compared to the input temperature field. Figure 3.8a depicts the case without any regularization. The solution becomes very unstable in the outer rings close to the wall, where the temperature gradients are the largest. For a weak Tikhonov regularization (zeroth order (Eq. 2.127) as well as first order (Eq. 2.131)) with a small regularization parameter of $\gamma = 5 \cdot 10^{-5}$, the strong deviations between the target profile and the reconstruction disappears and the errors ϵ_{sa} and ϵ_{rms} become significantly smaller. Particularly the error in the cross-sectionally averaged temperature reduces to less than 3 K, which is a very satisfying result. If the regularization parameter is further increased, both errors, especially ϵ_{rms}, become larger, which can be seen in Fig. 3.8c. A value of $\gamma = 0.01$ has been used here because this value will also be used in further studies with noisy projection data. It can be seen that the large temperature gradient is less accurately reconstructed compared to Fig. 3.8b. This is due to the fact that too large regularization parameters filter out the small scale characteristics of the field and thus cause a "smoothing" of the radial temperature profile. If γ is further increased, the reconstructed field converges to a horizontal line.

An indication that this is due to the ill-posedness of the problem is given by the condition number of the system matrix $\mathbf{L}$, which is plotted as a function of N_g in Fig. 3.9a. The differently colored curves represent the condition numbers of the system matrices evaluated for different numbers N_L of acoustic paths as shown in Figs. 3.7b and 3.7c. For each experimental setup, the maximum condition number is found where the number of rings equals the number of acoustic paths.

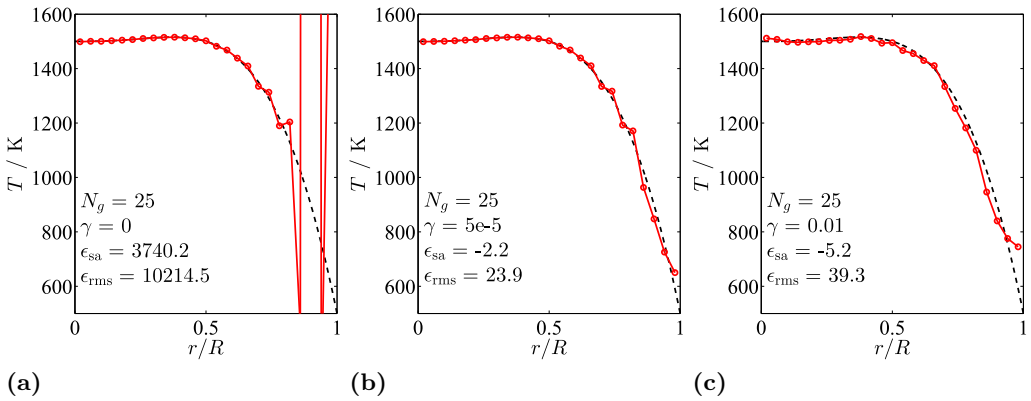

Figure 3.8: Onion peeling reconstructed (markers) and initial (dashed) one-dimensional temperature profile without noise on the arrival times; the field is discretized by means of 25 rings, a number of $N_L = 56$ acoustic ray paths are used corresponding to Fig. 3.7c. **(a)**: No Tikhonov regularization applied. **(b)**: Tikhonov regularization with $\gamma = 5 \cdot 10^{-5}$. **(c)**: Tikhonov regularization with $\gamma = 1 \cdot 10^{-2}$.

The impact of the Tikhonov regularization can be seen in the same graph (Fig. 3.9a) by the condition number β_{LM} of the extended system matrix $[\mathbf{L}; \quad \gamma\mathbf{M}]$ which is plotted for the two regularization parameters $\gamma = 5 \cdot 10^{-5}$ and $\gamma = 0.01$ that have been used in Figs. 3.8b and 3.8c, respectively. The condition number is reduced by more than one order of magnitude for $\gamma = 5 \cdot 10^{-5}$ and by almost three orders of magnitude in case of $\gamma = 0.01$. The difference between the different numbers N_L of acoustic paths becomes marginal. This shows that the system of linear equations that is set up by the onion peeling approach becomes better posed due to the Tikhonov regularization. Above $N_g \approx 20$, the number of discretization rings does not significantly affect the condition number anymore. Furthermore, it can be seen that it does not matter whether the original system is underdetermined ($N_g < N_L$) or overdetermined ($N_g > N_L$).

The results in Fig. 3.9a, however, do not necessarily mean that the reconstructed field fits better to the input field if the condition number is lowered. In Fig. 3.9b, the two error measures, ϵ_{sa} and ϵ_{rms}, are plotted with respect to N_g. As it has already been observed in Fig. 3.8, the deviation in the cross-sectionally averaged temperature ϵ_{sa} is by far smaller than ϵ_{rms}. The reconstructed field that has been evaluated with a regularization parameter of $\gamma = 5 \cdot 10^{-5}$ exhibits less deviations than the field obtained with a higher regularization value, which, according to Fig. 3.9a, provides a better condition number.

From this phantom study of the onion peeling reconstruction method without noise it is derived that the regularization parameter γ is of high importance and has to be selected carefully. If the number of rings is greater than approximately $N_g = 30$, the cross-sectionally averaged temperature can be reproduced with an accuracy of far less than 10 K.

3.2.2 Implementation of noise

In realistic measurement setups, the projection data are affected by noise. This could be the uncertainty of the exact location of the acoustic source or random "temperature noise" between the emitter and the receiver. This noise is represented in this phantom

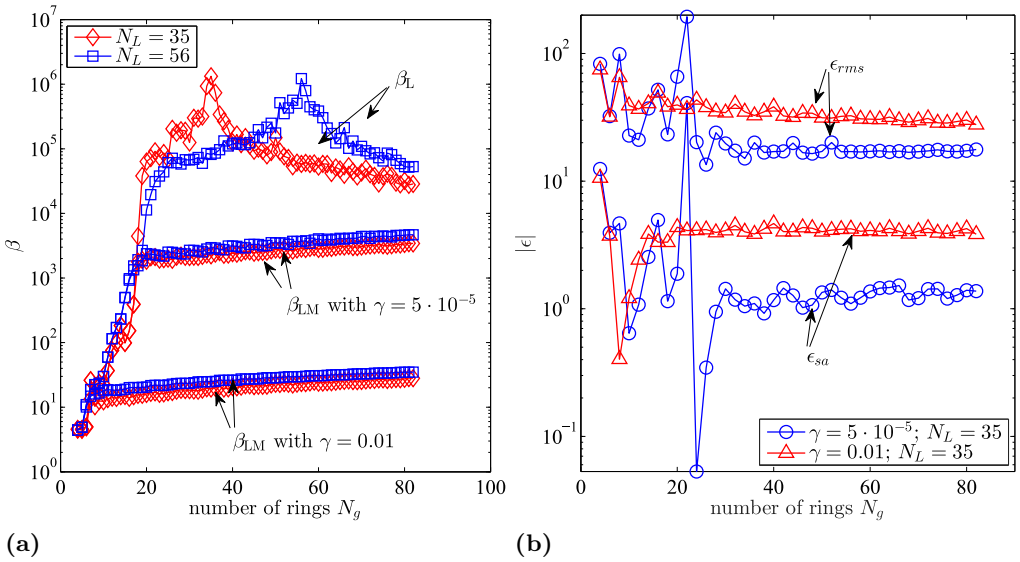

Figure 3.9: **(a)**: Condition number β_{L} of the system matrix $\mathbf{L}$ as a function of the number of discretization rings N_g for different numbers of acoustic paths N_L. Condition number β_{LM} of the extended system matrix $[\mathbf{L}; \quad \gamma\mathbf{M}]$ with a Tikhonov regularization parameter of $\gamma = 5 \cdot 10^{-5}$ as a function of N_g. **(b)**: Error measures ϵ_{sa} and ϵ_{rms} with respect to the number of discretization rings N_g.

study by a random fluctuation of the arrival times within a certain band. In the experimental investigations it is found that a realistic value for the noise in the arrival times is somewhere between 1 μs and 3 μs. In Fig. 3.10, an example of a relative noise level of the flight times that is artificially generated and superimposed to the numerically obtained arrival times is depicted as a function of the acoustic path lengths. Each marker represents one of the 56 arrival times of the setup shown in Fig. 3.7c. The solid lines denote the standard deviation of the arrival time distribution.

It is important to note that the results of the tomographic reconstruction methods strongly deviate from each other dependent on the random noise distribution, even though the same noise level has been adjusted. To compensate for these significant statistic fluctuations, the error measures and other parameters shown in this section are averaged over a sufficient number of events (> 80).

3.2.2.1 Effect of noise on the onion peeling approach

If noise is added to the projection vector for the onion peeling, Tikhonov regularization (see Eq. 2.127) becomes indispensable, as otherwise the field solution becomes highly unstable. A Tikhonov regularized solution for a number of $N_g = 25$ rings and $N_L = 56$ ray paths (Fig. 3.7c) is shown in Fig. 3.11a. A regularization parameter of $\gamma = 0.01$ has been found to provide a minimum error ϵ_{sa} in the obtained cross-sectionally averaged temperature. Additionally, a sufficiently accurate reconstruction of the one-dimensional temperature profile is obtained, which is associated to the error measure ϵ_{rms}. In terms of the cross-sectionally averaged temperature, the difference between the input temperature and the reconstructed temperature is less than 1 K, which is a promising result with regards to the entropy wave extraction. The reconstructed spatial temperature profile,

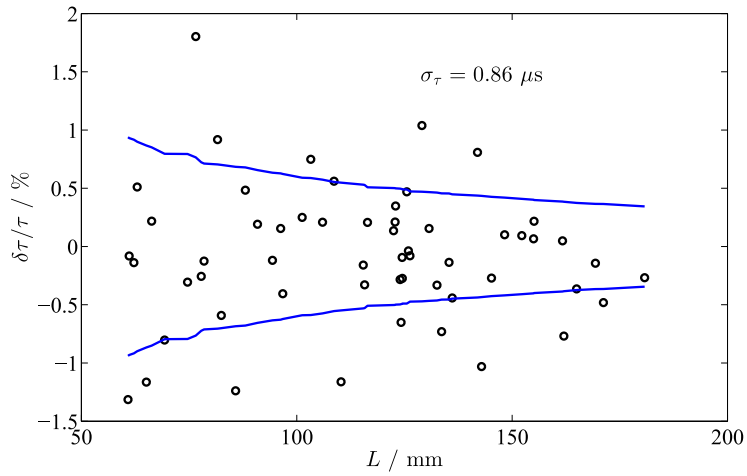

Figure 3.10: Relative deviations of the flight times (markers) for the different acoustic paths (sorted by length); according to findings from measurements, a noise level of about $1\,\mu$s has been used. The lines denote the associated rms values.

however, is far more noisy compared to the temperature profile obtained without noise on the arrival times (see Fig. 3.8).

In the following, the focus will only be on the reconstruction of the temperature profile. However, it is important to keep in mind that the actual target parameter is the inverse speed of sound. Therefore, in Fig. 3.11b, the one-dimensional profile of the reconstructed inverse speed of sound is compared to the input profile. Due to the quadratic relation between speed of sound and temperature, the relative deviation and with it the noise obtained on the estimated profile are smaller in case of the inverse speed of sound compared to the temperature.

An important parameter for the onion peeling approach is the number of discretization rings the field is defined on. Employing the same regularization parameter $\gamma = 0.01$ as in Fig. 3.11, the two different error measures introduced in Eqs. 3.1 and 3.2 are depicted in Fig. 3.12. An important message is contained in Fig. 3.12a, where the deviation between the reconstructed and the initial cross-sectionally averaged temperatures is plotted. For all various amounts of acoustic paths, the error values are in an acceptable range. Particularly for $N_L \geq 35$ and a number of rings that is of the order of $N_g \geq N_L$, the deviation drops below 3 K. At the same time, however, ϵ_{rms} increases to values above 80 K (see Fig. 3.12b). This demonstrates how important it is to distinguish between these two different types of errors.

However, it is also important to note that the high values of ϵ_{rms} might be misleading. If the regularization value is properly selected, a polynomial fit through the discrete temperatures obtained from the onion peeling approach is in good accordance with the input temperature field.

Note that the Tikhonov regularization used in Fig. 3.11 is the Tikhonov regularization of first order (see Eq. 2.131). In case of a zeroth order Tikhonov regularization, ϵ_{sa} as well as ϵ_{rms} become unacceptably large. Alternatively to the first order Tikhonov regularization, the randomized Kaczamarz method (see Eq. 2.123) converges to the same result, which is shown in Pause (2017). There, it is also shown that the SIRT algorithm

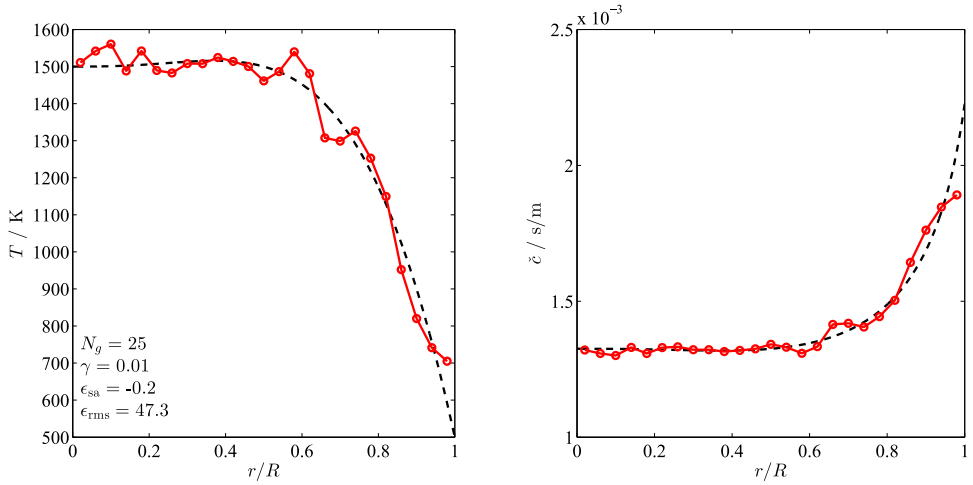

(a) **(b)**

Figure 3.11: Onion peeling reconstructed field profile (markers) and input profile (dashed line) of the onion peeling algorithm with $N_g = 25$ rings and $N_L = 56$ acoustic paths (see. Fig. 3.7c). The projection data (arrival times) are superimposed by random noise with a standard deviation of about 1 μs; Tikhonov regularization is applied according to Eq. 2.127 with $\gamma = 0.01$. **(a)**: Temperature profile. **(b)**: Profile of the inverse speed of sound.

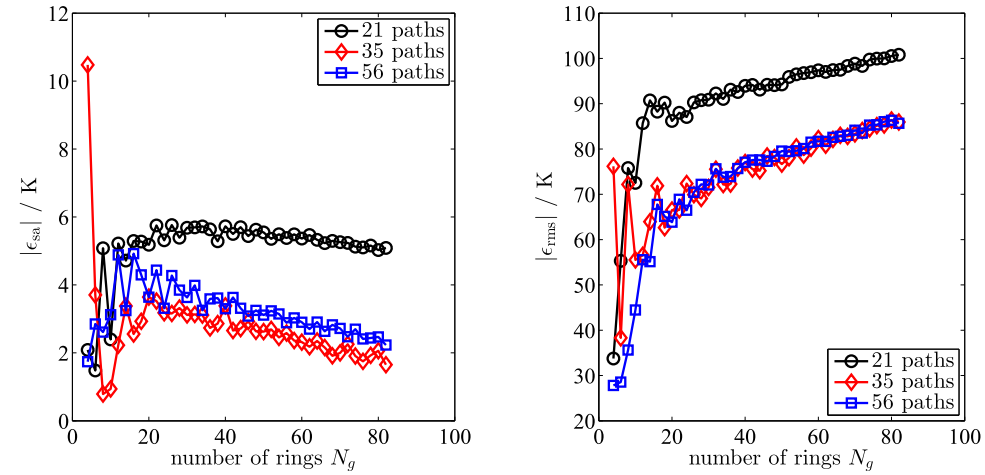

(a) **(b)**

Figure 3.12: Error measures of the comparison between the reconstructed temperature field by means of onion peeling and the input temperature field of the phantom study as a function of the number of discretization rings N_g; the projection data, which are the arrival times, are superimposed by noise with std(τ)$\approx$ 1 μs; a Tikhonov regularization parameter of $\gamma = 0.01$ i applied. **(a)**: Error of the cross-sectionally averaged temperature (Eq. 3.1). **(b)**: rms error of all spatially discretized temperatures (Eq. 3.2).

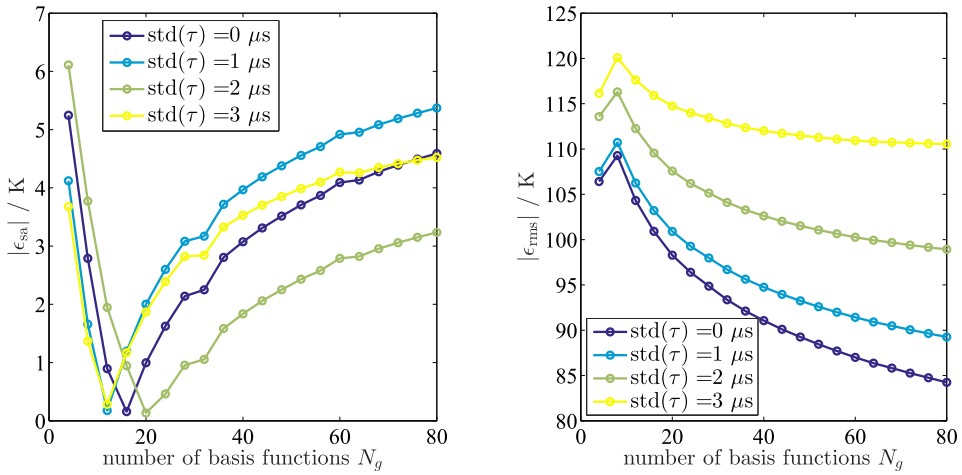

(a) **(b)**

Figure 3.13: Error measures of the one-dimensional collocation approach applied on the experimental setup with $N_L = 56$ acoustic paths (see Fig. 3.7c). For all various noise levels, the parameter $\zeta = 500$ has been employed. **(a)**: Error of the cross-sectionally averaged temperature (Eq. 3.1). **(b)**: rms error of all spatially discretized temperatures (Eq. 3.2).

(see Eq. 2.124) provides as well a sufficiently stable and accurate solution of the onion peeling approach, the error measures are of the same magnitude compared to the first order Tikhonov regularization.

3.2.2.2 Phantom study on one-dimensional collocation

The phantom study of the one-dimensional collocation approach introduced in Section 2.3.2.3 is not presented as detailed as it has been done for the onion peeling in the preceding subsection. This is because the results look qualitatively as well as quantitatively very similar to the results of the onion peeling approach. To obtain a stable solution for the system of linear equations in Eq. 2.121, also here, Tikhonov regularization has to be applied. It is worth noting that in the case of one-dimensional collocation, the best results are obtained with a zeroth order Tikhonov regularization. This is in contrast to the onion peeling approach, where a first order Tikhonov regularization was required to obtain proper results. There, a zeroth order Tikhonov regularization did not sufficiently improve the results quality.

Besides the regularization parameter γ, the parameter μ, which is introduced in Eq. 2.118, has to be selected. As both parameters affect the damping of the noisy oscillations of the reconstructed field, a new parameter $\zeta = \mu/\gamma$ is introduced (see Pause (2017)). Additionally, the number of basis functions N_g plays an important role for the result's quality as does the number of discretization rings in case of onion peeling.

The two error measures ϵ_{sa} and ϵ_{rms} are depicted for the one-dimensional collocation approach in Fig. 3.13 as a functions of the number of basis functions N_g. A value of $\zeta = 500$ has been found to provide sufficient damping of the reconstructed field in the relevant range of noise levels up to $3\,\mu$s as well as for the different numbers of basis functions the field solution is based on. The cross-sectionally averaged temperature of

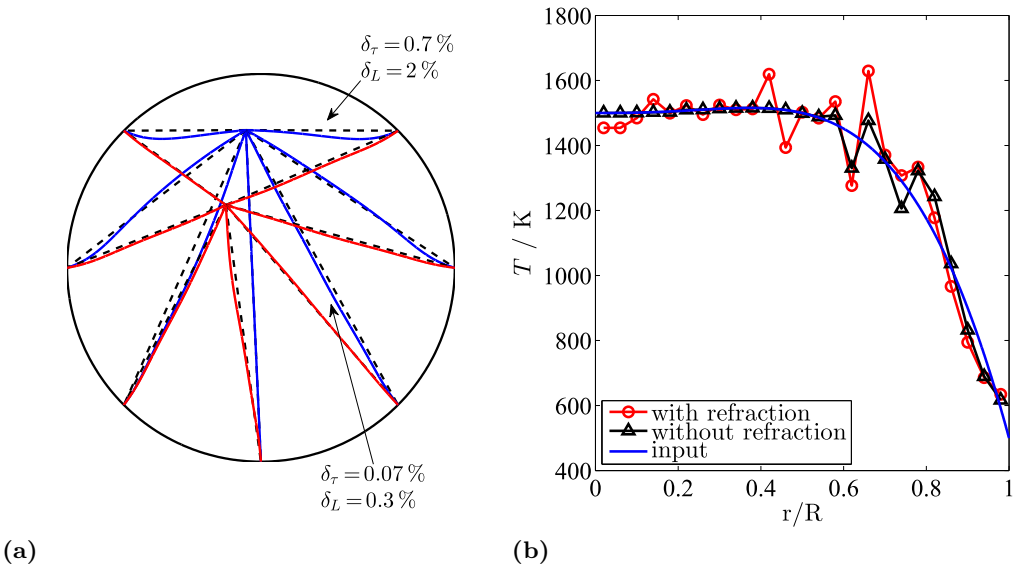

(a) **(b)**

Figure 3.14: **(a)**: Deflected acoustic paths (solid lines) and the corresponding straight paths (dashed) for two different discharge locations. **(b)**: Onion peeling reconstructed radial temperature profiles with (◯) and without (△) accounting for the deflection of the acoustic paths; $N_g = 25$, based on setup shown in Fig. 3.7a.

the reconstruction matches well with the input field. Even for higher noise levels, the deviation is less than 5 K in the relevant range of N_g (see Fig. 3.13a). A prominent dependence on the noise level is also observed for ϵ_{rms}, which can be seen in Fig. 3.13b. This error measure is far larger than ϵ_{sa}. However, it is of similar order as it has been obtained by using the onion peeling approach in Fig. 3.12b.

A further investigation of the one-dimensional collocation will not be presented in this section. It has been found that for an appropriate choice of the parameters μ and γ, the characteristics of the reconstructed temperature fields are the same as obtained from the onion peeling approach. Obviously, both methods finally converge to the same solution. More detailed information on the validation of the tomographic approaches applied to the specific measurement setup in this study can be found in Pause (2017).

3.2.3 Effect of refraction on the reconstructed field

In Sec. 2.2.3 we discussed the influence of refraction due to field inhomogeneities on the propagation of the acoustic pulse. Two methods were presented which allow for an estimation of the actual acoustic path trajectory. In this section, we solve the boundary value problem derived in Eq. 2.86 applied on the temperature field shown in Fig. 3.1b. The inverse problem becomes non-linear, because the geometry matrix $\mathbf{L}$ (see, e.g., Eq. 2.115) is now a function of the solution vector $\check{\boldsymbol{c}}$. The solution of the inverse problem has to be found iteratively. The deflected paths and the corresponding straight paths are shown in Fig. 3.14a for two different discharge locations. The relative deviation of the length of the acoustic path δ_L and the corresponding flight time between the straight paths and the deflected path δ_τ depend strongly on the position of the acoustic path. If the path's direction is rather perpendicular to the temperature gradients in the field, the effect of refraction is negligible. However, if the discharge location is close to the

wall, especially the short paths, which are aligned rather in parallel to the temperature iso-lines, are significantly deflected. For the latter, a relative deviation in path length of up to $\approx 2\,\%$ has been found, whereas the relative deviation in flight time counts only $\delta_\tau = 0.7\,\%$.

Due to the unconventional path arrangement of the present experimental setup, i.e. with the origin of the paths within the field, the strong temperature gradients are mainly perpendicularly oriented to the paths' direction. Therefore, when accounting for the acoustic refraction, the reconstructed temperature field does not change significantly compared to the reconstruction based on straight acoustic paths. The reconstructed temperature fields are depicted in Fig. 3.14b; note that different Tikhonov regularization parameters are applied for solving the inverse problems.

Summary on phantom study

Regarding the SVD method, the phantom study revealed that this method provides an accurate and robust measure of the cross-sectionally averaged temperature fluctuation. The cross-sectionally averaged amplitudes are reconstructed with a deviation from the actual amplitudes of less than $5\,\%$. This also holds true for noisy projections, which demonstrates that the SVD method is a tool applicable for the flight time measurements in a combustion chamber.

In terms of the one-dimensional approaches, it can be concluded that a reconstruction of the cross-sectionally averaged temperature can be achieved with sufficient accuracy. However, a careful selection of the (regularization) parameters and the spatial field resolution is required. If an appropriate set of parameters is found, also the spatial distribution of the temperature field is well recovered by the results of the one-dimensional methods. Furthermore it has been found that the influence of refraction due to inhomogeneities in the temperature field can be neglected for the experimental setup used in this study.

In the later experimental study of this work, it will also be investigated how the violation of the assumption of a rotationally symmetric field affects the solutions of the one-dimensional methods. To address this issue, an additional phantom study has been conducted (see Sec. 5.3.4).

4 Experimental Realization of the Time-of-Flight Method

The TOF measurement technique, as described in the previous chapter, has to be applicable in full scale gas turbine engines. Hence, for the technical implementation of the TOF method, the following three major challenges have to be addressed:

- High-temperature (>1800 K), corrosive, and humid environment
- High background noise level
- High-pressure (>20 bar).

In contrast to other studies, where the TOF method is employed in unconfined setups (J. Li et al., 2013; C. Cai and Regtien, 1993), here, acoustic waves are reflected at the combustion chamber walls. Therefore, the generation of pulse trains or continuous sweeps, as for example used by Bramanti et al. (1996) or Zhang et al. (2015), is practically difficult to realize. Such continuous excitation methods allow for a cross-correlation analysis to estimate the traveling time of the acoustic signal. Reflecting waves would significantly corrupt these evaluations. To avoid the influence of disturbing reflections, a short pulse, detectable by its first pressure maximum, is required. In this study, the acoustic pulse generated by an electric discharge is utilized. This experimental method addresses the first two bullet points listed above. A spark discharge can occurs at very high temperatures (its generation is even facilitated at elevated temperatures) and its high-frequency content allows for a detection even in the presence of high-level background noise. The realization and characterization of this technique will be presented in Sec. 4.1.

All these aforementioned requirements reduce the amount of feasible options for the realization of the acoustic excitation as well as the acquisition. In the following subsections, the selected techniques are presented and characterized. The experimental setup has partly been published in Wassmer, Schuermans, et al. (2016).

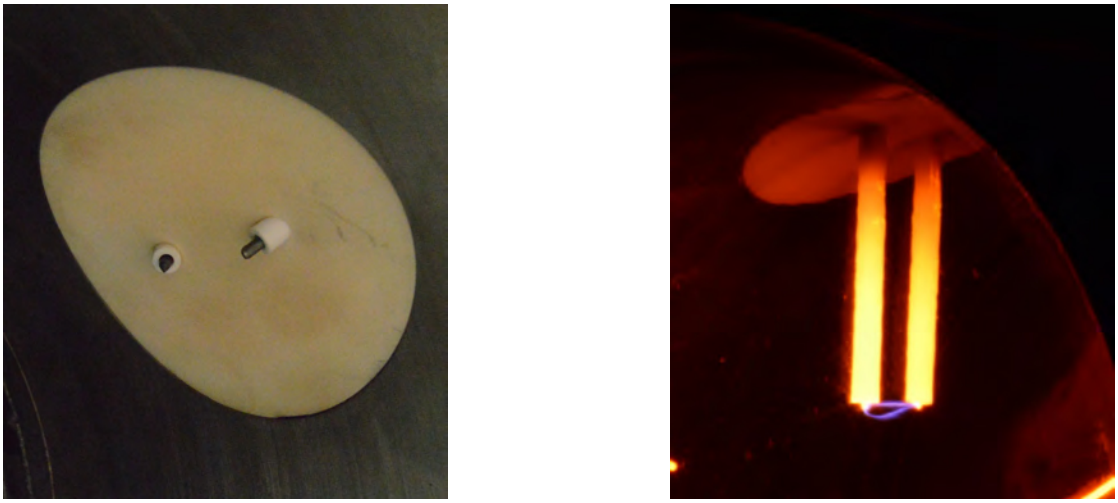

(a) **(b)**

Figure 4.1: Acoustic source shown from inside the combustor **(a)**: Electrodes embedded into ceramic sleeves, penetrating into the combustion chamber through a ceramic adapter; tapered electrodes arrangement used for the experimental setup shown in Fig. 4.23. **(b)**: Electrodes embedded into ceramic sleeves in a parallel arrangement (used for the experimental setup in Fig. 4.25). During operation of the combustor, the ceramic sleeves as well as the electrodes' tips are glowing.

4.1 Acoustic excitation

The generation of a very short acoustic pulse ($\lessapprox 1$ ms) is realized by an electric discharge between two electrodes. The acoustic characteristics of a spark discharge have been analyzed amongst others by Wyber (1975), Wright (1983), Martinson and Delsing (2010), and Ayrault et al. (2012). A main advantage of such an acoustic source is its durability in terms of temperature and pressure. The material of the electrodes is tungsten (as it is also used in welding machines) that can withstand far higher temperatures than present downstream of the flame in the investigated experimental setup. Figure 4.1a shows the two electrodes from inside the combustion rig. The electrodes are penetrated into the rig through a ceramic adapter. In order to prevent a discharge taking place on the surface of the electrode adapter, each electrode is separately embedded into a ceramic sleeve.

In Fig. 4.1a, the electrodes are arranged in a tapered manner, where the electrodes are inserted under an opening angle of 60°. This allows for a continuous adjustment of the electrodes gap width. However, this design links the penetration depth of the electrodes' tips to the gap width and thus limits the maximum insertion length of the acoustic source.

A different electrode arrangement, which is presented in Fig. 4.1b, enforces a fixed distance between the electrodes, however allows for a continuous variation of the penetration depth of the electrodes' tips. Here, the electrodes are depicted under operational conditions. Due to an extended exposure time of the camera, several discharges are visible between the tips of the electrodes. The reason for the two different electrode designs that are used in the experimental setups in this work will be discussed in Sec. 4.3.

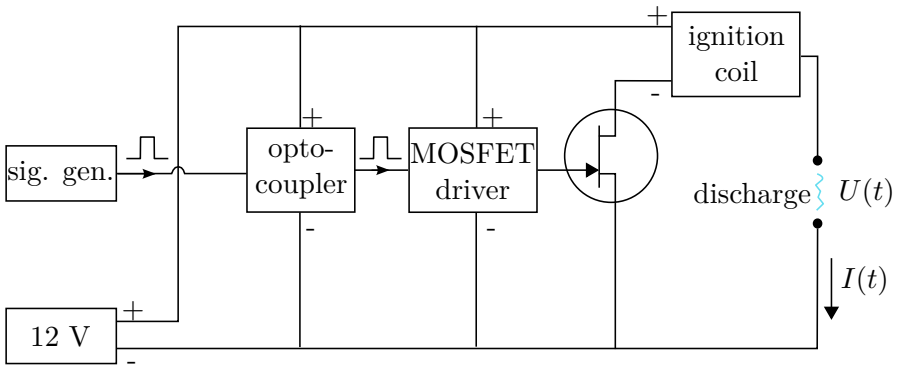

Figure 4.2: Schematic of the high-voltage setup to generate an electric discharge. A MOSFET together with a 60 kV ignition coil (with a primary resistance of $R_p = 0.45\ \Omega$) is used to provide a controlled discharge between the two electrodes on the right-hand side of the electrical layout.

In this study, a MOSFET[1] together with a 60 kV ignition coil (with a primary resistance of $R_p = 0.45\ \Omega$) is used to provide a controlled discharge between the two tungsten electrodes of diameter $\varnothing = 2.4\,\text{mm}$. The schematic of the high-voltage setup is depicted in Fig. 4.2. The MOSEFT is triggered by a 5 V square wave provided by a signal generator.

If the gap between the electrodes is too large, the electric energy is discharged within the ignition coil. If such a misfire occurs consistently, the ignition coil overheats and breaks. To prevent damage from surrounding measurement equipment due to high voltage pulses, the primary power supply is provided by a 12 V car battery (capacity: 120 Ah). Thus, no external grounding is required. An opto-coupler is implemented between signal generator and MOSFET driver to protect the signal generator from potential disturbing feedback signals.

4.1.1 Non-linear acoustic effects

If the voltage between the two electrodes, which are separated by a gap of width d_e, increases above a certain level U_b, the air within the gap is ionized and the voltage immediately breaks down. The electric current, that is induced due to the voltage breakdown, flows through a plasma channel between the electrodes. Consequently, the air along the channel is heated up abruptly to several thousand Kelvin, which implies a rapid expansion of the gas. This, in turn, induces a shock front that propagates mainly in perpendicular direction away from the plasma channel. The pressure rise due to the shock front might reach more than 1 kPa (Yuldashev et al., 2010). In literature, this intense acoustic transients are known as *N waves*, as their appearance in time and space resembles N waves (Wright, 1983). A schematic of the transformation of the acoustic pulse generated by the discharge to a N wave is depicted in Fig. 4.3. The pressure pulse forms two very steep gradients in time and space, whereas these sharp characteristics disappear after a certain time and a certain propagation length due to dissipative effects. Subsequently, the pressure wave propagates ideally in a harmonic sinusoidal fashion as considered in linear acoustics theory.

[1] Metal-Oxide-Semiconductor Field-Effect Transistor

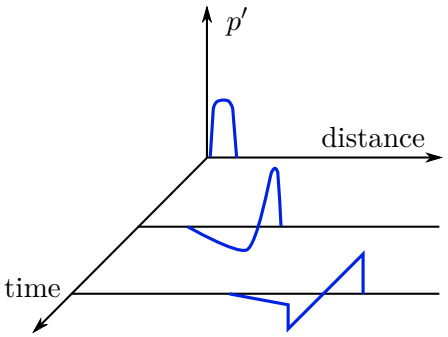

Figure 4.3: Schematic of the transformation of a pressure pulse caused by an electric discharge to a N wave; the schematic is based on Klinkowstein (1974).

This non linear acoustic phenomenon has been investigated extensively within the last six decades, comprehensive discussions can be found by, e.g., Freeman and Cragg (1969), Wyber (1975), Page and McKelvie (1977), Wright (1983), and Ayrault et al. (2012).

As the TOF approach relies on the assumption that the propagation velocity of the acoustic pulse equals the speed of sound, it is crucial to estimate the propagation velocity of such a N wave. Sedov (1959) provides a dimensionless solution for the expansion of a shock wave. He defines a dimensionless propagation length $l^\star = l/l_0$ with $l_0 = \sqrt[3]{E_s/p_0}$ and a dimensionless time $t^\star = t/t_0$ with $t_0 = p_0^{-5/6}\sqrt[3]{E_s}\sqrt{\rho_0}$. Finally, he formulates the propagation length l as a function of time:

$$l(t) = c\frac{l^\star}{t^\star}t, \tag{4.1}$$

where c denotes the adiabatic speed of sound as derived in Eq. 2.48 and E_s represents the energy content of the discharge. He further postulates that the propagation velocity $v = l(t)/t$ lasts until $t = 8t_0$, whereas from that time on the propagation velocity is assumed to drop to the adiabatic speed of sound. In order to validate this theory, Loeb et al. (1985) measured the velocity of the expansion of a shock wave. Their results exhibit, that the propagation velocity exceeds the speed of sound by several 100 m/s. However, their results cannot directly be related to the experimental situation in this study, as they performed the discharges below atmospheric pressure and at ambient temperatures.

To estimate the propagation velocity by means of Eq. 4.1 for the experimental setup in this study, the energy E_s, which is released by the electric discharge and determines Eq. 4.1, needs to be assessed. E_s can be estimated from the electric energy E_e which is disposed during the discharge process and the electro-acoustic efficiency η_{ea}: $E_s = \eta_{ea}E_e$. The values of η_{ea} that are found in literature scatter quite strongly. Referring to Wyber (1975) and Loeb et al. (1985), we consider a value of $\eta_{ea} = 10\,\%$. The electric energy can be assessed based on theoretical consideration as $E_e = \frac{1}{2}CU_b^2$, where C denotes the electric capacity of the discharge setup. Since latter is not trivial to determine in the measurement setup used in this work, a second, more practical approach, has been employed (Zhong et al., 2015):

$$E_e = \int P(t)dt = \int U(t)I(t)dt, \tag{4.2}$$

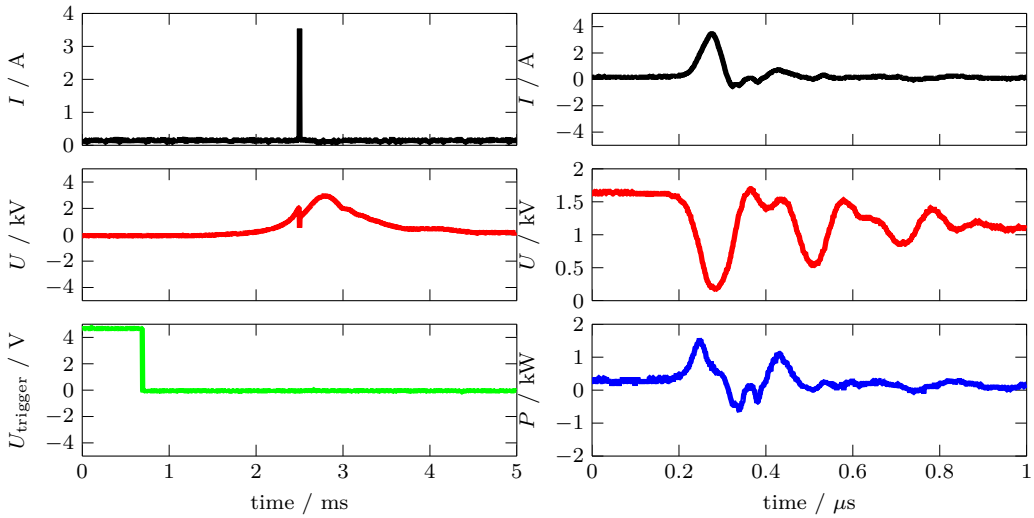

Figure 4.4: (left): Time series of the current, the voltage, and the trigger signal (as depicted in Fig. 4.2) of one discharge at a temperature of approximately 1800 K and a gap width of $d_e = 22$ mm. **(right)**: Zoomed time series of the current and the voltage as shown on the left, at the bottom the electrical power is depicted.

where $P(t)$ denotes the electric power and $I(t)$ and $U(t)$ are the current and the voltage at the electrodes, respectively. Current and voltage have been measured at the locations indicated by the variables on the very right-hand side in the schematic in Fig. 4.2. The current strength is assessed by means of a Hall effect sensor (Pearson Electronics model 6585) and the voltage is measured with a high-voltage probe of type PMK 4002 close to the electrodes. The measurements have been conducted in presence of combustion as it is the case for the typical measurements.

The time signals of the trigger signal, the current, and the voltage is shown in Fig. 4.4 on the left. The current flow corresponds directly to the occurrence of the plasma channel. Thus, its measurement exhibits that this event happens within a very short period of time (≈ 100 ns). At the same time, the voltage, which has so far been rising, breaks down. Since the existence of the plasma channel is too short to fully discharge the high-voltage coil, the voltage increases again after the breakdown, however, this does not lead to another discharge.

It is further important to note that the discharge occurs almost two milliseconds after the falling edge of the trigger signal arrived at the MOSFET. This time delay depends on the breakdown voltage and thus is a function of the gas temperature between the electrodes. The reason for this issue and why it might be challenging will be discussed in Sec. 4.2.2.1. To assess the electric energy, the integral in Eq. 4.2 is evaluated only within the period of time the discharge actually occurs. This instance of time is depicted in Fig. 4.4 on the right-hand side. The very bottom plot shows the electric power as the product of the voltage and the current. The oscillations of the voltage measure after the main breakdown are due to the specific electrical layout used in this study.

The measurements have been performed at different gas temperatures, in Fig. 4.5 the discharge energy is plotted as a function of these gas temperatures. The values shown are the medians evaluated over 20 measurements that have been conducted consecutively at 30 Hz, the error bars denote the corresponding standard deviation.

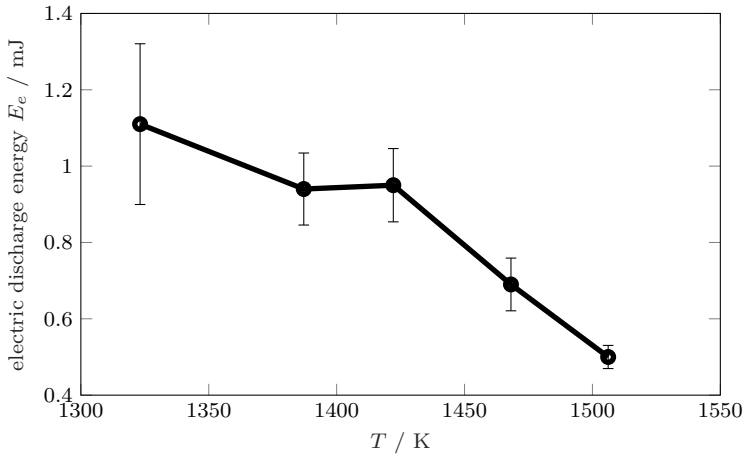

Figure 4.5: Electric discharge energy evaluated according to Eq. 4.2 as median over 20 measurements; the error bars represent the standard deviation. By means of the equivalence ratio, different gas temperatures have been adjusted in the combustion chamber the electrodes had been plugged to.

It is well known from literature, e.g., Küchler (2009), that the breakdown voltage decreases with increasing temperature. This is reflected in Fig. 4.5 by the drop of the discharge energy for higher gas temperatures. Consequently, the largest effect of the non-linear acoustic phenomenon is expected to happen at the lowest temperature (provided that the electro-acoustic efficiency η_{ea} does not depend on the gas temperature). Especially at lower temperatures, the measurement uncertainty of the discharge energy becomes larger which might be associated to the randomness of the shape of the plasma channel's trajectory. This phenomenon will be discussed in a following paragraph. Another source of error for the determination of the discharge energy is a time delay between the measurement of voltage and current. Freeman and Cragg (1969) estimate an error of up to 20 % in case of a time delay between current and voltage measurement of approximately 10 ns. The occurrence of such a time delay cannot be excluded for the measurements presented in Fig. 4.5 and are thus considered in the following evaluation of the propagation velocity of the acoustic pulse.

In a worst case scenario, so for the lowest temperature ($T \approx 1300\,\mathrm{K}$), a discharge energy of approximately 1.7 mJ has to be considered. If we apply an electro-acoustic efficiency of $\eta_{ea} \approx 10\,\%$ given by Wyber (1975), an acoustic energy E_a of less than 0.2 mJ is obtained. The resulting propagation velocities evaluated according to Sedov (1959) and based on the acoustic energy estimation are plotted as a function of the radial distance from the discharge location in Fig. 4.6. Apart from the electric energy $E_e = 0.2\,\mathrm{mJ}$, which has been estimated for the experiments in this study, the propagation velocity has been evaluated as well for $E_e = 1\,\mathrm{mJ}$ and $E_e = 10\,\mathrm{mJ}$. For $E_e = 0.2\,\mathrm{mJ}$, a significant increase of the propagation velocity compared to the expected speed of sound is observed only within a radius of $r < 1\,\mathrm{mm}$ around the plasma channel. For higher electric energies, this area is expanded up to $r \approx 3\,\mathrm{mm}$ in case of $E_e = 10\,\mathrm{mJ}$. Even though the spatial sphere of influence might be quite small, the propagation speed within this area could exceed the adiabatic speed of sound by more than its double.

In order to assess whether or not the results presented in Fig. 4.6 are problematic for the assumption of pure linear acoustic in the TOF approach, an arrival time τ_c, which

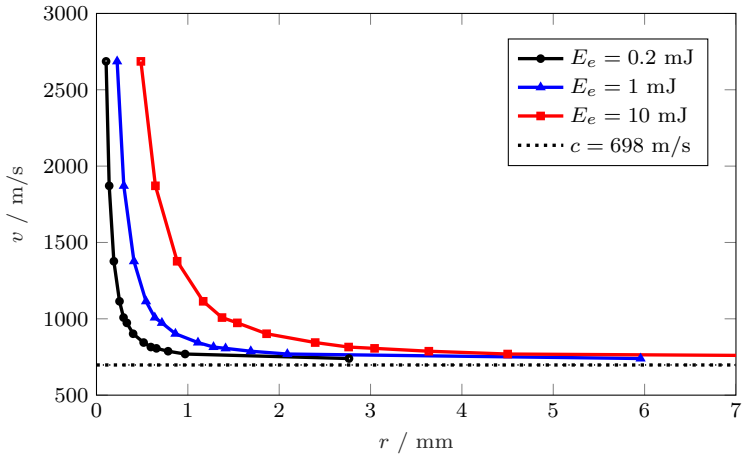

Figure 4.6: Propagation velocity of the acoustic pulse due to a discharge as a function of the radial distance from the plasma channel location (see Eq. 4.1). The evaluation is done based on Sedov (1959) for three different values of the electric discharge energy E_e; the expected adiabatic speed of sound for a temperature of $T = 1323\,\mathrm{K}$ is plotted as dotted line.

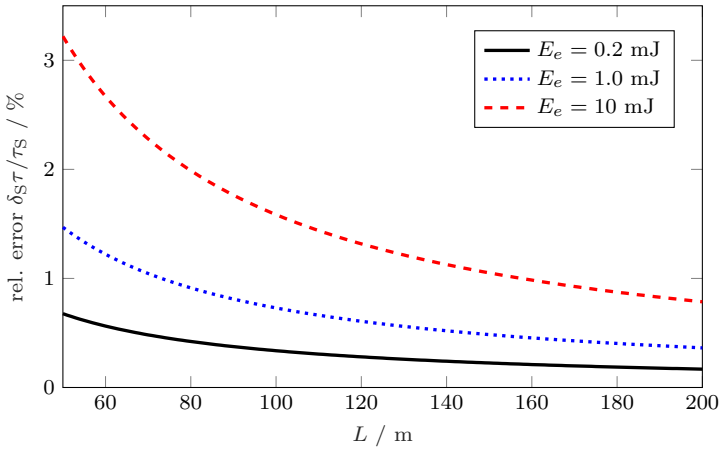

Figure 4.7: Relative deviation between the flight time based on the adiabatic speed of sound τ_c (Eq. 4.3) and the resulting flight time derived from Sedov's solution (Eq. 4.4); the different curves refer to three electric energies supposed in the evaluation of Sedov's solution.

is based on the adiabatic speed of sound with

$$\tau_c = \int_0^L \frac{1}{c} dl \tag{4.3}$$

is compared to an arrival time τ_S, which is evaluated based on Sedov's results as

$$\tau_S = \int_0^{L_S} \frac{1}{v} dl + \int_{L_S}^{L} \frac{1}{c} dl. \tag{4.4}$$

The length L denotes the distance between the discharge location and the receiver and the length L_S represents the radius within which Sedov's solution is defined. In the case of $L < L_S$, the integral on the right-hand side in Eq. 4.4 is omitted. The difference between the two arrival times is defined as $\delta_S\tau = \tau_c - \tau_S$. In Fig. 4.7, the relative error $\delta_S\tau/\tau_S$ is plotted versus the acoustic path length L. The range of L as shown in Fig. 4.7

refers to sender-receiver distances that are of relevance for the experimental setups used in this study (see Sec. 4.3). The solid black line represents the case based on an electric discharge energy of $E_e = 0.2\,\mathrm{mJ}$. Even for the shortest acoustic path lengths considered, where the relative error of course becomes larger, the relative error stays below 1 %; for most path lengths the relative error is well below 0.3 %. For higher values of the electric discharge energy, however, the relative error becomes considerably high.

Transforming the error in arrival time estimation to an error in the temperature assessment (see Eq. 2.90), a relative error of $\delta_S T/T \leqslant 2\,\%$ has to be considered. In case of a gas temperature of $T = 1323\,\mathrm{K}$ which has been used as reference so far, an absolute error of approximately 20 K is obtained.

4.1.2 Discharge characteristics

Breakdown voltage For the practical use of a spark discharge as acoustic source, two characteristics are important: the dependence on the breakdown voltage on the distance between the electrodes d_e and its dependence of the gas temperature T between the electrodes. In order to obtain a reliable discharge, which in turn generates a predictable acoustic pulse, both parameters have to be selected carefully. The experimental setup exhibits significant radial steady-state temperature inhomogeneities, as shown in Sec. 5.3, and the induced temperature fluctuations can go up to 150 K. An electrode gap width must be found, that allows for the generation of a discharge at various radial positions at the measurement plane and at all phase angles of the temperature fluctuation. However, the gap width cannot be adjusted to arbitrarily small values as this evokes the observed phenomenon of a "double discharge", which will be discussed in one of the subsequent paragraphs. First, basic considerations regarding the dependence between breakdown voltage and temperature will be presented in the following.

In Küchler (2009), the breakdown voltage can be approximated according to *Paschen's law* as

$$U_b = (\Xi p_0 d_e + \Upsilon \sqrt{p_0 d_e}) k_t k_h. \tag{4.5}$$

For ambient air temperature ($T_0 = 293$ K), the parameters Ξ and Υ are constants and empirically derived as $\Xi = 24.4\,\mathrm{V/(Pa{\cdot}m)}$ and $\Upsilon = 21.2\,\mathrm{V/(Pa{\cdot}m)^{\frac{1}{2}}}$. The factors k_t and k_h consider the influence of temperature and humidity, respectively. In case of a constant ambient pressure p_0 the temperature factor writes

$$k_t = (T_0/T)^m. \tag{4.6}$$

If an electrically homogeneous field is assumed, where the total discharge happens immediately without any pre-discharges, according to Küchler (2009), the exponent m is found as $m \approx 1$. For this study it is assumed that the gas temperature and the gas properties are homogeneous in the gap between the electrodes, This is why $m \approx 1$ can be considered as valid in this study. The humidity factor k_h is empirically defined as

$$k_h = \left(1 + 0.012 \left(\frac{hT}{T_0} - 11\right)\right)^w, \tag{4.7}$$

where the absolute humidity h is given in $\mathrm{g/m^3}$. The exponent w becomes $w \approx 1$ for electric discharges relevant in this study (Küchler, 2009). Thus, given that the pressure

is constant, the breakdown voltage depends basically on the gap width d_e and on the inverse temperature T^{-1}. This is because the resistance for building a plasma channel in air is reduced with increasing temperature, where the ionization of the gas is already on an elevated level. Due to the empirical character of the parameters in Eqs. 4.6 and 4.7 and due to the fact that the measurements in this study are conducted in combustion exhaust gases rather than in air, the prediction of the breakdown voltage by means of Eq. 4.5 is subject to uncertainties. In addition, the discharge characteristic is influenced be the electrodes' geometry and the surface condition (Bane et al., 2015). Both significantly alter during the measurements due to corrosion and abrasion.

In an experimental study, Abdel-Fattah and Lehtonen (2013) investigated the impact of high temperatures on the breakdown voltage. Based on their measurements with temperatures up to 1313 K and with gap widths between 4 mm and 12 mm, they derive a new formulation of the Paschen curve for air under atmospheric pressure as

$$U_b = \Xi^* \left(\frac{d_e}{T}\right) + \Upsilon^* \sqrt{\left(\frac{d_e}{T}\right)}, \tag{4.8}$$

where $\Xi^* = 744.22\,\mathrm{V\cdot K/m}$ and $\Upsilon^* = 35.95\,\mathrm{V\cdot (K/m)^{\frac{1}{2}}}$. The most interesting finding in their investigations, however, is the characteristic of the breakdown voltage for $T > 1313\,\mathrm{K}$, which is the temperature range relevant for the experimental investigations in this study. They observe a significant drop of the breakdown voltage which does not at all correspond to the trend of the Paschen curve anymore. This abrupt decay seems to be regardless of the gap width. Abdel-Fattah and Lehtonen (2013) propose the increased effect of thermal ionization as a potential reason for this phenomenon.

The observation of Abdel-Fattah and Lehtonen (2013) justifies the comparably low breakdown voltage of about 2 kV measured in the high-temperature environment in the combustion chamber which is shown in Fig. 4.4. Equations 4.5 and 4.8 both predict a breakdown voltage that is approximately one order of magnitude larger for $d_e = 22\,\mathrm{mm}$ and $T = 1400\,\mathrm{K}$.

Plasma channel trajectory Throughout the experiments it has been observed that the trajectory of the spark discharge does not necessarily appear as a straight line between the tips of the electrodes (Martinson and Delsing, 2010; Schäfer, 2016). The plasma tunnel is randomly shaped without following any identifiable structure. Twelve examples of these bent plasma channels are depicted in Fig. 4.8. These discharges have been generated in series with a repetition rate of 60 Hz.

The major driver for this random trajectory seems to be the breakdown voltage that is required for the generation of a spark discharge. The most significant trajectory variations are found at a very short penetration depth of the electrodes. There, close to the wall, the temperature is much lower compared to the inner region of the circular combustion chamber (see Sec. 5.3). Thus, according to Eq. 4.5, for a constant gap width d_e the breakdown voltage becomes much larger. The flow field also changes in radial direction according to a fully developed turbulent duct flow. The inner area of the combustion chamber is governed by an axial velocity component parallel to the plasma channel. However, closer to the wall, in the shear layer, the radial flow components

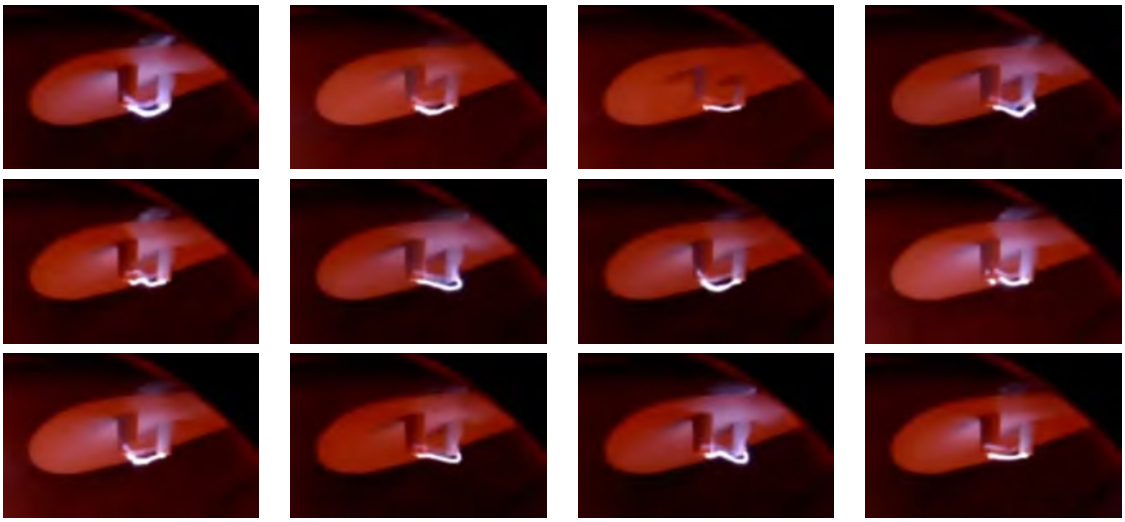

Figure 4.8: Random selection of different spark discharges taken from the same series of repetitive discharges performed with a repetition frequency of 60 Hz; distance between electrodes $d_e = 22\,\text{mm}$; gas temperature $T \approx 1000\,\text{K}$.

impinge perpendicularly on the plasma channel. This may cause radial advection of ionized gas particles and may also lead to an inhomogeneity of the gas properties between the electrodes. In opposition to the strong variation of the discharge trajectory shown Fig. 4.8, a continuous perfectly straight discharge channel has been observed in the center region of the duct. This is shown in Fig. 4.9a, where a series of 40 spark discharges has been superimposed.

Another effect that plays a role for the shape of the plasma channel is the geometry of the electrodes' tips. In this study, the electrodes have generally been conically sharpened. However, in the case of the setup where the electrodes are not arranged in parallel, the way the two electrodes face each other becomes a function of the penetration depth of the electrodes' tips. Regarding the combustion experiments, the tungsten electrodes suffered from massive oxidation and they have been worn out in a way that the tips' shape changed significantly during the exposure time to the hot exhaust gases. The assessment of the different tip shapes and their impact on the discharge trajectory is not straight forward and was not possible in this study. However, it is worth noting that in almost all cases, where the electrodes were nearly completely corroded, a sufficiently reliable spark discharge has been achieved.

Additionally, an operation mode has been observed, where two or maximum three distinct discharge trajectories have alternately been taken. In Fig. 4.9b, this is visualized by means of a long time exposed picture taken over a number of 40 discharges. In this particular case, one trajectory leads from the very tip of an electrode to the contact point of the neighboring electrode with the inner edge of its ceramic sleeve. The second distinct plasma channel is created on te geometrically shortest way.

The randomness of the shape of the plasma tunnel significantly affects the TOF measurement as the spatial origin of the acoustic pulse is alternated and not fixed. As a consequence, averaging over a sufficient number of discharge events must be performed. An estimation of the discharge shape variation in terms of the resulting measured flight times is conducted in Sec.4.2.2.2.

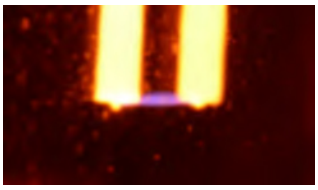

(a)

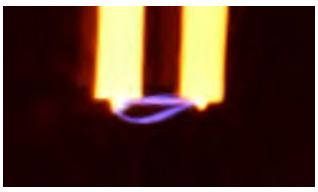

(b)

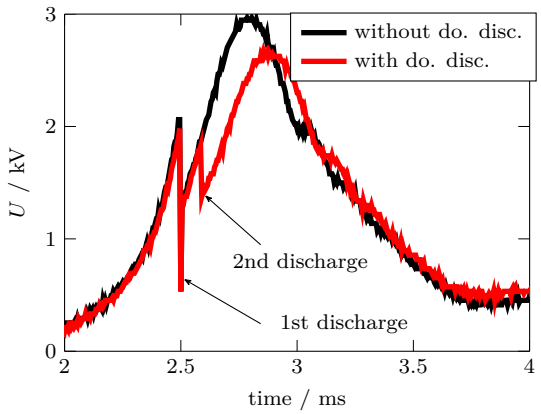

(c)

Figure 4.9: **(a)+(b)**: Picture of spark discharges generated with a repetition rate of 40 Hz taken with an exposure time of one second. The visualization of 40 plasma tunnels reveals the two phenomena that have been observed in the measurements: **(a)**: One perfectly straight path trajectory without any exceptional discharge path; **(b)**: Two distinct path trajectories, a preference path is not necessarily detected. **(c)**: Time signal of the voltage between the electrodes during a spark discharge with a usual single discharge (black) and another time signal where a double discharge occurred (red).

"Double discharge" phenomenon A rather disturbing phenomenon that has unexpectedly been observed during the measurements are the "double discharges". These are discharges that happen sequentially within a very short period of time of the order of $\approx 0.2\,\text{ms}$. This is also the scale of the flight times that are measured in the experimental setup at the combustion chamber. That means that the electromagnetic disturbance signal (see Sec. 4.2.2.1) of the second discharge massively corrupts the evaluation of the acoustic signal of the first discharge. Thus, a flight time estimation of such a discharge event is practically impossible. The voltage time signal, as it has also been measured in Fig. 4.4, is depicted in Fig. 4.9c for the case of no double discharge (black) and for the case of a double discharge. It might not be surprising that this second discharge occurs as the voltage is still rising after the first discharge and reaches even a higher level than was required for the first discharge to happen.

However, this double discharge phenomenon has only been observed for gap widths between the electrodes that are smaller than actually required. This means that the breakdown voltage has been "too low" compared to the voltage provided by the ignition coil. In turn, an optimal operation mode without double discharges has always been found by adjusting the electrodes' gap width such, that the required breakdown voltage is close to the maximum voltage made available by the coil. Thus, there are two means to avoid a double discharge: The gap width has to be increased or the voltage provided by the coil has to be reduced. The first method is most often not feasible, either due to constructive restrictions or due to the risk that for an occasionally colder gas temperature the required breakdown voltage becomes unachievably large. So reducing the disposable voltage has been found to be the only practicable procedure. In the following paragraph it will be discussed how the control of the discharge occurrence has been put into practice.

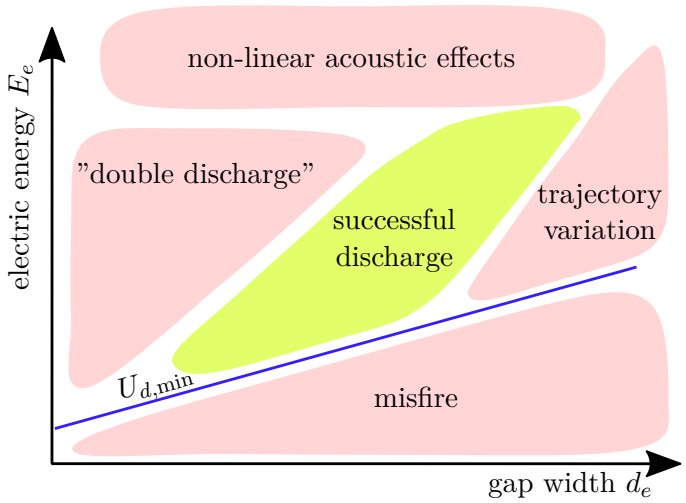

Figure 4.10: Qualitative graph of the different discharge characteristics as functions of the electrodes' gap width d_e and the electric energy E_e. The blue curve denotes the minimum breakdown voltage $U_{b,\min}$ that is required to generate a plasma channel. The variation of the trajectory of the plasma channel may also occur at low gap width. However, in terms of a displacement of the acoustic source, its impact is most significant at large gap widths.

Control options It has been worked out in this section that the generation of a proper discharge as source of an acoustic pulse depends on various parameters, which in turn give rise to different phenomena. The distance between the electrodes' tips as well as the available discharge voltage have to be selected carefully to keep the balance between the occurrence of a double discharge and a misfire. The latter occurs due to an unattainable breakdown voltage which leads to the electric discharge taking place within the ignition coil. Furthermore, the balance between a sufficiently high acoustic amplitude, which is achieved by providing high electric energy, and the suppression of non-linear acoustic effects has to be ensured. The major aspects are plotted qualitatively in Fig. 4.10 as functions of the adjustable parameters, i.e. the gap width d_e and the electric energy E_e. This chart provides an overview over all the constraints that have to be considered when operating a discharge.

To adjust the voltage provided for the discharge, the width of the 5 V square signal that is sent to the MOSFET (see Fig. 4.2 and Fig. 4.4 (left bottom plot)) is altered. The pulse width of the trigger signal determines the time, which is available for the ignition coil to increase the voltage. If the voltage loading process is prematurely cut due to the falling edge of the square wave, the maximum voltage that can break down, i.e. the electric energy, is reduced. However, note that this manual control scheme reaches its limit if the pulse width of the square wave sent to the MOSFET becomes larger than approximately half a period of the repetition frequency of the spark discharge. In this case, the available time for the voltage to reach the minimum voltage required, i.e. the breakdown voltage, is too short. Here, reducing the gap width would be the only possible solution.

For the experimental setup developed and built in this study, the maximum achievable repetition frequency is approximately 120 Hz. As worked out above, this maximum frequency decreases if a higher breakdown voltage is required. Consequently, for a given gap width, the highest repetition rates are achieved for very high gas temperatures between

the electrodes. It is worth noting that this frequency threshold could be shifted to way higher values if more advanced electric hardware and a more elaborate electric layout is used. For the investigation on entropy waves conducted in this study, a frequency in the range 50–100 Hz was sufficient. Due to the required phase averaging of the flight time measurements in this study, an increased repetition rate of the discharges does not necessarily increase the phase resolution of the measured entropy fluctuation (however, it would reduce the measurement time required for a desired phase resolution). A further development of the electric excitation technique was out of the scope of this work.

Additional insight into the performance of the acoustic pulse excitation via discharges is provided in Sec. 4.2. There, the influences of the here discussed discharge characteristics are investigated in terms of the acquired acoustic traveling times.

Summary on excitation technique

In this work, an experimental technique for the generation of an acoustic pulse has been developed and investigated. It is based on an electric discharge between two electrodes that are inserted into the TOF measurement plane at the combustion test rig. Key parameters, i.e. the electrodes' gap width and the maximum voltage of the ignition coil, have been identified, which enable the control of (unwanted) phenomena to occur. These are the occasional variation of the discharge channel trajectory, "double discharges", and misfires. An electric circuit has been adapted that allows for the control of these events. The technique worked very well in the measurements at the atmospheric combustion chamber conducted in this study. The corrosive exhaust gases did not affect the generation of the acoustic pulses and the detection of the short acoustic pulses worked fine, even in presence of a high level of background noise.

This acoustic excitation technique is fully applicable to real gas turbine combustors. An elevated static pressure would lead to increased breakdown voltages required for an electrical discharge. This issue could be addressed by using more advanced hardware (e.g., a more powerful ignition coil, s different MOSFET, etc.), and a more elaborate electric circuit. These improvements may also increase the maximum possible repetition frequency of the discharges to more than 200 Hz. Furthermore, an improved performance might be achieved by further investigating the role of the electrodes' geometries in terms of the generation of an acoustic pulse and by developing a setup which allows a continuous variation of the electrodes' gap width.

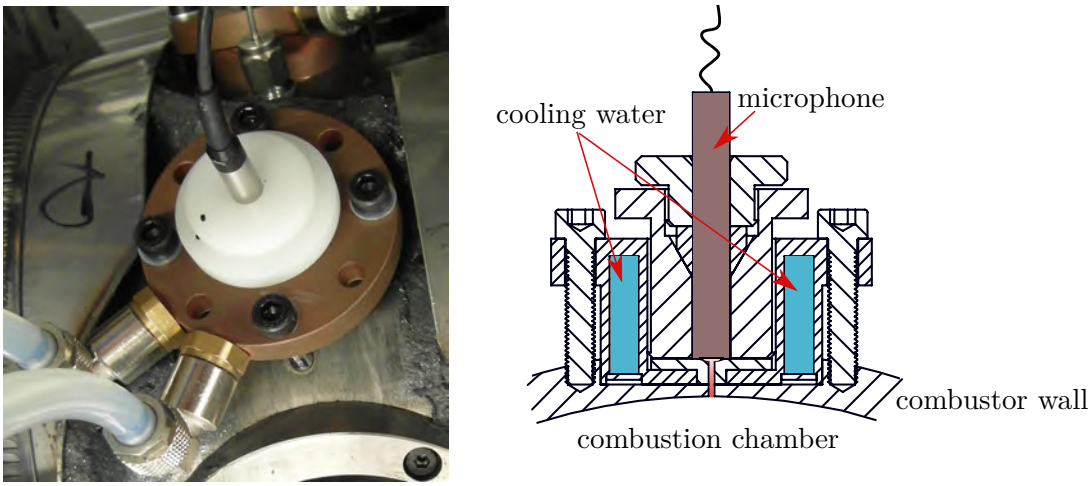

Figure 4.11: **(a)**: Picture of a condenser microphone embedded in a water-cooled holder which is mounted at the combustion rig. **(b)**: Sketch of the water-cooled microphone holder; the microphone is connected to the combustion chamber via a capillary with a diameter of 1 mm and a length of 6 mm.

4.2 Acoustic acquisition technique

In this subsection, the hardware used for the acquisition of the traveling times is introduced and special aspects with regard to the particular experimental setup are discussed (Sec. 4.2.1). Furthermore, the time signal of an arriving acoustic pulse is examined and the detection procedure for the flight time will be presented (Sec. 4.2.2). According to the Nyquist-Shannon theorem, the sampling frequency f_s needs to be at least double the maximum frequency detectable (Marks, 1991).

4.2.1 Acquisition hardware

The acquisition of the acoustic pulse generated by the electric discharge is done by means of 1/4" condenser microphones (G.R.A.S. type 40BP-S2 with preamplifieres of type 26AC-S7). For the amplification of the microphone signals amplifiers of type Brüel&Kjær 2610 are used, which provide a low-pass filter with a corner frequency of 200 kHz. The frequency response of the microphones given in the manufacturer's calibration chart guarantees a constant pressure amplitude up to 20 kHz. Above this frequency, the amplitude starts to drop, however, up to 60 kHz, the amplitude stays at a sufficiently high level. This limit is related to the diameter of the microphone's membrane of 3 mm. For an ambient temperature of 293 K, the wave lengths of frequencies higher than 60 kHz are of the order of the membrane diameter and thus cause the membrane to be bent.

For the combustion rig measurements, the microphones must be embedded into water-cooled holders which protect the microphone membranes and pre-amplifiers from hot combustion gases. A photograph and a sketch of the microphone holders used in this study are given in Fig. 4.11. The holder affects the estimation of the arrival time, as the microphone's membrane is connected to the combustion chamber via a capillary which is filled with combustion gases that are significantly cooled down. This impact will further be discussed in Sec. 5.2.

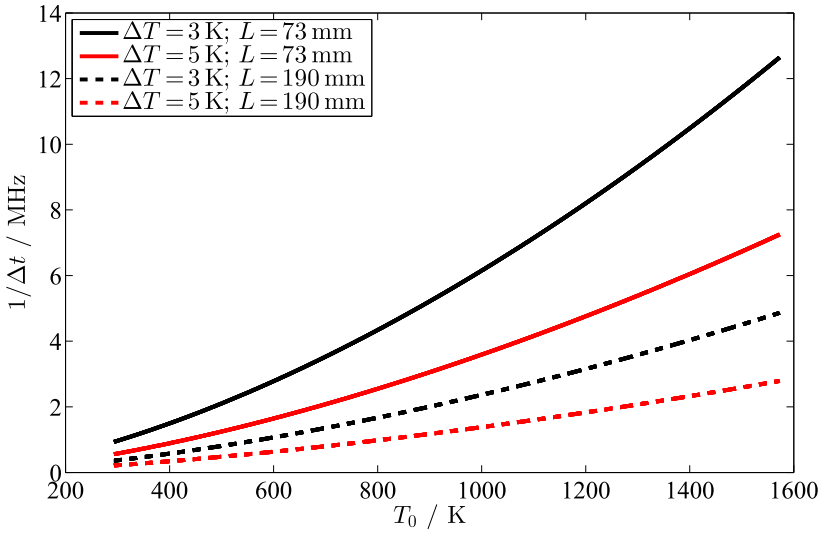

Figure 4.12: Inverse time difference between two arrival times propagating through air at temperature T and $T + \Delta T$; black: $\Delta T = 3\,\mathrm{K}$, red: $\Delta T = 5\,\mathrm{K}$; solid line: $L = 73\,\mathrm{mm}$, dashed line: $L = 190\,\mathrm{mm}$.

An important aspect regarding the detection of the arrival times of acoustic pulses is the sampling rate of the microphone time signal. The sampling rate required for the time of flight method depends on the desired accuracy of the traveling time estimation. If we assume a homogeneous gas temperature, the difference in the arrival time $\Delta\tau$ between two signals that propagate along a path of length L through identical gas mixtures of temperature T_0 and temperature $T_0 + \Delta T$, respectively, writes

$$\Delta\tau = \frac{L}{\sqrt{\gamma R_g}} \left(\frac{1}{\sqrt{T_0 + \Delta T}} - \frac{1}{\sqrt{T_0}} \right). \tag{4.9}$$

To resolve a temperature change ΔT, the microphone time signal must be sampled with a sampling rate f_s of minimum $f_{s,\min} = 1/\Delta\tau$. In Fig. 4.12 the values of $f_{s,\min}$ as function of the gas temperature T_0 are plotted for two different ΔT and two different propagation lengths L. The latter correspond to relevant distances between discharge location and microphone in the combustion rig measurement setup. For a given sampling rate, the accuracy decreases for increasing temperatures as well as for shorter distances between the discharge location and the microphones. To achieve a temperature resolution of $\Delta T = 3\,\mathrm{K}$ and considering the shortest distance L and the highest temperatures occurring in the experiments, the sampling rate must be on the order of 10 MHz.

In this study, the data acquisition of the microphone time series is performed with an AD converter board of type *Spectrum* M2i4652 which offers a sampling rate of 3 MHz synchronously for eight channels. As will be demonstrated in the following subsections, the application of phase averaging minimizes the error of the arrival time estimation as such that a sampling rate of 3 MHz is shown to be sufficient.

4.2.2 Acquisition of the arrival time

In this subsection, the acquisition procedure from the recorded raw microphone time trace to the estimation of the flight time is presented. A typical microphone time signal is depicted in Figs. 4.13 and 4.14. It is important to note that the presented time trace

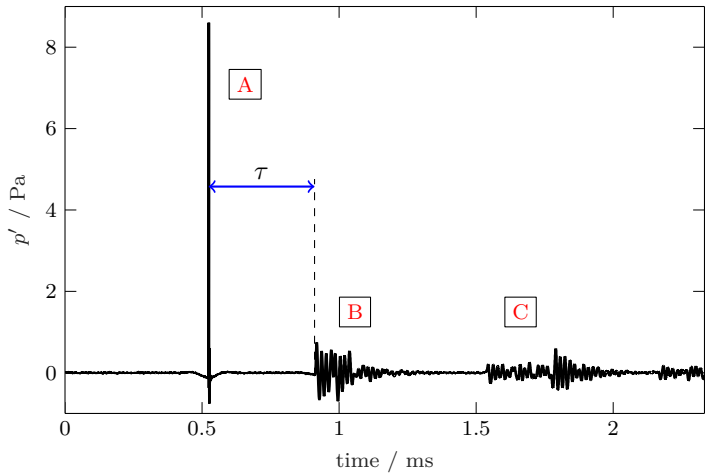

Figure 4.13: Microphone time signal after a discharge in the combustion chamber setup; gas temperature: $T = 296\,\mathrm{K}$. The time signal has been high-pass filtered at 20 kHz to suppress the high-amplitude low-frequency noise present in a combustor.

is high-pass filtered at 20 kHz in order to cut off background noise. Especially in gas turbine combustors, as investigated in this study, the noise level exceeds the amplitude of the acoustic discharge pulse by more than one order of magnitude. However, this high-amplitude noise is related to frequencies far below 10 kHz and thus does not affect the actual pulse signal. A detailed analysis on this will be given in Sec. 4.2.2.2.

A crucial feature of the discharge time signal acquired by the microphone is the electromagnetic disturbance signal. It defines the time stamp at which the discharge happens. This serves as a reference time for the actual flight time determination. The characteristics of the electromagnetic disturbance signal will be further investigated in Sec. 4.2.2.1.

4.2.2.1 Electromagnetic disturbance signal

The electromagnetic disturbance signal impinges on the microphone's preamplifiers (see Fig. 4.14a) prior to the actual acoustic signal. It radiates from the magnetic field that is created due to the current flowing from one electrode to the other during the discharge. It travels with speed of light ($\approx 300 \cdot 10^6\ \frac{m}{s}$) and therefore it can be considered to reach all microphones at the "same" instance of time compared to the acoustic time scales, which are about six orders of magnitude higher. Hence, the time stamp at which this disturbance signal reaches its maximum is referred to the time when the actual discharge occurs. The arrival time of the electromagnetic signal is used in this study as time $t = 0$ for the estimation of the acoustic flight time.

The utilization of the electromagnetic disturbance signal as reference time is indispensable because the rising edge of the pulse signal sent to the MOSFET driver does not represent the actual occurrence of the discharge. The time delay τ_e between the switch of the MOSFET driver and the discharge depends on the breakdown voltage that is required for the discharge to happen. This is because the high-voltage loading of the ignition coil is a transient process. The breakdown voltage in return depends on the gas temperature between the electrodes. Thus, utilizing the initial square wave signal for

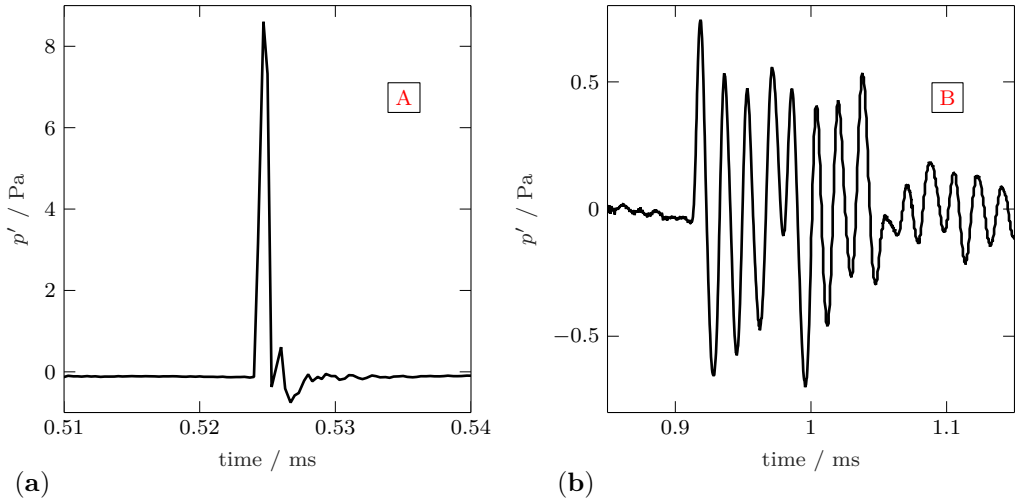

Figure 4.14: **(a)**: Electromagnetic disturbance signal detected in the microphone's time signal. The time stamp of the maximum of this signal is considered as the time $t = 0$ when the plasma tunnel is generated. **(b)**: Typical acoustic pulse signal detected by a microphone due to a discharge.

the MOSFET driver would lead to an inherent error in the flight time estimation (see also Eq. 4.5).

To get an estimation of how precisely the discharge is delayed from the initial trigger pulse sent to the MOSFET driver and how strong this delay depends on the temperature, measurements were performed at the combustion test rig. The steady temperature at the measurement plane is varied by means of an air preheater (no combustion operation), the flow velocity is kept at a constant level. At various temperatures in the range of $T = 293 - 600\,\mathrm{K}$ a number of 250 electric discharges are forced with a repetition frequency of 20 Hz. The distance d_e between the electrodes is changed in three steps. The latter had to be done to prevent misfires within the ignition coil (see Sec. 4.1).

Figure 4.15a shows the measured time stamps of the electromagnetic disturbance signal for the 250 discharges. Two configurations with different gap widths d_e between the electrodes and air temperatures are depicted exemplarily. Even though all measurements were performed subsequently with the same setup, the standard deviation σ_e varies strongly, especially for larger gap widths d_e, which can be seen in Fig. 4.15b. This indicates that the exact time of the occurrence of an electric discharge cannot be estimated by control parameters (e.g. the trigger signal of the MOSFET driver). To some extent, it seems to be governed by random processes. Compared to the acoustic time scales, however, the maximum standard deviations of the electromagnetic disturbance signal are very small (of the order of 5 μs).

The time dependence of the delay time τ_e is estimated for each configuration by taking the median value $\tilde{\tau}_e$ of the 250 shots. The median value offers the advantage that outliers, which occasionally occur due to failed discharges, do not affect the estimation of the mean value. In Fig.4.16a, the values of $\tilde{\tau}_e$ are plotted for three different gap widths with respect to the gas temperature. It can be seen that the time delay, and thus the breakdown voltage, decreases for higher temperatures as predicted by Eq. 4.5. Besides that, the time delay clearly enlarges for larger gap sizes at similar temperatures. If the

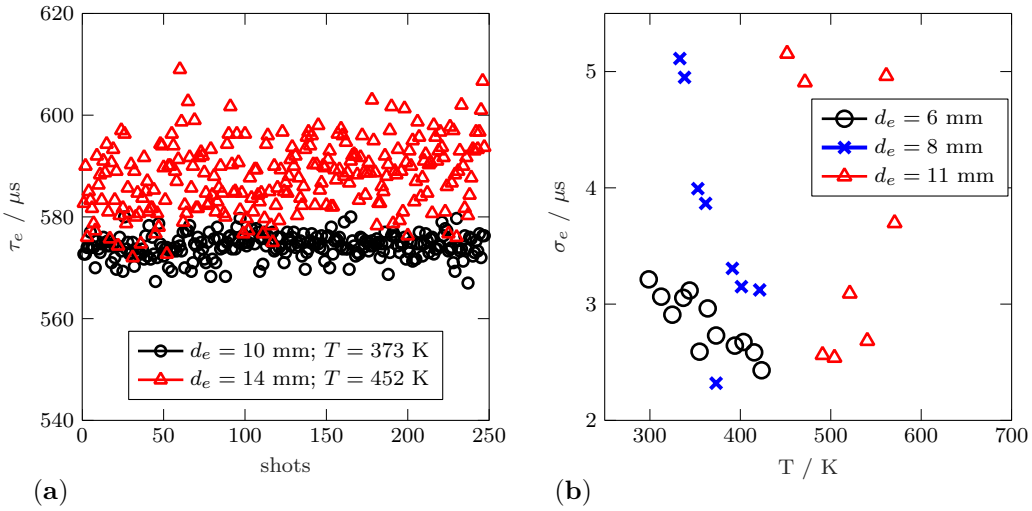

Figure 4.15: **(a)**: Measurements of the time stamps of the electromagnetic disturbance signals, the 250 shots were sequentially generated with a frequency of 40 Hz. The same measurement has been conducted at different temperatures and therefore different gap widths d_e. **(b)**: Standard deviations over 250 time stamps of the electromagnetic disturbance signal as shown in (a); the measurements have been conducted for various gas temperatures and three different gap widths.

trigger signal sent to the MOSFET driver would be used as guess for the time $t = 0$, the error in the arrival time estimation would be more than 50 μs in the case of $d_e = 14$ mm. This corresponds to more than 100 K error in temperature estimation for the shortest acoustic travel path existent in the combustion rig setup.

To prove the validity of *Paschen's law* in Eq. 4.5 for the experimental setup used in this study, the same data as shown in Fig. 4.16a are plotted in Fig.4.16b with respect to the gap width d_e scaled by the gas pressure p, the gas temperature T, and a reference temperature T_0. This formulation is commonly used in literature (e.g. Küchler (2009); Sili et al. (2011)). Here, the ambient pressure p as well as the reference temperature T_0 are constant for all configurations. It can clearly be seen that all three curves almost collapse to one single curve. Thus, after conducting a calibration, this correlation could be used to estimate the gas temperature between the electrodes.

4.2.2.2 Acoustic time signal

As has already been mentioned in Sec. 4.1, one major advantage of the acoustic pulse generated by means of an electric discharge is its high frequency content. Referring to the time period of the first two oscillations (see Fig. 4.14b), the frequency of the acoustic pulse is of the order of 40 kHz to 60 kHz. Without the application of a high-pass filter, a detection of the acoustic pulse signal and a subsequent arrival time picking would be impossible. This is illustrated in Fig. 4.17, where in Fig. 4.17a the raw microphone time traces of 100 acoustic pulses, acquired at the same gas temperature, are plotted. The amplitudes of the acoustic pulses (which could be seen at $t \approx 0.5$ ms) are substantially smaller compared to the low-frequency noise amplitudes. Particularly with regard to the TOF application, for the high-pass filter, whose application is shown in Fig. 4.17b, it is important to use a zero-phase filter approach (finite impulse response (FIR) filter).

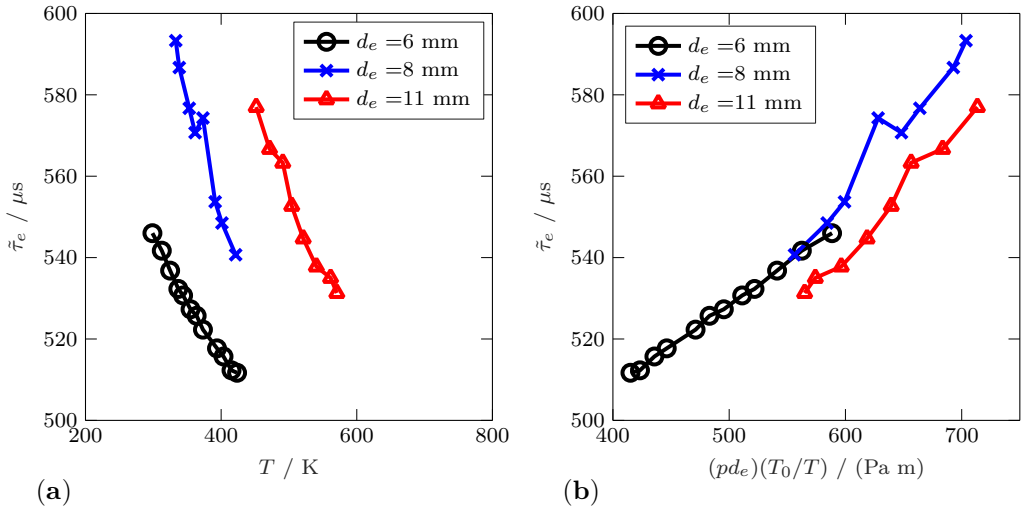

Figure 4.16: **(a)**: Median over 250 time stamps of the electromagnetic disturbance signal (see Fig. 4.15a) of different measurement configurations at various gas temperatures and gap widths. **(b)**: Same measurement data as used in (a), but plotted over the term $(pd_e)(T_0/T)$, which refers to the breakdown voltage defined in Eq. 4.5.

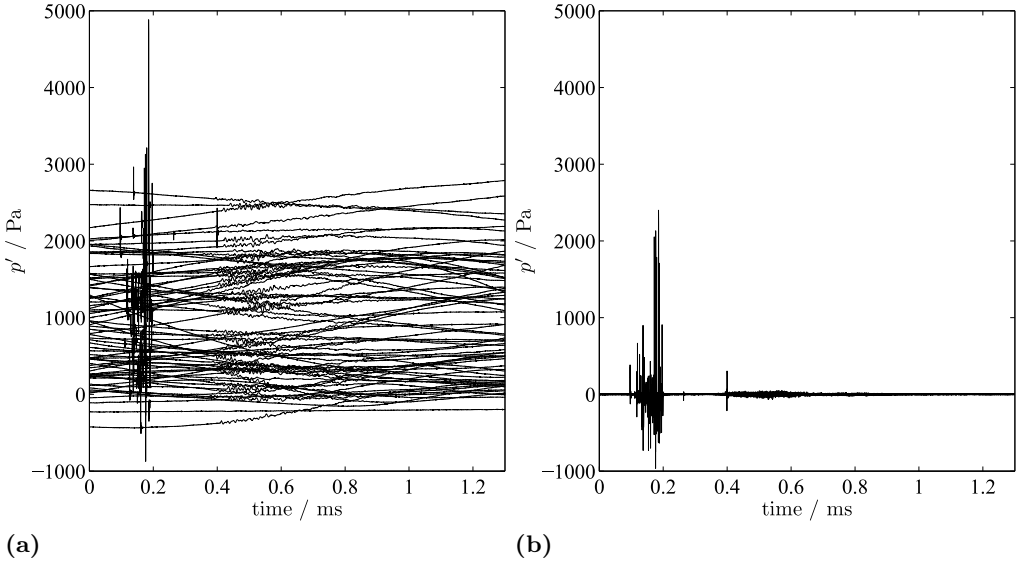

Figure 4.17: **(a)**: Raw time traces of 100 acoustic pulse signals that are acquired at the same gas temperature. **(b)**: Same microphone time traces as shown in (a) but zero-phase high-pass filtered at 20 kHz.

In Fig. 4.18a, the time traces of 100 shots taken at the same temperatures in the combustion chamber with a repetition frequency of 40 Hz are plotted. Their phase corresponds to the square wave trigger signal sent to the MOSFET driver. The time stamps of the high frequency peaks of the electromagnetic disturbance signal vary within a range of approximately 100 µs and the acoustic pulse signals are not aligned with respect to time. Figure. 4.18b shows the same time traces but phase sorted with respect to the electromagnetic disturbance signal. The sinusoidal character of the 100 acoustic pulse signals can now clearly be identified as their phases match significantly better.

To determine the arrival time, the time stamp of the very first maximum is detected

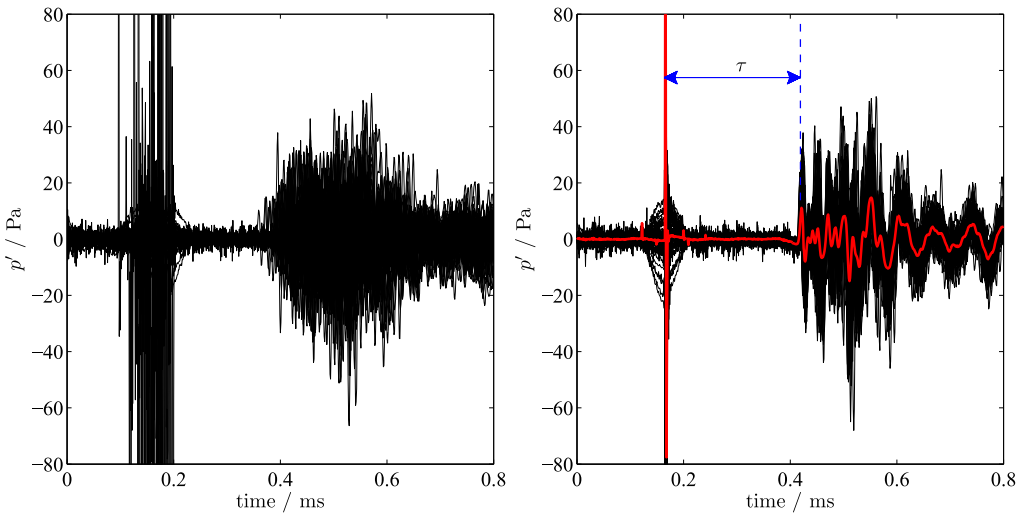

Figure 4.18: 100 high-pass filtered measured microphone time traces of the acoustic pulse signal: **(a)** phase sorted with respect to the square wave signal sent to MOSFET driver. **(b)** phase sorted by means of the electromagnetic disturbance signals; the red curve denotes the median over all 100 curves.

via a threshold based search algorithm, which is depicted as an example in Fig. 4.19a. This kind of flight time picking method requires manual operations due to amplitude variations, caused by changes in the average gas temperature, and thus is rather time consuming. There exist more advanced and automated methods for the detection of the arrival time, such as statistical methods based on the Akaike information criterion (e.g., C. Li et al. (2009) or Küperkoch et al. (2010)). However, as this study is comprised of a limited number of measurements, the application of one of these methods has not been considered. Particularly, since a manual quality control had to be conducted anyway.

Figure 4.19b shows microphone time traces that are acquired within one period of a temperature oscillation (caused by an entropy wave). Beside the expected shift in time due to the speed of sound variation, significant variations in amplitude are observed. This makes a general threshold definition for the considered time and amplitude range for the overall post-processing rather complicated and prone to errors.

4.2.2.3 Assessment of the flight time measurement error

The temporal deviations of the measured arrival times shown in Fig. 4.18b are due to the variation of the exact location where the acoustic pulse is generated. This phenomenon has elaborately been discussed in Sec. 4.1.2. In the following, the scattering of the flight time data is analyzed and a measurement error of the measurement technique is estimated.

The flight time measurements that are presented in the following have been conducted at the combustion chamber test rig operated without combustion. An air preheater has been deployed for a continuous temperature variation. In Fig. 4.20a, the probability densities of a typical series of arrival times are depicted for seven microphones (the experimental setup is depicted in Fig. 4.23). Apart from small quantitative deviations

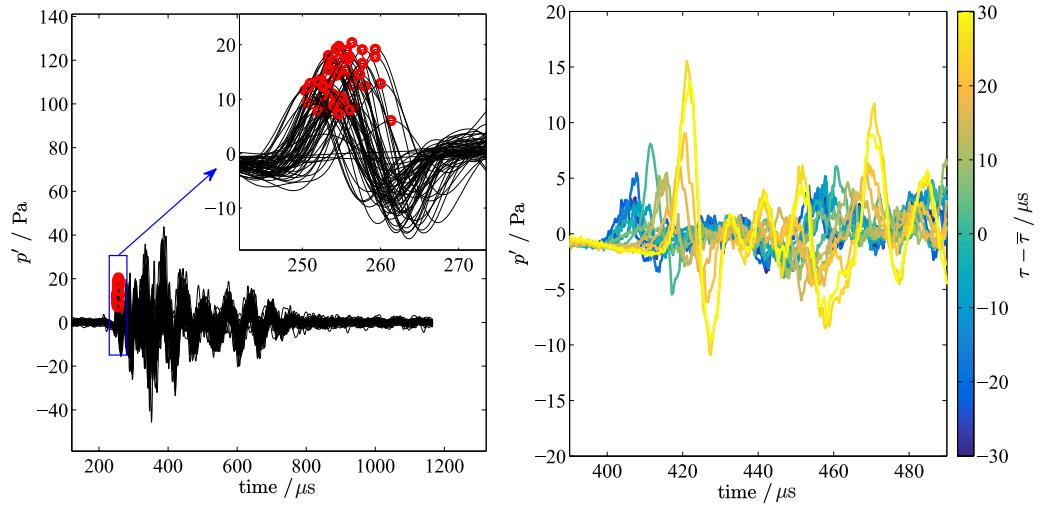

Figure 4.19: **(a)**: Threshold based arrival time picking using the first pressure maximum; this plot shows the microphone signals of 100 discharge events that are acquired at the same gas temperature and are temporally synchronized with respect to the electromagnetic disturbance signal. **(b)**: Instantaneous microphone time signals of the very first acoustic pressure oscillations for various temperatures (typical variation within one period of an entropy wave). The colors correspond to different temperatures, τ refers to the actual arrival time and $\overline{\tau}$ to the average arrival time within the presented temperature variation (dark blue $\rightarrow$ small τ $\rightarrow$ high temperature; yellow $\rightarrow$ large τ $\rightarrow$ low temperature).

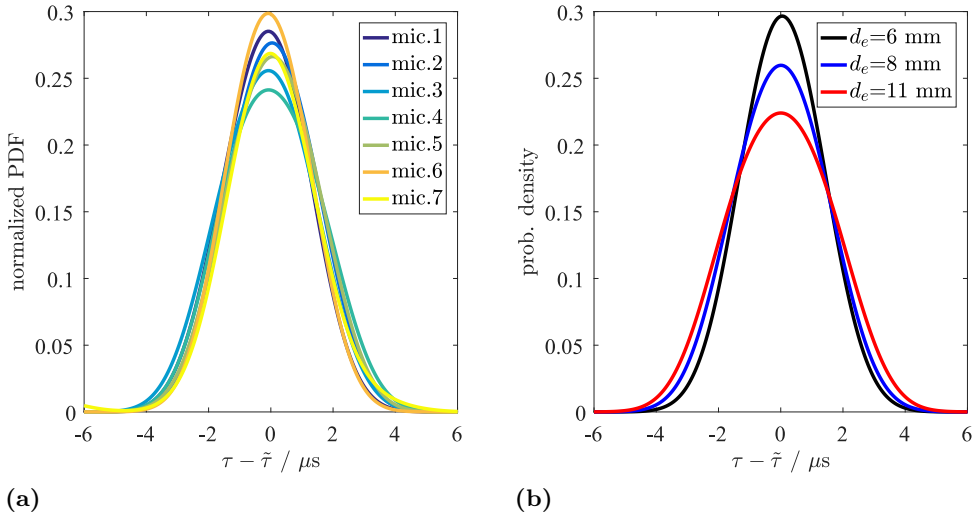

Figure 4.20: Probability density functions of the arrival time τ: (a) all microphones for $d_e = 8\,\text{mm}$ and $T = 421\,\text{K}$; (b) microphone 2 for different electrode gap widths d_e; each evaluated over 250 shots.

between the different microphones, the probability density distribution exhibits qualitatively the same shape. Looking at the probability distribution of one microphone for different electrode gap widths d_e, a clear trend of wider distributions for increasing gap sizes is obtained. This can be seen in Fig. 4.20b.

To assess the accuracy of the TOF measurements, the standard deviation σ is used. It

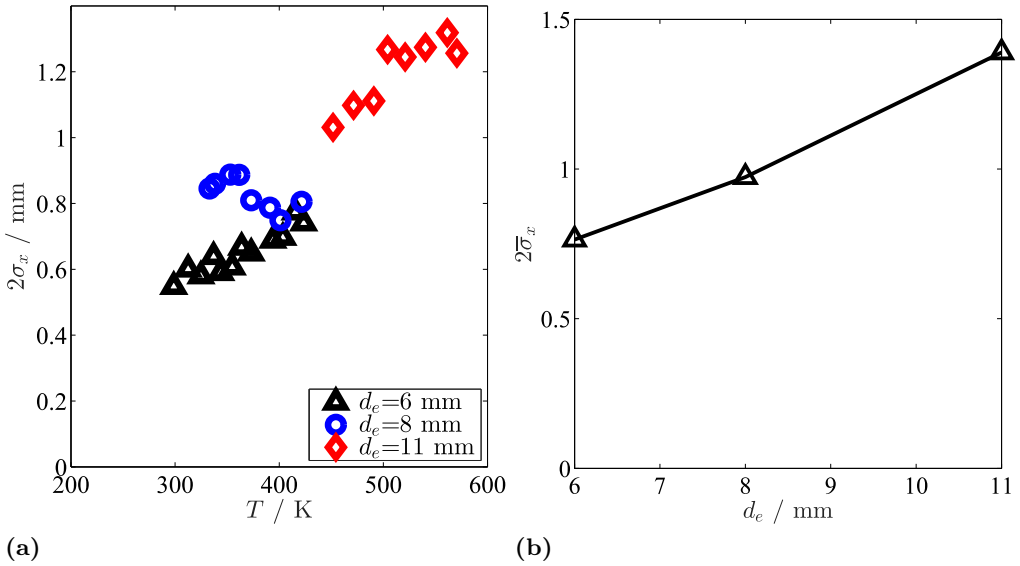

Figure 4.21: Standard deviation $2\sigma_x$ of the discharge location evaluated from arrival times: (a) measured with one microphone (acoustic path length $L = 0.14\,\mathrm{m}$) at different temperatures of the preheated air and three different electrode gap widths; (b) average standard deviation for measurements with all microphones (i.e., various acoustic path lengths) and for all temperatures of the preheated air.

is a measure of the width of the probability function obtained from the scattered data. The standard deviation of a series of N_s arrival times τ reads

$$\sigma_\tau = \sqrt{\frac{1}{N_s - 1} \sum_{j=1}^{N_s} \left(\tau_j - \left(\frac{1}{N_s} \sum_{j=1}^{N_s} \tau_j \right) \right)^2}. \tag{4.10}$$

σ_τ represents the range of deviations that covers approximately 68 % of the events. For the measurements shown in Fig. 4.20a, the standard deviation is less than 1.5 μs.

From the deviation of the arrival times σ_τ, the variation of the discharge location in space σ_x can be derived as

$$\sigma_x = \sqrt{\gamma R_g T}\sigma_\tau, \tag{4.11}$$

where T represents the (ideally homogeneous) gas temperature within the measurement plane. Note, in the following, we may use the measure 2σ, which provides the deviation that covers approximately 95.5 % of all 250 discharge events. Figure 4.21a shows the standard deviation in space measured with one microphone for different temperatures and gap widths d_e. According to Eq. 4.11, the deviation increases with higher temperatures for a constant electrode gap width. The 2σ deviations are of the order of 1 mm, which is a reasonable value. The average deviations over all microphones and all temperatures of the preheated air are depicted in Fig. 4.21b.

We are finally interested in an estimation of the measurement accuracy with respect to the temperature. Based on the variation of the discharge location σ_x, a standard deviation of the temperature estimate σ_T can be obtained from Eq. 2.91. In Fig. 4.22, the standard deviations of the estimated line-integrated temperatures are depicted for various steady-state temperatures of the preheated air and electrode gap widths. Here, the distance between the discharge location and the microphone is $L = 0.14\,\mathrm{m}$. The absolute

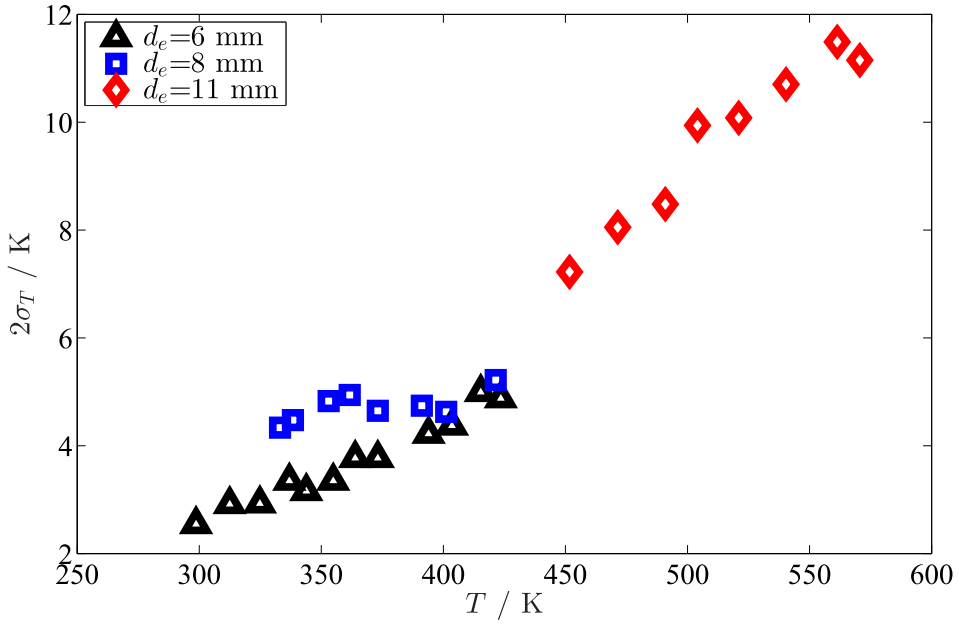

Figure 4.22: Standard deviation $2\sigma_T$ of the temperature obtained from arrival time measurements of 250 discharge events evaluated from measurements of one microphone (acoustic path length $L = 0.14\,\mathrm{m}$) at various temperatures of the preheated air and three different electrode gap widths d_e.

variation in temperature increases clearly for increasing pre-heated air temperatures. A deviation in temperature estimation of $\delta T = 10\,\mathrm{K}$ at a steady-state air temperature of $T = 550\,\mathrm{K}$ yields an error of about 2 %.

An extrapolation of these findings (i.e. Fig. 4.22) to higher temperatures relevant for combustion chambers may, however, not be straight forward. There, the gap width between the electrodes is significantly larger and the steady state temperature field is far more inhomogeneous. Furthermore, the flow field is more complex and may affect the discharge characteristic. Therefore, an estimation of the scattering of the flight time measures will be given separately when presenting the results in Chapter 5.

However, note that this error would only apply if the temperature would be evaluated separately for each flight time. In case of averaging over a sufficient number of flight times, as it will be done in the combustion rig experiments, this error does not need to be considered anymore.

Summary on the flight time acquisition

For the acquisition of the acoustic pulse signal, condenser microphones have been employed. They enable a reliable detection of the high-frequency pulse and thanks to water-cooled holders, they can also be operated at the combustion rig. With the electromagnetic disturbance signal, a reliable and accurate measure of the time stamp, when the actual discharge occurs, has been found. Based on this essential point in time, the flight time is evaluated by a threshold detection of the first pressure maximum. A significant scattering of the arrival times has been observed, even in the case of a steady-state temperature field. These deviation are mainly caused by the variation of the electric

discharge trajectory. Thus, averaging over a sufficient number of flight times is required, a real-time measurement would yield significant errors.

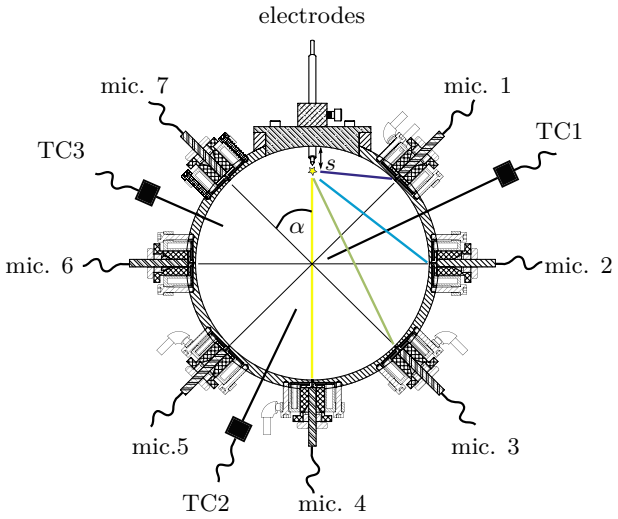

Figure 4.23: Measurement plane of the symmetric TOF setup; the electrodes are inserted conically, the penetration depth s is determined by the electrodes' gap width (see Fig. 4.1a). The seven microphones are evenly distributed along the circumference with an angle of $\alpha = 45°$.

4.3 Experimental setups

For the experimental investigations conducted in this study, basically two different measurement setups for the TOF have been designed and employed. Both are adapted to the atmospheric combustion test rig at TU Berlin. More details about the test rig are provided in Sec. 5.1, in this section only the TOF related components are presented.

The first setup, which in the following will be referred to as the "symmetric setup", employs the ceramic electrode adapter as it is shown in Fig. 4.1a. The electrodes are conically inserted into the combustion rig and therefore the penetration depth of the electrodes' tips is determined by the electrodes' gap width that is required to establish a reliable spark discharge (see Fig. 4.10). This setup has been designed to allow for a flexible adjustment of the electrodes' gap width, and in a phantom study (see Sec. 3) it has been found that this acoustic sender and acoustic receiver arrangement is very beneficial in terms of the measurement of entropy waves. In Fig. 4.23, the measurement plane is depicted; the electrodes are installed on top, seven microphones are evenly distributed along the circumference with $\alpha = 45°$. By means of three access holes, thermocouples are installed with different radial penetration depths to monitor the static temperature field, they do not affect the acoustic propagation of the pulse and thus do not affect the TOF measurement.

Due to the reflectional symmetry, the acoustic path lengths of microphones 1-3 are the same as of 7-5. The lengths of the acoustic paths are plotted in Fig. 4.24a with respect to relevant penetration depths s. A penetration depth of 20 mm corresponds to an electrode gap width of about 6 mm, which has only been used for measurements at ambient temperatures. In case of the high-temperature combustor experiments, the penetration depth did not exceed more than approximately 12 mm, as a larger distance

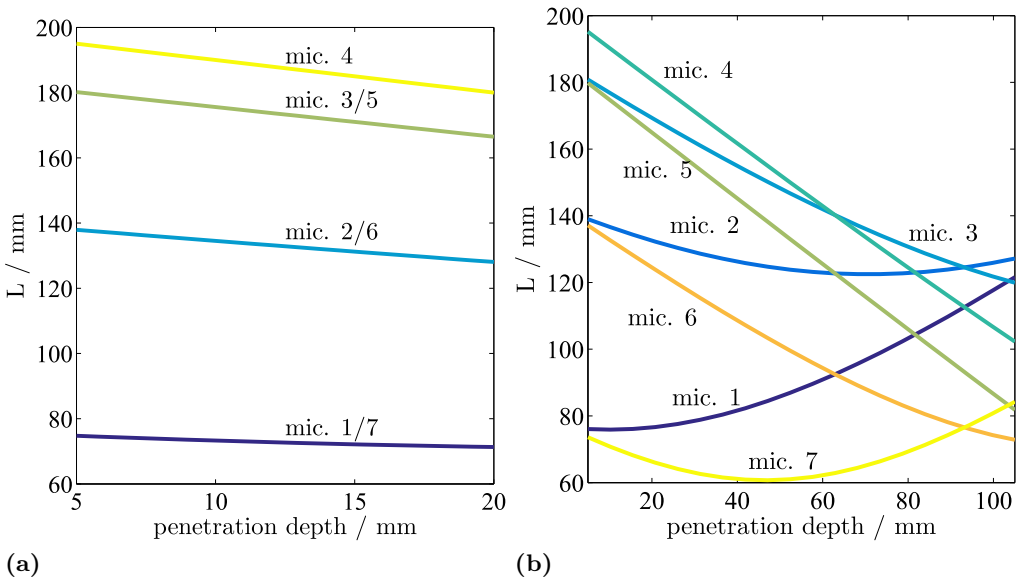

Figure 4.24: Acoustic path lengths of the microphones as function of the electrodes penetration depth for **(a)**: Symmetric setup according to Fig. 4.23 and **(b)**: Asymmetric setup according to Fig. 4.25.

between the electrodes of more than $d_e = 14\,\text{mm}$ is required to avoid detrimental double discharges (see Sec. 4.1.2).

Another TOF setup that has been employed in this study is the "asymmetric setup", which is depicted in Fig. 4.25. The only difference to the symmetric arrangement in Fig. 4.23 is the ceramic electrodes adapter. Here, the electrodes are inserted asymmetrically with an angle of $\beta = 15°$. An important difference to the first design is also, that the electrodes are penetrated parallel to each other with a fixed electrodes' gap width of $d_e = 22\,\text{mm}$.

The asymmetric arrangement has been designed to enlarge the information density with regards to the tomographic reconstruction, where the geometry matrix (e.g., Eq. 2.113) would be rank deficient in case of the symmetric setup and the information obtained from the measurement of the arrival times of one event would be significantly less. The corresponding acoustic path lengths are presented in Fig. 4.24b. Here, the range of possible penetration depths is much broader and only limited by the minimum distance between the electrodes' tips and the combustor wall to prevent the occurrence of a spark discharge between electrodes and the wall.

It has been shown in Sec. 2.2.4 and in Eq.2.91, that the relative error of the temperature estimation decreases for increasing acoustic path lengths. It is obvious from Fig. 4.24b that certain positions of the spark discharges seem to be more beneficial than others.

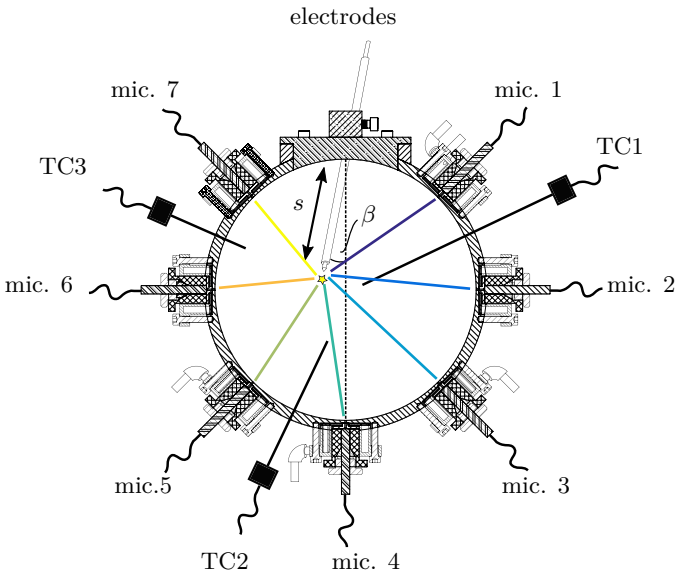

Figure 4.25: Measurement plane of the asymmetric TOF setup with $\beta = 15°$; the electrodes are inserted parallel to each other (see Fig. 4.1b).

5 Experimental Study

In this chapter, the experimental results obtained from measurements at the atmospheric combustion rig at TU Berlin are presented and discussed.

In a first step, the TOF measurement technique and the temperature extraction methods are validated. Therefore, TOF measurements are conducted at the combustion test rig without flame but with preheated air only. This guarantees a well-defined temperature field in the measurement plane without significant radial gradients or asymmetries. The latter is particularly important for the one-dimensional reconstruction techniques.
⇒ Section 5.2

Before the measurement of dynamic temperatures in the combustion rig operated with a premixed flame, a comprehensive study on the steady temperature field is carried out. This comprises an assessment of the radial temperature profile by traversing a thermocouple, whereas a detailed evaluation of the measurement accuracy of the type-S thermocouples has been conducted. The radial temperature profiles obtained from the thermocouple measurements serve in a second step as references for the reconstructed temperature fields by means of the one-dimensional tomographic reconstruction approaches.
⇒ Section 5.3

The last section of this chapter contains the discussion of the TOF measurements with unsteady combustion. Firstly, the characteristic of the fuel modulation is analyzed. This allows for a profound investigation on the relation between equivalence ratio and temperature in the measurement plane for the experimental setup deployed in this work. In a second step, the temperature amplitudes obtained from the zero-dimensional and the one-dimensional extraction methods are discussed and compared to each other. Finally, the evaluation of the measurements at different axial locations and with various bulk flow velocities in the combustion rig enable the characterization of dissipation mechanisms of entropy waves.
⇒ Section 5.4

5.1 Combustion Rig Setup

The atmospheric combustion test rig employed in this study has already been described in detail by others, e.g, Schimek et al. (2011) or Ćosić, Terhaar, et al. (2015). For the experimental investigations in this work, some special features that are provided by the rig, e.g., the adjustable upstream acoustic impedance or the high power woofers, are not used.

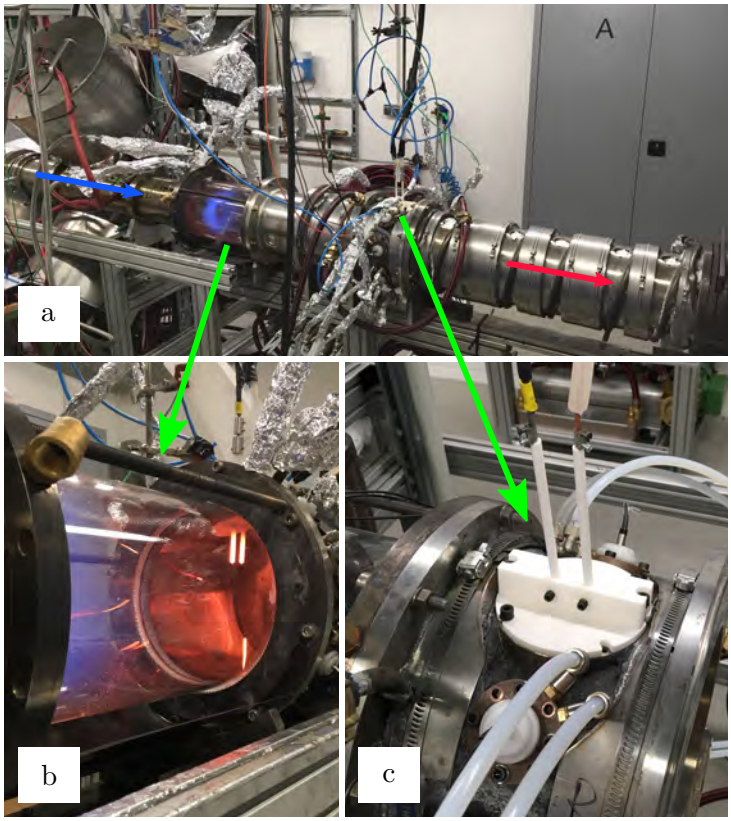

Figure 5.1: **(a)**: Picture of the atmospheric combustion test rig at ISTA/TU Berlin; the blue and red arrows indicate the flow direction. The trombone as well as the large woofers on the very left-hand side upstream of the flame are not used in this study (more details of the entire rig can be found in, e.g., Ćosić, Wassmer, et al., 2015). **(b)**: Downstream view through the quartz glass which is installed just downstream of the burner inlet plate; the two parallel glowing sticks on the top are the ceramic sleeves guiding the electrodes. Moreover, at the same axial location, two glowing thermocouples are visible. **(c)**: View on the ceramic adapter with the ceramic sleeves embedded.

A picture of the test rig is shown in Fig. 5.1. All metal walls downstream of the flame are water-cooled, on the very downstream side of the rig, an orifice is mounted to attenuate strong natural acoustic perturbations. The optical access to the flame is used for OH^*-chemiluminescence measurements (see Sec. 5.4.1.2) and has proven helpful for monitoring the spark discharges exposed to high-temperature combustion gases (at least for the very upstream position of the measurement plane). The microphones' and electrodes' arrangement at the TOF measurement plane is described in detail in Sec. 4. The axial location of the measurement plane can be changed by adding or removing various cylindrical combustion chamber segments between the quartz glass and the TOF measurement segment. The different axial distances Δx that have been utilized in the measurements are depicted in Tab. 5.1. In case of the shortest distance $\Delta x1$, the TOF measurement segment is directly mounted to the quartz glass.

The swirl-stabilized premix burner is separately introduced in Sections 5.3 and 5.4, where the specific features required for the particular measurements are discussed. Upstream of the woofers and the trombone, an air preheater is installed (not visible in Fig. 5.1), which allows the operation of the combustor with increased air temperature as it would be the case in a real gas turbine combustor. However, in this study, the preheater has

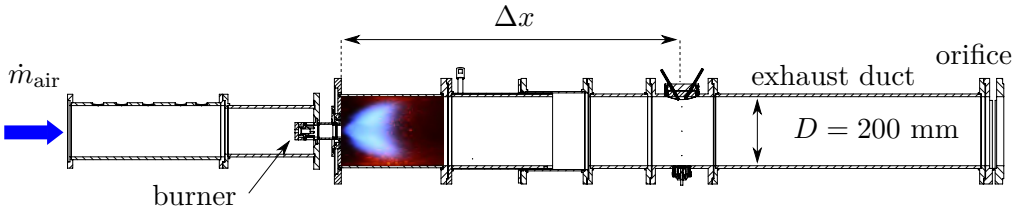

Figure 5.2: Sketch of the relevant parts and equipment of the atmospheric combustion test rig, the corresponding lengths Δx that have been used in this study are listed in Tab. 5.1.

Table 5.1: Distances between the burner inlet plane and the center between the electrodes at the TOF measurement plane that have been used in the measurements presented in this study (see also Fig. 5.2).

$\Delta x1$	$\Delta x2$	$\Delta x3$	$\Delta x4$	$\Delta x5$	$\Delta x6$
400 mm	580 mm	695 mm	780 mm	850 mm	950 mm

been used for the validation measurements presented in Sec. 5.2.

5.2 Combustion rig – validation measurements without flame at increased air temperatures

In order to validate the measurement technique described in Sec. 4 and the zero-dimensional and one-dimensional temperature extraction methods that have been introduced in Sec. 2.3, steady temperature measurements are conducted at the combustion rig. In Fig. 5.3, a sketch of the experimental setup is depicted. To ensure a maximum radial homogeneity of the temperature field in the measurement plane, an electric air preheater is used as heat source rather than a flame. This arrangement allows for a continuous variation of the temperature at the measurement plane between 293 K and 570 K. In this temperature range, thermocouples are considered sufficiently reliable to allow for an accurate validation of the absolute temperature values obtained from the one-dimensional TOF methods. As the water cooling of the combustor walls is not required for these rather low temperatures, it is expected that no steep radial temperature gradients in the vicinity of the walls corrupt the homogeneous temperature distribution in the TOF measurement plane.

The measurements are performed with the microphones embedded in water-cooled microphone holders. This complies with the conditions at the test rig under high-temperature operation conditions with combustion. The cooling water is kept at a constant temperature of 333 K in order to avoid condensation which otherwise would occur if hot air from the combustion chamber penetrates the cavity which connects the combustion rig to the microphone membrane. In Fig. 5.4, a sketch of the microphone holder is depicted, the capillary and the semi-spheric cavity in front of the microphone membrane are shown in a zoomed representation.

The length of the capillary and the cavity in front of the microphone's membrane extend the acoustic path length that is calculated based on the combustion chambers inner

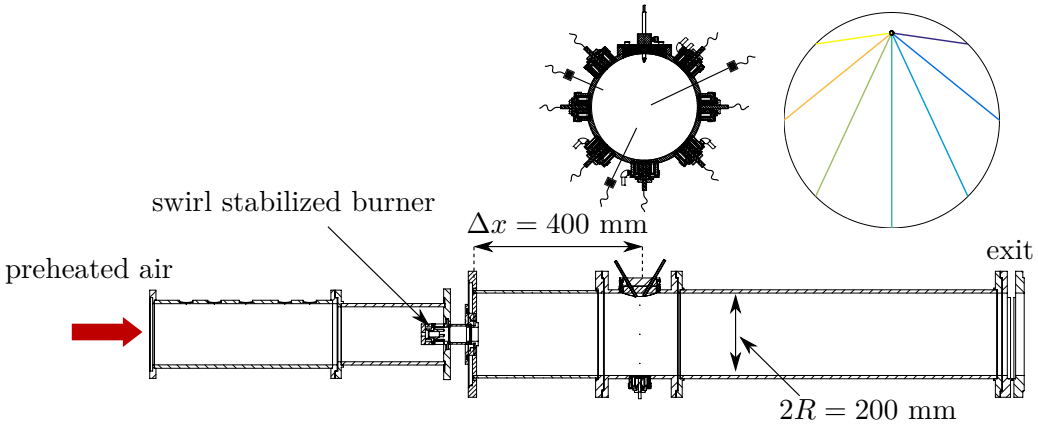

Figure 5.3: Experimental setup of the validation measurements conducted without flame but with pre-heated air. The measurement plane is installed at a distance of 400 mm downstream of the burner inlet plane, the air mass flow is set to $\dot{m}_{\mathrm{air}} = 200\,\mathrm{kg/h}$; the electrode setup corresponds to Fig. 4.23.

diameter and thus increase the arrival time by an additional time τ_{h} with

$$\tau_{\mathrm{h}} = \frac{l_c}{c_{\mathrm{h}}}. \tag{5.1}$$

l_c corresponds to the length of the capillary and the cavity and c_{h} refers to the speed of sound associated to the spatially averaged gas temperature in the capillary. The latter depends on the holder's temperature (which in turn dependent on the temperature of the cooling water).

If the temperature should be estimated directly from the arrival times measured with each microphone, it is of high importance to account for τ_{h}. Therefore, the time delay τ_{h} needs to be subtracted from the measured arrival times. If a homogeneous radial temperature distribution is assumed, the temperature measured with the j-th microphone reads

$$T_{\mathrm{direct},j} = \frac{d_j^2}{(\tau_j - \tau_{\mathrm{h}})^2 \kappa R_{\mathrm{gas}}}, \tag{5.2}$$

where d_j denotes the geometrical distance between the location of the acoustic source and the beginning of the capillary between the combustion chamber and the microphone membrane. The j-th arrival time τ_j corresponds to the j-th microphone. Due to tolerances in the manufacturing process of the microphone holders and the duct's connection holes, the exact estimation of the cavity length l_c is subject to uncertainties in the order of less than 1 mm.

The experimental arrangement shown in Fig. 4.23 has been employed for this validation study. The corresponding lengths of the acoustic paths of the seven microphones are depicted in Fig. 5.5a. These distances have been estimated based on averaged arrival time measurements at steady ambient temperature. The latter ensures a perfectly homogeneous temperature field. The error of the assessment of the penetration depth s is of the order of at least 1 mm. Additionally, potential manufacturing uncertainties have to be taken into account, effects due to thermal expansion, or slight shifts of parts due to assembling tolerances. The slight asymmetries that can be seen in Fig. 5.5a stem from the fact that the electrodes might have been installed with marginally different

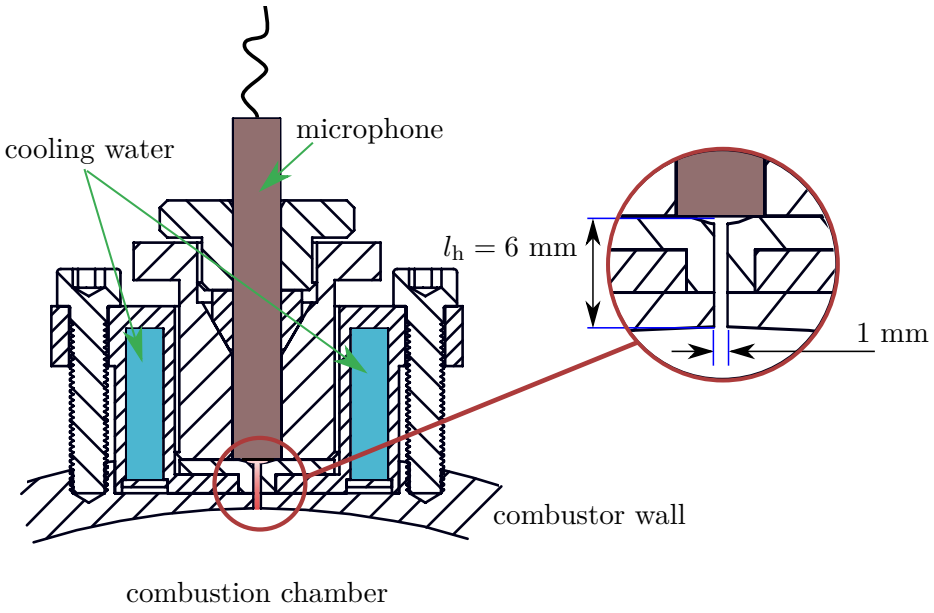

Figure 5.4: Sketch of a water-cooled microphone holder mounted at the wall of the combustion rig. The microphone's membrane is connected to the combustion chamber via a capillary with a diameter of 1 mm and a length of 6 mm, followed by a spherical volume in front of the membrane.

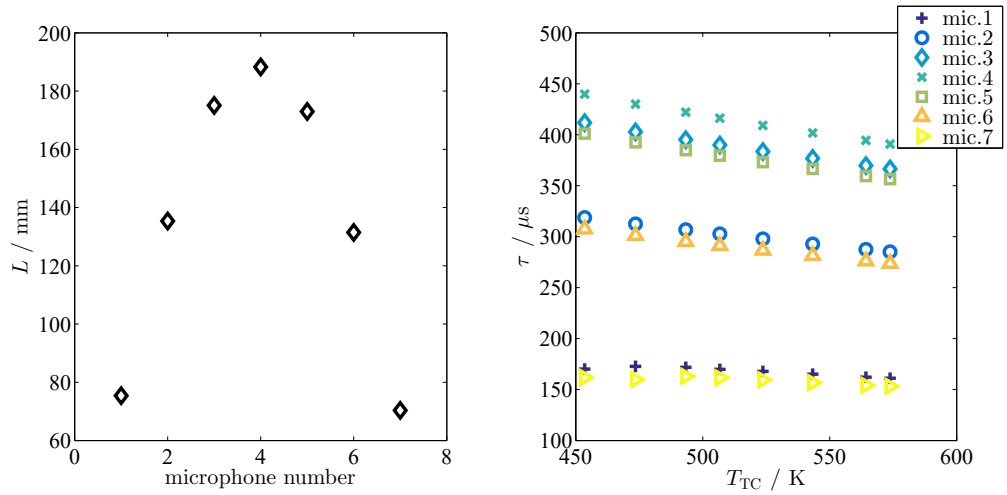

Figure 5.5: **(a)**: Lengths L of the acoustic paths that have been evaluated from TOF measurements (averaged over approximately 200 spark ignition events) at ambient temperature at the symmetric measurement setup shown in Fig. 4.23 with a penetration depth of $s = 12$ mm. The length l_h of the microphone holder (Fig. 5.4) is subtracted. **(b)**: Measured arrival times of the seven microphones for different temperatures of the preheated air. The temperatures T_{TC} are measured by means of thermocouples.

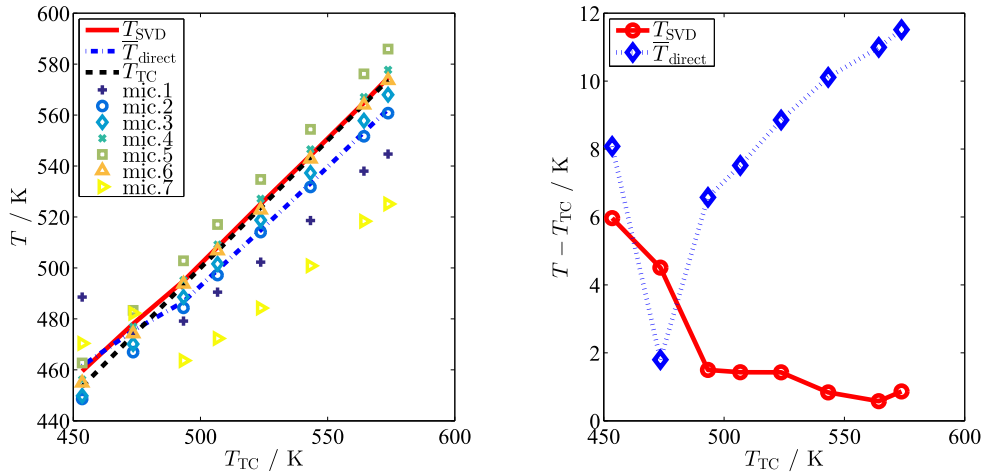

Figure 5.6: **(a)**: **Markers**: Temperatures obtained from the arrival times measured with the different microphones based on Eq. 5.2 by means of the known lengths of the acoustic paths. **Dashed-dotted line (blue)**: Mean value over the temperatures obtained from each microphone. **Dashed line (black)**: Mean value of the temperature measured by means of three thermocouples (angle bisector in this plot). **Solid line (red)**: Temperature array obtained from SVD method based on Eq. 2.103 with $\check{c}_{\mathrm{ref}} = 0.0022\,\mathrm{s/m}$. **(b)**: Difference between the average temperature measured by means of the three thermocouples $\overline{T}_{\mathrm{TC}}$ and the mean value of the direct temperature measurements with each microphone $\overline{T}_{\mathrm{direct}} = \sum_{j=1}^{N_{\mathrm{mics}}} T_{\mathrm{direct},j}$ according to Eq. 5.2.

penetration depths, which causes a small shift from the symmetry axis.

The arrival times are depicted in Fig. 5.5b as function of the temperature T_{TC}, which is the average of the temperatures measured in the TOF measurement plane by means of three type-K thermocouples installed at different radii (according to the thermocouples' positions depicted in Fig. 4.23). The temperature levels have been maintained for a sufficiently long time so that it can be assumed that the combustor walls have been in thermal equilibrium with the air and no significant radial temperature gradients are present. This has been verified via a thermocouple placed very close to the wall within the measurement plane.

Each arrival time shown in Fig. 5.5b represents the median value of approximately 200 arrival times of single spark ignition events. This is done to compensate for the strong oscillations of the plasma tunnel, which is discussed in Sec. 4.2.2.2. Within the temperature range shown in Fig. 5.5b, the gap width of the electrodes' tips does not require adjustment and thus the averaged spark location is the same for all temperatures.

5.2.1 Zero-dimensional temperature reconstruction

Prior to the application of the zero-dimensional SVD method (see Sec. 2.3.1) to the TOF measurements presented in Fig. 5.5b, it will be demonstrated how strong the uncertainties in the distance assessment and the arrival time measurement affect the temperature estimation. This is shown in Fig. 5.6a. Each of the markers represents a temperature estimation $T_{\mathrm{direct},j}$ according to Eq. 5.2 and based on the data provided in

Figs. 5.5. The different markers reflect the seven different acoustic paths; the dashed black curve denotes the temperature measured with the thermocouple and serves as reference. A significant scattering of $T_{\mathrm{direct},j}$ is observed. Especially the two microphones that are closest to the spark ignition (mics. 1 and 7) significantly deviate from the expected temperature, i.e. the black dashed line. This is primarily because their acoustic paths cover a region very close to the wall, where the temperature might still be lower than in the center of the duct due to heat conduction at the wall. Another reason could be the fact that these propagation paths are the shortest and consequently exhibit the largest relative errors. So if the arithmetic mean is calculated over the seven paths at each measurement, the blue dashed-dotted curve is obtained (Fig. 5.6a). It deviates from the expected temperatures by up to 10 K. The latter can be seen in Fig. 5.6b, where the diamonds represent the temperature difference between the thermocouple measurements and $\overline{T}_{\mathrm{direct}}$.

It could be discussed at this point, if the arithmetic mean should be weighted by the length of the paths or if the radii that are covered should as well be considered. However, as already motivated in Sec. 2.3, such a method will always be affected by the error done in assessing the exact distance between sender and receivers. So it is of interest to compare this straightforward and "coarse" approach with the zero-dimensional method introduced in Sec. 2.3.1. This method does not require input of the geometry but a measure of the average temperature of the investigated field.

In this particular case, the matrix $\boldsymbol{\tau}$ (see Eq. 2.93), which is decomposed by the SVD, becomes $\boldsymbol{\tau} \in \mathbb{R}^{8\times N_{\mathrm{mics}}}$ as a total of eight measurements are considered. The output temperature array $\boldsymbol{T}_{\mathrm{SVD}}$, which is calculated based on the left singular vector (see Eq. 2.103), is plotted as solid red line in Fig. 5.6a. The reference inverse speed of sound $\check{c}_{\mathrm{ref}}$ corresponds to the temperature average of the three thermocouple measurements over all eight measurements and yields $\check{c}_{\mathrm{ref}} = 0.0022\,\mathrm{s/m}$. The very good match between the temperature curve obtained from the SVD method with the dashed line of the thermocouple measurements can also be deduced from the solid line in Fig. 5.6b, which represents the temperature difference between $\boldsymbol{T}_{\mathrm{SVD}}$ and $\overline{T}_{\mathrm{TC}}$. The deviation is mostly far below the deviation obtained from the direct temperature measurement and of the order of 2 %.

The major advantage of the SVD method is the fact that it does not require geometrical information, which are difficult to obtain and thus are prone to errors. It merely requires an estimate of the (cross-sectionally) average temperature in the measurement plane. The latter is, especially in this case where temperatures are not very high and temporarily as well as spatially steady, reliably measurable. Eventually, the SVD approach leads to more accurate results.

5.2.2 One-dimensional temperature reconstruction

Besides the zero-dimensional method based on the SVD approach, the measurements using pre-heated air are also used to validate the one-dimensional tomographic approaches. Due to the assumption of a homogeneous radial temperature profile, a verification of the spatial temperature reconstruction of one-dimensional methods like onion peeling and collocation is straight forward. An example of the onion peeling approach applied to the same measurement data as used for the zero-dimensional analysis presented above

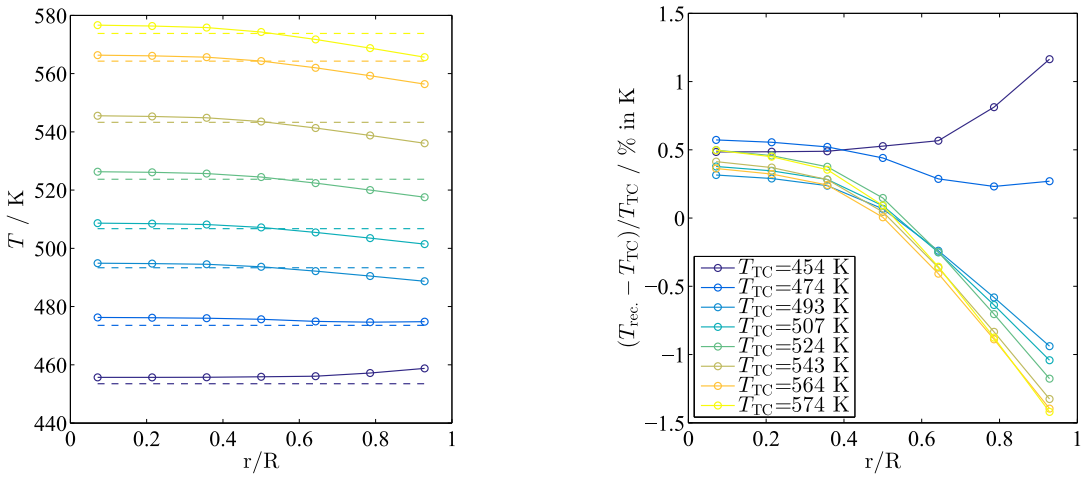

(a) **(b)**

Figure 5.7: (a): **Markers**: Results of the onion peeling approach applied on the measurement data presented in Fig. 5.5b based on $N_g = 7$ discretization rings and a regularization with $\gamma = 0.3$; the colors denote measurements at different preheat temperatures. **Dashed lines**: Corresponding average temperature of three thermocouple measurements at different radii in the measurement plane. **(b)**: Relative deviation between the temperatures reconstructed by the onion peeling approach and the temperatures obtained from thermocouple measurements (based on the data in (a)).

(Fig. 5.5b) is shown in Fig. 5.7a. The various dashed lines represent the averaged temperature over the three thermocouples at the different preheat temperatures at the measurement plane. The markers represent the temperatures obtained from the onion peeling as a function of the dimensionless radius r/R. A number of seven equidistant rings for the temperature field's discretization has been found to provide a good compromise between the stability of the solution and a sufficient spatial resolution. The problem is ill-posed as the information obtained from microphones 1 to 3 are very similar to the information obtained from microphones 5 to 7. Therefore, Tikhonov regularization is required. The regularization parameter is set to $\gamma = 0.3$ for all measurements. It can be seen that the reconstructed radial temperatures match the corresponding temperature levels well and exhibit a flat profile. However, for most reconstructed temperature profiles the deviation from the expected temperature becomes more prominent in the outer rings that are located close to the combustor walls. These deviations seem to be due to the slight temperature inhomogeneities, which are most significant in the near-wall region. In Fig. 5.7b, the relative deviation in temperature between the thermocouples' average temperature and the temperatures estimated by the onion peeling is plotted corresponding to Fig. 5.7a as a function of the dimensionless radius. The relative deviation is smaller than 1.5 % and thus tolerable for further investigations.

Another quantity, which is especially of interest for the investigation of entropy waves, is the cross-sectionally averaged temperature. Based on the onion peeling results presented in Fig. 5.7a and further measurements at different temperature levels, the cross-sectionally averaged temperature is obtained from the temperatures of the seven rings. The results are plotted in Fig. 5.8.

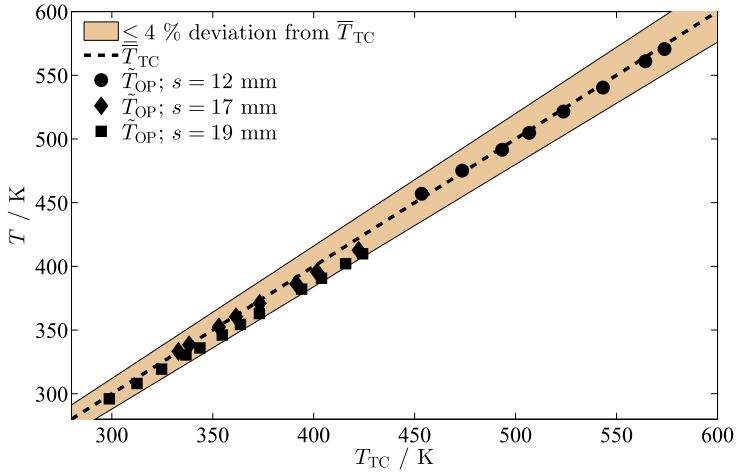

Figure 5.8: Cross-sectionally averaged temperatures (markers) reconstructed by an onion peeling approach conducted with $N_g = 7$ rings based on arrival time measurements with $N_L = 7$ acoustic paths. The dashed line denotes the temperature measured with the thermocouples in the TOF measurement plane and thus serves as reference of the expected cross-sectionally averaged temperature. The shaded area indicates the temperature area in which the deviation from the thermocouple measurements is less than 4 %.

As the optimal electrode gap width changed for the different temperature ranges in the experiments, it had been adjusted varying the penetration depth of the electrodes' tips (see Sec. 4.3) between $s = 12\,\text{mm}$ and $s = 19\,\text{mm}$. The colored area denotes the band within which the deviation between the expected cross-sectionally averaged temperature and the one obtained from the onion peeling $\tilde{T}_{OP}$ is smaller than 4 %. It can clearly be seen that the majority of the measurements exhibit a deviation that is far less than 4 % and thus within an acceptable range for further investigations on entropy fluctuations.

In case of the collocation method, the results are qualitatively as well as quantitatively very similar to the results of the onion peeling (for $\zeta = \mu/\gamma \approx 500$). This has already been observed in the phantom study (see Sec. 3.2) and again indicates that both methods eventually converge to a very similar solution for a similar spatial discretization resolution.

5.3 Combustion rig – static temperature measurements

Prior to the dynamic temperature measurements, where entropy waves are artificially generated (see Sec. 5.4), steady combustion measurements have been conducted. These measurements allow for the assessment of the radial temperature profile by means of thermocouples, which serve as important reference temperature measure and enable the validation of the temperature profiles extracted from the TOF measurements.

The thermocouple measurements are presented in Sec. 5.3.1 along with an elaborated analysis of the associated uncertainties. In this section, it is also investigated, how the equivalence ratio of the fuel-air mixture quantitatively influences the gas temperature at the measurement plane. The ratio between a change in equivalence ratio and its corresponding change in gas temperature is a crucial quantity for the characterization of the

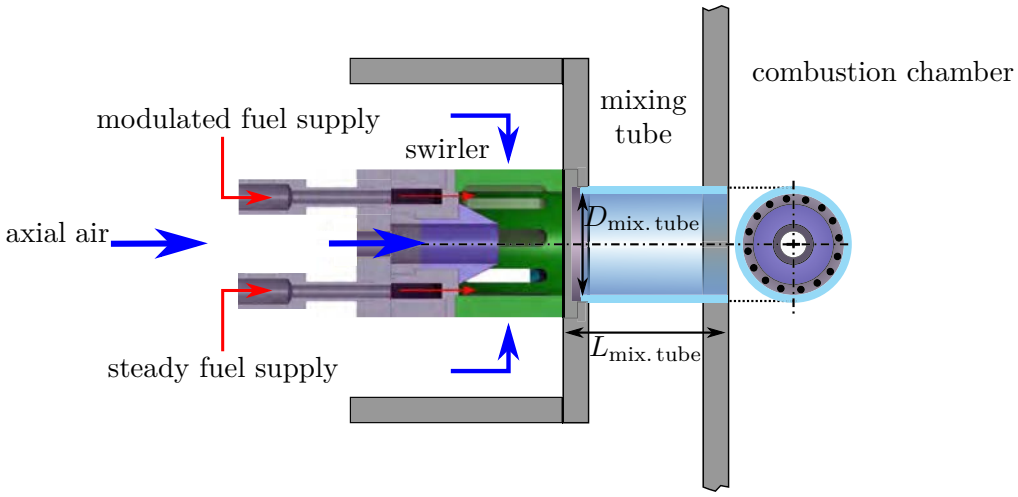

Figure 5.9: Scheme of the combustor consisting of a swirl generator followed by a mixing section; the sketch on the very right-hand side depicts the axial view into the mixing tube in upstream direction; $D_{\text{mix. tube}} = 34$ mm, $L_{\text{mix. tube}} = 60$ mm.

temperature fluctuation investigated in Sec. 5.4. Another purpose of the steady combustion measurements is the examination of the one-dimensional temperature extraction methods, which are presented in Sec. 5.3.4. The one-dimensional dynamic temperature reconstruction is essentially based on a phase sorted compilation of steady temperature measurements. The results presented in this section provide important information on the accuracy of the one-dimensional entropy wave reconstruction.

The burner, which has been employed in all combustion measurements presented in this study, is designed for the operation of a swirl-stabilized premixed flame. A schematic of the burner together with the mixing tube, which connects the swirl generator with the combustion chamber, is depicted in Fig. 5.9. The ratio between the air mass flow that enters axially into the swirler and the air mass flow that enters the swirler tangentially determines the strength of the swirl flow that stabilizes the flame. The swirl number S_{swirl}, which is defined as the relation of the axial flux of angular momentum to the axial flux of axial momentum, has been kept constant at S_{swirl}=0.7 throughout all measurements performed in this study.

5.3.1 Radial temperature profile

One thermocouple has been traversed radially to obtain a spatially resolved static radial temperature profile. Figure 5.10 shows the measured temperature as a function of the radial position of the thermocouple's tip, where $r/R = 0$ refers to the position in the center of the circular duct and $r/R = 1$ refers to the inner wall of the combustor. The three different curves correspond to different measurement conditions. The solid curve has been obtained for an equivalence ratio of $\phi = 0.7$. The validity of this measurement is proven by the same measurement with a lower equivalence ratio of $\phi = 0.65$ (dotted curve), which qualitatively exhibits the same curve but with a constant shift towards lower temperatures. With the same equivalence ratio of $\phi = 0.65$ but a lower mass flow of air entering the combustor, the dashed curve shows again the same pattern over the entire radius at lower temperatures compared to the dotted curve, where the power density in the combustor is higher due to a higher mass flow of fuel.

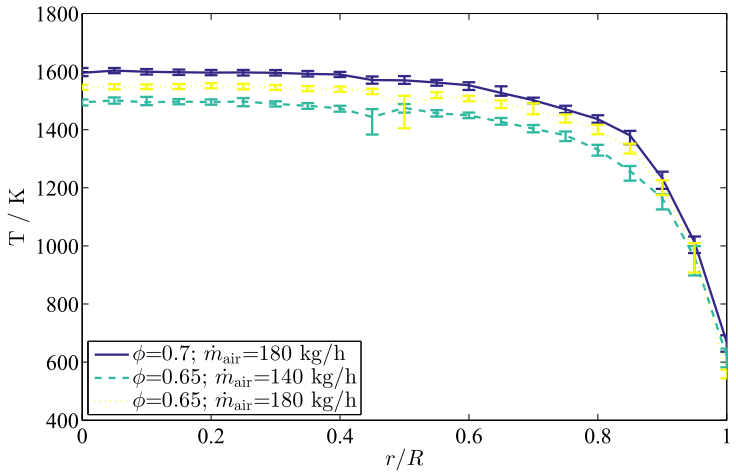

Figure 5.10: Steady temperature measured by means of a 1.5 mm type-S thermocouple for two different equivalence ratios $\phi = 0.65$ and $\phi = 0.7$ and two different air mass flows $\dot{m}_{\mathrm{air}} = 140\,\mathrm{kg/h}$ and $\dot{m}_{\mathrm{air}} = 180\,\mathrm{kg/h}$ at the axial position $\Delta x3$; error bars correspond (mainly) to the uncertainty of the exact thermocouple position.

The error bars have been evaluated based on the uncertainty of the position of the thermocouple's tip during the traversing (due to the bending of the wire); they also include stochastic fluctuations of the measured temperature values. The axial symmetry of the radial temperature field has been checked. Therefore, the temperature profile can be discussed in a reduced range of $0 < r/R < 1$.

Figure. 5.10 shows that the temperature drops rapidly close to the combustor wall. This is due to the outer water-cooling of the wall which is applied by means of copper tubes that are tightly helically wrapped around the combustor duct. It has not been possible to measure the wall temperature itself, however, we estimate a temperature of approximately 550 K. Thus, in the range of $0.6 < R/r < 1$, the temperature measured by means of a thermocouple is strongly sensitive to the penetration depth of the thermocouple's tip and consequently prone to errors.

Static temperature measurements for different relevant equivalence ratios are plotted as markers in Fig. 5.11 for two different axial locations and three different penetration depths of the type-S thermocouples. While the circular and triangular markers refer to positions of the thermocouple's tip more close to the center of the duct ($r/R < 0.5$), the squares represent measurements close to the wall. The linear dependence of the temperature with respect to the equivalence ratio can be seen by the very good matches between linear fits (lines) and the measurements. Besides much smaller absolute temperatures at the location close to the inner combustor wall, it is evident, that also the slope of the temperature increase becomes smaller.

For a quantification of the temperature amplitude caused by an equivalence ratio fluctuation, it is important to know this change in temperature with respect to the equivalence ratio, $dT/d\phi$, which is evaluated by means of Figs. 5.10 and 5.11 in the following subsection.

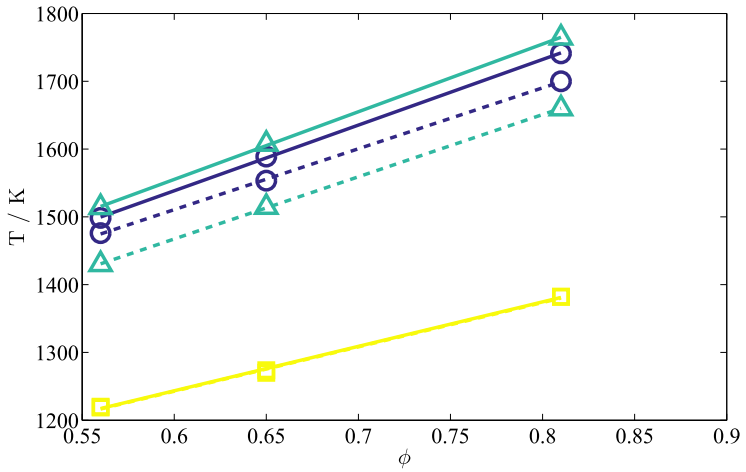

Figure 5.11: Measured static temperatures (markers) and the corresponding linear fits (lines) for different equivalence ratios ϕ and penetration depths s of the type-S thermocouples; (◯): $s = 70\,\mathrm{mm}$; (△): $s = 50\,\mathrm{mm}$; (□): $s = 10\,\mathrm{mm}$; two axial positions downstream of the burner $\Delta x2$ (solid) and $\Delta x3$ (dashed) with $\Delta x2 < \Delta x3$.

5.3.2 Measurement of static $\phi - T-$ relation

As we have seen in Fig. 5.11, $dT/d\phi$ depends slightly on the radius. In Fig. 5.12, this becomes more obvious by plotting the measured values of $dT/d\phi$ with respect to the radial measurement position. In a range of $0 < r/R < 0.5$, the values are found to be on a constant level of approximately $dT/d\phi = 950\,\mathrm{K}$, whereas for higher radii this value drops to values of around $dT/d\phi = 700\,\mathrm{K}$. This originates from the highly non-adiabatic combustor wall that imposes a low gas temperature in the vicinity of the wall. Thereby, the sensitivity of the near-wall temperature towards changes of the overall temperature level, which is caused by a change in equivalence ratio at the flame location, is reduced.

Based on the measured values for $dT/d\phi$ in Fig. 5.12, the static temperature amplitude T'_s, which is defined as the temperature oscillation amplitude due to an equivalence ratio fluctuation of infinitely small frequency, can be estimated. If a harmonic distortion of ϕ and T is assumed and the fluctuation amplitudes ϕ' and T' are defined as the zero to peak amplitudes of the perturbation, T'_s reads

$$T'_s = \frac{\phi_{\max} - \phi_{\min}}{2} \frac{dT}{d\phi}. \tag{5.3}$$

The values $\phi_{\min}$ and $\phi_{\max}$ represent the minimum and maximum value of the equivalence ratio within one period of fluctuation.

In Fig. 5.13a, the calculated values for T'_s are plotted with respect to the relative equivalence ratio fluctuation $\phi'/\overline{\phi}$ for two different values of $dT/d\phi$ and two mean equivalence ratios $\overline{\phi}$. The range of relative equivalence ratio fluctuations has been chosen such that for a maximum relative distortion of 30 %, the maximum equivalence ratio is still in the lean combustion regime. There, a linear dependence between temperature and equivalence ratio, as depicted in Fig. 5.11, can be assumed. This assumption is also employed for the range of equivalence ratio fluctuation amplitudes that have been applied to the

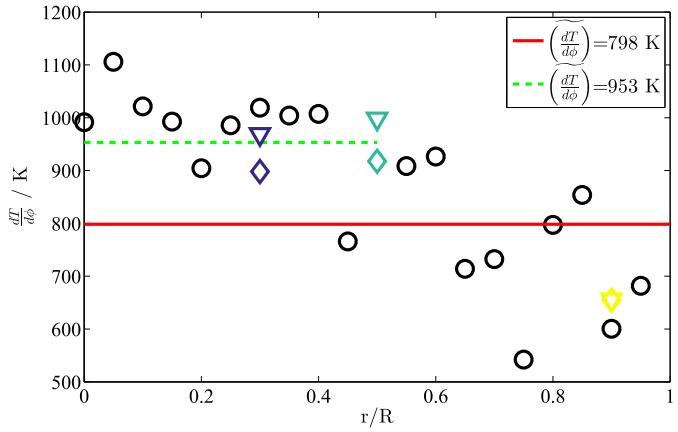

Figure 5.12: Values of $dT/d\phi$ based on the static temperature measurements shown in Fig. 5.10 (black circles) and Fig. 5.11 (colors associated to the different penetration depths; $\bigtriangledown$: $\Delta x2$, $\diamondsuit$: $Deltax3$); the solid line represents the cross-sectional average of all values of $dT/d\phi$, the dashed line refers to the cross-sectional average of $dT/d\phi$ within $0 < r/R < 0.5$.

combustion rig measurements presented in Section 5.4. Note that the lines in Fig. 5.13a would all collapse into an angle bisector if the relative temperature fluctuation $T_s'/\overline{T}$ would be considered on the y-axis rather than T_s'.

Besides the dependence on the radial position within the duct, the value of $dT/d\phi$ is also affected by the axial location of the measurement plane. Therefore, type-S thermocouple measurements at the same penetration depth of $s = 0.5R$ but at various axial locations within the combustion rig are plotted with respect to the equivalence ratio in Fig. 5.13b. A slight decrease of the slope $dT/d\phi$ is observed for measurement positions further downstream of the flame, however, this difference is small compared to the variation of $dT/d\phi$ with respect to the radial measurement location (see Fig. 5.12).

The reason why $dT/d\phi$ is affected by the axial position can again be found in the highly non-adiabatic combustor walls. As the thermal conductivity is a function of the difference between the gas temperature and the wall temperature, the heat loss becomes more prominent for higher values of the equivalence ratio. Thus, the temperatures of the high equivalence ratio flow drops stronger while advecting through the cooled exhaust duct than the gas flow at lower temperatures.

This explanation is further confirmed when looking at the adiabatic combustion temperature of CH_4 that has been calculated by means of the GRI 3.0 mechanism (Smith et al., 2000) ($\diamondsuit$) in Fig. 5.13b). The growth of the temperature for increasing equivalence ratios is still linear, however, the slope is significantly steeper. This reveals the importance of taking the heat losses due to the wall cooling and the quartz glass section into account. A reliable determination of $dT/d\phi$ based on adiabatic considerations would be highly inaccurate.

5.3.3 Thermocouples and their uncertainties

Thermocouple measurements are an essential means in this study. They provide the measure of the average temperature that is required to calibrate the SVD method (see

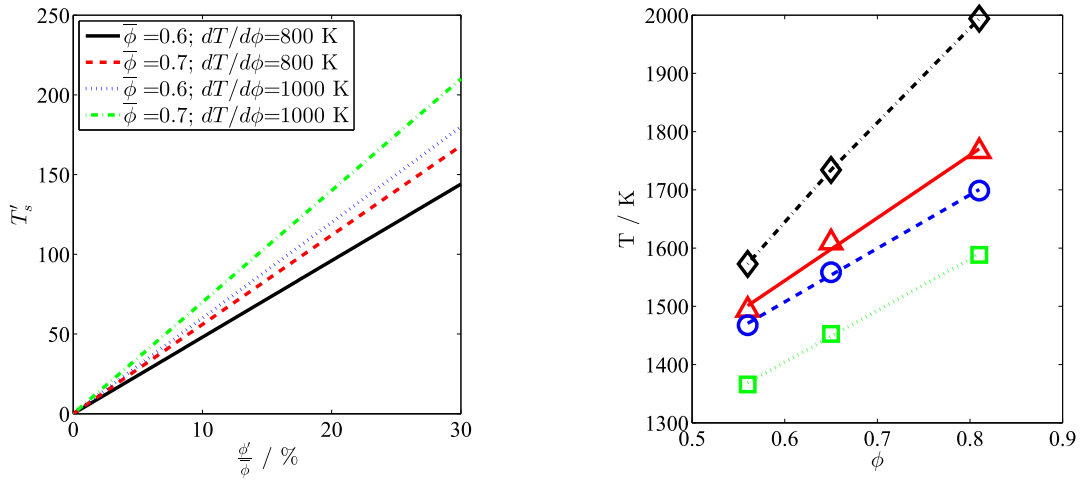

(a) **(b)**

Figure 5.13: **(a)**: Estimation of the temperature fluctuation amplitude T' as function of the relative equivalence ratio fluctuation $\phi'/\overline{\phi}$. **(b)**: Static temperature measurements by means of type-S thermocouples at a penetration depth of $s = 0.5R$ at different axial positions of the measurement plane: (△): $\Delta x1$, (○): $\Delta x2$, and (□): $\Delta x3$; $\dot{m}_{\text{air}} = 140\,\text{kg/h}$; (◇): calculated adiabatic temperature of CH_4 by means of the GRI 3.0 mechanism.

Sec. 2.3.1) and they serve as a reference static temperature measure for the tomographic reconstruction methods (see Sec. 2.3.2).

All thermocouples that have been employed in this study are shielded, which means that the two thermocouple wires are embedded in a metallic mantle from the shaft up to the tip. This equips the thermocouple with a higher capability to withstand corrosive environments and features an increased stiffness. This, however, coincides with some disadvantages, such as an increased thermal inertia and enhanced conductive heat transfer rates.

In this section, the different heat fluxes, which need to be considered when employing a thermocouple at the combustion test rig, are assessed. These mechanisms contribute to the deviation between the real gas temperature and the temperature indicated by the thermocouple (Tewes, 1941; Lechner and Bothien, 2005; Hindasageri et al., 2013; Bernhard, 2014). In Fig. 5.14, the relevant heat transfer paths are sketched according to Bernhard (2014).

Table 5.2: Types of thermocouples used in this study.

name	material	operating mode	diameter D / mm	T-range / K
type-K	NiCr-Ni	shielded	1.5 and 3	0 - 1550
type-S	Pt10Rh	shielded	1 and 1.5	220 - 2000

Two different types of thermocouples are used in this study. For high-temperature measurements, typ-S thermocouples are employed whereas for the gas temperature measurements at $T < 1000\,\text{K}$, type-K thermocouples were sufficient. In Tab. 5.2, the relevant parameters of the thermocouples used throughout this study are listed. The typical

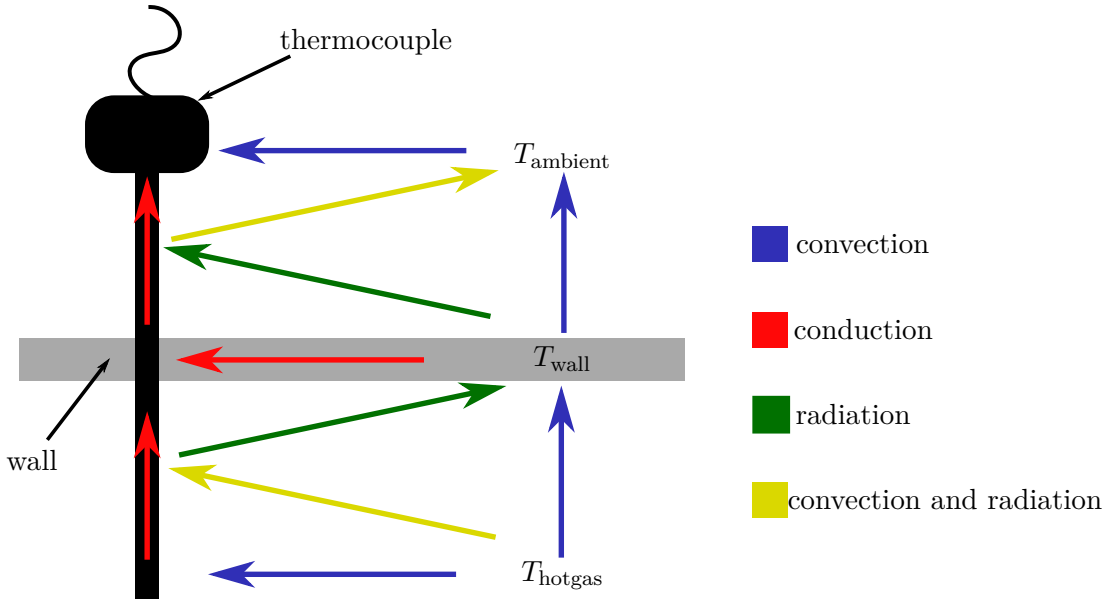

Figure 5.14: Scheme of the various heat transfer mechanisms present at a typical thermocouple arrangement (based on Bernhard (2014)).

temperature application range might vary in literature, the values shown here are approximated from Bernhard (2014).

Convective heat transfer

The operating principle of a thermocouple is based on the *Seebeck* effect, which utilizes the dependence of the electrical resistance of metallic materials on their temperature. Therefore, to measure the gas temperature, the thermocouple wires have to match the gas temperature, which happens essentially by convective heat transfer $\dot{Q}_{\text{conv}} = \alpha_q S_{\text{wire}}(T_{\text{gas}} - T_{\text{wire}})$. S_{wire} denotes the wires' conduction surface and the heat transfer coefficient α_q depends on the *Nusselt number* Nu with $\alpha_q = (Nu\lambda_q)/D$. Here, λ_q denotes the thermal conductivity. The Nusselt number, which relates the total heat transfer to the conductive heat transfer, can be expressed by the *Prandtl number* (relating the viscous diffusion rate to the thermal diffusion rate) and the *Reynolds number* (relating the inertial forces to the viscous forces). This indicates the complexity of the correct determination of α_q. The heat transfer coefficient becomes a function of the flow field parameters at the thermocouple's tip as well as of the gas properties.

Conductive heat transfer

The thermocouples are inserted into the combustion rig at various penetration depths, as due to the radial inhomogeneous temperature field, the static temperature has to be assessed at different radial positions. This provokes different conditions for the conductive heat transfer that takes place between the tip of the thermocouple and any other location along the shielded thermocouple wire. The significant axial temperature gradients along the probe lead to a conductive heat transfer from the hot tip to the much colder shaft. A hot temperature spot at a certain axial position of the probe, however, might cause a heat transfer from this particular location to the tip. In order to assess the

conductive heat flux, the temperatures along the probe and especially at the attachment point between the mantle and the combustor wall have to be estimated. If this effect is not considered, the temperature measure might be corrupted.

Radiation losses

Another mechanism that becomes very important for high-temperature applications are radiation losses. The relation between the heat transfer due to radiation and the wire temperature and the wall temperature, respectively, writes according to the *Stefan-Boltzmann* law $\dot{Q}_{\mathrm{rad}} \propto \epsilon_{\mathrm{eff}}(T_{\mathrm{wire}}^4 - T_{\mathrm{wall}}^4)$. The emissivity, ϵ_{eff}, is a quantity that depends on the material and the surface texture of the wall and the thermocouple. An accurate determination of the different emissivities is difficult and prone to error. Lechner and Bothien (2005) define the effective emissivity as function of the emissivity of the wall, the thermocouple, and of the corresponding surface areas. For the thermocouple, an approximation of the emissivity can be found in Bradley and Entwistle (1961). The emissivity of the steel, the combustor wall material in this experiment, can be estimated with a correlation found in Shi et al. (2015).

The radiative energy exchange does not only take place between wall and thermocouple but also between the solid material and the gaseous fluid. The emissivity of the gas mixture or its different species can be found in Farag (1982) and VDI (2013).

Stagnation temperature and recovery factor

Ideally, the temperature measured at the thermocouple's tip could be considered as the stagnation temperature (also known as the total temperature). This is valid if the kinetic energy of the gas flow would fully be converted into thermal energy in the stagnation point at the surface: $T_{\mathrm{stag}} = T_{\mathrm{gas}} + u^2/2/c_p$. However, this also implies that the conditions at the thermocouple's tip are adiabatic, which is not the case in a realistic view. Therefore, a recovery factor r_{rec} is defined, which allows for the estimation of the temperature at the thermocouple's tip by $T_{\mathrm{rec}} = T_{\mathrm{gas}} + r_{\mathrm{rec}} u^2/2/c_p$. An approximation of r_{rec} can be obtained by use of the Prandtl number and is stated by Bernhard (2014) in the range of $\sqrt[3]{\mathrm{Pr}} \leq r_{\mathrm{rec}} \leq \sqrt{\mathrm{Pr}}$. As the determination of Pr is not unique but subject to assumptions, this provokes another uncertainty in the measurement of the actual gas temperature.

Quantification of the temperature deviations

In the framework of this study, the heat transfer compensation has been applied by solving the differential equation given by Fischer (1941), who set up a integral thermal balance of the system sketched in Fig. 5.14. The idea is to divide the thermocouple into several small volumes to which the energy balance is applied. This approach has been extended by Bettermann (1964) to account for the radiation of the gas. The length of the thermocouple L_{TC} can be expressed as an integral in the form

$$L_{\mathrm{TC}} = \int_0^{L_{\mathrm{TC}}} dx = \int_0^{\Delta T} \frac{1}{\sqrt{2F + \frac{d(\Delta T)}{dx^2}}} d(\Delta T), \tag{5.4}$$

where F is defined as

$$F(\Delta T) = C_1 \left[(\Delta T)^5 - (\Delta T_{\text{wire}})^5\right] + C_2 \left[(\Delta T)^4 - (\Delta T_{\text{wire}})^4\right] + C_3 \left[(\Delta T)^2 - (\Delta T_{\text{wire}})^2\right] + C_4 \left[(\Delta T) - (\Delta T_{\text{wire}})\right] \quad (5.5)$$

and $\Delta T = T_{\text{gas}} - T_{\text{wall}}$ refers to the difference between the actual gas temperature and the wall temperature. $\Delta T_{\text{wire}} = T_{\text{wire}} - T_{\text{wall}}$ denotes the temperature difference between the thermocouple and the wall. The variables C_1, C_2, C_3, and C_4 represent correlations that contain parameters regarding the heat convection, the heat conduction, heat radiation, the flow field, material parameters, and gas properties. The integral in Eq. 5.4 van numerically be solved and finally provides the gas temperature. For typical arrangements of the thermocouples in the combustion test rig, the heat flux compensation leads to a deviation of the temperature indicated by the thermocouple and the actual gas temperature of 50 K to 110 K.

As indicated in the preceding subsections, the determination of all these parameters, in particular the empirical parameters such as the dimensionless parameters Nu, Pr, and Re, are subject to errors. Most often, they have to be gauged based on empirical values provided in literature.

Associated with the heat flux compensation, the uncertainty of the temperature assessment increases. The maximum deviation given in literature for a type-S thermocouple is of the order of ±1 K to ±4 K. Lechner and Bothien (2005) worked out that this deviation becomes significantly larger when considering all the uncertainties in the determination of the parameters in C_1, C_2, C_3, and C_4. By adding all these uncertainties, they state a final uncertainty of about ≈ 23 K including the uncertainty of the measurement chain (whose contribution counts only 1 K).

5.3.4 One-dimensional approach

The one-dimensional algebraic methods, i.e., the onion peeling and collocation approaches, have been introduced in Sec. 2.3.2 and analytically investigated in a phantom study in Sec. 3.2. In this section, these tomographic approaches are applied to experimental data. The arrival times have been measured at the combustion rig operated under steady conditions. The experimental setup is sketched and explained in Fig. 5.15.

The arrangement of the electrodes' tips and the microphones corresponds to the asymmetric setup depicted in Fig. 4.25, which enables to gain as much spatial information from one acoustic pulse as possible. The electrodes have been traversed to up to eight different positions, allowing for a tomographic evaluation based on $N_L = 56$ acoustic paths. In contrast to the measurements with preheated air only (see Sec. 5.2), the radial temperature field is now highly inhomogeneous, which has been shown in Fig. 5.10 in Sec. 5.3.1.

5.3.4.1 Onion peeling

For the discretization of the temperature field, equidistant rings are employed. The number N_g of rings has been varied as well as the regularization value γ, to obtain

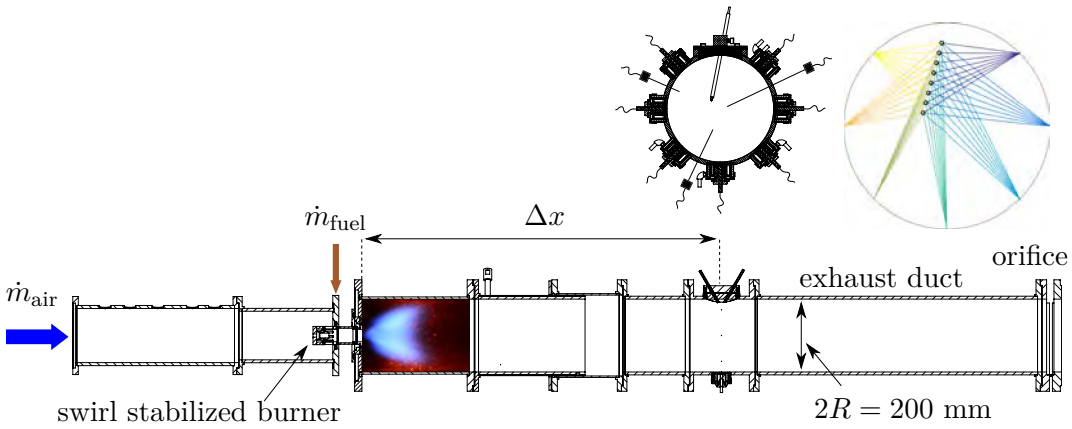

Figure 5.15: Experimental setup used for tomographic investigations on the steady temperature field. The swirl stabilized premix burner is fed with a steady fuel mass flow $\dot{m}_{\text{fuel}}$ to establish lean operation at $\phi = 0.6 - 0.7$, the air mass flow $\dot{m}_{\text{air}}$ is varied between 180 kg/h and 220 kg/h. The measurement segment, which corresponds to Fig. 4.25, has been installed at different positions Δx downstream of the burner front plate ($\Delta x = 400$ mm to 950 mm). An orifice is installed at the downstream end of the exhaust duct to attenuate high-amplitude (thermo-) acoustic oscillations.

a stable, i.e., less noisy, solution. However, if regularization is too strong, the actual "correct" solution for the radial temperature profile would be smoothed out.

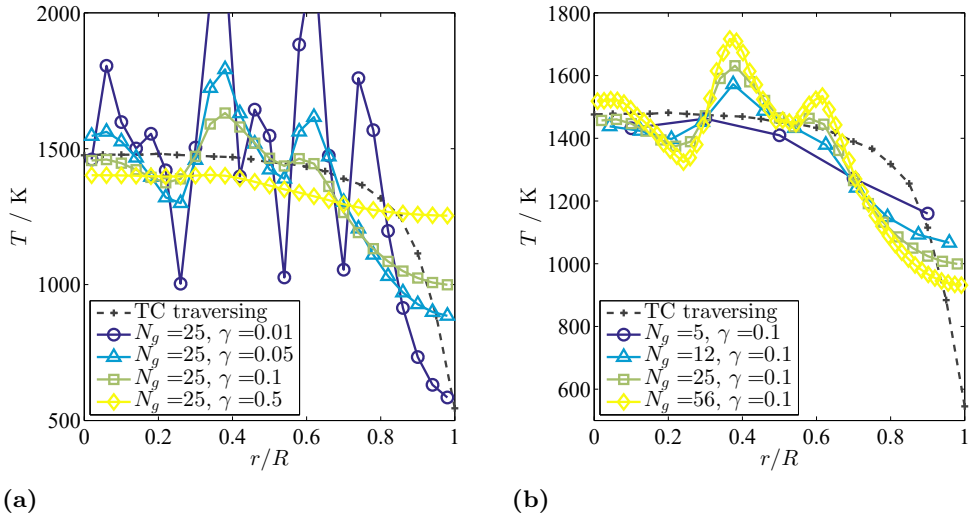

(a) **(b)**

Figure 5.16: Reconstructed radial temperature profiles (markers) evaluated by the onion peeling approach based on the arrival time measurements over $N_L = 56$ acoustic paths. The arrival times are averaged over 300 acoustic excitation events. The measurement plane is installed at $\Delta x = 400$ mm downstream of the burner inlet plane, the burner is operated with steady fuel supply only, the equivalence ratio is kept constant at $\phi = 0.65$. The corresponding temperature profile measured by thermocouples is depicted by the black dashed curve. The markers are located at dimensionless radii positions that correspond to the centers of the rings. **(a)**: Variation of the Tikhonov regularization parameter γ for a constant number of rings $N_g = 25$. **(b)**: Variation of the number of rings N_g with a constant Tikhonov regularization parameter of $\gamma = 0.1$.

The reconstructed radial temperature profiles obtained for various Tikhonov regulariza-

tion parameters γ are compared to the radial temperature profile measured by means of the type-S thermocouples (see Fig. 5.10) in Fig. 5.16a. The number of equidistant discretization rings is fixed to $N_g = 25$, the markers correspond to the respective center between the inner and outer radius of each ring. The influence of the Tikhonov regularization on the field solution is evident. For the smallest regularization parameter $\gamma = 0.01$, the solution is very unstable with some rings displaying temperatures far beyond physically meaningful values. However, if the regularization parameter is too large (here, e.g., $\gamma = 0.5$), even large scale radial temperature variations, and with them the actual solution, are strongly damped. Finally, for very high numbers of γ, the temperature profile converges to a radially homogeneous profile. A regularization parameter in the range between $\gamma = 0.05$ and $\gamma = 0.1$ turned out to best match the expected radial temperature profile.

A notable feature of the onion peeling results becomes more evident in Fig. 5.16b. There, the regularization parameter remains constant at $\gamma = 0.1$ but the number of rings is varied. It is interesting to see that the spatial characteristics of the temperature field – the prominent peak at $r/R \approx 0.4$, the local maximum in the center, and the decrease of the radial temperature gradient for $r/R > 0.8$ – are all maintained for ring numbers $N_g \geqslant 12$. For a lower number of discretization rings, the spatial resolution is too low to reproduce the smaller scales of the characteristic pattern. The observation of these spatial features also applies to measurements performed at different equivalence ratios ϕ, axial locations Δx, and air mass flows $\dot{m}_{\mathrm{air}}$. It is unquestionable that such significant spatial peaks in the radial temperature profile are physically not justifiable, especially since the thermocouple measurements do not exhibit such characteristics at all. But given the fact that this pattern is found for all measurement configurations, these oscillations do not correspond to numerical noise, as this would be randomly shaped and vary for different numbers of rings or regularization parameters.

An explanation is found by reconsidering the requirements that are needed for setting up a one-dimensional tomographic method such as onion peeling. Here, rotational symmetry is a crucial assumption and it has to be validated whether this condition holds true for the experimental setup used in this study.

The thermocouple measurements of the steady radial temperature profile presented in Sec. 5.3.1 might not allow for a profound assertion on the rotational symmetry of the temperature field. Firstly, the restricted number of access holes for the thermocouples limits the number of available radial paths on which the temperature can be measured. Secondly, the spatial error of the thermocouples' measurements becomes highest in the vicinity of the wall, where the maximum radial temperature gradient is found. As the steady temperature field is plateau-shaped, however, a potential asymmetry would mainly be detectable in this near-wall region.

Due to these experimental shortcomings, the symmetry of the temperature field is analytically investigated. Therefore, an additional phantom study is conducted, where the input temperature field is slightly shifted in its radial centerpoint. Qualitative examples of such asymmetric input temperature fields are depicted in the four contour plots on the right-hand side in Fig. 5.17. The asymmetry is induced by means of the superposition of the symmetric temperature field plotted in the lower left corner of Fig. 5.17 with a factor that is a function of the radial coordinates with respect to a certain axis

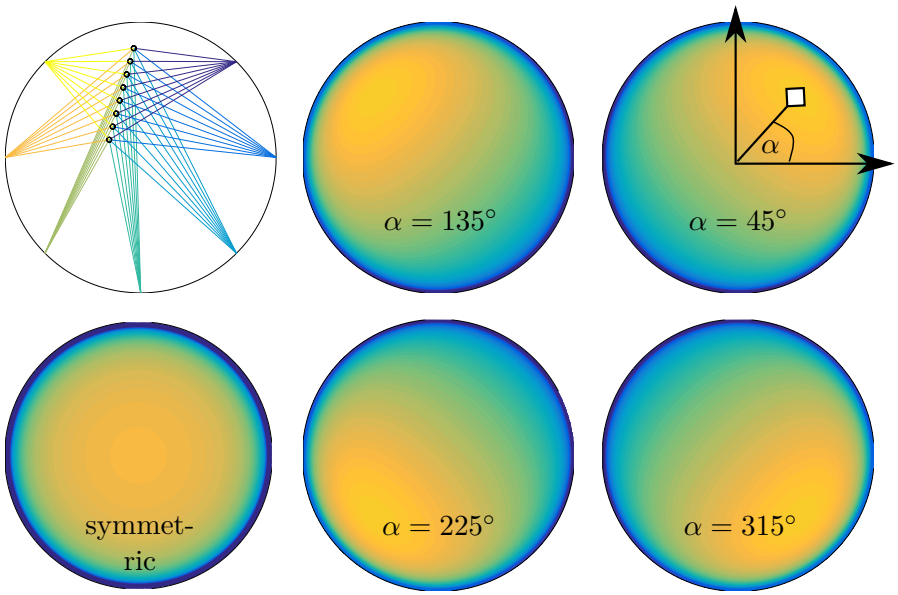

Figure 5.17: Experimental setup used for tomographic investigations on the steady temperature field. The swirl stabilized premix burner is fed with a steady fuel mass flow $\dot{m}_{\text{fuel}}$ to establish lean operation at $\phi = 0.6 - 0.7$, the air mass flow $\dot{m}_{\text{air}}$ is varied between 180 kg/h and 220 kg/h. The measurement segment, which corresponds to Fig. 4.25, has been installed at different positions Δx downstream of the burner front plate ($\Delta x = 400$ mm to 950 mm). An orifice is installed at the downstream end of the exhaust duct to attenuate high-amplitude (thermo-) acoustic oscillations.

defined in the field. The asymmetry is thus characterized by an angle α, which defines the location of the maximum temperature spot as shown in the upper right contour plot in Fig. 5.17. As the distribution of the acoustic paths of the measurement setup is highly non-symmetric, the investigation of different asymmetries in terms of α is necessary.

The arrival times which are numerically obtained from such temperature distributions serve as input to the onion peeling algorithm. The resulting reconstructed radial temperature profiles based on $N_g = 25$ rings are depicted in Fig. 5.18a as a function of the angle α. A very strong dependence of the radial temperature profile on the spatial distribution of the asymmetry is observed. For values between $\alpha = 250°$ and $\alpha = 350°$, the resulting temperature profiles reach values that are physically not meaningful at all. The best match with the onion peeling reconstruction based on the experimentally obtained arrival times in Fig. 5.16b is found for an artificial asymmetry with $\alpha \approx 190°$, which can be seen in Fig. 5.18b. Four different reconstructed radial temperature profiles are plotted for different values of α together with the onion peeling reconstruction based on the experimentally obtained arrival times (red stars).

It can clearly be seen that the radial temperature profiles for $\alpha = 169°$ and $\alpha = 191°$ reproduce the experimentally obtained radial temperature profile much better than the profiles obtained for an asymmetry with, e.g., $\alpha = 45°$ or $\alpha = 270°$. The latter exhibit a completely different radial characteristic.

In addition to the reconstructed radial temperature profiles by onion peeling, the radial temperature profile obtained by means of the thermocouples and the angle averaged radial temperature profile of the artificial asymmetric temperature profiles are plotted

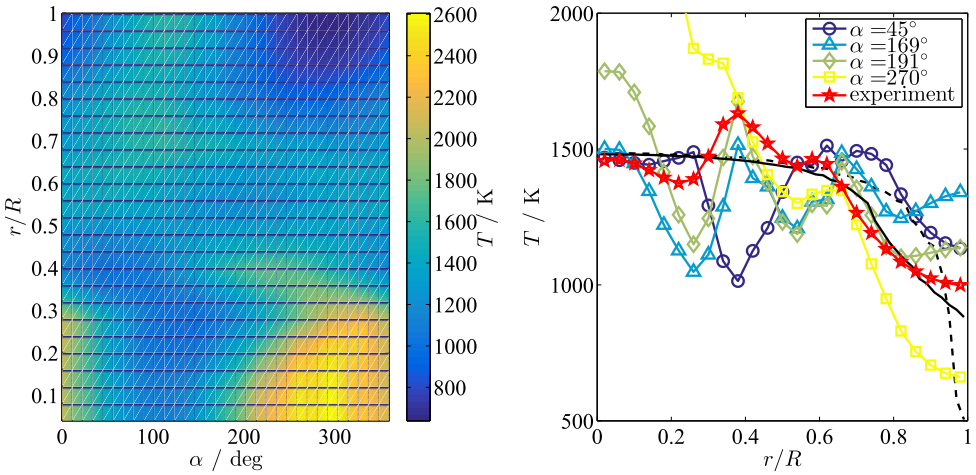

(a) (b)

Figure 5.18: **(a)**: Contour plot of the reconstructed radial temperature distribution as a function of the angle α, which defines the location of the asymmetric temperature maximum in the input temperature field to the onion peeling phantom study according to Fig. 5.17. The onion peeling has been evaluated on $N_g = 25$ rings with an artificial noise level of $\delta\tau = 1$ μs and a regularization parameter of $\gamma = 0.065$. **(b)**: **Markers**: Onion peeling reconstructed radial temperature profiles based on artificial and asymmetric temperature profiles ($\circ$,$\triangle$,$\Diamond$,$\square$) as shown in (a) and onion peeling reconstructed radial temperature profile based on experimentally obtained arrival times ($\star$). The onion peeling is based on $N_g = 25$ discretization rings and a regularization parameter of $\gamma = 0.065$ is applied. **Dashed line**: Temperature profile measured by means of thermocouples (see also Fig. 5.10). **Solid line**: Angle averaged radial temperature profile obtained from the artificial asymmetric temperature profiles as depicted in Fig. 5.17.

in Fig. 5.18b. While the two curves are very similar at the center of the combustor ($r/R < 0.6$), they strongly deviate towards the wall. It is noticeable that the overall match of the angle averaged profile with the onion peeling reconstruction of the experimental data is significantly better compared to the temperature profile obtained via thermocouples.

All this suggests that there is a non-negligible asymmetry in the experimental setup which causes the temperature field to be not rotationally symmetric. This asymmetry in temperature can, however, clearly be identified in terms of the location of the spot of highest temperature. Apparently, this non-symmetric temperature field is qualitatively the same at all measurement days, for all different air mass flows, and for all equivalence ratios.

Although the onion peeling approach might not be an appropriate means to extract the radial temperature distribution due to the asymmetry in the radial temperature field in the measurement plane, its output temperatures can still be of high value for the investigation of entropy waves. There, the cross-sectionally averaged temperature $\tilde{T}$ denotes a crucial measure. The temperatures reconstructed by onion peeling might significantly deviate from the expected radial temperature distribution obtained via thermocouple measurements at most radial positions. However, the deviation in the reconstructed cross-sectionally averaged temperature could be substantially smaller. This is shown in Fig. 5.19a, where the radial temperature profiles obtained by means of traversing a

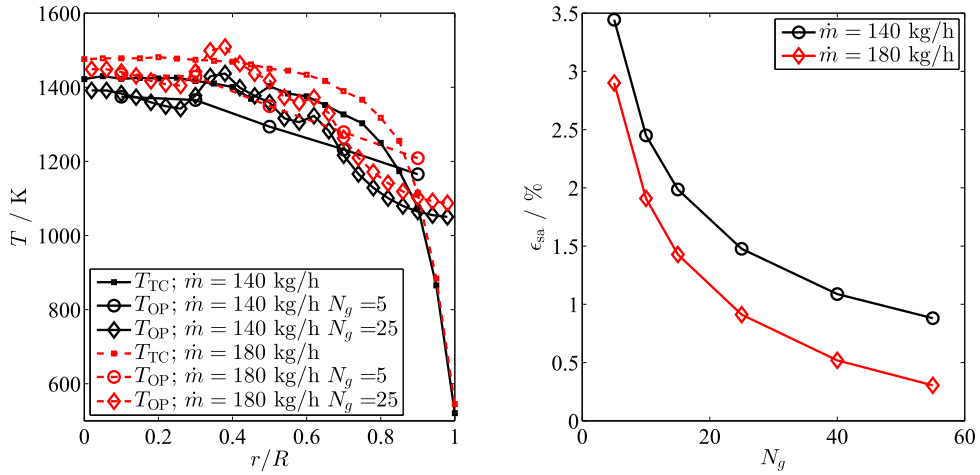

(a) **(b)**

Figure 5.19: (a): Radial temperature profiles obtained from an onion peeling reconstruction of TOF measurements ($\circ$ and $\Diamond$) and measured by means of type-S thermocouple traversing. Both measurement techniques have been conducted at two different air mass flows and at the same axial position of the measurement plane at $\Delta x3$. The onion peeling reconstruction is evaluated based on two different numbers of discretization rings N_g with the rgularization parameter $\gamma = 0.1$, the TOF measurement has been conducted at $N_L = 21$ acoustic paths (because of this, the reconstructed temperature profiles at $\dot{m} = 180\,\mathrm{kg/h}$ look slightly different compared to the ones in Fig. 5.16b). **(b)**: Percentage deviation $\epsilon_{\mathrm{sa}} = (\tilde{T}_{\mathrm{OP}} - \tilde{T}_{\mathrm{TC}})/\tilde{T}_{\mathrm{OP}} \cdot 100$ between the cross-sectionally averaged temperatures obtained by onion peeling and via thermocouple traversing as a function of the number N_g of discretization rings (based on data shown in (a)).

type-S thermocouple at two different mass flows of air are compared to the corresponding onion peeling reconstruction based on TOF measurements that have been conducted under the exact same conditions. A higher temperature is measured in case of a larger air mass flow; this is well reproduced by the onion peeling reconstructed radial temperature profile. Even though the overall shape of the reconstructed radial temperature field looks very different to the one measured via thermocouples, the deviation in the cross-sectionally averaged temperature is fairly small. Figure 5.19b depicts the percentage deviation $\epsilon_{\mathrm{sa}} = (\tilde{T}_{\mathrm{OP}} - \tilde{T}_{\mathrm{TC}})/\tilde{T}_{\mathrm{OP}}$ between the cross-sectionally averaged temperature of the onion peeling reconstruction and the thermocouple's traversing. For a number of discretization rings $N_g > 20$, the deviation is of the order of 1 %, which is adequate for the investigations conducted in this work.

The quantitative assessment of the amplitude of a cross-sectionally averaged temperature fluctuation is essential for the investigation of entropy waves. This means that the temperature difference caused by a certain variation in equivalence ratio in the fuel-air mixture needs to be estimated accurately. The onion peeling reconstructed temperature profile based on steady TOF measurements at three different equivalence ratios $\phi = [0.56, 0.65, 0.81]$ is depicted in Fig. 5.20a. Qualitatively, the shape of the radial temperature profiles remains almost the same for the different equivalence ratios. An increase in equivalence ratio causes merely a shift towards higher temperatures. It can also be seen that the temperature shift in the inner rings, i.e., the inner region of the

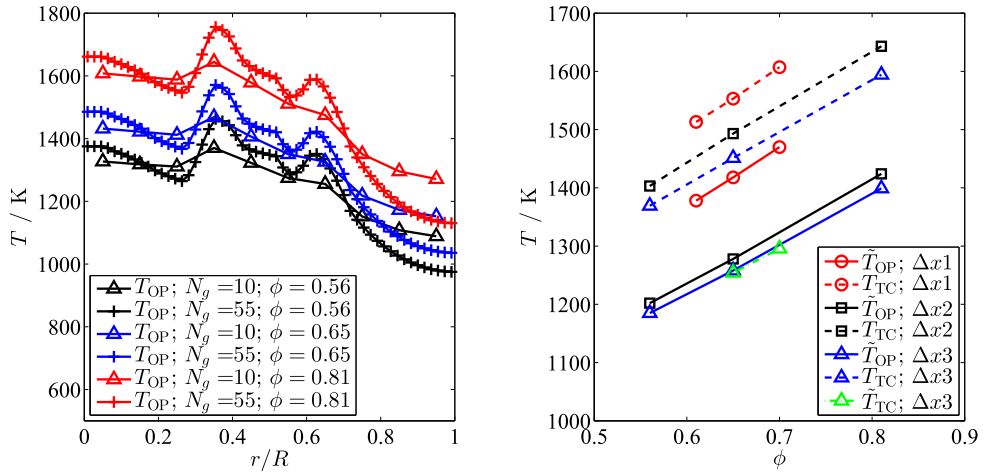

Figure 5.20: **(a)**: Onion peeling reconstructed radial temperature profiles based on TOF measurements at an axial position of $\Delta x3 = 0.7\,\mathrm{m}$ with $N_L = 21$ acoustic paths and at an air mass flow of $\dot{m} = 180\,\mathrm{kg/h}$; $\gamma = 0.1$ is used for the Tikhonov regularization. **(b)**: **Solid lines**: Measured cross-sectionally averaged temperatures based on onion peeling reconstructed radial temperature profiles ($\gamma = 0.1$, $N_g = 55$); **dashed lines**: Type-S thermocouple measurements at $r/R = 0.5$; **dashed-dotted line**: Cross-sectionally averaged temperatures estimated from the thermocouples' traversing; all measurements are conducted with an air mass flow of $\dot{m} = 180\,\mathrm{kg/h}$.

combustor, is significantly larger compared to the most outer rings close to the combustor wall. This is physically meaningful as the temperature close to the wall is strongly dominated by the wall cooling which is the same for all measurements.

It will be shown in Sec. 5.4 that the assessment of an entropy wave essentially relies on a phase-sorted series of steady temperature measures. Thus, in order to accurately reproduce a cross-sectionally averaged temperature amplitude due to equivalence ratio oscillation by onion peeling, the gradient $d\tilde{T}/d\phi$ has to be estimated correctly. The cross-sectionally averaged temperature of radial temperature profiles that are onion peeling reconstructed on $N_g = 55$ rings are plotted in Fig. 5.20b (solid lines). The markers of the solid blue line (△) denote the three cross-sectionally averaged temperatures of the profiles shown in Fig. 5.20a. The other solid lines represent the same parameters based on measurements at different axial locations. The temperatures increase for positions closer to the flame, as expected. The resulting linearly increasing curves are compared to the cross-sectionally averaged temperatures evaluated based on the thermocouple's traversing shown in Fig. 5.10 (the two curves at $\dot{m} = 180\,\mathrm{kg/h}$ therein). As the traversing of the thermocouple has been conducted at $\Delta x3$, the results collapse almost perfectly with the onion peeling reconstructed cross-sectionally averaged temperatures at $\Delta x3$. This is a remarkably good match considering that the overall shape of the radial profiles are quite different. Due to the lack of further data of traversed thermocouple measurements at $\Delta x1$ or $\Delta x2$, the temperatures assessed with a thermocouple at a radial position of $r/R = 0.5$ at $\Delta x1$ and $\Delta x2$ are additionally plotted in Fig. 5.20b. Of course, the temperatures at $r/R = 0.5$ are higher than the cross-sectionally averaged temperatures, but the temperature increase with respect to the equivalence ratio is of the same order.

Table 5.3: Gradients of the curves plotted in Fig. 5.20b; the values are evaluated by linear interpolation and given in units K (and °C).

$\Delta x1$		$\Delta x2$		$\Delta x3$		
$\frac{d\tilde{T}_{\mathrm{OP}}}{d\phi}$	$\frac{dT_{\mathrm{TC}}}{d\phi}$	$\frac{d\tilde{T}_{\mathrm{OP}}}{d\phi}$	$\frac{dT_{\mathrm{TC}}}{d\phi}$	$\frac{d\tilde{T}_{\mathrm{OP}}}{d\phi}$	$\frac{d\tilde{T}_{\mathrm{TC}}}{d\phi}$	$\frac{dT_{\mathrm{TC}}}{d\phi}$
1023	1046	891	957	859	899	826

The corresponding values of the gradients $dT/d\phi$ to the curves depicted in Fig. 5.20b are provided in Tab. 5.3. Even though the evaluation of the gradients is based on a linear interpolation of only three or even two measures of the (cross-sectionally averaged) temperature, the values obtained by means of the onion peeling reconstruction are well aligned with the gradients obtained via thermocouple measurements. For both of these measurement methods, the gradients decrease at positions further downstream of the measurement plane. This decay is due to the wall cooling of the combustor, which has a stronger effect on the higher temperatures that are present at positions closer to the flame.

Summary: Onion peeling applied to steady combustion TOF measurements

In this section it has been shown that the onion peeling approach provides an appropriate measure of the cross-sectionally averaged temperature in the measurement plane. The temperatures are well aligned with reference temperature measures by means of thermocouples. However, regarding the spatial resolution of the onion peeling reconstructed temperature field, it has been found that the experimental setup does not exhibit a rotational symmetric temperature distribution. This is an essential requirement for a one-dimensional method. A phantom study based procedure has been derived that allows for the qualitative characterization of the asymmetric temperature field. The systematic asymmetry does eventually not affect the proper reproduction of the cross-sectionally averaged temperature which is crucial for the investigations of entropy waves.

5.3.4.2 One-dimensional collocation

In parallel to the onion peeling approach described above, the one-dimensional collocation method has been applied to the same TOF measurement data. In the phantom study, where artificial TOF data have been used as input to the tomographic methods, it has been found that the collocation ansatz provides qualitatively similar results compared to the onion peeling (see chapter 3.2). The same applies for experimentally obtained TOF data.

Figure 5.21a depicts radial temperature profiles that are reconstructed from measured TOF data for various numbers N_g of basis functions. The basis functions ϕ_j with $j = 1, ..., N_g$ are evenly distributed in radial direction, so for an identical number N_g, the collocation method provides the same spatial field resolution as the onion peeling approach (this is why the variable N_g can identically be used for both tomographic methods). The similarity of the reconstructed temperature profiles with the profiles gained from the onion peeling as shown in Fig. 5.16b is obvious. The same striking characteristics are observed, which again can be traced back to the asymmetric temperature field.

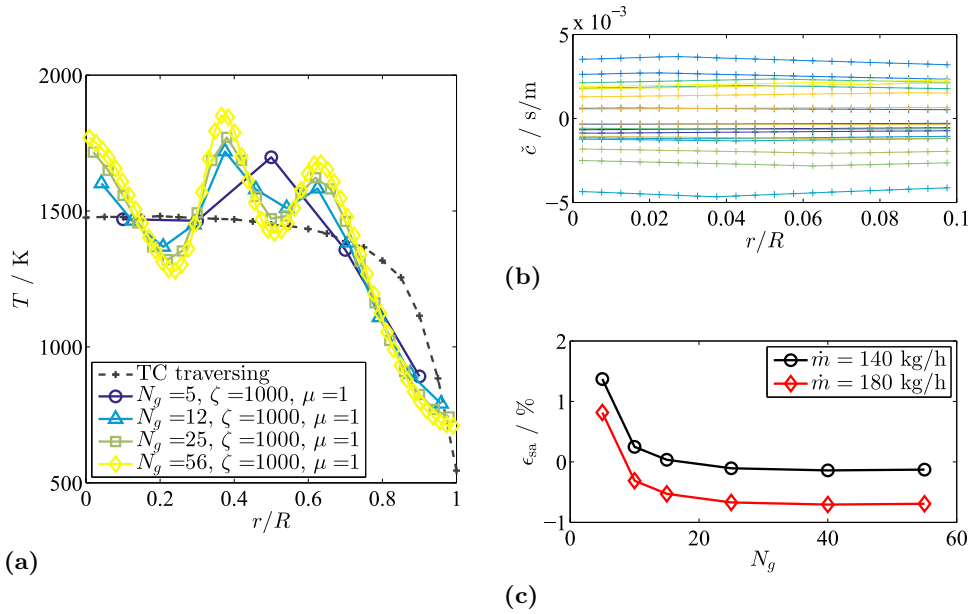

Figure 5.21: **(a)**: Radial temperature profiles reconstructed by means of one-dimensional colloaction based on meaured TOF data for a steady combustion with an equivalence ratio of $\phi = 0.65$ at an axial position $\Delta x3$ and with an air mass flow of $\dot{m} = 180\,\mathrm{kg/h}$; a number of $N_L = 56$ acoustic paths has been employed, the parameter $\zeta = \mu/\gamma = 1000$ with $\mu = 1$ is used. **(b)**: Basis functions in terms of the inverse speed of sound $\check{c}$ which lead to the reconstructed temperature fields as plotted in (a) (here with $N_g = 20$). **(c)**: Deviation between the cross-sectionally averaged temperature obtained from thermocouple traversing measurements and the collocation reconstruction based on measurements at two different mass flows of air.

For the parameter combination $\zeta = 1000$ with $\mu = 1$, the basis functions turn out to be triangularly shaped with linear gradients and a maximum at the location they are defined at. In Sec. 3.2, the parameter ratio $\zeta = \mu/\gamma$ is introduced for simplification of the parameter tuning. For $N_g = 20$, all 20 basis functions are plotted in terms of the inverse speed of sound $\check{c}$ in Fig. 5.21b. The small value of μ causes quite broad basis functions that do not reach the value of zero within the actual temperature field.

The important feature of recovering the cross-sectionally averaged temperature as estimated from the thermocouples' traversing is exhibited by the collocation method in the same way as observed for the onion peeling. The deviation between the cross-sectionally averaged temperature obtained from the thermocouple measurements and the collocation reconstruction is depicted in Fig. 5.21c as function of the number N_g of basis functions. In this case, the deviation is even smaller than observed for the onion peeling approach (see Fig. 5.19b).

It has already been discussed in the phantom study in Sec. 3.2 that the drawback of the one-dimensional collocation compared to the onion peeling is the required adjustment of two parameters. Beside the Tikhonov regularization parameter γ, the exponential factor μ has to be defined. The impact of an increase in μ from μ=1 to μ=10, which causes sharper (i.e. more localized) exponential basis functions, while leaving ζ unchanged is depicted in Fig. 5.22. The radial temperature profiles look qualitatively the same (Fig. 5.22a); the major difference is found in the shape of the basis functions shown

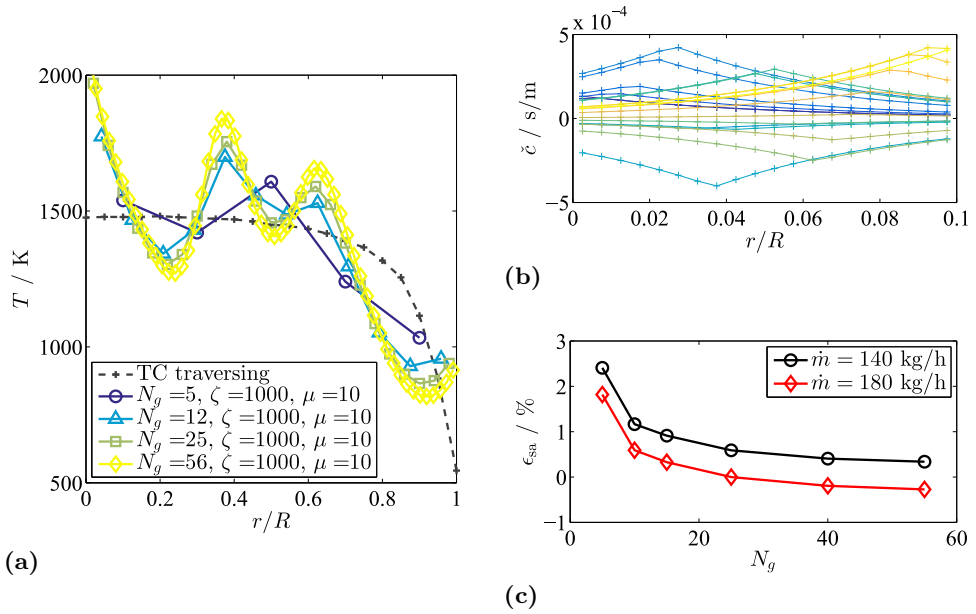

Figure 5.22: This figure provides the same plots as presented in Fig. 5.21 but with different parameters used for the collocation: the exponential factor μ is now increased to $\mu = 10$ (instead of $\mu = 1$ in Fig. 5.21), whereas $\zeta = 1000$ is left unchanged.

in Fig. 5.22b. They still exceed the actual computational domain (not zero within the domain) but are clearly more compact compared to the basis functions in Fig. 5.21b. However, for even higher values of μ the field solution becomes very noisy. The accurate estimate of the cross-sectionally averaged temperature is still achieved with this set of parameters, as can be seen in Fig. 5.22c. A more detailed analysis on the characteristics of the radial temperature profiles is given in Sec. 5.3.4.1. Since the differences between the results obtained by the one-dimensional collocation and by onion peeling are marginal, the findings in Sec. 5.3.4.1 are also valid for the one-dimensional collocation.

Tomography: Error discussion and outlook

The one-dimensional temperature fields obtained from the onion peeling approach and the one-dimensional collocation revealed some shortcomings of the actual experimental setup. Tomographic tools require knowledge of the exact geometrical lengths between acoustic sender and receiver. In this prototype setup, the geometrical uncertainties are relatively high. This may be due to inaccuracies in mounting the microphone holders or due to thermal expansion. However, it is mainly caused by the radial traversing of the electrodes. This had to be done manually which may lead to an uncertainty of about 1 mm. Note that a calibration measurement at ambient temperature with a perfectly homogeneous radial temperature field is not possible as the gap width between the electrodes is too large for such low temperatures, i.e., the breakdown voltage is too high. The gap width is not adjustable in the experimental setup used for tomographic investigations (Fig. 5.15).

An uncertainty that is related to the aforementioned one is the variation of the discharge location. Even though phase averaging is performed, it has been found that even the phase averaged trajectory might vary (see Fig. 4.9b). This uncertainty is as well in the order of 1 mm.

Errors due to non-linear acoustic effects in the close vicinity of the discharge location have been estimated to be smaller than 1 % (see Sec. 4.1.1). However, this estimation is based on acoustic energy measurements that are prone to errors, especially in terms of the electro-acoustic efficiency that has to be assumed. The quantification of an error in arrival time due to non-linear acoustic effects is thus difficult.

All measurement uncertainties that are related to the electric discharge could be eliminated by using an alternative acoustic excitation method. A possible technique, that also fulfills the requirements to withstand high temperatures and pressures, may be a laser induced pressure pulse (Bolaños et al., 2013).

Besides the measurement hardware, the quality in terms of accuracy and spatial resolution of the reconstructed temperature fields depends strongly on the distribution of the acoustic paths. In the case of a combustion test rig, as used in this study, the amount of microphones that can be mounted at the circumference is limited as well as the degree of freedom in terms of the positioning of the microphones and the acoustic source. However, an a priori estimation of an optimal arrangement in the presence of spatial restrictions is given by Twynstra and K. J. Daun (2012).

5.4 Combustion rig – dynamic temperature measurements

In this section, dynamic temperature measurements conducted at the atmospheric combustion rig are presented. The goal of these measurements is the assessment of well-defined entropy fluctuations under conditions that are as close to real gas turbine combustion chambers as possible.

In order to obtain entropy waves at the TOF measurement plane downstream of the combustion chamber, where the first turbine stage would be located in a real gas turbine engine, equivalence ratio fluctuations need to be generated. There are two options to create equivalence ratio oscillations: either the fuel mass flow or the air mass flow can be modulated periodically. As the volume flow of air is far larger than the volume flow of natural gas, the latter could only be realized by acoustic rather than valve excitation. However, the acoustic power required for a generation of an equivalence ratio fluctuation amplitude that is large enough to generate an entropy wave that is still detectable at the TOF measurement plane exceeds the capabilities of the test rig. Furthermore, it has been observed that entropy waves can only be detected at very low frequencies ($< 50\,\mathrm{Hz}$) in the presented combustion rig. This frequency range falls below the capabilities of conventional loudspeakers.

Therefore, the method of choice for the generation of entropy waves has been the modulation of a fraction of the fuel math flow via an automotive natural gas injector valve like it is used in internal combustion engines. The valve is controlled by means of a square wave signal from a signal generator. In parallel, this signal is sent to the data acquisition system and serves as reference signal for the phase averaging of the measurement signals introduced in the following. In the schematic of the full dynamic measurement setup in Fig. 5.23, the valve control unit is marked in grey color, more details about the valve control and its characteristics are provided in Section 5.4.1.

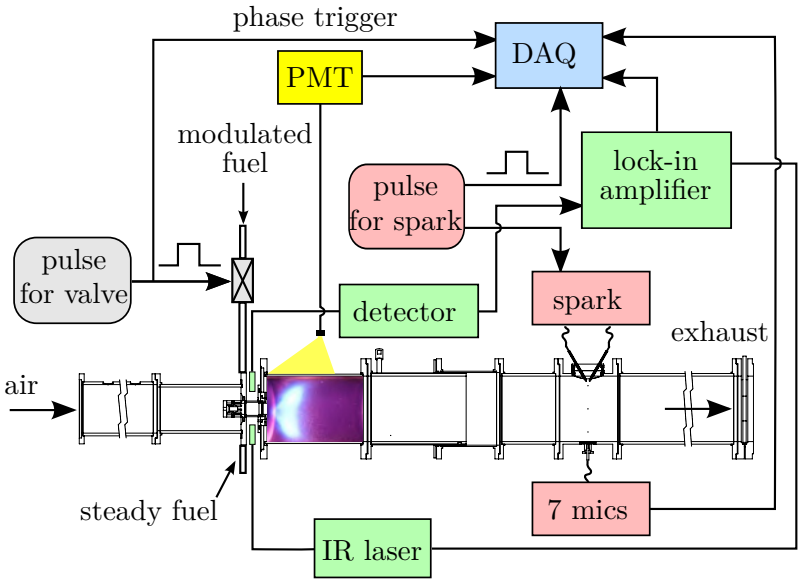

Figure 5.23: Schematic of the dynamic temperature measurement setup at the combustion test rig. The fuel modulation valve generates the equivalence ratio oscillations that lead to entropy fluctuations which can be assessed in the TOF measurement segment. An estimate of the frequency response of the equivalence ratio to the fuel modulation is obtained through measurements of the methane concentration in the quartz-glass mixing tube by means of TDLAS. The response of the flame in terms of the global heat release fluctuation is obtained from OH*-chemiluminescence intensity measurements. All signals are recorded simultaneously in the data acquisition system with an acquisition rate of $f_s = 3\,\mathrm{MHz}$.

The characterization of the equivalence ratio modulation is experimentally investigated by two measurement techniques. The equivalence ratio fluctuation is assessed in the mixing section of the burner by means of a TDLAS measurement, which is depicted in green color in Fig. 5.23. The technique, with all its advantages and disadvantages, and the corresponding results are presented in detail in Section 5.4.1.1. To measure the flame response to these equivalence ratio fluctuations, the OH*-chemiluminescence intensity in the reaction zone, which can be related to the global heat release rate, is assessed by means of a band-pass filtered photomultiplier. The latter is focused on the flame, which is optically accessible by a quartz glass mounted downstream of the burner. More details on the heat release rate fluctuation measurements can be found in Section 5.4.1.2.

Entropy waves obtained from the TOF measurements are finally presented in Section 5.4.2.1 in terms of a zero-dimensional temperature extraction and in Section 5.4.2.2 by applying one-dimensional tomographic reconstruction approaches.

5.4.1 Valve characteristic

To generate equivalence ratio fluctuations which in turn trigger the generation of entropy waves when reaching the combustion zone, a part of the fuel mass flow injected upstream of the swirl generator is modulated. Natural gas is injected through two supply lines into the swirler. Both fuel lines merge in a plenum just upstream of the fuel injector, where the fuel is axially injected into the air flow. A schematic of the air and fuel flows into the

swirl generator and the mixing tube, which connects the swirler with the combustion chamber, is depicted in Fig. 5.24.

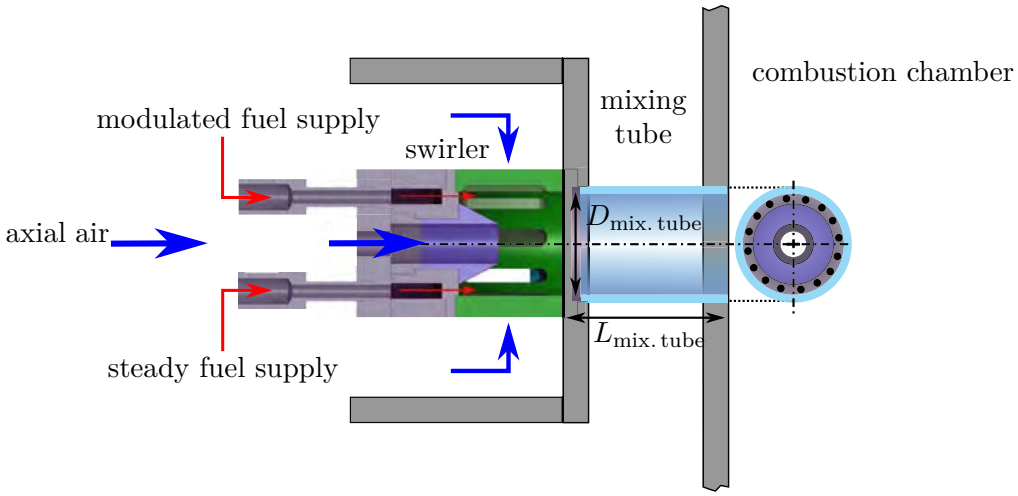

Figure 5.24: Scheme of swirler with steady and pulsed fuel injection lines; the sketch on the very right-hand side depicts the axial view into the mixing tube in upstream direction; $D_{\text{mix. tube}} = 34\,\text{mm}$, $L_{\text{mix. tube}} = 60\,\text{mm}$.

One of the fuel lines is equipped with a valve (Bosch automotive natural gas injection valve), which can operate in either a fully open or fully closed state. The response time between the two states can be neglected for the frequencies relevant in this study ($f_\text{v} < 50$ Hz). To characterize the behaviour of the valve, the equivalence ratio fluctuations in the mixing tube and the OH*-chemiluminescence intensity of the flame in the combustion chamber have been measured for various valve frequencies, duty cycles of the valve control signal, as well as various fractions of the total fuel mass flow that is forced through the modulated fuel supply line.

For an average equivalence ratio $\overline{\phi}_\text{set}$ within one valve cycle of duration $P_\text{valve} = 1/f_\text{v}$, the fuel mass flow reads according to Eq. 2.22:

$$\dot{m}_\text{fuel} = \varsigma \overline{\phi}_\text{set} \dot{m}_\text{air} = \int_0^{P_\text{valve}} \varsigma \phi(t) \dot{m}_\text{air} dt. \tag{5.6}$$

In the following, the split of the total fuel mass flow $\dot{m}_\text{fuel}$ into a steady-state flow $\dot{m}_\text{fuel,s}$ and a modulated flow $\dot{m}_\text{fuel,m}$ will be defined by the ratio $g = \dot{m}_\text{fuel,m}/(\dot{m}_\text{fuel,s} + \dot{m}_\text{fuel,m})$. We further define the duty cycle χ as the ratio between the time the valve is open and the period of one complete cycle: $\chi = t_\text{open}/P_\text{valve}$. Equation 5.6 can therefore be rewritten to

$$\dot{m}_\text{fuel} = \int_0^{\chi P_\text{valve}} \varsigma \phi_\text{max} \dot{m}_\text{air} dt + \int_{\chi P_\text{valve}}^{P_\text{valve}} \varsigma \phi_\text{min} \dot{m}_\text{air} dt, \tag{5.7}$$

where ϕ_max and ϕ_min are the maximum and minimum equivalence ratios that are imposed during the open and closed state of the valve, respectively. When mass conservation is

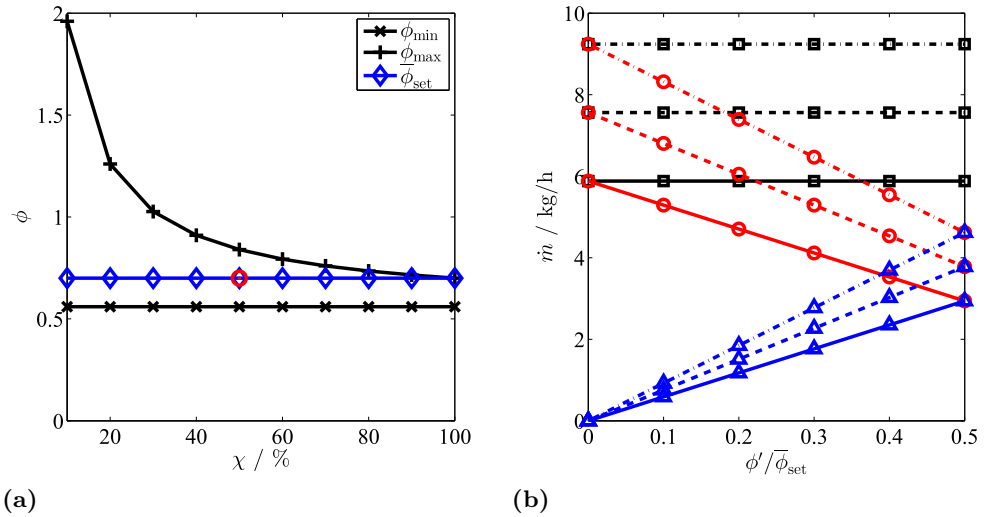

Figure 5.25: **(a)**: Calculated maximum and minimum equivalence ratios and the corresponding average value of one valve period for $g = 20\,\%$ as function of the duty cycle χ; $\overline{\phi}_{set} = 0.7$; $\dot{m}_{air} = 180\,kg/h$. **(b)**: Fuel mass flows $\dot{m}_{fuel}$ (□), $\dot{m}_{fuel,s}$ (○), and $\dot{m}_{fuel,m}$ (△) for three different mass flows of air $\dot{m}_{air}$: 140 kg/h (solid), 180 kg/h (dashed), and 220 kg/h (dashed-dotted); $\overline{\phi}_{set} = 0.7$; natural gas with $\varsigma = 0.06$.

applied to Eq. 5.7, ϕ_{min} and ϕ_{max} result in

$$\phi_{min} = \frac{1}{\varsigma} \frac{(1-g)\,\dot{m}_{fuel}}{\dot{m}_{air}} \tag{5.8}$$

$$\phi_{max} = \frac{1}{\varsigma} \frac{\left(1 + g\left(\frac{1}{\chi} - 1\right)\right)\dot{m}_{fuel}}{\dot{m}_{air}}. \tag{5.9}$$

Consequently, the mean equivalence ratio can be derived as $\overline{\phi}_{set} = (1-\chi)\phi_{min} + \chi\phi_{max}$.

Figure 5.25a depicts calculated values for ϕ_{min}, ϕ_{max}, and $\overline{\phi}_{set}$ for different duty cycles. Only for a duty cycle of $\chi = 50\,\%$, the actual deviation of the equivalence ratio corresponds to the value set by g and the maximum and minimum equivalence ratios have an equal absolute offset from the mean equivalence ratio.

If not specifically mentioned, in the following, a valve control signal with a duty cycle of $\chi = 50\,\%$ is employed. The various fuel mass flows required for creating distinct equivalence ratio fluctuations $\phi'/\overline{\phi}_{set}$ are shown in Fig. 5.25b for a mean equivalence ratio $\overline{\phi}_{set} = 0.7$ and typical air mass flows used in the experiments presented in this study.

5.4.1.1 TDLAS measurement

Tunable Diode Laser Absorption Spectroscopy (TDLAS) has been utilized in this work according to the measurement setup described by Blümner et al. (2016). The goal of the following summary of the methodology is to stress the challenges that have to be addressed when applying such a measurement technique and which potential errors may occur. More detailed and comprehensive explanations can be found in H. Li, Wehe, et al. (2011) and Blümner et al. (2016).

TDLAS is based on the Beer-Lambert law, which correlates the light absorbance of a material, e.g., a gas, to its properties like the concentration of a species, its pressure, temperature, and the thickness of the material sample. The absorbance can be expressed by a frequency dependent transmission coefficient $\Theta(f) = I_t(f)/I_i(f)$, where I_t and I_i are the transmitted and incident light intensities at an optical frequency f. The Beer-Lambert law allows for the following formulation of the transmission coefficient:

$$\Theta(f) = \exp\left(-p\mu_i\psi_f S_l(T)L\right), \tag{5.10}$$

where p denotes the pressure (atm), μ_i denotes the mole fraction of the species in the gas that is absorbing the light, ψ_f denotes the line shape function of the absorption feature, $S_l(T)$ represents the line strength (cm^{-2}) which is a function of the temperature T, and L refers to the absorption length.

The line strength S_l can be looked up in the HITRAN database for various species (Rothman et al., 2013). The line shape function depends on the type of molecular interaction, which in this case mainly depends on the gas pressure p.

To increase the signal-to-noise ratio, wavelength modulation spectroscopy (WMS) is commonly applied instead of direct absorption measurements. The interaction of the sinusoidally modulated wavelength with the non-linear absorption line shape leads to higher harmonics of the modulation frequency in the measured intensity signal, which can be assessed by means of a lock-in amplifier. These higher harmonics are strongly related to the gas properties we are interested in. As the higher harmonics are more sensitive to the line shape curvature rather than to the absolute value of the absorption level, this method is more sensitive compared to direct absorption spectroscopy. As a consequence, the second harmonic signal is normalized by the first harmonic signal, which cancels out non-absorption related signal perturbations. This makes the measurement method very robust in term of vibrations of the optical setup as well as window fouling.

Even though this measurement method is well suited for harsh environments, the main challenge for the implementation at the combustion rig setup used in this study was the narrowness and the unsteady ambient temperature at the mixing tube location. Furthermore, the radial distribution of the air-fuel mixture in the mixing tube is not known and radial temporal inhomogeneities might corrupt the line-of-sight measurement.

In Fig. 5.26a, a simplified scheme of the measurement setup is depicted. Due to the very high air temperature in the vicinity of the burner front plate, the air between the IR laser and the quartz glass mixing tube as well as the air in the gap between mixing tube and detector heats up above ambient air temperature. According to the operating condition of the burner in terms of total air mass flow and mean equivalence ratio, this ambient temperature might vary between different measurements.

Another error source of the equivalence ratio measurement stems from the laser and detector arrangement. Relatively small deviations of the actual laser path from the symmetry line of the cross-sectional surface could lead to noticeable changes of the absorption length, since the laser beam is strongly refracted at the round quartz glass surface.

To account for the latter, a calibration measurement of the measured equivalence ratio has been performed each time before running the actual experiments. The corresponding calibration curves for different measurement days are shown in Fig. 5.26b. These calibration values are obtained from measurements at steady-state fuel-air mixtures of known equivalence ratio. Two aspects are important to note in Fig. 5.26b. In particular for higher equivalence ratios, there are significant deviations between the adjusted and thus expected equivalence ratios and the measured values. Furthermore, the calibration values differ for different measurement days. Differences of almost 0.1 in equivalence ratio are obtained.

As the flame starts to extinguish at about $\phi < 0.5$, the calibration has been conducted in absence of combustion and consequently does not include the temperature effect of the air that surrounds the mixing tube as described above.

It is worth noting that the natural gas used in the measurements is taken from the public gas grid. The measurements presented in this study have been conducted in a time range of two years, the gas composition may have changed significantly between the different measurement campaigns. Information about the exact composition has not been available and thus, an error estimation is difficult. However, it will be shown in Sec. 5.4.2.3 that a good agreement between results of different measurement campaigns is found.

Variation of excitation frequency and amplitude

For the investigations of the temperature response to equivalence ratio fluctuations, it is inherently important to assess the frequency response of the equivalence ratio fluctuations to the fuel excitation valve. This is done in the following by experimentally

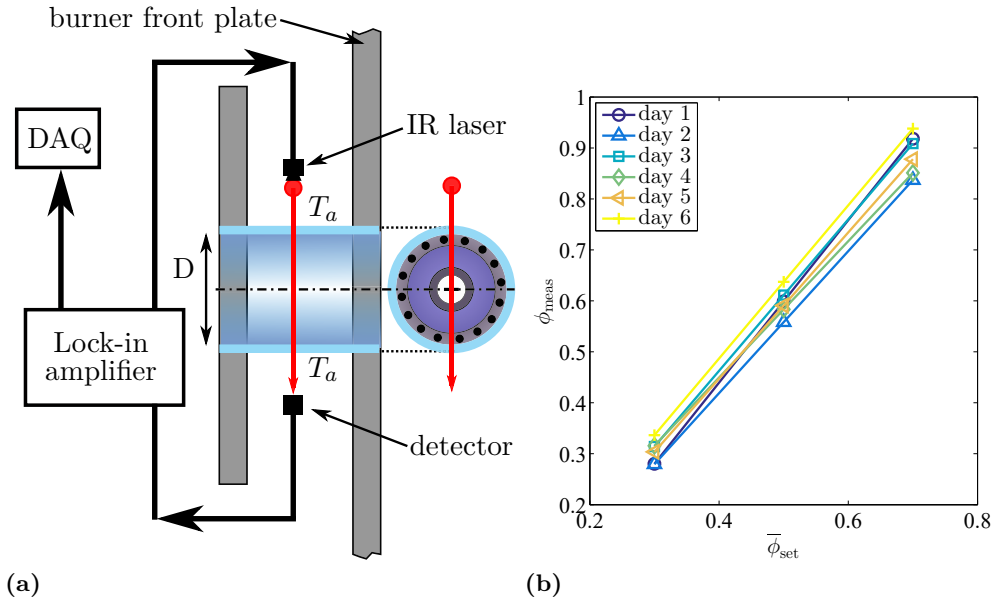

Figure 5.26: **(a)**: Scheme of the TDLAS measurement setup at the quartz glass mixing tube between swirl generator and combustion front plate. **(b)**: Calibration curves of the TDLAS measurement of the equivalence ratio at six different measurement days.

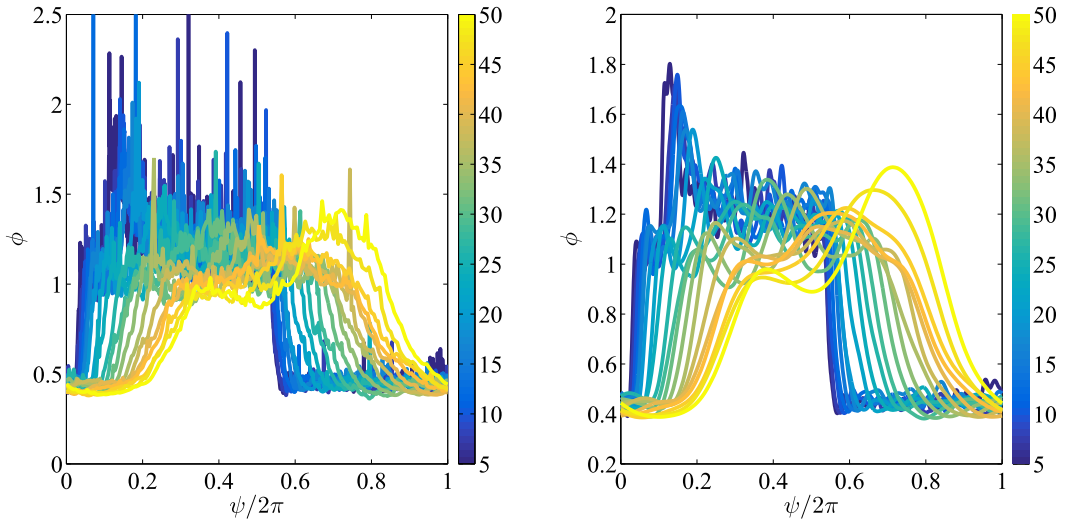

(a) **(b)**

Figure 5.27: **(a)**: Phase averaged TDLAS measurement of the equivalence ratio during one period of the fuel modulation cycle with a duty cycle of $\chi = 50\,\%$, the colors correspond to different fuel modulation frequencies according to the color bar (in Hz); $\overline{\phi}_{\text{set}} = 0.7$; $g = 25\,\%$; $\dot{m}_{\text{air}} = 180\,\text{kg/h}$. **(b)**: Same as (a) but with the signal being low-pass filtered at 300 Hz.

analyzing the equivalence ratio fluctuations obtained for different frequencies f_{v} and excitation amplitudes g.

The TDLAS measurement technique provides a qualitatively good measure of the equivalence ratio in the mixing tube. Even though it has been shown in the previous section that this measurement method is prone to errors regarding exact absolute values, it provides valuable information about the dynamic characteristic of the equivalence ratio fluctuations. In Fig. 5.27, one oscillation period of the phase averaged time signals of the TDLAS measurement are shown without (left) and with (right) application of a low-pass filter. The different lines in the plots correspond to different frequencies of the fuel modulation valve. The high-frequency oscillations contained in the raw phase averaged signal (Fig. 5.28a) comprise equivalence ratio peaks that are unphysically high and can thus be regarded as measurement noise which is efficiently attenuated by applying low-pass filtering at a corner frequency of 300 Hz.

However, some unexpected features are observed that seem to depend on the valve frequency. At very low frequencies, a prominent peak is observed within the first quarter of the fluctuation period. The reason for this short overshoot in equivalence ratio might be found in the extended time period of the valve being closed in case of low frequencies (note, the duty cycle is $\chi = 50\,\%$ for all frequencies). This increases the momentary static pressure in the fuel supply line upstream of the valve and leads to a release of the fuel at higher momentum when opening again.

It can clearly be seen in Fig. 5.27 that the obtained phase averaged values of the equivalence ratios exceed the expected values for a fuel split of $g = 25\,\%$ at a mean equivalence ratio of $\overline{\phi} = 0.7$ by far. While ϕ_{min} is on a reasonable level, the values for ϕ_{max} are in the order of $\phi_{\text{max}} = 1.5$, which most likely does not reflect the actual cross-sectionally

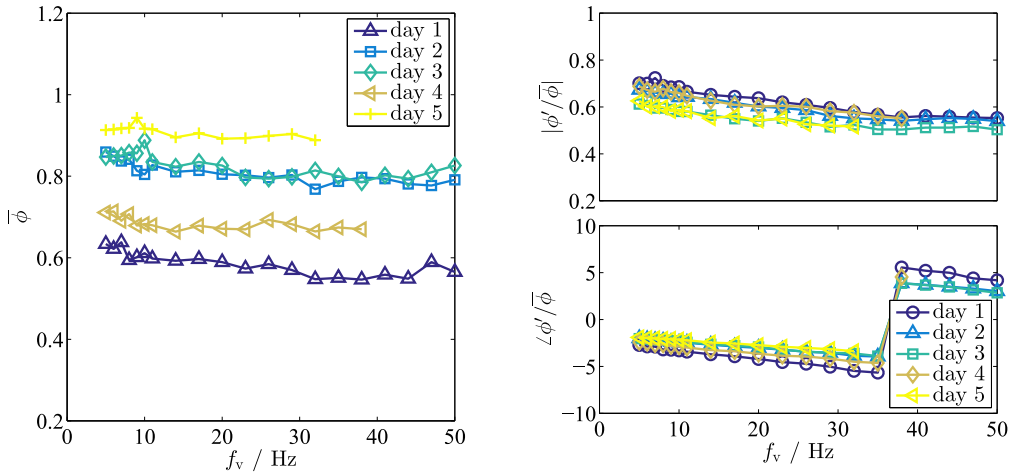

Figure 5.28: **(a)**: Mean values of the phase averaged TDLAS measurement of one period of the fuel modulation cycle with a duty cycles of $\chi = 50\,\%$. The different markers correspond to different measurement days, the relevant parameters are the same for each measurement day: $\overline{\phi}_{\text{set}} = 0.7$; $g = 25\,\%$; $\dot{m}_{\text{air}} = 180$ kg/h. **(b)**: Amplitudes and phases of the measured equivalence ratio fluctuations scaled by the measured mean equivalence ratio (see **(a)**) for five different measurement days.

averaged equivalence ratio in the mixing tube. Figure 5.28a depicts the mean equivalence ratio obtained from phase averaged measurements as plotted in Fig. 5.27 for five different measurement days. Although the same average value $\overline{\phi} = 0.7$ has been preset at each of the measurement days, the values obtained from the TDLAS measurement differ significantly. However, the measured average equivalence ratio at each measurement day reveals an approximately constant level throughout the variation of the modulation frequency.

For the estimation of the equivalence ratio fluctuations' amplitude, a Fourier transform is applied to the phase averaged signals shown in Fig. 5.27. Only the Fourier coefficient that corresponds to the excitation frequency is considered (see also Eq. 5.12). The amplitudes and the associated phases of the equivalence ratio fluctuations for various frequencies are shown in Fig. 5.28b at five measurement days.

As already observed in Fig. 5.27, the absolute values of the amplitudes of the equivalence ratio fluctuations are not in line with the expected value of $\phi'/\overline{\phi} \approx 0.25$ as set by means of the fraction of fuel that is forced through the modulated fuel supply line ($g = 25\,\%$). We assume that this significant deviation stems from a quantitative error of the TDLAS measurement method. However, if the relative amplitude of the equivalence ratio fluctuation is considered, the strong deviations between the measurement days, as observed in Fig. 5.28a, are strongly reduced in Fig. 5.28b. This shows that the qualitative assessment of the equivalence ratio fluctuation is correct, which is as well reflected in the good match of the phases in Fig. 5.28b.

An additional important observation that is made in Fig. 5.28b is the decreasing amplitude response of the equivalence ratio fluctuation for increasing modulation frequencies. This might be due to the short equivalence ratio overshoot directly after the valve opened

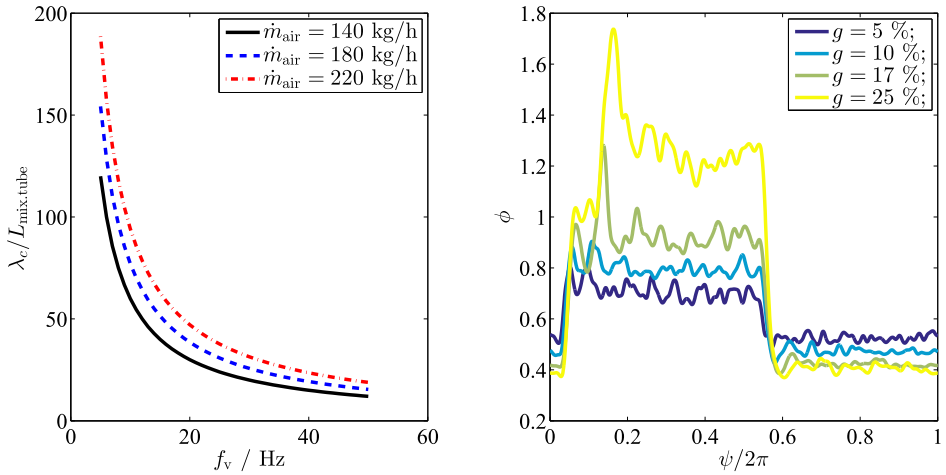

(a) **(b)**

Figure 5.29: (a): Convective wavelength λ_c scaled by the length of the mixing tube $L_{\mathrm{mix.tube}} = 60$ mm for three different air mass flows used in the experiments and for a gas temperature of 293 K. **(b)**: TDLAS measurement of the equivalence ratio fluctuation in the mixing tube at a valve modulation frequency $f_v = 8$ Hz and different amplitudes g; $\overline{\phi}_{\mathrm{set}} = 0.6$; $\dot{m}_{\mathrm{air}} = 180$ kg/h.

(see Fig. 5.27 at low frequencies) rather than due to dissipative effects. The latter would become important if the convective wavelength $\lambda_c = \overline{u}/f_v$ of the equivalence ratio fluctuation in the mixing tube is of the order of the length of the mixing tube $L_{\mathrm{mix.tube}}$. The ratio between the convective wavelength and the length of the mixing tube, which has been evaluated in the relevant frequency range, is depicted in Fig. 5.29a. Obviously, the convective wavelength is one order of magnitude larger compared to the convection length. This is even valid for the lowest air mass flow and the highest modulation frequency used in the measurements in this study.

To further investigate and understand the equivalence ratio response to the fuel modulation, the modulation amplitude g is varied in four steps between $g = 5\,\%$ and $g = 25\,\%$. The phase averaged time traces for a valve frequency of 8 Hz are shown in Fig. 5.29b. In order to quantify the deviation between the measured equivalence ratio and the expected equivalence ratio, the parameter $K_{\mathrm{TDLAS}} = \left(\overline{\phi'(f_v)/\overline{\phi}}\right)/g$ is introduced. Ideally, K_{TDLAS} equals unity, values of $K_{\mathrm{TDLAS}} > 1$ indicate the overestimation of the measured equivalence ratio fluctuation amplitude averaged over all modulation frequencies. Typical values for k_{TDLAS} are in the range between 2 and 3, slight differences have been obtained for different values of g.

In Fig. 5.30a, the relative amplitudes of the equivalence ratio fluctuations and the corresponding phases with respect to the valve oscillation are depicted as functions of the fuel modulation valve frequency f_v. The absolute values are corrected by the factor K_{TDLAS}, so the depicted values provide information about how strong the amplitude deviates from the expected excitation amplitude. The phases of the measurements with different amplitudes match well. For low modulation amplitudes, the amplitudes of the relative equivalence ratio fluctuations exhibit a rather constant level with respect to the modulation frequency. The higher the modulation amplitude, however, the larger becomes the decay of the relative amplitude with increasing modulation frequency. By means of

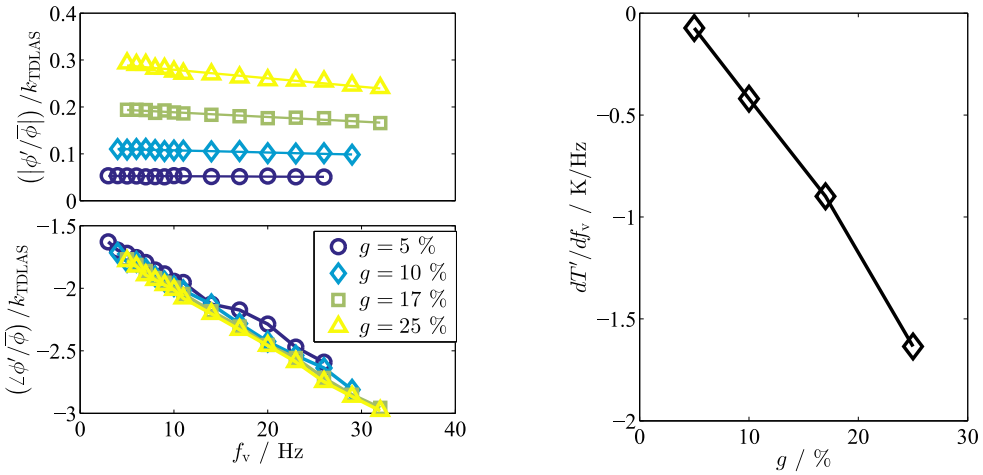

(a) **(b)**

Figure 5.30: **(a)**: Measured relative amplitudes of the equivalence ratio fluctuations corrected by the factor $K_{\mathrm{TDLAS}} = \left(\overline{\phi'(f_{\mathrm{v}})/\overline{\phi}}\right)/g$ to compensate for the overestimation of the adjusted equivalence ratio fluctuation measured by the TDLAS measurement; four different fuel modulation amplitudes g are used. **(b)**: Estimated value of the variation of the temperature fluctuation amplitude with respect to the fuel modulation frequency for different excitation amplitudes g. The values are evaluated based on the measurements in (a) and Fig. 5.12.

linear fits to the curves shown in Fig. 5.30a and by means of the estimated change in temperature with respect to a change in equivalence ratio presented in Fig. 5.12, the decay in temperature amplitude for increasing frequencies can be evaluated for each excitation level g. The results are plotted in Fig. 5.30b.

For a relative modulation amplitude of $g = 25\,\%$, which has typically been applied in this study, the amplitude of the temperature fluctuation which is triggered by the equivalence ratio fluctuation drops with approximately 1.2 K per Hz of fuel modulation frequency.

These results show clearly that the consideration of the frequency response of the equivalence ratio fluctuation is highly important and thus, the experimental assessment of the equivalence ratio fluctuations by means of the TDLAS measurement method is essential for the investigation of entropy waves in this study.

5.4.1.2 OH*-chemiluminescence measurements

The measurements of the fluctuation of the integral OH*-chemiluminescence intensity allows for a qualitative estimate of the integral heat release rate fluctuations in the flame (Lauer, 2011). In order to do so, a photomultiplier has been focused on the flame area, which is located in a quartz tube just downstream of the burner front plate. A sketch of the OH*-chemiluminescence measurement setup together with the TDLAS-technique, which has been introduced above, is shown in the left graph in Fig. 5.31. The OH*-chemiluminescence intensity is measured in photons per unit time and per unit volume. Thus, this intensity is proportional to the rate of heat release per volume the photomultiplier is focused on. This means that a variation of the air mass flow in presence of a constant

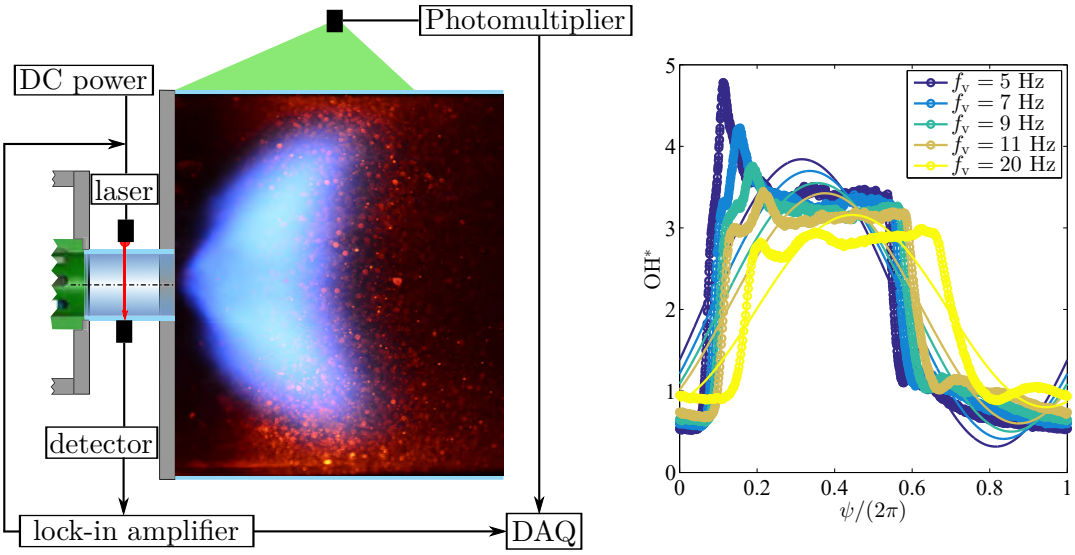

Figure 5.31: (**Left**): Scheme of the OH*-chemiluminescence intensity measurement by means of a photomultiplier together with the TDLAS measurement, which has been applied in parallel. (**Right**): Time trace of the phase averaged OH*-chemiluminescence intensity measurement for different fuel modulation frequencies f_v; the thin lines denote the associated reconstructed signals based on the first Fourier coefficient (see Eq. 5.12).

equivalence ratio or a variation of the equivalence ratio in presence of a constant air mass flow provoke a corresponding variation of the number of photons per unit time.

It is important to note that with the OH*-chemiluminescence intensity measurements presented in this study it is not claimed to provide a quantitative measure of the heat release rate. The results are used to allow for a qualitative insight into the relation between fluctuations of the heat release rate and the associated fluctuations of the equivalence ratio and the temperature, respectively.

Examples of phase averaged OH* intensities over a period of fuel modulation are depicted by the markers on the right-hand side in Fig. 5.31. The only parameter that has been varied between the measurements of the different curves is the fuel modulation frequency. The average equivalence ratio, the excitation amplitude g, and the air mass flow remained constant. The amplitude of the OH* intensity fluctuations drops significantly for increasing frequencies and the characteristic overshoot at the rising edge of the rectangular signal, which has already been observed for the equivalence ratio fluctuation at low frequencies (see Fig. 5.27), is reproduced.

The thin solid lines in the right-hand side plot of Fig. 5.31 depict the Fourier reconstructed OH* intensity oscillation associated with the respective excitation frequency. The amplitudes and the phases of these harmonic approximations are shown in Fig. 5.32a for three different air mass flows with respect to the fuel modulation frequency. Up to a certain frequency, a significant drop of the relative intensity amplitude is observed, whereas the frequency, at which the amplitude starts to rise, is shifted to higher values for increasing air mass flows. This indicates that a time scale exists which strongly affects the OH*-chemiluminescence intensity amplitude. The periodic excitation of the flame by means of the fuel modulation does only work efficiently, if the fuel-air mixture passes the flame zone and burns completely before the subsequent period of fuel modulation is

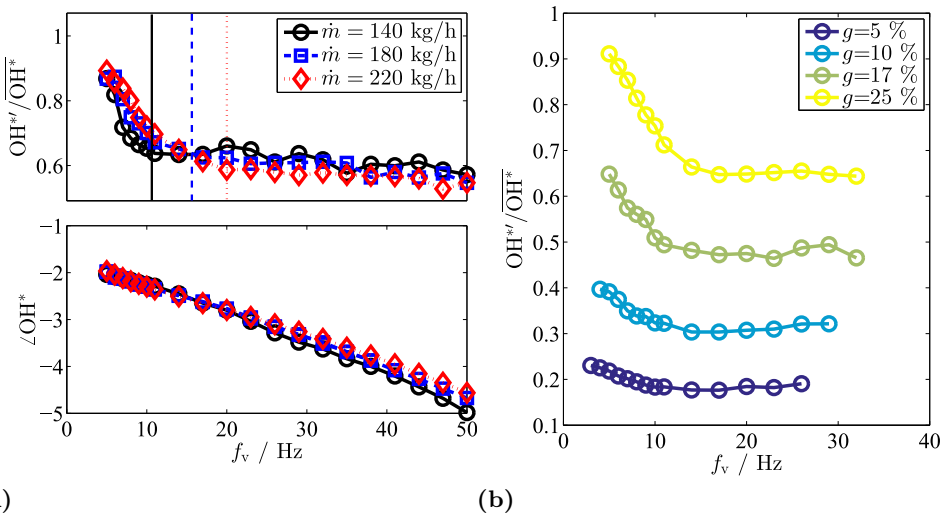

Figure 5.32: **(a)**: Relative amplitude and phase of the OH*-chemiluminescence intensity fluctuation with respect to the fuel modulation frequency f_v for three different air mass flows; the vertical lines indicate the respective corner frequency f_c below which a significant increase of the relative amplitude of the OH*-chemiluminescence intensity fluctuation is observed; $\overline{\phi} = 0.6$; $g = 25$ %. **(b)**: Relative amplitude of the OH*-chemiluminescence intensity fluctuation with respect to the fuel modulation frequency f_v for four different fuel modulation amplitudes; $\overline{\phi} = 0.6$; $\dot{m} = 180$ kg/h.

initiated. This characteristic time is referred to as the average residence time of a gas mixture particle in the flame zone. It is determined by the flow field in the reaction zone and the spatial expansion of the reaction zone. However, this study does not include a CFD analysis of the flow field in the combustor, which would allow for an estimation of the residence time distribution in the flame zone by means of the trajectory of tracers in the flow.

To verify the presumption that the increase of the OH*-chemiluminescence intensity amplitude towards low frequencies is related to the flame zone residence time, a simplified evaluation is performed in the following. If we consider a bulk flow with a velocity u_b in a straight duct, the bulk flow residence time t_b reads $t_b = L_d/u_b = V/\dot{V}$, where L_d denotes the duct's length and V and $\dot{V}$ denote the volume of the duct and the volumetric flow rate, respectively. In case of a simple plug flow, the residence time is a function of the density (and thus of the gas temperature), the reactor volume, and the air mass flow. Due to the recirculation zone in the flame zone, the expected residence time t_e is significantly higher than t_b. From Fig. 5.32a we can extract the corner frequency f_c, below which the OH*-chemiluminescence intensity amplitude increases. The proposed minimum residence time t_e, which is the time required for a flow particle to convect through the flame zone, thus denotes $t_e = 1/f_c$. In Tab. 5.4, the values for the residence times are evaluated for the three mass flows that are shown in Fig. 5.32a. The ratio between the expected residence time and the residence time based on the simple bulk flow consideration is the same for all three mass flows; the residence time of the plug flow is extended by a factor of approximately 2.4 due to the recirculation zone. This is a reasonable magnitude if one considers that a flow particle might be advected in a circular loop by the recirculation flow.

Table 5.4: Expected residence time $t_e = 1/f_c$ based on the corner frequency extracted from Fig. 5.32a and the residence t_b, which is calculated based on the bulk flow velocity for different mass flows of air.

$\dot{m}_{air}$ [kg/h]	u_b [m/s]	f_c [Hz]	t_e [ms]	t_b [ms]	t_e/t_b
140	5.8	12	83	35	2.42
180	7.5	15	67	27	2.48
220	9.1	19	53	22	2.40

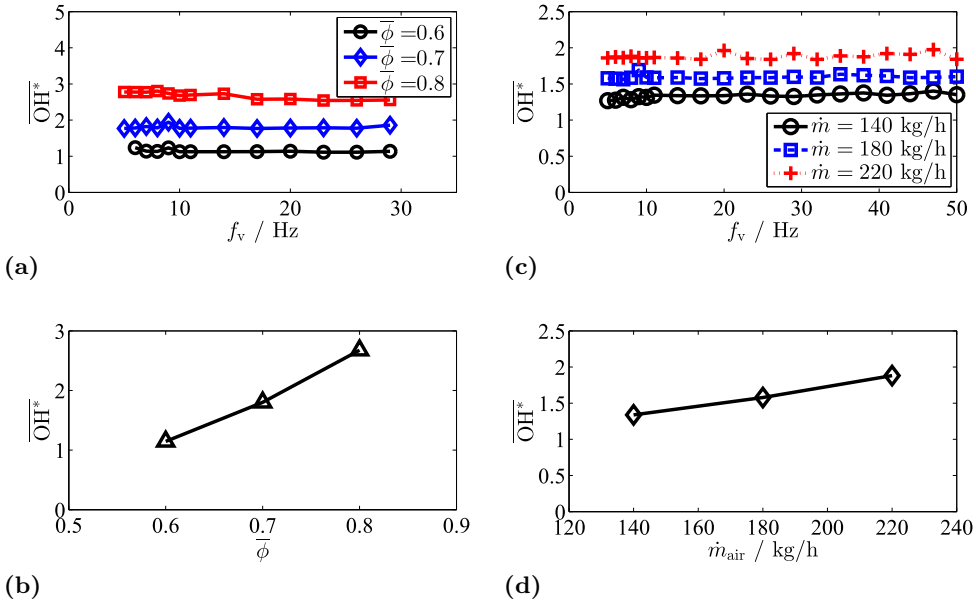

Figure 5.33: **(a)**: Mean OH*-chemiluminescence intensity over a phase averaged period of fuel modulation as function of the fuel modulation frequency and for different values of the mean equivalence ratio; $\dot{m} = 180\,\mathrm{kg/h}$; $g = 25\,\%$. **(b)**: Average value over all frequencies of the mean OH*-chemiluminescence intensities depicted in (a). **(c)**: Mean OH*-chemiluminescence intensity over a phase averaged period of fuel modulation as function of the fuel modulation frequency and for different air mass flows; $\bar{\phi} = 0.6$; $g = 25\,\%$. **(d)**: Average value over all frequencies of the mean OH*-chemiluminescence intensities depicted in (c).

By variation of the gas temperature, which is also a guess based on the adiabatic flame temperature (here we chose $T = 1600\,\mathrm{K}$), or by variation of the length of the flame zone, which has been optically estimated by the flame length to $L_f = 0.2\,\mathrm{m}$, the values of the residence times are also altered. However, this does not affect that the corner frequency scales well with the bulk flow velocity and, thus, with the average residence time in the flame zone. In Fig. 5.32b, the relative amplitude of the measured OH*-chemiluminescence fluctuation is plotted for four different values of the fuel modulation amplitude g at one constant air mass flow. The corner frequency remains approximately the same, which shows that the significant increase of the OH*-chemiluminescence intensity amplitude is not caused by an extinction and reignition process. In fact, for $g = 25\,\%$, which is the standard excitation amplitude in this study, a short extinction of the flame and its immediate reignition can optically be detected for low frequencies ($\lesssim 8\,\mathrm{Hz}$). For fuel modulation amplitudes of $g \leq 10\,\%$, however, the minimum equivalence ratio within one modulation period is still high enough to ensure a continuous combustion process.

In the present analysis of the frequency dependence of the relative OH*-chemilumines-

cence intensity amplitude, it is of course important that the average OH*-chemiluminescence intensity over one period of fuel modulation remains constant within the frequency band considered in this study. By means of measurements of the mean OH*-chemiluminescence intensity over one period of fuel modulation, Figs. 5.33a and 5.33c show that this is the case, for different average equivalence ratios as well as for different air mass flows. The slight deviations of the mean OH*-chemiluminescence intensity with respect to the modulation frequencies are within the measurement accuracy. The corresponding mean values over all frequencies are depicted in the respective bottom graphs (Figs. 5.33b and 5.33d). The mean OH*-chemiluminescence intensity depends nearly linearly on the mean equivalence ratio as well as on the air mass flow. This is an expected result, as the total heat release rate has to rise for an increased fuel mass flow, which is the case for an increase of the mean equivalence ratio $\overline{\phi}$ as well as for an increase of the air mass flow at a constant equivalence ratio.

The results of these OH*-chemiluminescence intensity measurements will be utilized in Chapter 6, as they provide helpful information on the reactor residence times. This information serves as input for the reactor model and thus supports the modeling of the generation mechanisms of entropy waves that are measured further downstream in the combustor. Additionally, the OH*-chemiluminescence fluctuations can be used as trigger signal for the phase averaging of the flight time measurements. In this study, where the entropy fluctuations have artificially been generated by fuel modulation, the valve control signal has been utilized as phase reference. In the case of a natural combustion instability, whose frequency is unknown, the OH*-chemiluminescence could serve as reliable reference.

5.4.2 TOF measurements

The dynamic TOF-based temperature measurements are based on phase sorted steady-state temperature measurements as they have been discussed in Sec. 5.3. This means that for a particular phase angle of the entropy oscillation, flight time measurements have to be averaged over a sufficiently high number of acoustic excitation events.

The duration of the measurements depends on the number of spark events N_s that are required for the signal averaging and thus also on the excitation frequency f_v. Furthermore, it strongly depends on the frequency f_spark the acoustic signal is generated with. The latter has to be selected such that it sweeps through distinct phase angles of the valve oscillation period. The maximum excitation frequency is given by the hardware of the spark generation, e.g., the MOSFET (see also Sec. 4.1). Therefore, the following formula is derived:

$$f_\mathrm{spark} = f_\mathrm{v} \frac{N_\psi}{k}. \tag{5.11}$$

The parameter $N_\psi \in \mathbb{P}$ denotes the number of phase angles a period of valve oscillation should be resolved with and $k \in \mathbb{N} \setminus 0$ has to be chosen such that f_spark does not exceed its allowed maximum. To avoid an irregular and inefficient phase sweep, it is required that N_ψ is a prime number. Throughout all measurements conducted in this study, $N_\psi = 31$ has been applied as it provides the best balance between a sufficient temporal resolution of the entropy fluctuation period, so that the amplitude and the phase can be properly extracted, and a reasonable measurement duration. The latter can be evaluated

as $T_{\mathrm{meas}} = N_s / f_{\mathrm{spark}}$, the total number of spark events per measurement consequently writes $N_{\mathrm{spark}} = T_{\mathrm{meas}} / f_{\mathrm{spark}}$.

Due to the high sampling frequency of $f_s = 3\,\mathrm{MHz}$ and the large number of spark events per phase angle N_s, only short time periods around the arrivals of the acoustic pulse signals and the preceding electromagnetic disturbance signals are acquired. Otherwise, the storage requirements would be unreasonably high. The trigger for the acquisition is provided by the rectangular pulse signal that is sent to the MOSFET driver, which finally induces the spark discharge (see also Section 4). Each acoustic pulse signal can then be allocated to a phase angle by means of a sawtooth signal which is in-phase with the valve control signal.

Determination of Amplitude and Phase The most relevant parameters for the characterization of the entropy (or temperature) fluctuations are the amplitude and the phase. By assuming harmonic oscillations, they are evaluated by means of a discrete Fourier transform. The transform is applied to the single period oscillation obtained from the zero-dimensional or one-dimensional reconstruction. The analytic expression T_{analytic} is a complex number, which comprises the amplitude $|T|$ as well as the phase $\angle T$ of the temperature fluctuation, and is obtained from the reconstructed temperature vector T_{rec} as:

$$T_{\mathrm{analytic}} = \frac{2}{N_\psi} \sum_{k=1}^{N_\psi} T_{\mathrm{rec}}(k) e^{-2\pi i \frac{k-1}{N_\psi}} . \tag{5.12}$$

In the subsequent sections, the fluctuation amplitude $|T_{\mathrm{analytic}}|$ will be defined as the zero ($\hat{=}\overline{T}$) to peak temperature difference and it will be denoted as $|T_{\mathrm{analytic}}| = T'$. With the formulation in Eq. 5.12 only the response to the valve excitation frequency is taken into account, higher frequency content is not considered. The amplitudes of the equivalence ratio fluctuations and of the OH*-chemiluminescence measurements are evaluated in the same way and are as well denoted as ϕ' and OH$^{*\prime}$, respectively.

Note that in the following two chapters, where the actual reconstruction of entropy waves from TOF measurements is presented, we will in a first step mainly focus on temperature fluctuations rather than entropy fluctuations. This is because of two reasons: Firstly, the quantity temperature is more intuitive and tangible for the reader, absolute values or deviations could more easily be rated. The second reason is the approximately linear dependence between temperature and entropy, which makes qualitative findings in advecting temperature fluctuations directly applicable to entropy waves (see Eq. 2.21).

5.4.2.1 Zero-dimensional dynamic temperature measurements

The zero-dimensional temperature reconstruction is based on TOF measurements that have been performed with the measurement setup presented in Fig. 4.23. There, the electrodes' tips are located close to the inner combustor wall. The phantom study in Sec. 3.1 revealed that this setup provides a favourable arrangement of the acoustic paths in terms of an accurate reconstruction of the cross-sectionally averaged temperature in the measurement plane. A sketch of the measurement setup is depicted in Fig. 5.34a. Changes in equivalence ratio, air mass flow, or of the axial location of the measurement plane might cause a variation in gas temperature at the electrodes' tips. Therefore, the

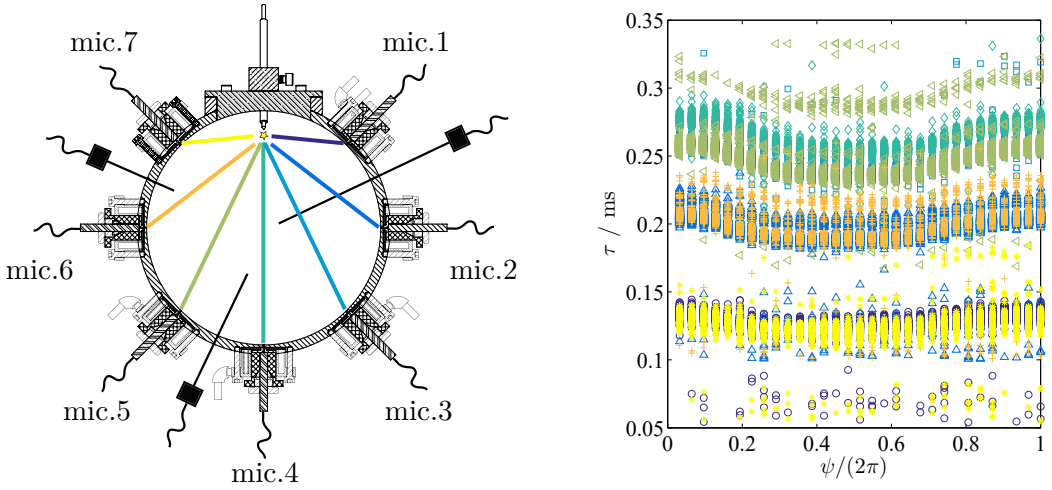

(a) **(b)**

Figure 5.34: **(a)**: Arrangement of the acoustic paths for the zero-dimensional temperature extraction; view in downstream direction. **(b)**: Example of phase sorted arrival times of the seven microphones obtained for a fuel modulation frequency $f_v = 5\,\mathrm{Hz}$, the colors correspond to the line colors in (a); about $N_s = 200$ spark events are performed at each of the $N_\psi = 31$ phase angles; here: $\overline{\phi} = 0.6$, $g = 25\,\%$, $\Delta x1$, $\dot{m} = 180\,\mathrm{kg/h}$.

gap width between the tips, and with it the penetration depth of the spark location, had to be slightly readjusted for different parameter settings applied to the measurements.

A typical result of a fuel modulated TOF measurement is shown in Fig. 5.34b. Spark discharges are generated with a frequency of about 60 Hz to 90 Hz according to Eq. 5.11 until approximately $N_s = 200$ flight times are acquired for each of the $N_\psi = 31$ phase angles. The colors of the flight times in Fig. 5.34b correspond to the acoustic paths depicted in Fig. 5.34a. The values of the arrival times of the different microphones are roughly aligned with the acoustic path lengths, i.e., for example the measured flight time of microphones 1 and 2 are smaller than in case of microphone 4. The variation of the flight times with respect to the phase angle is clearly visible, as well as the deviations between the microphone pairs that should ideally, so for a perfectly symmetric experimental setup and a perfectly axisymmetric radial temperature field, exhibit the same absolute flight times. Both, slight asymmetries in the electrodes-microphone arrangement as well as a marginal decentered radial temperature field, might be the reasons for the observed deviations.

The flight time measurement presented in Fig. 5.34b represent rather a worst case scenario in terms of the scattering of the arrival times. This is because the measurement has been performed at the axial position $\Delta x1$, which is the one closest to the flame (see Tab. 5.1), and with the lowest possible fuel modulation frequency $f_v = 5\,\mathrm{Hz}$. Consequently, the temperature amplitudes measured with these parameter settings are the highest considered in this study.

Figure 5.34b reveals a significant scattering of the arrival times at each phase angle. Besides the clear outliers, which are most probably due to failures of the extrema seeking in the microphones' time signals, a much narrower and rather normally distributed

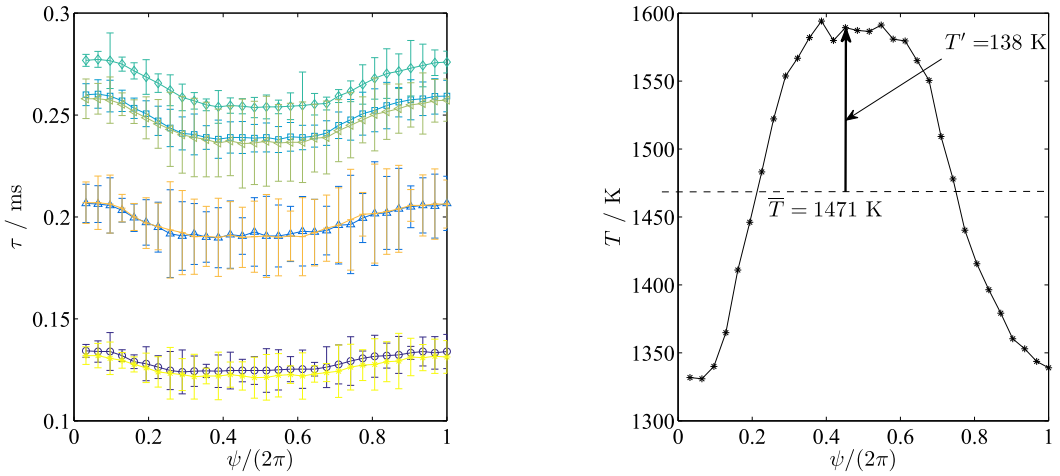

(a) **(b)**

Figure 5.35: **(a)**: Median of the TOF measurements depicted in Fig. 5.34b; the error bars depict the standard deviations obtained for each phase angle. **(b)**: Reconstructed temperature as function of the fuel modulation phase angle based on the flight times depicted in Fig. 5.34b; the temperature used to define the reference speed of sound in Eq. 2.103 has been obtained by a thermocouple at the radial position $r/R = 0.5$ and denotes in this case $T_{\mathrm{ref,SVD}} = 1471\,\mathrm{K}$; here, a fluctuation amplitude of $T' = 138\,\mathrm{K}$ is obtained by means of Eq. 5.12.

scattering is observed around distinct values. Thanks to the sufficiently large number of spark events to average over, the median value provides an appropriate estimate of the effective arrival time at each phase angle ψ. A quantification of the scattering is evaluated by means of the standard deviation (see Eq. 4.10). The medians along with their associated standard deviations expressed as error bars are plotted in Fig. 5.35a for the TOF data shown in Fig. 5.34b. The differences in standard deviation between the microphones are due to the specific assembly situations or might also be related to the different aging of the microphones' membranes. In case of very large temperature fluctuations, it can also be observed that the scattering of the arrival times becomes a function of the phase angle. This is because the gap between the electrodes' tips might not be favourable for all gas temperatures present within one oscillation cycle.

Another feature, that is sometimes observed in the measurements and that has been pointed out in Sec. 4.1.2, is the incidence of a weak accumulation of arrival times at distinct values with a slight offset to the median value. This might be due to the phenomenon discussed in Sec. 4.1.2, where the discharges might occur on a second trajectory beside its most favourable trajectory (e.g., the row of flight times of microphone 6 few microseconds later than the major ones in Fig. 5.34b). It could, however, also be caused by ambiguities in the maxima seeking of the arrival time in the microphones' time traces (the second peak might be detected rather than the first one), which seems to be the case for microphone 5, where a row of flight times is obtained at around $\tau = 0.3\,\mathrm{ms}$. In such cases, where the flight time assessment is corrupted by all these sources of errors, the large number of data points at each phase angle is essential to obtain reliable flight time measures.

We now apply the zero-dimensional temperature reconstruction method on the medians

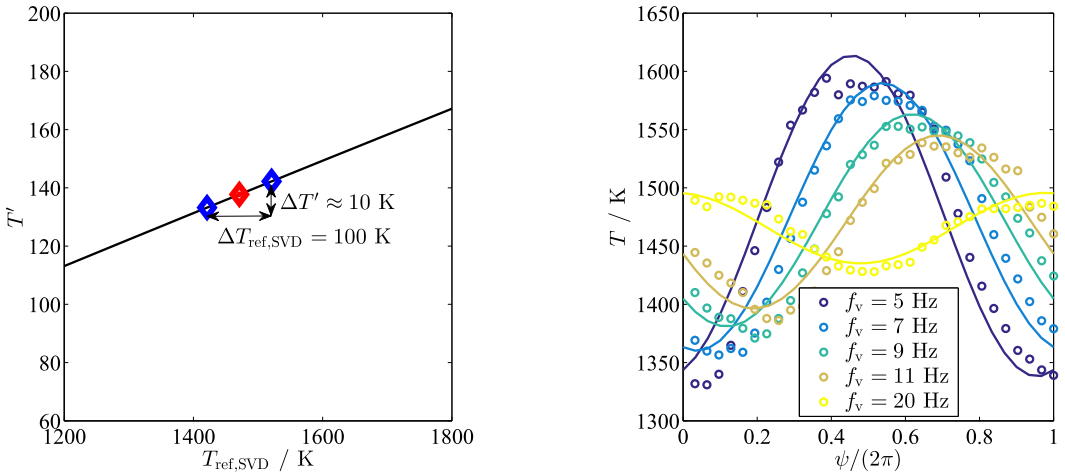

(a) **(b)**

Figure 5.36: **(a)**: SVD-reconstructed temperature amplitudes as function of the reference temperature $T_{\mathrm{ref,SVD}}$, which is used to define the reference speed of sound in Eq. 2.103. The reference temperature at the red diamond marker corresponds to the temperature $T_{\mathrm{ref,SVD}} \approx 1470$ used to obtain the temperature reconstruction shown in Fig. 5.35b and has been obtained from a thermocouple at the radial position $r/R = 0.5$; the blue marker refer to temperature amplitudes that would be obtained for a deviation of $T_{\mathrm{ref,SVD}}$ of $\pm 50\,\mathrm{K}$. **(b)**: SVD-reconstructed temperatures as function of the fuel modulation phase angle ψ (markers) and the corresponding waveform reconstruction by means of the first Fourier coefficient obtained from Eq. 5.12 (solid lines); the reference temperature $T_{\mathrm{ref,SVD}}$ is the same for all reconstructions.

of the flight times depicted in Fig. 5.35a. The mean temperature acquired by a type-S thermocouple at a radial position of $r/R = 0.5$ serves as reference temperature measure which is required for the evaluation of the temperature fluctuation (see Eq. 2.104). The resulting temperature fluctuation is depicted in Fig. 5.35b. According to Eq. 5.12, the temperature amplitude yields $T' = 142\,\mathrm{K}$. Here, it is important to note that the amplitude of the SVD reconstructed temperature fluctuation depends linearly on the reference temperature that is derived in Eq. 2.104. The straight line in Fig. 5.36a depicts the reconstructed temperature amplitudes as function of the reference temperature $T_{\mathrm{ref,SVD}}$ that is used to define the reference speed of sound in Eq. 2.103. The red diamond denotes the reference temperature and the corresponding amplitude that has been applied to obtain the reconstructed temperature shown in Fig. 5.35b. This reference temperature has been acquired by a thermocouple, which is prone to errors (see Section. 5.3.3) and which provides a temperature in only one point within the measurement plane. It is not trivial to determine, which temperature measure might be the most appropriate one. In this study, the temperature obtained from the thermocouple at $r/R = 0.5$ has been chosen. However, if we assume an uncertainty of $\pm 50\,\mathrm{K}$ for the measurement or for the definition of $T_{\mathrm{ref,SVD}}$, the maximum difference is smaller than 10 K. This corresponds to maximum 7 % of the temperature amplitude estimation (see Fig. 5.36a).

To characterize the transport mechanisms of entropy waves, the variation of the following three parameters is of main interest: the modulation frequency f_{v}, the axial measurement position Δx, and the bulk flow velocity $\overline{u}$. We first look at a variation of the excitation

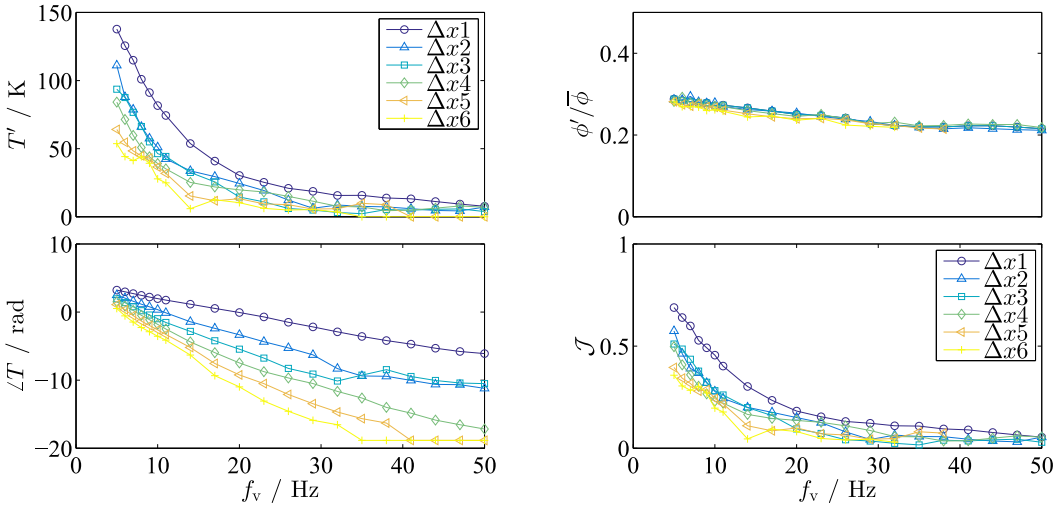

(a) **(b)**

Figure 5.37: **(a)**: Amplitude (top) and phase (bottom) of the SVD reconstructed temperature fluctuations as function of the fuel modulation frequency and for the 6 different axial positions used in this study; the reference temperature $T_{\mathrm{ref,SVD}}$ is selected according to the thermocouple measurements at each individual measurement point. **(b)**: **Top**: Relative amplitudes of the equivalence ratio measured by the TDLAS measurements; the measurements have been corrected for measurement errors such that the average value of $\phi'/\overline{\phi}$ meets the adjusted fuel modulation amplitude of $g = 25\,\%$. **Bottom**: Measured ratio between temperature amplitude and equivalence ratio amplitude divided by the ratio $\mathrm{d}T/\mathrm{d}\phi$ obtained from the static temperature measurements (see Sec. 5.3.2).

frequency f_{v}. In Fig. 5.36b, the reconstructed temperature fluctuations of measurements at the same axial location and with the same bulk flow velocity but different modulation frequencies are depicted (markers). The shape of the $f_{\mathrm{v}} = 5\,\mathrm{Hz}$ oscillations is conserved for the higher frequencies, but the amplitude as well as the phase with respect to the modulation signal clearly changes.

The solid lines in Fig. 5.36b denote the harmonic approximations of the temperature oscillations by means of the first Fourier coefficient (see Eq. 5.12). The sinusoidal curves fit well to the experimentally reconstructed temperatures; consequently, the amplitude and phase values provided by the Fourier transform could be referred to as the correct wave characteristics of the temperature fluctuation. If we consider a constant amplitude of the equivalence ratio fluctuation for the different valve frequencies applied in Fig. 5.36b, the decrease in temperature amplitude is merely caused by an increase of dissipation due to a reduction of the convective wavelength $\lambda_{\mathrm{c}} = u/f_{\mathrm{v}}$. The bulk flow velocity is a function of the air mass flow and the temperature only, both of these parameters are not altered for different modulation frequencies.

The amplitudes and phases for various frequencies as well as for the different axial measurement positions introduced in Tab. 5.1 are plotted in Fig. 5.37a. Beside the strong decay of the temperature amplitudes for increasing frequencies, the temperature amplitudes are also damped for axial positions further downstream with respect to the burner front plate. The corresponding phase decays are, as expected, linear with respect

to the modulation frequency and the negative slope becomes larger for increasing axial distances between flame and measurement plane.

A more detailed discussion of the phase decay with respect to the frequency and with respect to the axial measurement location will be given in the subsequent Chapter 6. There, also the phase measure will be analyzed in order to quantify the convective bulk flow velocity, which is an essential parameter for the modeling of the propagation of entropy waves.

To verify the plausibility of the temperature amplitudes that are reconstructed with the SVD-method, we scale the temperature amplitudes T' with the amplitudes of the equivalence ratio fluctuations ϕ'. In the upper plot of Fig. 5.37b, the relative equivalence ratio fluctuations measured via the TDLAS method are plotted for the same measurements as shown in Fig. 5.37a. The TDLAS measurements have been conducted in parallel to the TOF measurements. The relative equivalence ratio fluctuations, as they are depicted in Fig. 5.37b, have been corrected such that their frequency averaged value corresponds to the value adjusted by the fuel split (here: $g = 25\,\%$). This is because of measurement uncertainties which are discussed in more detail in Sec. 5.4.1.1. We then compare the ratio T'/ϕ' to the ratio of a change in temperature due to a change in equivalence ratio $\mathrm{d}T/\mathrm{d}\phi$ that has been assessed by means of thermocouple measurements under steady temperature conditions in Sec. 5.3.2. For a theoretical modulation frequency of $f_\mathrm{v} = 0\,\mathrm{Hz}$, the ratio between the measured temperature and the measured equivalence ratio should equal the ratio obtained in the steady combustion measurements:

$$\mathcal{J} := \frac{\left(\frac{T'}{\phi'}\right)_{\text{measured}}}{\left(\frac{\mathrm{d}T}{\mathrm{d}\phi}\right)_{\text{steady}}} = 1 \quad \text{for} \quad f_\mathrm{v} \to 0. \tag{5.13}$$

In the bottom plot of Fig. 5.37b, $\mathcal{J}$ is plotted for the same measurements as shown in Fig. 5.37a. It is obvious that an extrapolation of the rising values of $\mathcal{J}$ with decreasing fuel modulation frequencies would end up at approximately unity. This would by far not be reached without the aforementioned correction of the equivalence ratio measurements and thus shows, that this is a reasonable action.

In terms of entropy fluctuations, we use the correlation for the specific entropy in Eq. 2.21 to convert temperature fluctuations into entropy fluctuations. The mean temperature $\overline{T}$ is defined by type-S thermocouple measurements. In Fig. 5.38a, the amplitudes of the specific entropy fluctuations are plotted as function of the fuel modulation frequency. This graph is basically equal to the upper plot in Fig. 5.37a but with the temperature amplitudes multiplied by $c_p/\overline{T}$. Note that the temperature dependence of the specific heat capacity c_p is considered in this analysis. Hence, the scaling factor also becomes a function of the axial measurement location, as the average temperature decreases for axial positions further downstream of the flame.

For a non-dimensional representation of the entropy fluctuation, analog to the definition of $\mathcal{J}$, we define the static change of the specific entropy Δs_static as

$$\Delta s_\text{static} = \frac{c_p}{\overline{T}} \left(\frac{\mathrm{d}T}{\mathrm{d}\phi}\right)_\text{static} \phi'. \tag{5.14}$$

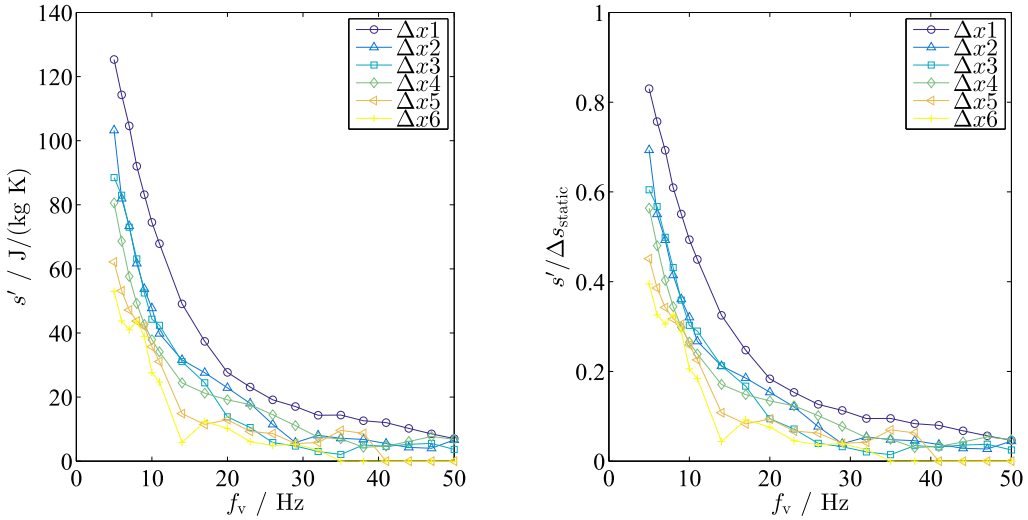

(a) **(b)**

Figure 5.38: **(a)**: Amplitudes of the specific entropy fluctuations as function of the fuel modulation frequency measured at different axial positions of the TOF measurement segment; $\dot{m} = 180\,\mathrm{kg/h}$, $\overline{\phi} = 0.6$, $g = 25\,\%$. **(b)**: Amplitudes of the normalized specific entropy fluctuations as function of the fuel modulation frequency measured at different axial positions of the TOF measurement segment, the normalization is done by the static entropy change defined in Eq. 5.14; $\dot{m} = 180\,\mathrm{kg/h}$, $\overline{\phi} = 0.6$, $g = 25\,\%$.

Normalization of the specific entropy amplitudes with $\Delta s_{\mathrm{static}}$ provides values between 0 and 1, whereas unity should be reached for zero excitation frequency $f_{\mathrm{v}} = 0\,\mathrm{Hz}$. The corresponding values of $s'/\Delta s_{\mathrm{static}}$ are depicted in Fig. 5.38b, similar to the bottom plot in Fig. 5.37b, an extrapolation of the curves towards $f_{\mathrm{v}} = 0$ would lead to $s'/\Delta s_{\mathrm{static}} = 1$.

5.4.2.2 One-dimensional dynamic temperature measurements

In this section, the tomographic approaches, which have been theoretically introduced in Sec. 2.3.2 and which have been applied to steady TOF measurements in Sec. 5.3.4, are used to extract the modulated temperature fluctuations. These results have partly been published in Wassmer, Pause, et al. (2017).

Except for the modulation of a part of the fuel by means of a fuel injection valve, the experimental setup is identical to the one introduced in Sec. 5.3.4. A sketch of the arrangement of the acoustic paths is depicted again in Fig. 5.39a. The number of the evaluated flight times is a product of the number of microphones (seven) and the number of penetration depths (3 to 8) of the electrodes' tips. In contrast to the zero-dimensional SVD approach presented in the previous section, the $\boldsymbol{\tau}$-matrix shown in Fig. 5.39b (with $\boldsymbol{\tau} \in \mathbb{R}^{N_\psi \times N_L}$) is not processed as a whole but the flight time array of each of the phase angles N_ψ actually serves as an input to a single steady temperature measurement. Each marker in Fig. 5.39b represents the median value of $N_s = 200$ to $N_s = 300$ spark discharge events.

For the purpose of a clearer illustration of the TOF results, the flight times for only one penetration depth of the electrodes are plotted in Figs. 5.40a and 5.40b at the ax-

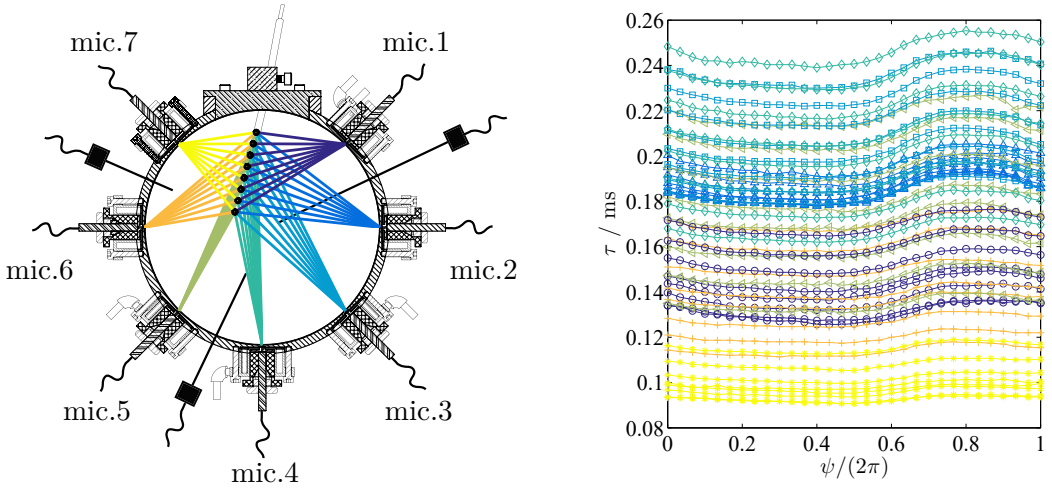

(a) **(b)**

Figure 5.39: **(a)**: Arrangement of the acoustic paths for the one-dimensional temperature extraction for a number of 8 penetration depths of the electrodes' tips; view in downstream direction. **(b)**: Phase sorted arrival times along the 56 acoustic paths shown in (a) for a fuel modulation frequency $f_\mathrm{v} = 5\,\mathrm{Hz}$, the colors correspond to the line colors in (a); about $N_s = 250$ spark events are performed at each of the $N_\psi = 31$ phase angles for each acoustic paths, the median values are shown here; parameters: $\overline{\phi} = 0.65$, $g = 25\,\%$, $\Delta x3$, $\dot{m} = 180\,\mathrm{kg/h}$.

ial location $\Delta x1$. The comparison of Fig. 5.40a as well as Fig. 5.40b with Fig. 5.34b clearly reveals that the scattering of the arrival times is significantly smaller in case of the asymmetric measurements conducted for the tomographic reconstruction. This is because of the larger penetration depth of the electrodes' tips. The higher gas temperature at locations closer to the combustor's center entail a lower breakdown voltage required for the spark discharge. Consequently, the resulting plasma trajectory is less noisy and more stable (see also Sec. 4.1.2). Note, this is a typical example, however, for spark discharge locations closer to the wall, the standard deviation also increases with this setup to values obtained in Fig. 5.35a. Apart from some outliers, it can be stated that the standard deviation is of the order of $\epsilon_\tau \approx 2\ \mu\mathrm{s}$.

The tomographic reconstruction study in Sec. 5.3.4 revealed that there is no significant difference between the results obtained by the OP approach and the collocation method. Therefore, in this tomographic study on the dynamic temperature measurements, we will primarily focus on just one method, the collocation approach. The stringing together of the evaluated one-dimensional temperature profiles for each of the $N_\psi = 31$ phase angles is plotted in Fig. 5.41a. This example is based on measurements with $N_L = 56$ acoustic paths with a fuel modulation frequency of $f_\mathrm{v} = 5$ Hz. The regularization parameters are the same as used in Fig. 5.21a, where this set of parameters has been found to provide the best compromise between an over-regularized, and thus strongly damped solution, and a very noisy resulting radial temperature profile.

The very characteristic shape of the radial temperature distribution with its distinct maximum can be observed for each of the phase angles of the fuel modulation period ψ. This again confirms that the peaks are not related to numeric noise or to random artifacts caused by the solution algorithm of the tomographic method. The same holds

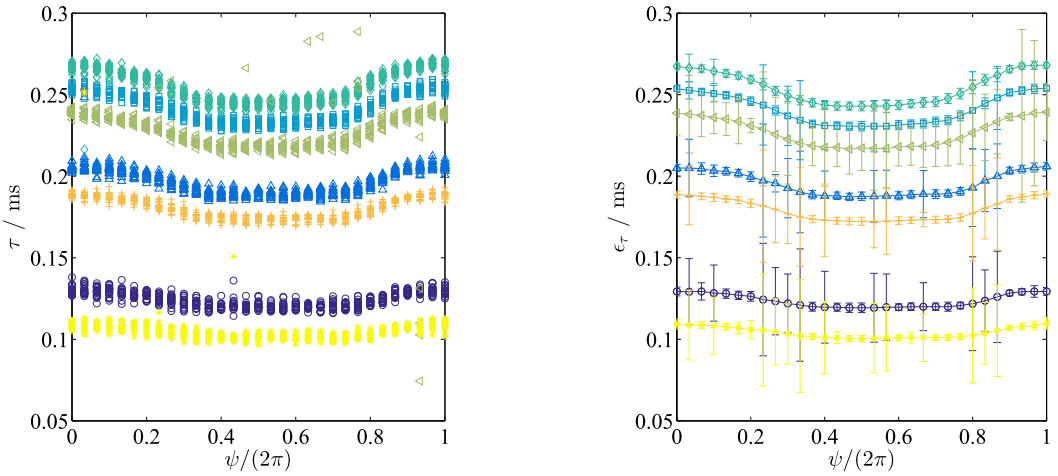

(a) **(b)**

Figure 5.40: **(a)**: Example of phase sorted arrival times of the seven microphones obtained for a penetration depth of the electrodes' tips of $s = 30\,\text{mm}$ and a fuel modulation frequency $f_\text{v} = 5\,\text{Hz}$, the colors correspond to different microphones as shown in Fig. 5.39a; about $N_s = 250$ spark events are performed at each of the $N_\psi = 31$ phase angles; parameters: $\overline{\phi} = 0.65$, $g = 25\,\%$, $\Delta x1$, $\dot{m} = 180\,\text{kg/h}$. **(b)**: Median values and corresponding error bars of the flight times shown in (a); for the majority of the flight times, the standard deviation is well below $3\,\mu\text{s}$.

true for an increased number of basis functions the temperature distribution is evaluated on in case of the collocation method. This case depicted in Fig. 5.41b. It has already been derived in Sec. 5.3.4 that the three characteristic peaks most probably originate from an asymmetry of the temperature field which violates the basic assumption of a rotational symmetric temperature field in the combustion chamber.

Variations of the regularization parameter and the exponential parameter μ, which determines the sharpness of the exponential basis functions, exhibit for all phase angles ψ the same results as already observed in Sec. 5.3.4. In Figs. 5.41c and 5.41d, μ is increased, which leads to (unphysically) strong peaks in the center of the combustion rig at $r/R = 0$. In further studies, the parameters are fixed to $\gamma = 1000$ and $\mu = 1$.

A clearer picture of the temperature fluctuations as function of the modulation phase angles is gained by subtracting the mean temperatures of all phase angles at each radius from the absolute temperatures shown in Fig. 5.41. The result is shown in Fig. 5.42 by means of measurements performed at different axial distances with respect to the burner front plate. The frequency and the amplitude of the fuel modulation as well as the air mass flow and the mean equivalence ratio are the same, respectively. As expected, the amplitude of the fluctuation decreases for further downstream positions, also the phase shift of the oscillation can clearly be seen in the plots.

Although we know that the radial distributions of the temperature fields reconstructed by the tomographic methods do not represent the real temperature field, some findings can nevertheless be taken from this study. In Fig. 5.43a, the temperature amplitude and the corresponding phase is plotted as a function of the radial position r/R and for four different axial positions of the TOF measurement plane. The phase refers to the fuel valve control signal. Here, a fuel modulation frequency of 7 Hz is applied, the

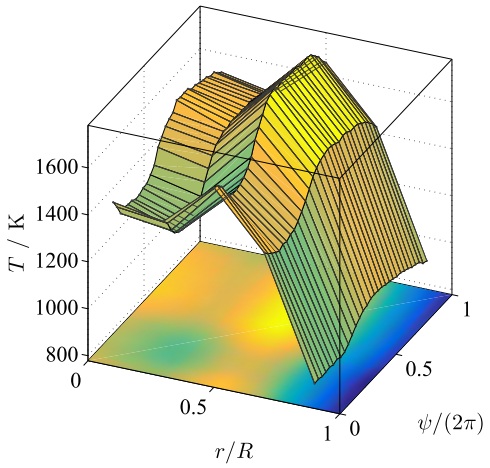

(a) $N_g = 5$; $\zeta = 1000$, $\mu = 1$.

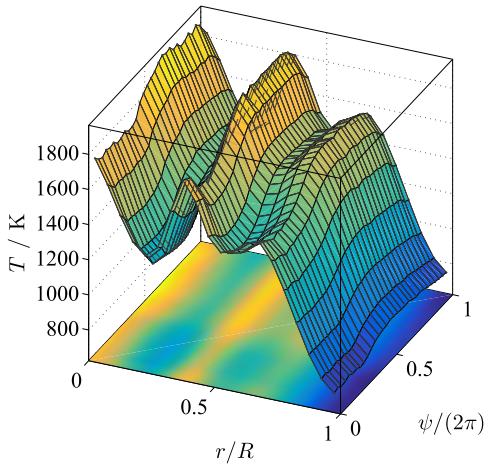

(b) $N_g = 20$; $\zeta = 1000$, $\mu = 1$.

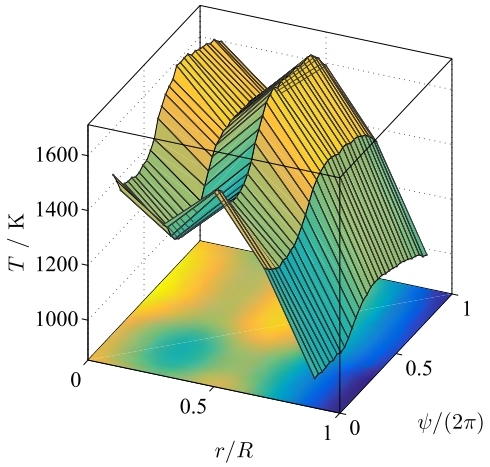

(c) $N_g = 5$; $\zeta = 1000$, $\mu = 10$.

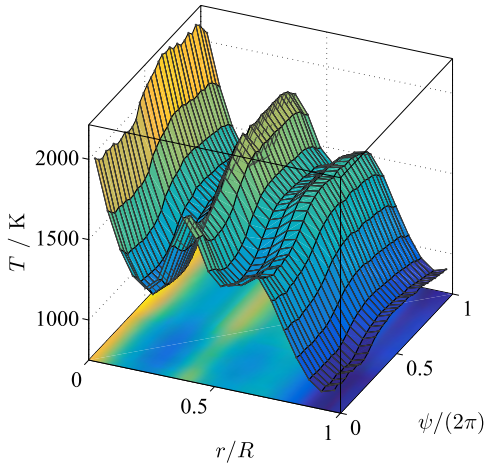

(d) $N_g = 20$; $\zeta = 1000$, $\mu = 10$.

Figure 5.41: Reconstructed temperature fields of a $f_v = 5\,\mathrm{Hz}$ modulated temperature fluctuation based on the one-dimensional collocation method for different numbers of basis functions N_g, that are evenly distributed along the radius, and for different Tikhonov regularization parameters γ and exponential parameters μ of the basis function ($N_L = 56$, $N_\psi = 31$); $\Delta x3$, $\dot{m} = 180\,\mathrm{kg/h}$, $\overline{\phi} = 0.65$, $g = 25\,\%$.

excitation amplitude and the average equivalence ratio is the same in all cases. In the upper graph, where the amplitudes are depicted, the dashed lines refer to the amplitude of the cross-sectionally averaged temperature fluctuation, which is calculated from the temperature amplitudes at all radial positions.

One clear message can be taken from all measurement positions shown in Fig. 5.43a: the fluctuation amplitude is significantly higher in the center region of the duct compared to the area close to the wall. This is expected due to two reasons: the flow field within the circular duct and the wall-cooling. The thermal boundary layer at the wall attenuates the temperature fluctuations as it imposes the (well approximated) constant wall temperature to the gas. It can also be seen from Fig. 5.43a that the measurements at the different axial position (thus different measurement days) all exhibit a local maximum of the temperature amplitude at about $r/R = 0.5$. The more “noisy” radial distribution

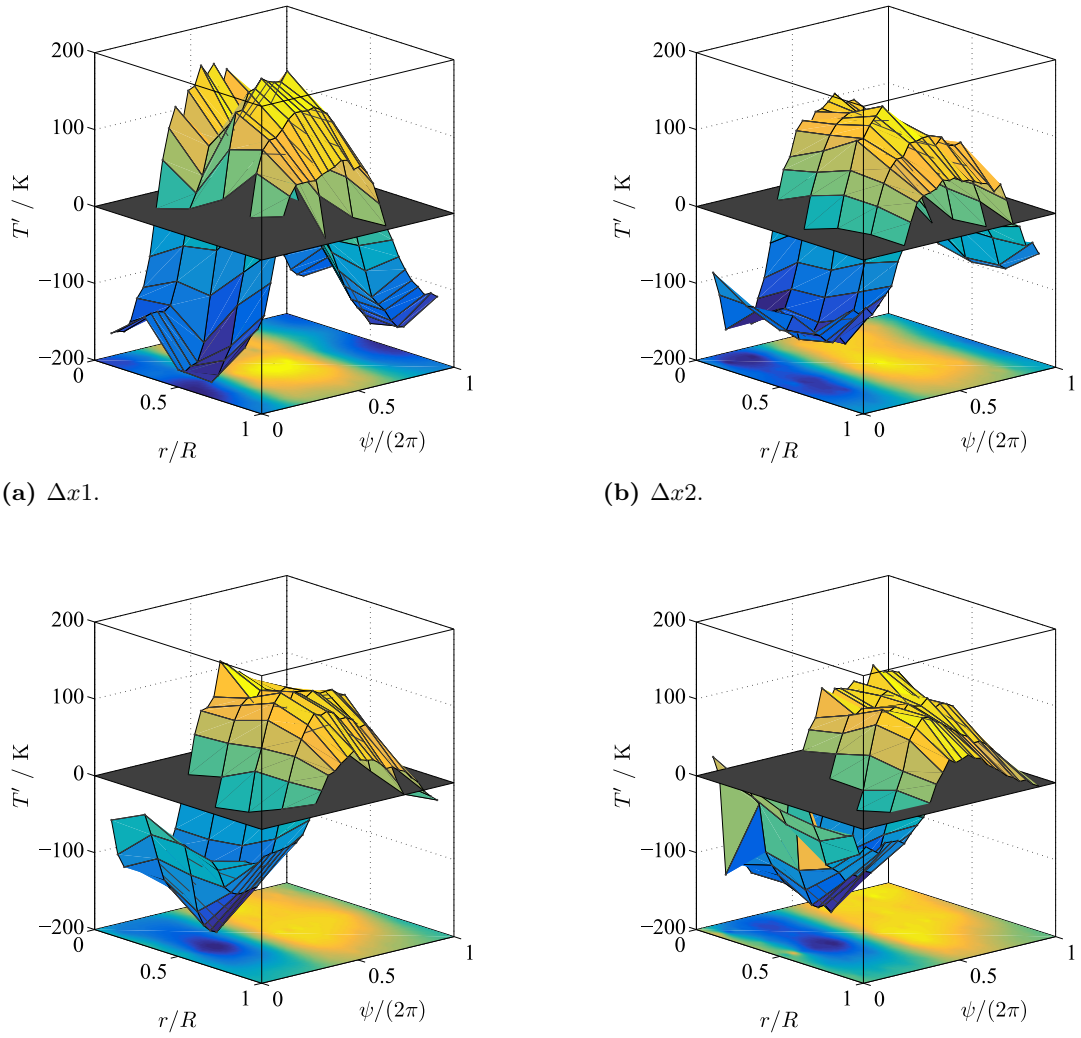

(a) $\Delta x1$.

(b) $\Delta x2$.

(c) $\Delta x3$.

(d) $\Delta x4$.

Figure 5.42: Phase sorted temperature fluctuation amplitude (absolute value of the temperature measurement at $N_g = 5$ radial positions and $N_\psi = 31$ phase angles minus the average temperature over all phase angles at each radial position) forced by a $f_\mathrm{v} = 5\,\mathrm{Hz}$ fuel modulation frequency calculated with a one-dimensional collocation ($\zeta = 1000$, $\mu = 1$); $\dot{m} = 180\,\mathrm{kg/h}$; $\overline{\phi} = 0.65$; $g = 25\,\%$.

of the temperature amplitude for axial positions closer to the flame (especially for $\Delta x1$) might be a hint to a more complex flow field at these axial locations compared to further downstream positions, where the flow might be more close to a well-established duct flow. In such a case, the phase provided in the bottom plot in Fig. 5.43a would correspond to the axial convective velocity at the different radial locations in the combustors duct. Here, a smaller value refers to a higher convective velocity and a higher phase value indicates that the fluctuation arrives later in time. All measurements at the different axial locations exhibit an increase of the phase value for higher radii. This is a reasonable observation, as the axial velocity is of course expected to be lower in the region close to the wall. Apart from $\Delta x2$, a local minimum of the phase is found at about $0.2 < r/R < 0.4$. This might be an indicator that the recirculation zone of the swirl-stabilized combustor flow field is still present at the TOF-measurement plane locations. There, the highest

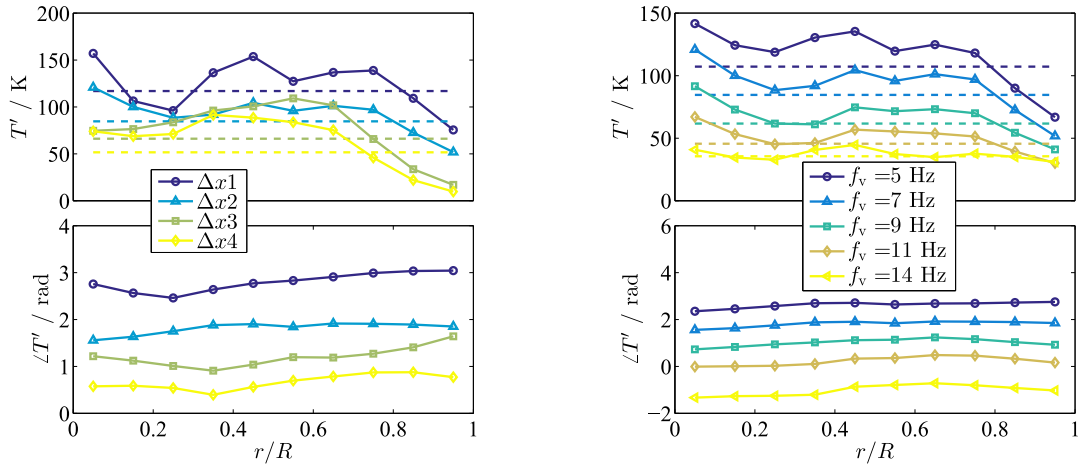

(a) **(b)**

Figure 5.43: **(a)**: Amplitude and phase of a $f_\mathrm{v} = 7$ Hz temperature fluctuation reconstructed via one-dimensional collocation ($\zeta = 1000$, $\mu = 1$) as function of the dimensionless combustor radius r/R; $\dot{m} = 180\,\mathrm{kg/h}$; $\overline{\phi} = 0.65$; $g = 25\,\%$. The dashed lines in the upper plot indicate the cross-sectionally surface averaged temperature amplitude. **(b)**: Same plot as in (a) but for various fuel modulation frequencies and at only one axial location of the TOF measurement plane ($\Delta x2$).

axial velocities are reached at a radius between the recirculation bubble in the center of the duct and the boundary layer at the wall.

The radial features of the temperature fluctuation amplitude are maintained for different frequencies of the fuel modulation, as can be seen in Fig. 5.43b for $\Delta x2$. However they become less prominent at higher modulation frequencies, where the shorter convective wavelength causes an overall increased dispersion of the temperature spot. Especially the steep gradient of the temperature amplitude towards the near-wall region flattens significantly.

However, at this stage it is important to note that the flow field needs to be considered as three-dimensional and rather complex including, e.g., vortices that have of course significant influence on the dispersion of the temperature spot. At least, due to the extensive phase averaging over a large number of fuel modulation periods ($N_s \approx 250$), incoherent flow phenomena are averaged out in the results shown here.

When transforming the temperature measurements to entropy measurements, for the case of a one-dimensional consideration it has to be clarified how the absolute temperature $\overline{T}$ in Eq. 2.21 is defined. One could consider the cross-sectionally averaged mean temperature; however, here we use specifically for each radial position the average temperature evaluated over all phase angles. Looking at Eq. 2.21, this means that the low amplitude fluctuations in the near-wall region are scaled with a lower temperature and the high temperature amplitudes in the center of the duct are divided by a higher temperature. This leads to a radially more even distribution of the entropy fluctuation compared to the temperature fluctuation. This has to be kept in mind when converting the here shown one-dimensional temperature fluctuations to fluctuations in entropy. A comparison between the one-dimensional amplitude fields of both thermody-

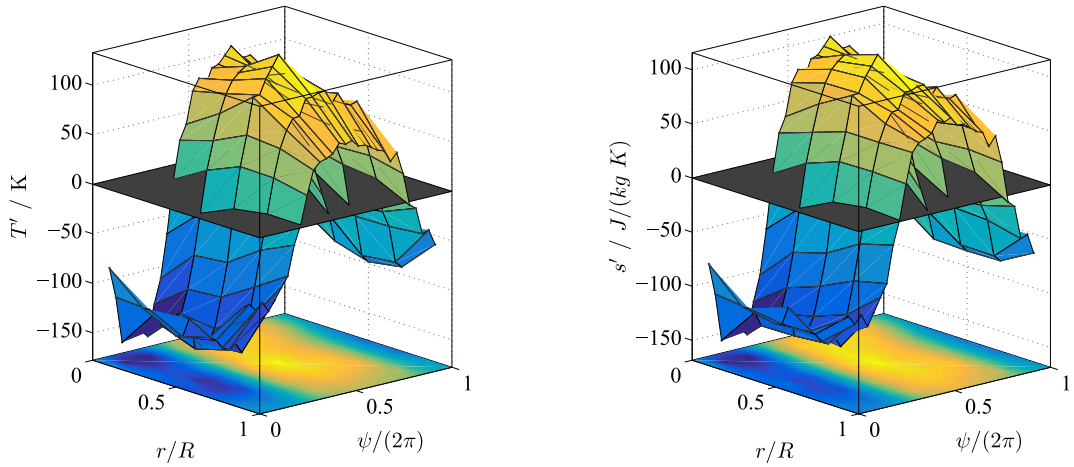

(a) **(b)**

Figure 5.44: (a): Phase sorted temperature fluctuation (as shown in Fig. 5.42b) generated with a $f_v = 5$ Hz fuel modulation calculated by the one-dimensional collocation ($\zeta = 1000$, $\mu = 1$); $\dot{m} = 180\,\mathrm{kg/h}$; $\overline{\phi} = 0.65$; $g = 25\,\%$. **(b)**: One-dimensional entropy fluctuation based on the temperature obtained from the collocation in (a) and Eq. 2.21.

namic quantities is given in Fig. 5.44. The fact that the values of both quantities, the temperature fluctuation as well as the entropy fluctuation, are almost the same is caused by the very similar values of the mass specific heat capacity and the mean temperature ($c_p/\overline{T} \approx 1\,\mathrm{J/kg/K^2}$). The mean temperature $\overline{T}$ is evaluated from the temperatures obtained by the collocation and not from thermocouple measurements at different radial positions.

Besides the estimation of a radially resolved one-dimensional temperature fluctuation field, the results of the tomographic methods can also be used to derive a zero-dimensional temperature fluctuation as obtained in Sec. 5.4.2.1. Therefore, the cross-sectionally averaged temperature is evaluated based on the temperature field received from the one-dimensional collocation method. The results are shown in Sec. 5.4.2.3. There, they are compared to the results obtained by the SVD method in Sec. 5.4.2.1.

5.4.2.3 Comparison between zero- and one-dimensional methods

The one-dimensional collocation method applied to the dynamic TOF measurements in Sec. 5.4.2.2 allows for an estimation of the fluctuation amplitude of the cross-sectionally averaged temperature. This amplitude should ideally be the same as the one obtained from the zero-dimensional analysis in Sec. 5.4.2.1. In this subsection, the results of both methods are compared in terms of amplitude and phase of the temperature fluctuations.

In Fig. 5.45a, the temperature amplitude T' and the oscillation phase $\angle T$, which is evaluated with regards to the control signal of the fuel modulation valve, are plotted for both extraction methodologies. The TOF measurement setups that have been used for the different temperature (fluctuation) extraction methods are slightly different (see Sec. 4.3). Therefore, it is important to note that the TOF measurements of the

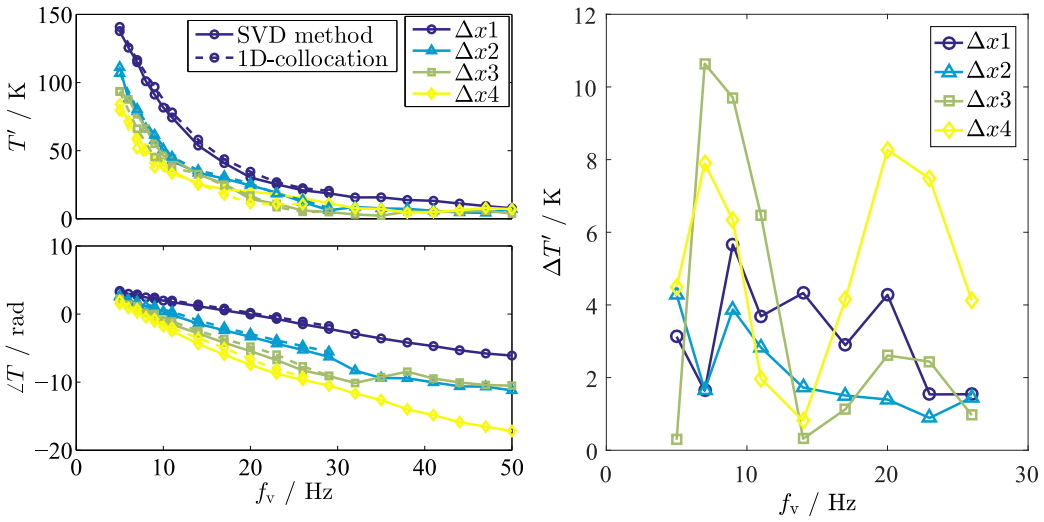

(a) **(b)**

Figure 5.45: **(a)**: Amplitude and phase of the cross-sectionally averaged temperature fluctuation due to fuel modulation with frequency f_v at different axial positions of the TOF measurement plane ($\dot{m} = 180\,\mathrm{kg/h}$); (solid line): Zero-dimensional reconstruction based on the SVD by using the TOF measurement setup shown in Fig. 4.23; $\overline{\phi} = 0.6$, $g = 25\,\%$. (dashed line): One-dimensional reconstruction based on collocation and on TOF measurements with the measurement setup shown in Fig. 4.25; $\overline{\phi} = 0.65$, $g = 25\,\%$. **(b)**: Difference in cross-sectionally averaged temperature amplitude between the two different extraction methods shown in the upper plot of (a).

temperature fluctuations depicted in Fig. 5.45a have been conducted at two separate measurement campaigns, where all relevant parts (including the burner itself) of the atmospheric combustion test rig have been disassembled in between. Consequently this comparison does not only include the methodical aspects but also comprises to some extent the overall measurement uncertainty.

The difference in the temperature amplitude, which is the most relevant parameter, is shown separately in Fig. 5.45b. Apart from some outliers, the deviation between the amplitudes of the cross-sectionally averaged temperature fluctuation evaluated by the two different methods is below approximately 6 K. This is especially at low fuel modulation frequencies, where the temperature amplitudes reach values of up to 140 K, an absolutely tolerable uncertainty. For higher frequencies, where the temperature amplitudes drop below about 30 K, the "temperature noise" obtained from the TOF measurements becomes large compared to the expected temperature oscillation due to the fuel modulation. Thus, the deviation of about 5 K, which then might be of the order of 20 % of the expected amplitude, is still acceptable.

6 Characterization and Modelling of Entropy Waves

In the previous section (Sec. 5.4), the temperature and entropy fluctuations that have been measured due to imposed equivalence ratio fluctuations have been presented. This chapter now deals with the interpretation and the analysis of these results. The focus lies on the generation of entropy waves in the flame zone (Sec. 6.1) and on the transport characteristics of the entropy waves downstream of the combustion zone (Sec. 6.2). This analysis has to some extend already been published in Wassmer, Schuermans, et al. (2017).

6.1 Generation of entropy waves

In Sec. 5.4.1.2, where the results of the OH*-chemiluminescence intensity fluctuations are presented and analyzed, we already observed a dependence of the OH*-chemiluminescence intensity fluctuation amplitude on the residence time of a gas particle within the flame zone and thus an amplitude dependence on the fuel modulation frequency. In the following, a reactor model is derived (Sec. 6.1.1), which allows for an estimation of the relation between the equivalence ratio fluctuations and the temperature fluctuations in the flame zone. In a second step, we validate the model by means of the measurement data of equivalence ratio fluctuations and temperature fluctuations presented in Sec. 5.4. This enables the identification of key parameters that are required to transfer the findings from the combustor used in these experiments to general combustor designs.

6.1.1 Reactor model: theory

The actual combustion process in the swirl-stabilized combustor investigated in this study is rather complicated and not easy to model in detail. The fresh (and cold) air-fuel mixture is partly mixed with the hot burnt gases, which are recirculated back towards the combustor inlet when entering the circular combustion chamber. The mixedness of air and fuel, the gas temperature, and thus also the reaction rate are spatially inhomogeneous within the reaction zone. A well-stirred reactor model allows the simplification of the entire process down to a zero-dimensional model by defining the following assumptions for a certain reactor volume: the Damköhler number is very high, a constant mass flow of air-fuel mixture is entering the reactor, and the hot gas, which is leaving the reactor, is homogeneous and has the same composition and temperature as the gas within the reactor. Furthermore, we assume that the combustion process is complete

(no combustible gases left), the gas behaves as an ideal gas, and the boundaries of the reactor are considered to be adiabatic.

Such models are known as *reactor models* and they are commonly used for modeling steady-state combustion systems. T. Lieuwen, Neumeier, et al. (1998), however, derive a well-stirred reactor model that considers unsteady (periodic) variations of the mixture properties, such as the equivalence ratio, of the inlet flow.

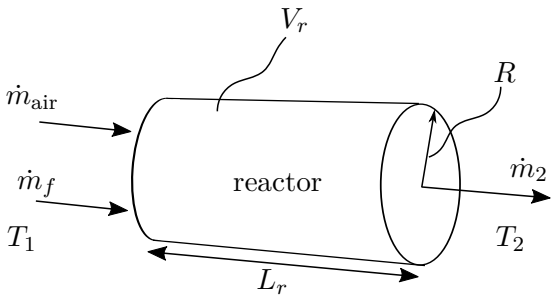

Figure 6.1: Schematic of the reactor model with the constant volume $V_r = \pi R^2 L_r$ and a homogeneous gas temperature T_r.

The volume of the homogeneous reactor is defined as $V_r = \pi R^2 L_r$, where R denotes the radius of the circular combustor and L_r refers to the axial extent of the reaction zone. The length L_r has to be estimated and may correlate with the flame length or the length of the recirculation zone. A sketch of the reactor model is depicted in Fig. 6.1. A steady-state cold air mass flow $\dot{m}_{\text{air}}$ enters the reactor along with a fuel mass flow $\dot{m}_f$ ($\dot{m}_1 = \dot{m}_{\text{mixture}} = \dot{m}_{\text{air}} + \dot{m}_{\text{fuel}}$), and a hot exhaust gas mass flow $\dot{m}_2$ leaves the reactor at its downstream end. The energy balance for the adiabatic reactor at steady-state conditions reads

$$\dot{m}_1 c_{p1} T_1 + \dot{Q} = \dot{m}_2 c_{p2} T_2, \tag{6.1}$$

with the heat release rate $\dot{Q} = \dot{m}_f h_f$, where h_f denotes the reaction enthalpy per unit mass of fuel. This formulation for the heat release rate is only possible in the case of isobaric combustion, where the term for the pressure work $V\,dp$ in the enthalpy definition (Eq. 2.4) vanishes. If we further assume that the specific heat capacity c_p is the same in the fresh air-fuel mixture as it is in the exhaust gas ($c_{p1} = c_{p2}$) and that the fuel mass flow is much smaller than the air mass flow ($\dot{m}_f / \dot{m}_1 \ll 1$), we obtain $\dot{Q} = \dot{m}_1 c_p \Delta T$ as an expression for the heat release rate. $\Delta T = T_2 - T_1$ represents the temperature difference from the cold state upstream of the flame to the combustion temperature at the exit of the reactor.

We are now interested in the response of the system to a perturbation in the equivalence ratio, which occurs due to imperfect mixing of fuel and air or, in our case, due to the fuel modulation upstream of the mixing tube. It is assumed that the perturbations, denoted with $()'$, are sufficiently small in terms of amplitude, which justifies linearization around a mean value, denoted by $\overline{()}$. Linearization of Eq. 6.1 yields an expression for the fluctuating heat release rate

$$\dot{Q}' = S_r \overline{\rho}_2 \overline{u}_2 \overline{T}_2 c_p \left(\frac{\rho_2'}{\overline{\rho}_2} + \frac{u_2'}{\overline{u}_2} + \frac{T_2'}{\overline{T}_2} \right), \tag{6.2}$$

where S_r denotes the cross-section area of the combustion chamber. The assumption of a high Damköhler number in the reactor is, of course, only valid if the time scales

of the equivalence ratio fluctuations are significantly larger than those of the reaction rate. Since the highest frequency considered in this study is of the order of 50 Hz, this requirement is easily met. Here, the effect of upstream velocity fluctuations on downstream entropy fluctuations is neglected; we only consider the effect of heat release rate fluctuations per unit mass of mixture on the quantities within the reaction zone. Therefore, the heat release rate fluctuation in Eq. 6.2 corresponds to the non-isentropic part of the total heat release rate fluctuation $\dot{Q}'_{\mathrm{tot}}$ with $\dot{Q}' = \dot{Q}'_{\mathrm{tot}} - S_r \overline{\rho}_2 c_p \Delta T u'_1$ (A. P. Dowling and Stow, 2003). Furthermore, it is also assumed in this study that there are no entropy disturbances upstream of the reactor ($s'_1 = 0$).

In order to obtain an expression for the correlation between temperature and equivalence ratio fluctuation, the state equation of the ideal gas $p_2/\rho_2 = R_g T_2$ and the mass conservation equation $V \partial\rho/\partial t = \dot{m}_1 - \dot{m}_2$ have to be linearized as well, which respectively read:

$$\frac{p'_2}{\overline{p}_2} = \frac{\rho'_2}{\overline{\rho}_2} + \frac{T'_2}{\overline{T}_2}, \tag{6.3}$$

$$\frac{1}{\overline{\rho}_2 \overline{u}_2} \frac{V}{S_r} \frac{\partial \rho_2}{\partial t} = \frac{\rho'_1}{\overline{\rho}_1} + \frac{u'_1}{\overline{u}_1} - \frac{\rho'_2}{\overline{\rho}_2} - \frac{u'_2}{\overline{u}_2}. \tag{6.4}$$

Both equations can be simplified by the following considerations: For low Mach numbers in the combustor, which can be considered in this study, the relative pressure fluctuations are much smaller compared to the relative velocity fluctuations ($p'/\overline{p} \ll u'/\overline{u}$). As the relative temperature fluctuations, however, are of the order of the equivalence ratio fluctuations, which in turn are of the order of the velocity fluctuations (see. Eq. 2.26), we can neglect the pressure amplitudes on the left-hand side of Eq. 6.3. In case of the linearized mass conservation equation, an almost constant upstream mass flow of the fuel–air mixture can be assumed, which makes the first two terms on the right-hand side of Eq. 6.4 also disappear. Finally we obtain:

$$\frac{\rho'_2}{\overline{\rho}_2} + \frac{T'_2}{\overline{T}_2} = 0, \tag{6.5}$$

$$\frac{1}{\overline{\rho}_2 \overline{u}_2} \frac{V}{S_r} \frac{\partial \rho_2}{\partial t} = -\frac{\rho'_2}{\overline{\rho}_2} - \frac{u'_2}{\overline{u}_2}. \tag{6.6}$$

In order to support the assumptions made above, which are based on the scale comparison of the different properties, the relative fluctuations of some properties have been evaluated in Tab. 6.2. This estimation is based on the state equation, mass conservation, and the caloric equation of state; the parameters have been chosen according to typical measurement parameters employed in this study. Here, only perturbations are considered that stem from the periodic modulation of a part of the fuel mass flow. Although this is rather a simple approach, it allows for a good comparison of the orders of magnitudes of the relative fluctuations of various quantities. The upstream relative fluctuations of the velocity and the density, for example, are one order of magnitude smaller than the associated fluctuations downstream of the reactor. This confirms that the assumption made to obtain Eq. 6.6 from Eq. 6.4 is reasonable.

We can rewrite the linearized heat release rate equation (Eq. 6.2) by combining it with Eq. 6.5 and dividing it by the average heat release rate $\overline{\dot{Q}} = \dot{m}_1 c_p \Delta T$. Thus, an expression for the downstream relative velocity fluctuation as a function of the relative heat

Table 6.1: Calculated relative fluctuations of the equivalence ratio, the fuel mass flow, the total mass flow of the fuel–air mixture, the upstream velocity and density fluctuations due to the fuel modulation, and the relative heat release rate fluctuations in the reactor and the downstream relative fluctuations of temperature, velocity, and density for $g = 10\,\%$ and $g = 25\,\%$. The values are evaluated for $\dot{m}_{\mathrm{air}} = 180\,\mathrm{kg/h}$, $\overline{\phi} = 0.68$, $h_f = 30\,\mathrm{MJ/kg}$, $\varsigma = 0.06$, and by using the relation between equivalence ratio and temperature obtained from the GRI mechanism (see Fig. 5.13b).

$\frac{\phi'}{\overline{\phi}}$	$\frac{\dot{m}'_{\mathrm{fuel}}}{\overline{\dot{m}}_{\mathrm{fuel}}}$	$\frac{\dot{m}'_{\mathrm{mixture}}}{\overline{\dot{m}}_{\mathrm{mixture}}}$	$\frac{u'_1}{\overline{u}_1}$	$\frac{\rho'_1}{\overline{\rho}_1}$	$\frac{\dot{Q}'}{\overline{\dot{Q}}}$	$\frac{T'_2}{\overline{T}_2} \simeq \frac{s'_2}{\overline{c}_p}$	$\frac{u'_2}{\overline{u}_2}$	$\frac{\rho'_2}{\overline{\rho}_2}$
0.10	0.053	0.002	0.003	0.002	0.053	0.045	0.047	0.046
0.25	0.143	0.005	0.009	0.004	0.143	0.117	0.122	0.127

release rate fluctuation and the scaled mean temperature increase over the reactor is obtained:

$$\frac{u'_2}{\overline{u}_2} = \frac{\dot{Q}'}{\overline{\dot{Q}}} \frac{\Delta T}{\overline{T}_2}. \tag{6.7}$$

If we replace the expression for the downstream density fluctuation in Eq. 6.6 by the downstream temperature fluctuation (due to Eq. 6.5) and the relative velocity fluctuation by the expression found in Eq. 6.7, the normalized temperature fluctuation at the reactor exit is obtained:

$$\frac{T'_2}{\overline{T}_2} = \frac{V_r}{\overline{u}_2 S_r} \frac{\partial}{\partial t} \frac{T'_2}{\overline{T}_2} + \frac{\dot{Q}'}{\overline{\dot{Q}}} \frac{\Delta T}{\overline{T}_2}. \tag{6.8}$$

From the definition of the equivalence ratio in Eq. 2.22 and the heat release rate as $\dot{Q} = \dot{m}_f h_f$, we derive the proportionality between the equivalence ratio and the heat release rate:

$$\phi = \frac{1}{\varsigma h_f \dot{m}_{\mathrm{air}}} \dot{Q} \quad \Longrightarrow \quad \phi \propto \dot{Q} \qquad \text{for} \quad \phi \leq 1. \tag{6.9}$$

The stoichiometric coefficient ς, the reaction enthalpy h_f, as well as the air mass flow do not vary throughout a period of equivalence ratio oscillation. Using this proportionality, an expression for the transfer function between the temperature fluctuations, normalized by the temperature increase over the reactor, and the associated relative equivalence ratio fluctuations is finally obtained in the frequency domain (with the temporal Fourier transform defined such that $(\partial/\partial t) \mapsto i\omega$):

$$\hat{H}_{r,T}(\omega) = \frac{\hat{T}_2/\Delta T}{\hat{\phi}/\overline{\phi}} = \frac{1}{i\omega \frac{V_r}{\overline{u}_2 S_r} + 1}, \tag{6.10}$$

with the angular frequency $\omega = 2\pi f$. The superscript $\hat{()}$ denotes a fluctuating quantity in frequency domain. Equation 6.10 corresponds to a first-order low pass; a similar response was also found by Karimi et al. (2008), who studied the frequency dependence of entropy generation due to acoustic and entropic excitation in a one-dimensional non-diffusive flow. They considered cases with steady as well as unsteady heat addition into the flow and derived a formulation for a corner frequency of the generated entropy waves. In terms of entropy waves, the transfer function $\hat{H}_{r,T}$ can be transformed to relative entropy fluctuations by the following definition:

$$\frac{\hat{s}}{\Delta s_{\mathrm{static}}} = \frac{\Delta T}{\overline{T}} \frac{c_p}{\Delta s_{\mathrm{static}}} \frac{\hat{\phi}}{\overline{\phi}} \hat{H}_{r,T}(\omega), \tag{6.11}$$

where $\Delta s_{\mathrm{static}}$ denotes the static entropy change according to the equivalence ratio amplitude applied (see Eq. 5.14).

We will now have a closer look on the very right-hand side term in Eq. 6.10. If we rewrite the term in the denominator as

$$i\omega \frac{V_r}{\overline{u}_2 S_r} = i2\pi \frac{f L_r}{\overline{u}_2} = i2\pi f t_r, \tag{6.12}$$

it becomes obvious that the frequency response of $\hat{H}_{r,T}$ only depends on a length scale, i.e., the reactor length, and a velocity scale, which is the average velocity in the reactor. Thus, it is appropriate to introduce a Strouhal number $\mathrm{St}_r = f L_r / u_r$, which can also be considered as the ratio between the reactor length scale L_r and the convective length scale u_r/f. The average velocity in the reactor u_r is introduced and determines the average residence time $t_r = L_f / u_r$ of a gas particle in the reactor volume. Equation 6.10 finally reads

$$\hat{H}_{r,T}(\mathrm{St}_r) = \frac{1}{i2\pi \mathrm{St}_r + 1}. \tag{6.13}$$

For $\mathrm{St}_r = 1$, the reactor length is equivalent to the convective wavelength $\lambda_c = u_r/f$ which corresponds to the idea of the corner frequency proposed by Karimi et al. (2008). They state that the generation of entropic disturbances becomes small if "the entropic disturbance views a homogeneous region", which is the case for convective wavelengths of the equivalence ratio fluctuations that are smaller than the flame length. Another kind of interpretation of the Strouhal number in this context is the ratio between the reactor residence time t_r and the duration of an oscillation period as $\mathrm{St}_r = t_r/(1/f)$. These different approaches for interpreting the Strouhal number do actually not affect its value. However, by choosing an appropriate interpretation, its parameters, which have to be determined by measurement or by guess, may be more intuitive.

The derivation of this model has partly been conducted based on Schuermans, Polifke, et al. (1999) and private communication with its first author. This reactor model will be compared in the following section to the measurement data acquired in this study.

6.1.2 Reactor model: results

For the validation of the reactor model derived in the preceding section, temperature fluctuations assessed in the reaction zone are required. It has already been mentioned before that the length of the reactor L_r has to be guessed, as it cannot explicitly be measured. It correlates with the flame length as well as with the extent of the recirculation zone. The experimental setup in this study did not allow for TOF measurements closer than $\Delta x1 = 400\,\mathrm{mm}$ to the burner front plate (see Sec. 5.1). Consequently, the volume between the burner front plate and the TOF measurement plane at $\Delta x1$ would have to be defined as the reactor volume. The question arises, whether this assumption is reasonable, as the visible flame length fills typically maximum half of the quartz glass duct, which corresponds to $L_{\mathrm{quartz\,glass}}/2 = 150\,\mathrm{mm}$. In order to shed more light on this issue, in Fig. 6.2, pictures of the flame taken at ten different phase angles of one period of fuel modulation at $f_{\mathrm{v}} = 11\,\mathrm{Hz}$ are shown. These pictures underline the fact that the

assumption of a constant volume of the reactor might not strictly hold. One has to consider an average reactor volume, around which the flame is moving within one period of fuel modulation. This becomes even more significant at lower excitation frequencies.

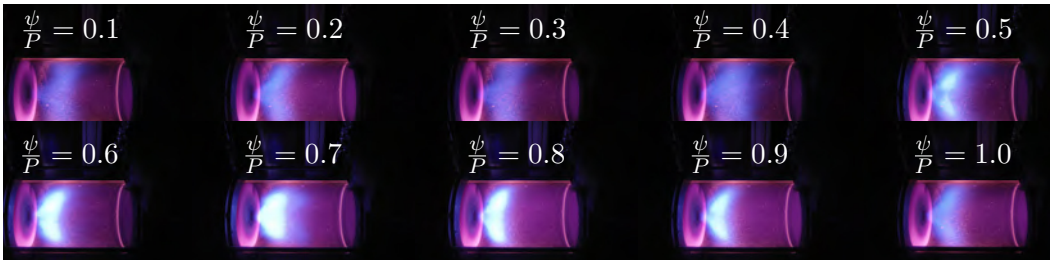

Figure 6.2: Instantaneous pictures of the flame excited with a fuel modulation frequency of $f_\mathrm{v} = 11\,\mathrm{Hz}$ and an amplitude of $g = 25\,\%$ at $\overline{\phi} = 0.6$ at different phase angles ψ of a full period P of the fuel modulation. On the left side of each picture, the glowing inlet plate is visible, on the very right-hand side of each picture one can see the glowing metal sealing between the quartz glass and the TOF measurement segment (only in the case of $\Delta x1$); the length of the quartz tube is 0.3 m.

However, the recirculation zone, which is established in the combustor due to the swirl stabilization of the flame, has a significantly larger axial extent compared to the heat release zone (which approximately corresponds to the visible flame zone in Fig. 6.2). PIV measurements of the steady-state flow field in the combustor are depicted in Fig. 6.3, the axial coordinate is scaled by the distance between the burner front plate and the nearest possible TOF measurement position $\Delta x1$. Unfortunately, there are no PIV data available for axial positions further downstream than $x/\Delta x1 = 0.6$. Nevertheless, the flow field data reveal that the recirculation of hot exhaust gases back towards the flame root clearly exceeds $x/\Delta x1 = 0.6$ and might reach at least $x/\Delta x1 = 0.8$ or even $x/\Delta x1 = 1$. Note, the results presented in Fig. 6.3 have been conducted with an air mass flow rate of $\dot{m} = 100\,\mathrm{kg/h}$, which is considerably less than what has typically been used for the TOF measurements in this study ($\dot{m} \approx 180\,\mathrm{kg/h}$). Therefore, it can be assumed that the recirculation zone might expand to axial positions that are even further downstream.

In order to feed the model (Eq. 6.13) with reasonable parameters, the reactor length L_r and the reactor velocity u_r need to be estimated. The reactor length L_r is defined as $L_r = \Delta x1 = 400\,\mathrm{mm}$, this is because the temperature is assessed at this particular axial position. The definition of the reactor velocity u_r is more complicated, as it cannot be explicitly measured. The mean flow velocity, however, could serve as a useful scale. There are two possibilities of estimating the bulk flow velocity: it could simply be calculated by means of the mass conservation via $u_\mathrm{bulk} = \dot{m}/\rho/S_r$, or it can be extracted from the phase measurements of the equivalence ratio fluctuation by the TDLAS method $\angle\phi'$ in the mixing tube and the phase of the temperature fluctuations assessed by the TOF method $\angle T'$ at $\Delta x1$

$$u_\angle(f_\mathrm{v}) = \frac{2\pi f \Delta x_1}{(\angle T' - \angle\phi')}. \tag{6.14}$$

Equation 6.14 reveals that the velocity assessed by the phase measurements is a function of the modulation frequency f_v. However, as no considerable variations in $u_\angle$ with respect to the fuel modulation frequency have been observed, the average value over all frequencies is taken as the velocity measure $u_\angle = \overline{u_\angle(f)}$.

Both velocities obtained from the two methods are depicted in Fig. 6.4a for three mass

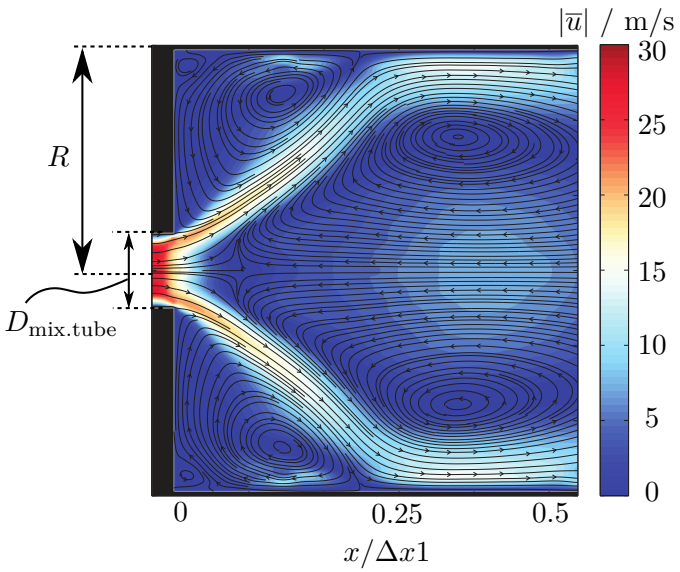

Figure 6.3: PIV measurements of the steady-state flow field at the flame zone; the swirl number is the same as the one used throughout all measurements conducted in this study ($S_{\text{swirl}} = 0.7$); $\dot{m} = 100\,\text{kg/h}$, $\phi = 0.7$; $R = 100\,\text{mm}$; $D_{\text{mix. tube}} = 34\,\text{mm}$. The data are taken from measurements done by Oberleithner and Paschereit (2016).

flow rates of air and a mean equivalence ratio $\overline{\phi} = 0.6$. The velocities exhibit a linear increase with respect to the air mass flow. The quantitative difference stems most likely from an incorrect guess of the average temperature T_r in the reactor. The temperature affects the density estimate, which is required to evaluate u_{bulk}. Note that the calculation of the bulk flow velocity u_{bulk}, as it is shown in Fig. 6.4a, already includes the flow velocity in the mixing tube. The mixing tube needs to be considered, as $u_{\angle}$ represents the integrated flow velocity from the TDLAS measurement plane (which is located in the mixing tube) to the axial TOF measurement position. However, u_{bulk} remains considerably smaller than $u_{\angle}$.

Quantitatively, both velocities shown in Fig. 6.4a do of course not represent the average reactor velocity and, thus, L_r/u_{bulk} cannot be the "true" residence time. Nevertheless, the bulk flow velocity serves as an initial value for the fitting process between the model and the measured transfer function $\hat{H}_{r,T}$. The resulting modeled transfer function is compared to the measured transfer function in Fig. 6.4b for three different air mass flow rates. The model parameters are $L_r = \Delta x1 = 400\,\text{mm}$ and $u_r = u_{\angle} k_{\text{opt}}$, whereas $k_{\text{opt}} = 0.56$ has been found to be an optimization parameter suitable for all mass flow rates. The curves fit well to each other; the trend to higher values of $\hat{H}_{r,T}$ for an increasing mass flow is well reproduced. The only parameter that is subject to optimization is the residence time $\tau_r = L_r/u_r$, which in this case here has to be multiplied by a factor of 1.8 compared to the "plug flow residence time" L_r/u_{bulk}. The input parameters for the model and for the estimate of the bulk flow velocities are presented in Tab. 6.2. The reactor temperature has been estimated based on the measured mean temperature at the TOF measurement plane by means of thermocouple measurements and the expected adiabatic flame temperature.

The fact that the residence times obtained from the reactor model are of the order of the residence times derived in the OH*-chemiluminescence measurements (see Tab. 5.4) and the fact that the set of model parameters leads to a good match between model

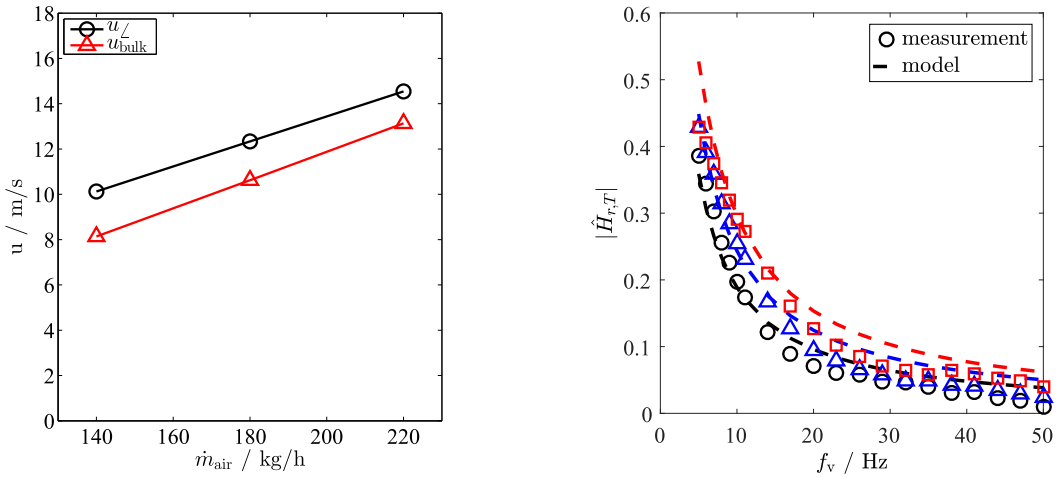

(a) **(b)**

Figure 6.4: **(a)**: Flow velocity estimated by means of mass conservation (u_{bulk}) and by means of the phase difference between equivalence ratio fluctuations in the mixing tube and the temperature fluctuations at the axial position $\Delta x1 = 400\,\text{mm}$ ($u_\angle$); $\overline{\phi} = 0.6$, $g = 25\,\%$. **(b)**: Measured (markers) and modeled (dashed) absolute value of the reactor transfer function $\hat{H}_{r,T}$ as a function of the fuel modulation frequency f_v for three different mass flows of air: (◯ black): 140 kg/h, (△ blue): 180 kg/h, and (□ red): 220 kg/h. The Strouhal number in the model (Eq. 6.13) is defined as $\text{St}_r = f\Delta x1/(u_\angle k_{\text{opt}})$ with $k_{\text{opt}} = 2.1$; mean equivalence ratio and excitation amplitude: $\overline{\phi} = 0.6$, $g = 25\,\%$.

Table 6.2: Input parameters for the reactor model leading to the model results depicted in Fig. 6.4b; the fresh gas temperature T_{cold} to determine $\Delta T = T_r - T_{\text{cold}}$ is constant for all air mass flows: $T_{\text{cold}} = 293\,\text{K}$.

$\dot{m}$ / kg/h	T_r / K	L_r / mm	u_{bulk} / m/s	τ_{bulk} / ms	τ_r / ms	$\tau_r/\tau_{\text{bulk}}$
140	1580	400	8.1	49	88	1.8
180	1620	400	10.6	38	68	1.8
220	1650	400	13.1	31	55	1.8

and measurement for all different mass flows proves the validity of this zero-dimensional reactor model.

In addition to the absolute value of the transfer function in Fig. 6.4b, its associated phase is depicted in Fig. 6.5a as a function of the fuel modulation frequency. The phase is reconstructed with $-2\pi L_r f_v/u_{\text{bulk}}$ and does, as expected, not exactly match the measured phase due to the velocity difference observed in Fig. 6.4a. The considerably stronger deviation for higher frequencies stems from the increased uncertainty in phase detection due to the low temperature fluctuation amplitudes at such high excitation frequencies.

In terms of entropy fluctuations, we can rewrite the transfer function in Eq. 6.13 according to Eq. 6.11. A plot of the absolute value of the relative entropy fluctuation as a function of the Strouhal number $\text{St}_r = fL_r/u_r$ is shown in Fig. 6.5b. For both, the model and the measurements, the curves for the different mass flows lie on top of each other. The measured values of the relative entropy fluctuations seem to approach unity for $f_v \to 0\,\text{Hz}$.

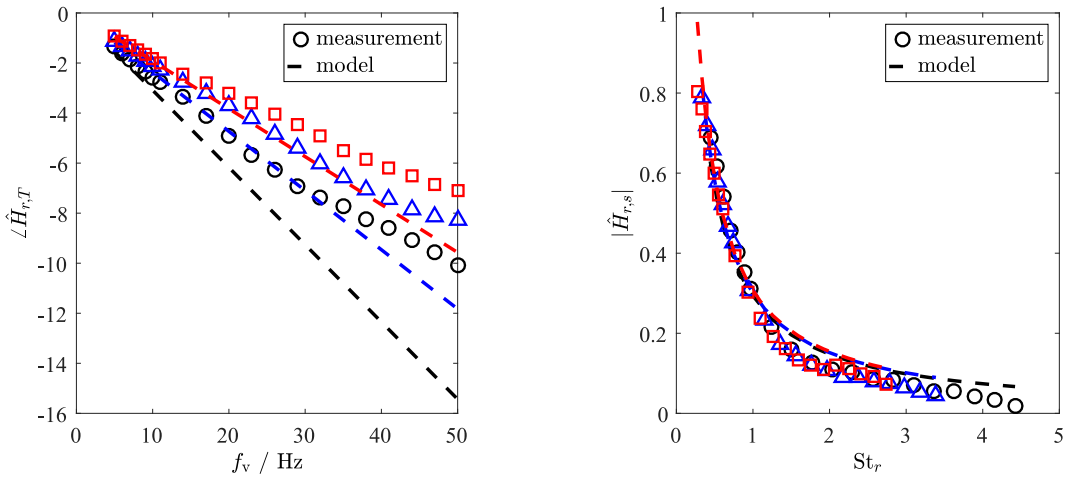

(a) **(b)**

Figure 6.5: **(a)**: **Markers**: Phase of the measured transfer function $\hat{H}_{r,T}$, which represents the phase difference between the equivalence ratio fluctuations in the mixing tube and the temperature fluctuation at the exit of the reactor at $L_r = \Delta x1$; (○ black): 140 kg/h, (△ blue): 180 kg/h, and (□ red): 220 kg/h. **Dashed lines**: Reconstructed phase difference by means of the estimated bulk flow velocity based on mass conservation (see Tab. 6.2). **(b)**: Relative entropy fluctuations as a function of the Strouhal number $St_r = fL_r/u_r$, the symbols correspond to the measured values and the dashed line to the model shown in Eq. 6.11.

The good match between the model and the measurement is striking, as only one parameter is optimized to fit the model to the measured transfer function. Furthermore, this model comprises a lot of simplifications and assumptions, which might partly be questionable. In addition to all the strict assumptions for the consideration of a well-stirred reactor, the application of linearization supposes a small perturbation around the mean values. In case of the equivalence ratio fluctuations with an amplitude of $g = 25\,\%$, this requirement might be violated. Additionally, upstream acoustic perturbations are neglected, which are definitively present. The good results nevertheless demonstrate that, in the present case, the model is applicable.

Reactor model: summary

Based on the linearized mass conservation, energy conservation, and state equation, a (well-stirred) reactor model is derived. Even though such a zero-dimensional model comprises several assumptions and simplifications, its resulting transfer function between the equivalence ratio fluctuations upstream of the burner and the temperature fluctuations close to the flame fits very well to the measured transfer function. The amplitudes of the temperature fluctuations decrease strongly for increasing fuel modulation frequencies. The model reveals that this characteristic is governed by the average residence time of a gas particle in the combustion zone. This average residence time can be derived from the bulk flow velocity estimated by means of the known air mass flow rate and the steady temperature in the reaction zone. The latter can be obtained from thermocouples.

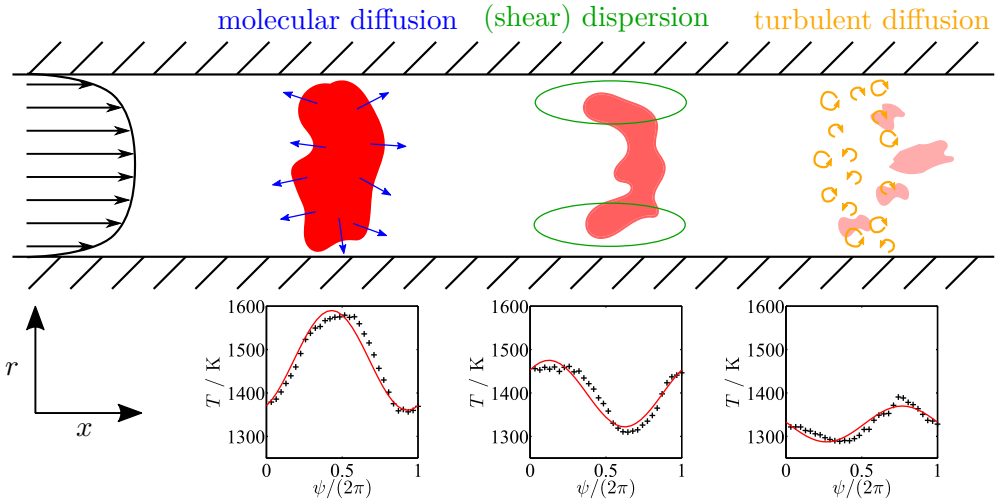

Figure 6.6: Schematic illustration of the dissipation of a temperature spot in a circular duct flow; the different mechanisms are shown schematically at three different axial positions in the duct; it is important to note that all dissipation mechanisms happen in parallel and at all axial locations. The bottom graphs depict measured temperature fluctuations of a $f_v = 7\,\mathrm{Hz}$ fuel modulation at three different axial locations $\Delta x1$, $\Delta x3$, and $\Delta x6$, respectively.

6.2 Transport of entropy waves

In Sec. 6.1, we investigated the frequency response of temperature fluctuations due to equivalence ratio fluctuations close to the reaction zone. Provided that the amplitude of the equivalence ratio fluctuation can be approximated, this allows an estimation of the temperature fluctuation amplitude and thus of the strength of the entropy waves at the reaction zone. In a typical combustor design, such entropy waves are convectively transported over a certain distance to the combustor exit. This transport, however, is not a pure advection process, but the entropy wave is subject to dispersive and diffusive effects. For the occurrence of indirect combustion noise it is crucial to know the strength of the entropy fluctuation that arrives at the contraction of the first turbine stage. The analysis and quantification of this transport mechanism is the objective of this section.

In Fig. 6.6, the different mechanisms that lead to the dissipation of the strength of an advected entropy wave in a duct flow are illustrated. The molecular diffusion is driven by the temperature gradient and does not depend on the flow field. The turbulent diffusion, i.e. the mass transport due to turbulent motions in the flow, is of course a function of the flow field (this turbulent diffusion might also be referred to *turbulent dispersion*, which is investigated amongst others by H. A. Becker et al. (1966)). The term dispersion describes the distortion of the temperature spot due to non-uniformities in the flow field. For a typical turbulent flow field in a duct, as it is shown in Fig. 6.6 on the very left-hand side, the largest gradient of the mean axial velocity is found in the near-wall region in the shear layer. This is the reason why it is often termed *shear dispersion* in the literature (e.g., Morgans, Goh, et al. (2013)).

The theory of the transport model deployed in this study is introduced in Sec. 6.2.1. The model was conceived by Jonas Moeck [1] and its detailed derivation is yet unpublished.

[1] Hermann-Föttinger Institut, Combustion Dynamics, TU Berlin (part of the reviewer committee for this thesis)

However, an application of this particular model can be found in Bobusch et al. (2013), where the mixing process between fuel and air due to diffusion and dispersion has been modeled.

6.2.1 Transport model: theory

Analytic investigations of the transport of entropy waves have already been performed by Morgans, Goh, et al. (2013). They found dispersion to be the governing mechanism which triggers the damping of entropy waves that are advected by a fully developed turbulent duct flow. The entropy transport model they derived, however, requires knowledge about the radial distribution of the actual velocity field. In this study, we did not assess the radial profile of the axial velocity and thus cannot apply this type of model.

Comprehensive investigations conducted by Taylor (1953) and Taylor (1954) showed that dispersive effects could also be modeled by means of an *effective* or *virtual* diffusivity, which can be treated as the (molecular) diffusion coefficient that appears in the one-dimensional transport equation. The assumptions that have to be made in order to be allowed to apply Taylor's ansatz will be discussed in the following. However, we will derive the transport equation in a general, three-dimensional manner first.

For the derivation of the one-dimensional transport model, in this study we consider the spatio-temporal evolution of the perturbation of a scalar, here the perturbation of the gas temperature T, within a duct flow field. It is assumed that this flow field is unaffected by the scalar. This is valid in case of small temperature perturbations compared to the mean temperature. Hence, gas properties like the gas density or the specific heat capacity are considered to be independent of the periodic temperature variation. In case of a source-free domain, the transport equation of the temperature field writes

$$\frac{\partial T}{\partial t} + \mathbf{u} \cdot \nabla T = \underbrace{\nabla \cdot (\alpha_{md} \nabla T)}_{\text{diffusion}} - \underbrace{\nabla \cdot \left(\overline{\mathbf{u}'T'}\right)}_{\text{turbulent flux}}, \tag{6.15}$$

with the mean velocity vector $\mathbf{u}$, the molecular diffusion coefficient α_{md}, an the ∇-operator, which denotes the spatial derivative in all three directions. The term on the right-hand side denotes the molecular diffusion according to Fick's law and the turbulent mass transport, respectively. The term for the turbulent flux as it is written in Eq. 6.15 introduces two more unknowns and thus causes the system to be not closed anymore. If one assumes that the diffusion process is Fickian, which means that the mass transport due to turbulence is proportional to the mean spatial gradient of the scalar field, an eddy diffusivity coefficient α_{ed} can be introduced as: $\overline{\mathbf{u}'T'} = -\alpha_{\mathrm{ed}}(\partial T/\partial x)$. The coefficient α_{ed} comprises the turbulent characteristic of the underlying flow field and can be determined by $\alpha_{\mathrm{ed}} = \nu_t/\mathrm{Pr}_t$, with the eddy viscosity ν_t and the turbulent Prandtl number Pr_t. Note, for our study we can assume that the turbulent time scales are distinctively smaller than the time scales of the temperature perturbations that are transported through the domain.

We now define an effective diffusivity $\alpha_{\mathrm{eff}} = \alpha_{\mathrm{md}} + \alpha_{\mathrm{ed}}$, which contains the molecular diffusivity as well as the turbulent diffusivity, which allows to write the transport equation

as

$$\frac{\partial T}{\partial t} + \mathbf{u} \cdot \nabla T = \nabla \cdot (\alpha_{\text{eff}} \nabla T) \,. \tag{6.16}$$

The effective diffusivity is assumed to be not affected by the temperature perturbations, which holds true for sufficiently small perturbation amplitudes. We further assume a stationary flow field, so $\mathbf{u}$ and α_{eff} do not vary in time. By introducing a harmonic perturbation of the temperature in time at the domain's boundary with the angular frequency ω, the Fourier transformed transport equation allows for an analysis of the temperature transport in the frequency domain:

$$i\omega \hat{T} + \mathbf{u} \cdot \nabla \hat{T} = \nabla \cdot \left(\alpha_{\text{eff}} \nabla \hat{T} \right) . \tag{6.17}$$

Analog to the formalism in Sec. 6.1.1, the Fourier transform is defined as $\partial/(\partial t) \mapsto i\omega$ and the superscript $\hat{()}$ denotes the fluctuation amplitude in frequency domain. For a given frequency, the solution of Eq. 6.17 provides an amplitude and a phase of the temperature fluctuation at an arbitrary axial position in the computational domain. We are mainly interested in the evolution of the cross-sectionally averaged temperature in axial direction. Consequently, the transfer function is defined as

$$\hat{H}_{t,T}(\omega) = \frac{\hat{T}(\omega, \mathbf{x}_{\text{do}})}{\hat{T}(\omega, \mathbf{x}_{\text{up}})}. \tag{6.18}$$

This is the ratio between the temperature fluctuation amplitude at a certain axial location $\mathbf{x}_{\text{do}}$ and the temperature fluctuation amplitude at a location $\mathbf{x}_{\text{up}}$ further upstream.

So far we formulated the transport equation in a multi-dimensional manner. As we do not have information about the three-dimensional or two-dimensional flow field, we would like to simplify the model to a one-dimensional system. Here, the aforementioned problem rises, which is that dispersion could not exist since the one-dimensional consideration presupposes a radially uniform flow field. However, Taylor (1953) showed that the influence of a non-uniform flow field on the evolution of a scalar field could be represented by an effective longitudinal molecular diffusivity. For a one-dimensional formulation of Eq. 6.17, i.e.,

$$\frac{\partial T}{\partial t} + u \frac{\partial T}{\partial x} = \alpha_{\text{eff}} \frac{\partial^2 T}{\partial x^2}, \tag{6.19}$$

he derived an expression for the effective diffusivity as $\alpha_{\text{eff}} = \frac{R^2 u^2}{48 \alpha_{\text{md}}}$ with the duct's radius R and the usual molecular diffusivity α_{md}. He considered a laminar flow in a circular duct and investigated the concentration field of a soluble, e.g., salt, in water. The fact that the effective diffusivity is inversely proportional to the actual diffusivity in his correlation stems from the neglection of longitudinal molecular diffusion and the strong dominance of lateral diffusion:

$$\frac{\partial^2 T}{\partial x^2} \ll \frac{\partial^2 T}{\partial y^2} + \frac{1}{y} \frac{\partial T}{\partial y}. \tag{6.20}$$

Here, y denotes the spatial coordinate in radial direction. This assumption can be justified for low temperature fluctuation frequencies, where the convective wavelength, i.e., the spatial extent of the temperature distortion in axial direction, is sufficiently

large. In case of higher frequencies, however, it is questionable whether this assumption still holds true. At a later stage in this analysis, we will see that this assumption could be considered as valid for the measurements conducted in this study. In a subsequent investigation, Taylor (1954) studied the dispersion of a concentration field in a turbulent flow through a circular duct. There, he considers a typical radial velocity field and derives a virtual coefficient of diffusion

$$\alpha_{\text{eff}} = 10.1 R v^* \qquad \text{with} \qquad v^* = \sqrt{\frac{\tau_0}{\rho}}, \tag{6.21}$$

where v^* represents the wall shear velocity and τ_0 denotes the friction stress that is exerted by the turbulent fluid on the wall. The correlation in Eq. 6.21 also accounts for longitudinal diffusion. Taylor (1954) obtains in his analysis that the diffusion in axial direction contributes only marginally to the diffusion coefficient (factor 10.06 instead of 10.1 in Eq. 6.21 if longitudinal diffusion would be neglected). Obviously, the numbers derived for the virtual diffusivity depend on the radial flow field that is presumed and the wall shear velocity; both have not explicitly been determined in this study. Taylor (1954), however, provides the ratio $\overline{u}/v^*$ for a wide range of Reynolds numbers, which also comprises the Reynolds numbers relevant for the measurements conducted in this study ($\text{Re} \approx 6 \cdot 10^3$).

To solve Eq. 6.19 for $T(\omega, x)$, we first non-dimensionalize it by a characteristic length scale L and the constant mean flow velocity $\overline{u}$. If we assume a constant effective diffusivity α_{eff} and multiply Eq. 6.19 by $L/\overline{u}$, we obtain

$$\left(i \frac{L}{\overline{u}} \omega + L \frac{\partial}{\partial x} - \frac{\alpha_{\text{eff}}}{\overline{u} L} L^2 \frac{\partial^2}{\partial x^2} \right) \hat{T} = 0. \tag{6.22}$$

A more compact expression is obtained by introducing the Peclet number Pe, which denotes the ratio between a convective time scale and a diffusive time scale:

$$\text{Pe} = \frac{\tau_{\text{conv}}}{\tau_{\text{diff}}} = \frac{L^2/\alpha}{L/\overline{u}} = \frac{\overline{u} L}{\alpha_{\text{eff}}}. \tag{6.23}$$

Additionally, we define the dimensionless terms for the spatial derivatives $\hat{T}' = L\partial/(\partial x)$ and $\hat{T}'' = L^2\partial^2/(\partial x^2)$ and the dimensionless angular frequency $\omega^* = \omega L/\overline{u}$, which allows for the formulation of Eq. 6.22 in the form

$$\hat{T}'' - \text{Pe}\hat{T}' - i\omega^* \text{Pe} = 0. \tag{6.24}$$

The general solution for this second order differential equation reads

$$\hat{T}(\omega^*, x) = C_1 e^{k^+(\omega^*)x} + C_2 e^{k^-(\omega^*)x}, \tag{6.25}$$

with the exponential coefficients $k^{\pm}(\omega^*) = \frac{\text{Pe}}{2}\left(1 \pm \sqrt{4i\omega^* \text{Pe}^{-1} + 1}\right)$ and the integration constants C_1 and C_2. To determine the solution, we consider the real part of the exponential coefficients. In case of k^+, the real part is always greater than one, which means that the first term on the right-hand side in Eq. 6.25 would grow exponentially for positions further downstream in the duct. This can clearly be considered as unphysical and we set $C_1 = 0$. The second integration constant thus refers to the inlet temperature

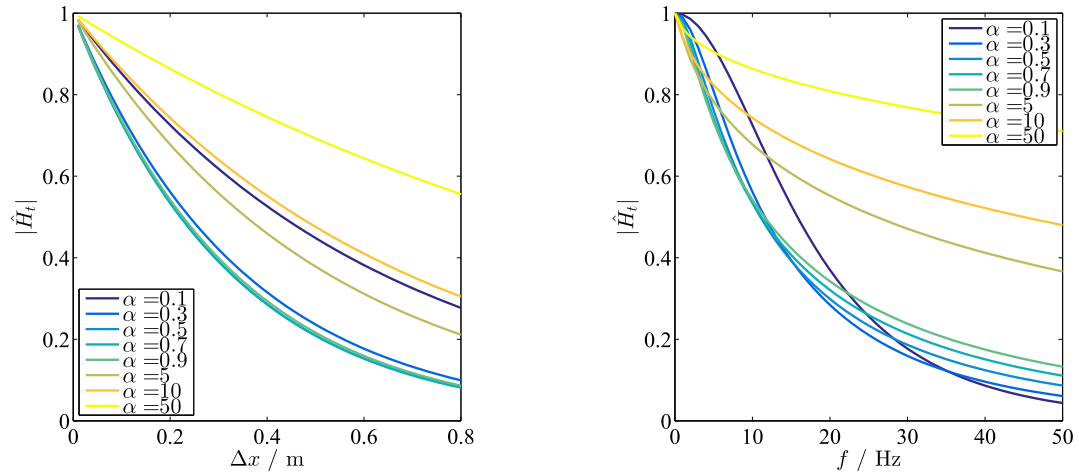

(a) **(b)**

Figure 6.7: Absolute value of the transport transfer function $\hat{H}_t$ as it is defined in Eq. 6.27 as a function of **(a)**: the transport distance Δx (with $f = 10\,\text{Hz}$). **(b)**: the perturbation frequency f (with $\Delta x = 0.2$ m); the bulk flow velocity is set to $\overline{u} = 6$ m/s, which is a typical value for the measurements in this study.

fluctuation $\hat{T}_{\text{inlet}}$ at the very upstream end of the duct, which leads to the final solution for the time harmonic temperature field as

$$\hat{T}(\omega^*, x) = \hat{T}_{\text{inlet}} e^{k^-(\omega^*)x}. \tag{6.26}$$

In terms of the transfer function between the temperature at a position x_{do} in the duct and a temperature fluctuation at an axial position x_{up} further upstream (see Eq. 6.18) we finally obtain

$$\hat{H}_t(\omega) = \exp\left[\frac{\text{Pe}}{2}\left(1 - \sqrt{4i\omega\frac{L}{\overline{u}\text{Pe}} + 1}\right)\right]. \tag{6.27}$$

Analogously to the reactor model in Sec. 6.1.1, we can identify a Strouhal number that we define as *transport Strouhal number* $\text{St}_t = f\Delta x/\overline{u}$ with the distance Δx defined as the advective length between the two axial locations in the duct the transfer function is evaluated at: $\Delta x = x_{\text{do}} - x_{\text{up}}$. Consequently, the transfer function $\hat{H}_t$ can be expressed in terms of this Strouhal number as

$$\hat{H}_t(\text{St}_t) = \exp\left[\frac{\text{Pe}}{2}\left(1 - \sqrt{8\pi i\frac{\text{St}_t}{\text{Pe}} + 1}\right)\right]. \tag{6.28}$$

The only variable parameter in Eq. 6.28 is the Peclet number, the Strouhal number is defined by the transport distance, the mean velocity in the duct, and the frequency of the temperature fluctuation. Thus, the Peclet number or the virtual diffusion coefficient will be used to fit this transport model to the measured spatial evolution of the temperature fluctuation. In Fig. 6.7, the absolute value of $\hat{H}_t$ is plotted as a function of the transport length Δx and of the frequency f for different values of the virtual diffusion coefficient (which will from now on be denoted as α). In case of the variation of the advection length Δx (Fig. 6.7a), the evolution of $|\hat{H}_t|$ as well as the trend for increasing values

of α meet the expectations. The larger the distance the temperature fluctuation has to pass, the more it is smeared out. Obviously, this process is enhanced if the diffusivity is increased.

This picture is not that clear in terms of a frequency variation as can be seen in Fig. 6.7b. Of course, the absolute value of $\hat{H}_t$ decays for increasing frequencies; however, the evolution with respect to an increasing virtual diffusion coefficient is not that plausible anymore. Up to $\alpha \approx 1$ and for small frequencies the decay becomes stronger for increasing diffusivities. This meets the expectation, but for higher values of α and for larger frequencies, this behaviour is reversed. As typical values for α are found to be $0.2 < \alpha < 1$ and a proper measurement of temperature fluctuation amplitudes becomes difficult for $f \gtrapprox 25\,\mathrm{Hz}$, this phenomenon does not affect the investigations in this study.

In the subsequent section, the model that we derived in this subsection, will be compared and fitted to the experimentally obtained temperature fluctuation amplitudes.

6.2.2 Strouhal number analysis

Before we compare the transport model, which has been derived in the preceding section, with the measured transfer function, we first have a more detailed look into the measured temperature fluctuations with respect to different parameter variations. They form the basis for the model validation conducted in the subsequent section. The TOF measurement results have been presented in Sec. 5.4.2, where we focused on the frequency response of the temperature perturbation to equivalence ratio fluctuations in the flame zone. The three major parameters that affect the dissipation of entropy waves and that have been varied in the measurements are the flow velocity u, the perturbation frequency f, and the advection length Δx. All these parameters are combined in the Strouhal number $\mathrm{St} = f\Delta x/u$, which enables the investigation of the characteristics of entropy waves in a multi-parameter domain. The strong dependence of the amplitude and the phase of an entropy wave on this dimensionless parameter can clearly be seen in Fig. 6.8. On the left-hand side, the normalized entropy fluctuations are plotted as functions of the fuel modulation frequency and on the right-hand side, the same measurement data are presented with respect to the Strouhal number.

As the amplitude and the phase of the entropy fluctuations depicted in Fig. 6.8 are normalized with the entropy fluctuation in the flame zone (see Eq. 5.14), the advection length comprised in the Strouhal number is here defined as the distance between the burner front plate and the TOF measurement plane (see Tab. 5.1). The corresponding bulk velocity $\overline{u}$ is evaluated as $\overline{u} = \dot{m}/\rho/S$, where the gas density ρ is a function of the time-averaged temperature, which in turn is a function of the air mass flow as well as of the axial location in the duct. Note, the entropy waves shown in Fig. 6.8 have been extracted by means of the SVD method (see Sec. 5.4.2.1). Only data that have been extracted with this method will be used for the investigations in the following since it has been shown in Sec. 5.4.2.3 that the difference to the alternative extraction method via tomographic means delivers very similar results.

The very good match of the amplitudes as well as of the phases with respect to the Strouhal number in Fig. 6.8 allows for an estimation of the temperature fluctuation amplitude for an arbitrary combination of flow velocity, perturbation frequency, and

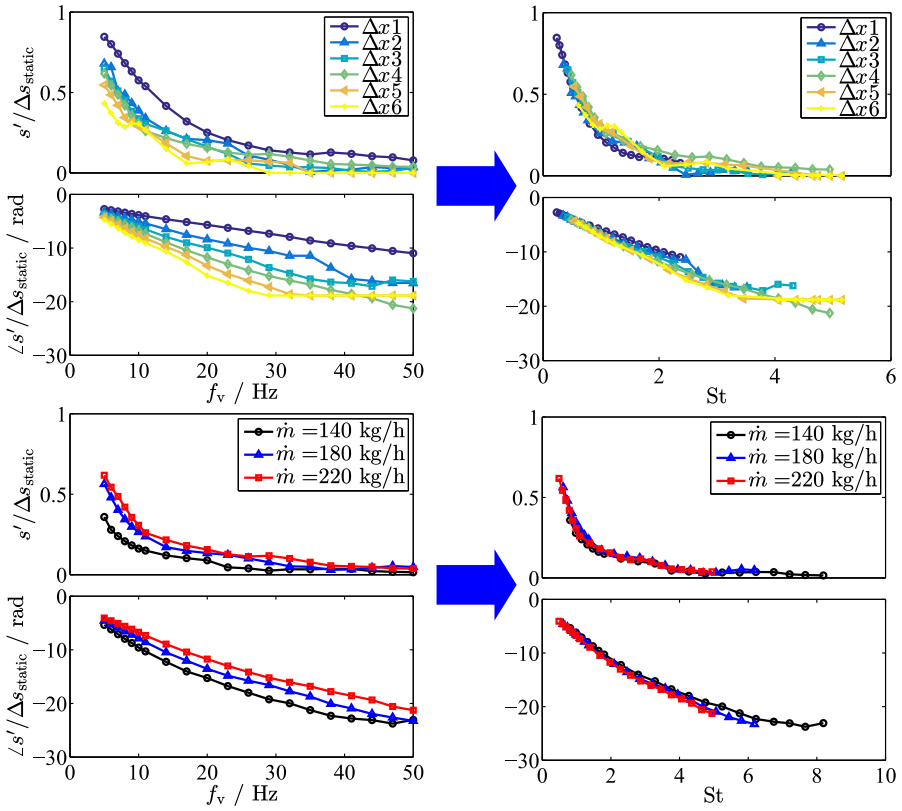

Figure 6.8: Amplitudes and phases of the normalized entropy fluctuations measured at different axial locations Δx and for different air mass flows $\dot{m}$ as function of the fuel modulation frequency (left) and as function of the Strouhal number $\mathrm{St} = f\Delta x/u$; the length Δx refers to the distance between burner front plate and the TOF measurement plane (see Tab. 5.1). The measurements depicted in the upper plot have been conducted with $\dot{m} = 220\,\mathrm{kg/h}$ and the measurements in the lower graphs have been performed at $\Delta x = 4$.

axial position with respect to the flame. The strongest decay of the amplitude is clearly found for Strouhal numbers $\mathrm{St} < 1$, above $\mathrm{St} \approx 1$ the fluctuation amplitude is less than 25 % of its initial value. This means that the dissipation of the entropy fluctuation is most prominent if the convective wavelength $\lambda_c = u/f$ is shorter than the advection length Δx.

6.2.3 Transport model: results

The wide experimental variation of the three parameters u, Δx, and f_v allows for a comprehensive validation of the transport model. If we consider the formulation used in Eq. 6.28, the virtual diffusion coefficient, which is comprised in the Peclet number, Pe, is the only parameter that is supposed to remain constant throughout the multi-dimensional parameter sweep. Therefore, a non-linear two-dimensional least square solver is employed to fit the model to the data by finding an optimal value for the virtual diffusivity α. All the measurement data that are employed for the model validation in this section are presented in Fig. 6.9. Frequencies above 12 Hz are not considered here. It can be deduced from Fig. 6.8 that the fluctuation amplitudes in the higher frequency range are already too small, i.e., the measurement error is of the order of the difference in amplitude between measurements at two different axial locations.

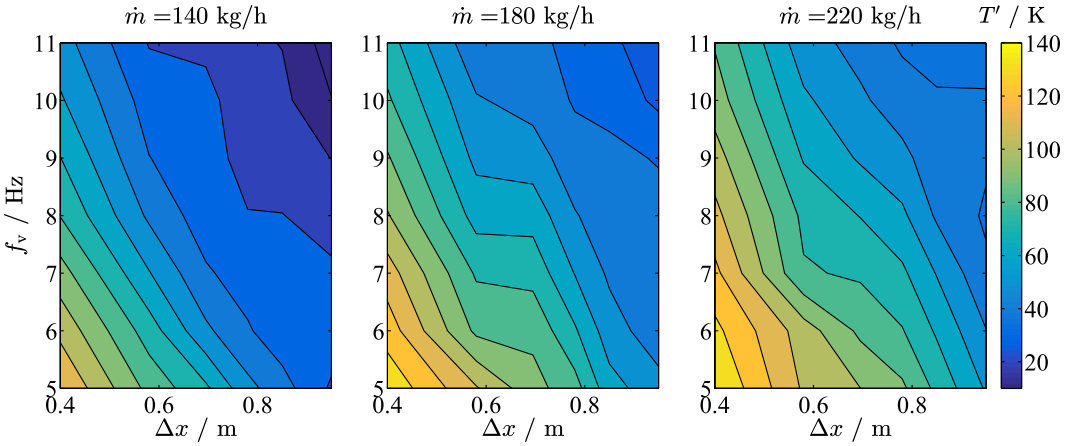

Figure 6.9: Measured temperature fluctuation amplitudes as functions of the fuel modulation frequency f_v and the distance between the burner front plate and the TOF measurement plane Δx for three different mass flows of air (=flow velocities).

To investigate the transport characteristics of entropy waves in the combustor duct, we do not consider the transportation from the flame zone to the measurement plane. In Sec. 6.1 it has been discussed that transport mechanisms in the flame zone are governed by the recirculation zone and the associated residence time. Here, the advection of entropy waves in a preferably fully developed flow field in the circular duct should be examined. Therefore, we focus on the amplitude and phase evolution of the periodic entropy perturbation between the six different axial locations the TOF measurements have been performed at (see Tab. 5.1). This provides 15 different advection distances between $\Delta x = 0.07\,\mathrm{m}$ and $\Delta x = 0.55$ m. As these sections are located at different axial positions in the duct, they experience different mean temperatures and consequently slightly different flow velocities for the same air mass flow.

The theory and the experimental study of Taylor (1953), which has been described in the preceding section, is actually based on the advection of a single concentration spot in a duct flow, harmonic perturbations are not taken into account. This is why we first seek to find an optimal match between the modeled and measured transport transfer function separately for each fuel modulation frequency. This enables us to detect potential dependencies of the virtual diffusion coefficient on the fuel modulation frequency. Furthermore, the optimization procedure has been performed discretely for the three different air mass flows. In Fig. 6.10, the results obtained from the model are compared to the measured absolute values and phases of $\hat{H}_t$. This plot should give an idea of the spread of the measurement data and it should as well provide an idea of the overall trend of the transport transfer function with respect to the various parameters. The meaning of the symbols and their size is explained in the caption. The expected decay of $|\hat{H}_t|$ for increasing Strouhal numbers (= smaller convective wavelengths λ_c compared to the transportation length) is very obvious. Also the linear decay of the phase and the clear match of all phases with respect to the Strouhal number prove the plausibility of the measurement results. The significantly wide spread of the measured absolute values of the transfer function has two reasons. Firstly, the amplitude values are affected by measurement uncertainties that are of the order of the differences in amplitude between to different axial locations that are close to each other (small Δx). The second reason for the large scattering of the measurement data is demonstrated by the coloring of the

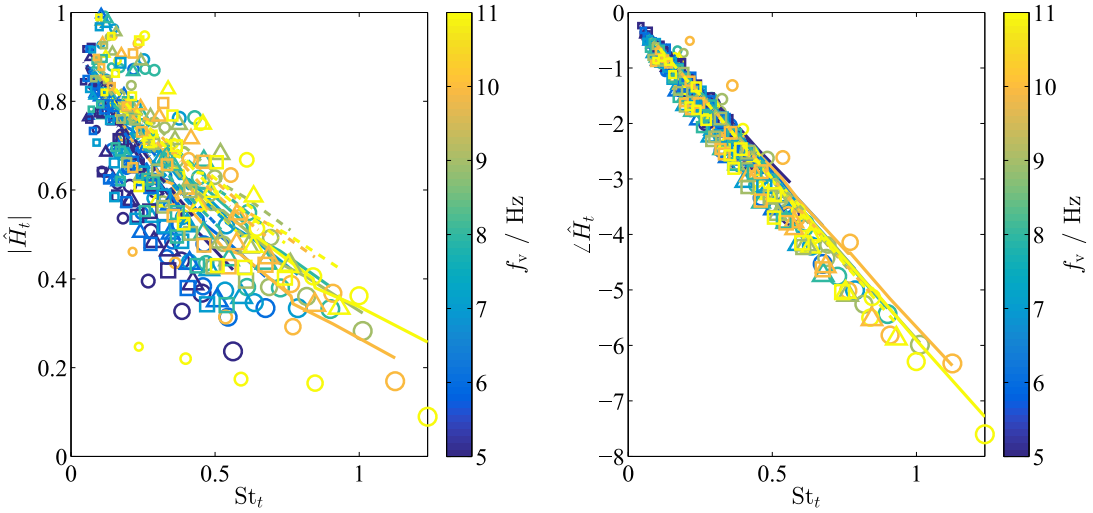

(a) **(b)**

Figure 6.10: Amplitude **(a)** and phase **(b)** of the measured (markers) and modeled (lines) transport transfer function $\hat{H}_t$ with a virtual diffusion coefficient optimized for each frequency and each mass flow ($\alpha \rightarrow \alpha(f_v, \dot{m})$); the colors correspond to the fuel modulation frequencies, the size of the markers corresponds to the advection length Δx (the larger the symbol the larger the distance), and the different symbols and line styles refer to the air mass flows $\dot{m}$ with (◯ and solid): 140 kg/h, (△ and dashed): 180 kg/h, and (□ and dashed-dotted): 220 kg/h. The Strouhal number St_t is defined by the advection length between two axial measurement positions.

markers. Obviously, the transport transfer functions which are evaluated for lower frequencies exhibit in average a larger drop in amplitude along the transportation distance compared to higher frequency cases of the same Strouhal number. This cannot be explained by measurement uncertainties but reveals that there is a slight dependence of the dissipation mechanisms on the frequency that is not covered by the Strouhal number.

A more lucid picture of the results of the model's fit to the measurements is given in Fig. 6.11. In Fig. 6.11a, the amplitude and the phase of the transport transfer function is plotted with respect to the advection distances Δx for three different air mass flows and a fuel modulation frequency $f_v = 6\,\mathrm{Hz}$. The optimization is performed such that it accounts for the absolute value $|\hat{H}_t|$ as well as for the phase $\angle\hat{H}_t$. This explains why the model underestimates the damping of the temperature amplitude but finds a very good match for the measured phase decay. The same applies when the transport transfer function is plotted against the fuel modulation frequency. Note that the variation in amplitude due to variations in frequency is very small. It even looks like the amplitude increases for higher frequencies, this is due to the fact that the changes in amplitude are of the same magnitude as the measurement uncertainty. The discontinuities that can be observed in the model's results in terms of the amplitude stem from the slightly different flow velocities along the various advection distances due to their different axial locations (which come along with different mean flow temperatures).

As the optimization of $\hat{H}_t$ for the virtual diffusion coefficient α was performed by means of the evolution of $\hat{H}$ with respect to the advection distance Δx, the resulting virtual diffusion coefficient is a function of the fuel modulation frequency and the air mass flow:

$\alpha = \alpha(f_v, \dot{m})$. Its values are depicted in the upper graph in Fig. 6.12a. A distinct dependency of α on the fuel modulation frequency as well as on the air mass flow is observed. However, both trends, the increasing diffusivity for decreasing frequencies as well as the larger values for α for increasing air mass flows are contradicting to what would be expected at a first glance. It seems that the model overestimates the decay of the temperature amplitudes for increasing frequencies as well as for decreasing air mass flows. Considering that the idea of the virtual diffusion coefficient is based on a single spot advection, one would expect that the increase of frequency would lead to an increased diffusivity. It is, however, worth noting that the increase of the fuel modulation frequency coincides with a significant drop in temperature amplitude. So it could be suggested that the variation of the virtual diffusion coefficient in the upper plot in Fig. 6.12a might also originate from the variation of the absolute values of the temperature amplitude rather than from the frequency variation.

Measurements of the high-temperature dependence of the molecular (self-) diffusivity have been conducted by Walker and Westenberg (1958) and Ember et al. (1962). It can be seen in Fig. 6.12b that there is a significant variation of the diffusivity with respect to the gas temperature ($\alpha \propto T^{1.65}$). The absolute values of the diffusion coefficients depend in fact on the properties of the gases that are investigated, in Fig. 6.12b, the diffusivity of CO_2 into N_2 has been considered. The trend towards higher diffusion coefficients for increasing temperatures, however, is observed for all kinds of gases and is found between $\alpha \propto T^{1.5}$ and $\alpha \propto T^{1.75}$ (H. Li, Wilhelmsen, et al., 2011). In our experiments, we measured amplitudes of the cross-sectionally averaged surface temperature of up to 140 K (they might be higher at certain radii in the duct) and changes of the mean temperature of maximum 160 K (from about 1300 K to 1460 K) due to the different air mass flows. Even if applied to the total virtual diffusion coefficient (the temperature dependence actually only applies for the molecular diffusivity), this would cause an increase from, e.g., $\alpha = 0.5$ m^2/s to $\alpha = 0.61$ m^2/s. This does not fully explain the slope of the virtual diffusion coefficient with respect to the frequency obtained in the upper plot in Fig. 6.12a. It is also worth noting that the order of magnitude of the molecular diffusion coefficients in Fig. 6.12b is by far less than the virtual diffusivities in the upper plot in Fig. 6.12a. This exhibits the importance of the dispersive effects on the advective transport of entropy fluctuations.

There is one aspect, however, that has not been taken into account so far. In contrast to the experimental investigations of Taylor (1954), the experimental setup in this study is highly non-adiabatic, as the walls of the combustor are massively cooled with water at about 330 K which flows through copper pipes wrapped around the combustor duct. This causes two phenomena to rise, that have not yet been considered: the heat conduction at the wall and the heat radiation of the exhaust gas. Both effects become more prominent at higher gas temperatures; in our case this might be caused by an increase of the mean temperature due to an increase of the air mass flow as well as by an increase of the absolute temperature amplitude. In a very recent study of Fattahi et al. (2017), it is shown that heat conduction at the wall significantly enhances the dissipation of advecting entropy fluctuations. They conducted a compressible large eddy simulation of a gas flow between two parallel plates. Their calculations exhibit an increased loss in amplitude as well as an enhanced loss in coherence for increased heat conduction at the plates.

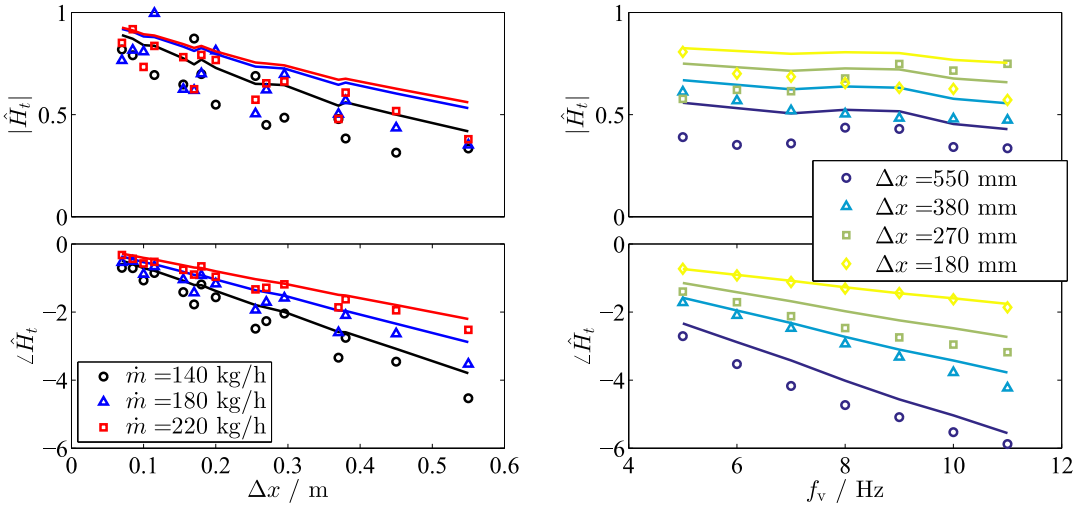

(a) **(b)**

Figure 6.11: **(a)**: Amplitude (top) and phase (bottom) of the measured (markers) and modeled (lines) transport transfer function $\hat{H}_t$ for three different air mass flows and a fuel modulation frequency $f_v = 6\,\text{Hz}$; the fit is achieved by a separate value of α for each air mass flow (see markers in the top plot in Fig. 6.12a). **(b)**: Amplitude (top) and phase (bottom) of the measured (markers) and modeled (lines) transport transfer function $\hat{H}_t$ as function of the fuel modulation frequency for three different transportation lengths and an air mass flow of $\dot{m} = 180\,\text{kg/h}$; the corresponding values of α can be found in the top plot of Fig. 6.12a.

A quantification of these additional dissipation mechanisms is not straightforward and would come along with further assumptions. We therefore decide to split the diffusion coefficient into a part α_{Taylor} as it is defined by Taylor (1954) and an additive part α_{add} which serves as optimization parameter used to fit the model to the measurement data. Besides the total diffusion coefficient α, Fig. 6.12a also depicts the values for the virtual diffusion coefficient α_{Taylor} predicted by Taylor (1954) based on Eq. 6.21 (dashed lines). These values are only a function of the flow velocity. They, of course, do not depend on the frequency as periodic fluctuations have not been considered in Taylor (1954). The additional part of the diffusion coefficient $\alpha_{\text{add}} = \alpha - \alpha_{\text{Taylor}}$ is shown in the bottom graph of Fig. 6.12a. Apart from some deviations it seems that α_{add} does not depend on the mean flow velocity and might cover the aforementioned effects. In the further use of the model in Eq. 6.28, a constant value $\alpha_{\text{add}} = -0.35$ was applied, which is the average value found in the relevant frequency range.

Comparison to other models in literature

The advection process and the associated dissipation of entropy waves has been studied by Sattelmayer (2002) and quite recently by Morgans, Goh, et al. (2013), Giusti et al. (2017), and Fattahi et al. (2017). Prior to these studies, the transport of entropy perturbations due to equivalence ratio fluctuations upstream of the flame has most often been considered to happen without attenuation, e.g., Hubbard and A. Dowling (1998); Polifke, Paschereit, et al. (2001); Leyko et al. (2009), where the entropy wave is advectively transported with the bulk flow velocity. Therefore, a simple time lag model

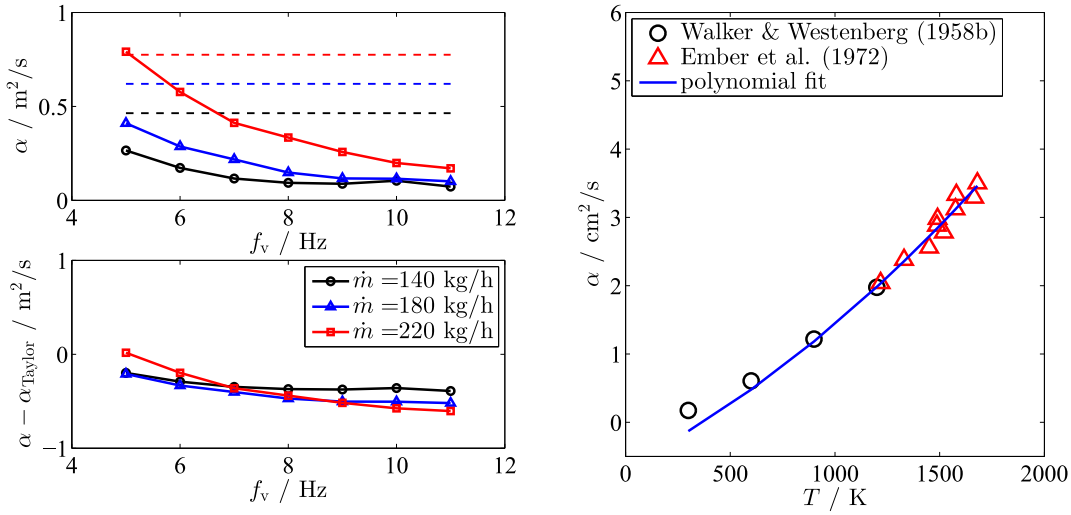

(a) **(b)**

Figure 6.12: **(a)**: (Top): Resulting virtual diffusion coefficients (markers) obtained from a least-square algorithm for fitting the measured transport transfer function $\hat{H}_t$ to the model shown in Eq. 6.28, the corresponding fits are shown in Figs. 6.10 and 6.11. The dashed lines denote the virtual diffusion coefficients α_{Taylor} based on Eq. 6.21. (Bottom): Additive diffusion coefficient $\alpha_{\text{add}} = \alpha - \alpha_{\text{Taylor}}$ based on the top graph. **(b)**: Temperature dependence of the molecular diffusion coefficient experimentally assessed by Walker and Westenberg (1958) and Ember et al. (1962).

with a constant amplitude serves as analytical means to relate the entropy fluctuation generated at the flame to the one arriving at the turbine inlet. As the other extreme it has been assumed that the entropy spot will fully smear out before reaching the turbine inlet (Stow and A. P. Dowling, 2001).

Sattelmayer (2002) was the first who considered aerodynamic phenomena, thus spatial (turbulent) dispersion due to recirculation zones or boundary layers, to significantly affect the transport characteristics of entropy waves in gas turbine combustors. Based on the radial distribution of residence times of particles in the combustor (the distribution is a function of the mean velocity field) he derived a probability density function (PDF) of the delay times of these particles at an arbitrary axial position in the combustor. This PDF corresponds to the impulse response to a pulse of a scalar at an axial position further upstream. The growth of the width of the impulse response in time, which is simplified to a rectangular shape, determines the decay of the scalar the impulse is associated to. This scalar could be an equivalence ratio perturbation in order to estimate its decay in the mixing section of a combustor or an entropy spot downstream of the flame. The model, which is finally derived by Sattelmayer (2002), reads in a slightly simplified manner (Eckstein and Sattelmayer, 2006):

$$\hat{H}_S(\omega) = \frac{\sin(\omega\Delta\tau)}{\omega\Delta\tau} e^{-i\omega\overline{\tau}_{\text{delay}}}. \tag{6.29}$$

In a one-dimensional consideration, the mean time delay $\overline{\tau}_{\text{delay}}$ refers to $\overline{\tau}_{\text{delay}} = \Delta x/\overline{u}$, where Δx and $\overline{u}$ denote the transportation length and the mean flow velocity, respectively. The time $\Delta\tau$ represents half of the pulse width and serves as the optimization

variable to calibrate the model to measured data. Giusti et al. (2017) suggest a transformation of Eq. 6.29 to the Strouhal number space (they actually define a Helmholtz number He, which, however, is equal to the Strouhal number St_t used in this study). They assume a linear dependence of the growth of the width $\Delta\tau$ in time, which gives $\Delta\tau = k_S\overline{\tau}$ with the constant of proportionality k_S. This factor depends on the radial shape of the flow field and needs to be estimated if the spatial evolution of the flow field is unknown. With a Strouhal number defined as $\mathrm{St}_t = f\overline{\tau}_{\mathrm{delay}} = f\Delta x/\overline{u}$ the formulation in Eq. 6.29 becomes

$$\hat{H}_S(\mathrm{St}_t) = \frac{\sin(2\pi k_S \mathrm{St}_t)}{2\pi k_S \mathrm{St}_t} e^{-2i\pi \mathrm{St}_t}. \tag{6.30}$$

Based on the same principal idea, Schuermans, Bellucci, et al. (2004) and Morgans, Goh, et al. (2013) propose a model where the impulse response is modeled by a Gaussian profile rather than by a rectangular one. They make use of the convenient Fourier transform of a Gaussian pulse and derive the following expression for an input-output transfer function (here, the formulation presented in Morgans, Goh, et al. (2013) is used):

$$\hat{H}_M(\omega) = e^{-\frac{\omega^2}{4\pi A_{IR}^2}} e^{-i\omega\tau_s}. \tag{6.31}$$

Similar to the expression in Eq. 6.29, the phase of the entropy wave is modeled as a simple time lag; τ_s can be expressed as $\tau_s = \Delta x/\overline{u}$. The coefficient A_{IR} denotes the amplitude of the impulse response and can be assessed from the PDF of the residence times. This, of course, requires again knowledge about the radial flow field at the desired axial location the transfer function should be evaluated at. Again, Giusti et al. (2017) propose a way to rewrite this unknown coefficient and thereby transform $\hat{H}_M$ to a function of the Strouhal number. As the velocity field, and so A_{IR}, depends on the axial location Δx as well as on the flow velocity $\overline{u}$, they introduce another constant $k_M = A_{IR}\Delta/\overline{u}$ which leads to

$$\hat{H}_M(\mathrm{St}_t) = e^{-\pi\left(\frac{\mathrm{St}}{k_M}\right)^2} e^{-2i\pi \mathrm{St}_t}. \tag{6.32}$$

This formulation corresponds to the high-Pe limit of Eq. 6.28 (when convection dominates over diffusion), which becomes such a pure (undamped) time delay in combination with a Gaussian low-pass when expanding the argument of the exponential in inverse powers of Pe.

The two models presented in Eqs. 6.30 and 6.32 are compared to the measured transport transfer function and to the model $\hat{H}_t$ derived in Eq. 6.28 in Fig. 6.13. The transfer functions are plotted with respect to the Strouhal number and for variations of the model parameters k_S and k_M. As $\hat{H}_S$ and $\hat{H}_M$ both depend on the Strouhal number only, they are represented by a single curve whereas $\hat{H}_t$ depends additionally on the Peclet number. According to Fig. 6.10, $\hat{H}_t$ is therefore plotted for each fuel modulation frequency separately. The experimentally assessed data are represented by markers. Both models taken from literature exhibit a satisfying match to the measured data in certain Strouhal number ranges. It has already been shown in the study of Morgans, Goh, et al. (2013) that the frequency responses of the transfer functions $\hat{H}_S$ and $\hat{H}_M$ correspond well to each other; significant differences are not observed in this study either. As $\hat{H}_M$ employs a Gaussian distribution, the characteristic zeroes of the frequency response to a rectangular pulse do not exist. The wide spread of the measurement data

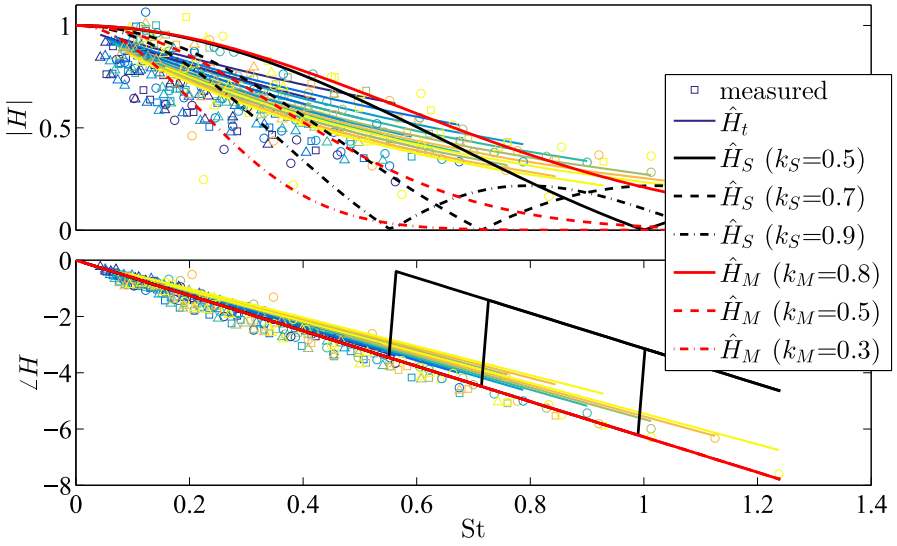

Figure 6.13: Comparison of the transport transfer function models $\hat{H}_S$ and $\hat{H}_M$ with the experimental results (markers) and the model $\hat{H}_t$ shown in Eq. 6.28; the diffusion coefficient α in $\hat{H}_t$ is evaluated with $\alpha = \alpha_{\text{Taylor}} + \alpha_{\text{add}}$ with a constant value $\alpha_{\text{add}} = -0.35$ (see bottom plot in Fig. 6.12a).

makes it difficult to judge which optimization parameter might fit best. In fact, the low frequency cases (bluish colored markers) in the low Strouhal number range are not well represented by all models. For larger values of k_S and smaller values of k_M, the measured transport transfer functions agree better to the models' predictions. However, this comes along with a too strong decay toward higher Strouhal numbers. It is worth noting that the phase of the measured transfer function is almost perfectly met by the models. This clearly shows that a consideration of the transport velocity by means of a time lag model, which comprises the axial transportation distance and the bulk velocity, is sufficient.

Experimental and numerical investigations of the propagation of entropy waves by Giusti et al. (2017) found a quite similar agreement in terms of the amplitudes between the models $\hat{H}_S$ and $\hat{H}_M$ with their measurement results. Only for some Helmholtz numbers (identical to the Strouhal number as it is used in this study), the models fit well to the experimental results. Their experimental approach is rather generic and thus is different to the combustion rig setup deployed in this thesis. They generated entropy waves in a circular duct with an inner diameter of $D = 21\,\text{mm}$ by means of periodic injection of methane into an axial air flow. Glow plugs at a position further downstream ignite the fuel air mixture whenever an ignitable mixture is passing. This causes a harmonic entropy perturbation traveling through the duct, which is detected via $25\,\mu\text{m}$ type K thermocouples at two positions further downstream in the duct ($\Delta x = 520\,\text{mm}$ and $\Delta x = 1020\,\text{mm}$). The use of bare-wired thermocouples is possible in their case as they experience only moderate temperatures. The temperature fluctuations, which by neglection of the pressure fluctuations correspond in their study to the entropy fluctuations, are analyzed in frequency domain. This allows for a time averaged temperature amplitude detection; however, phase information is not provided. It is not explicitly mentioned in their work at which frequencies the fuel is modulated. The presented

frequency response of their measured temperature amplitudes as well as the resulting Helmholtz numbers highly suggest that they performed the entropy excitation only with a frequency of $f = 10.7\,\mathrm{Hz}$. Consequently, the experimental variation in Helmholtz number in their measurements stems most probably only from variations of the bulk velocity and the two transportation lengths available.

The model they derive requires the radial velocity distribution $u(r)$ as an input, which in this study is not accessible:

$$\hat{H}_G(\mathrm{St}) = \frac{\hat{s}(x)}{\hat{s}_0} = \frac{2}{R^2\overline{u}} \int_0^R r u(r) e^{-2i\pi \mathrm{St} \frac{\overline{u}}{u(r)}} dr. \tag{6.33}$$

This formulation is derived from the one-dimensional formulation of the entropy transport as function of the duct's radius: $\partial s'/\partial t + u(r)\partial s'/\partial x = 0$. The entropy fluctuation $\hat{s}(x)$ corresponds to the mass-weighted radial average of the entropy, the reference entropy $\hat{s}_0$ denotes the radially uniform perturbation at the very upstream position. It is obvious that Eq. 6.33 behaves as a low-pass filter with respect to the Strouhal number. In terms of amplitude as well as of phase this model fits significantly better to their experimental data and to their CFD simulations. In contrast to our findings, the decay of the phase of the entropy waves is not well represented by a simple time lag based on the bulk velocity. Their numerical results exhibit a faster propagation of the entropy waves. Unfortunately, their experimental analysis lacks an assessment of the phase, and thus could not support their numerical finding.

Equation 6.33 is not directly applicable to the measurements of the investigations in this study. However, Giusti et al. (2017) provide additionally a more general expression of their model for the case of an unknown velocity field:

$$\hat{H}_G(\mathrm{St}) = e^{-(2i\pi\beta + B)\mathrm{St}}. \tag{6.34}$$

The constant β regulates the phase evolution with respect to the Strouhal number and B determines the amplitude decay. Both of these values require calibration. Due to the findings from the models in Eqs. 6.30 and 6.32, where we found a good correspondence between the measured phase and the time lag based on the bulk velocity, we fixed β as $\beta = 1$. In Fig. 6.14, the amplitude and the phase of $\hat{H}_G$ are compared to the measured transport transfer function. The constant B in the model is varied from $B = 0.5$ to $B = 3$, whereas a value of $B \approx 1.5$ seems to deliver the best overall match. Higher values of B lead to a better agreement between the model and the low-frequency measurements (bluish colored markers) at low Strouhal numbers. This again demonstrates that there seems to be a frequency dependence of the transport characteristics that is not covered by any of the models presented in this section.

It is worth noting that the values for the two constants β and B, that are found in Giusti et al. (2017) to fit best to their experimental as well as numerical results, are both different to the values obtained for the fit to our measurements in Fig. 6.14. Since their numerical results exhibit a higher propagation speed than the one obtained from the bulk velocity, they suggest $\beta \approx 0.8$. Regarding the attenuation of the amplitude with respect to the Strouhal number, they find a value $B \approx 0.45$ to match their experimental and numerical results best. Applied to the measurements presented in this study, their set of parameter would significantly underestimate the dissipation of the entropy waves

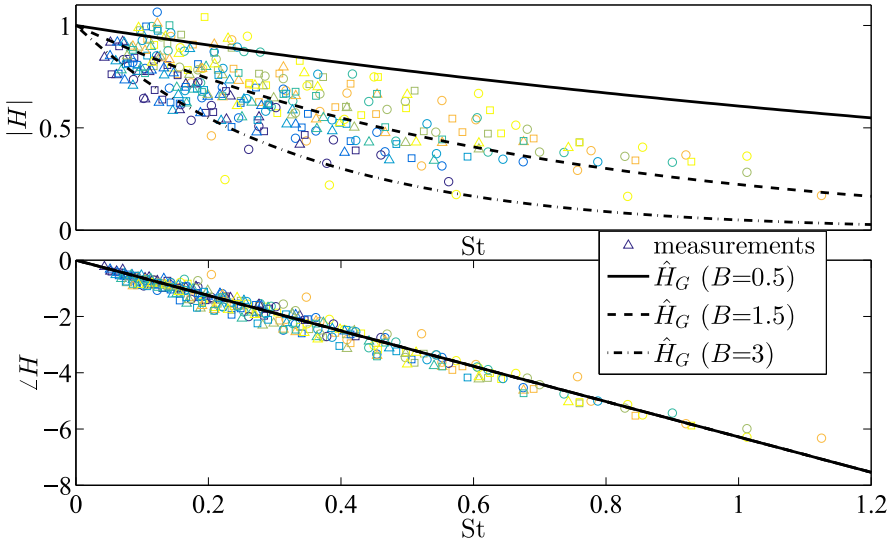

Figure 6.14: Comparison of the transport transfer function model $\hat{H}_G$ shown in Eq. 6.34 with the measured transport transfer function (markers); the different colors correspond to different frequencies (dark bluish: 5 Hz → yellow: 12 Hz). The measurements comprise three different axial velocities (marker styles corresponding to Fig. 6.10)

(see $\hat{H}_G$ with $B = 0.5$ in Fig. 6.14). Obviously, the flow field in the combustion rig measurements is more complex and causes a higher dispersion which leads to a stronger dissipation of the entropy waves. This is certainly conceivable as the flow field in the combustor might still be affected by the swirl flow and the recirculation zone which cause eddies and enhance strong velocity components in radial direction. This finding is also well aligned with a recent study by Xia et al. (2016), who investigated the dissipation of entropy waves numerically for a realistic flow field in a typical gas turbine combustor. There, higher dissipation is found with a time-varying instantaneous base flow field compared to a time-averaged flow field. Considering these complex flow phenomena, it is interesting to note that the experimentally assessed propagation velocity is found to depend on the bulk velocity only.

Summary: transport model

The goal of this subsection was to derive a general description of the propagation characteristics of entropy perturbations. Based on the spatio-temporal transport equation for a scalar that is advected through a duct, a transfer function has been formulated, which relates the amplitude and phase of the cross-sectionally averaged scalar at a downstream position in the duct to its associated value at a position further upstream. For the first time, such a model has been compared to entropy wave measurements in a realistic atmospheric combustion chamber. The general trend of the dissipation of the entropy waves with respect to a Strouhal number is well recovered; however, it has been observed that the dissipation is stronger than predicted by the model. This is also the case for other models found in literature (Sattelmayer, 2002; Schuermans, Bellucci, et al., 2004; Morgans, Goh, et al., 2013; Giusti et al., 2017). A possible explanation was found in the numerical study by Fattahi et al. (2017), which shows that besides dispersion and

diffusion, also heat conduction plays an important role.

Finally, this analysis and its results allow for a more accurate estimation of the transport of entropy fluctuations in realistic combustion chambers. It reveals more insight into the physical mechanisms that contribute to the attenuation process, which supports the development of effective countermeasures.

7 Conclusions and Outlook

Low frequency combustion instabilities are known to occur in (aero-engine) gas turbine combustors. They cause significant noise emissions and high pressure oscillations that impede the operation of an engine at desirable load conditions. The associated acoustic perturbations originate from accelerated entropy spots at the turbine inlet, whereas these so-called entropy waves are generated in the reaction zone through equivalence ratio fluctuations in the fuel-air mixture. In order to develop a means for the suppression of advecting entropy perturbations or for the a priori estimation of their strength, substantial knowledge about the generation and transport mechanisms of entropy waves is required. Previously, investigations of these topics have been based on theoretical considerations or generic experiments rather than focused on a systematic study of such entropy waves. This work has presented a focused study toward this objective, with the following results.

Firstly, a measurement technique has been developed, allowing for the assessment of advecting entropy spots in a model gas turbine combustor. A non-intrusive acoustic time-of-flight measurement technique was adapted for use under high-temperature conditions. Measurement of the flight time of an acoustic pulse enabled the deduction of the line-integrated inverse speed of sound along the acoustic path between an emitter and a receiver. An electric discharge setup was developed for the generation of the acoustic pulse, which provided a sufficiently short pulse signal. This pulse remained detectable even in the very noisy environment of the combustor. The flight time was measured on radial acoustic paths with multiple water-cooled microphones distributed around the circumference of the combustor. A zero-dimensional, SVD-based method was developed to extract the amplitude and phase of a cross-sectionally averaged temperature fluctuation at the measurement plane. Information about the acoustic path lengths was not required, as a reference temperature obtained from a thermocouple was sufficient. Furthermore, the developed experimental setup allowed for the evaluation of a one- or two-dimensional radial temperature field at an axial location in the combustor rig. Appropriate tomographic tools were identified and adapted for the particular spatial arrangement of the acoustic paths. Via phantom studies, all temperature extraction methods were successfully validated.

The present experimental analysis demonstrated under academic conditions that this measurement technique works well for the investigation of entropy waves in atmospheric combustion chambers. However, the experimental hardware was designed such that it can also be used in real gas turbine combustors at higher pressures and velocities. The great need of an accurate real-time temperature monitoring with high spatial and temporal resolution in industrial applications, e.g., combustors, boilers, and furnances, is un-

deniable. This study has laid the foundation for further developments of this technique, which has high potential in practical applications compared to other point measurement techniques such as slow intrusive thermocouples or complex and costly optical measurements techniques, e.g. CARS. In the development of this prototype hardware, several challenges were identified for general use, such as the necessity for phase averaging and the significant data requirements for two-dimensional tomography. However, the thesis has presented solutions and suggestions for future users to overcome such hurdles.

In a second step, this measurement technique was implemented in an atmospheric, lean-premixed combustion test rig. The implementation of a valve at the burner's fuel supply enabled the generation of well defined equivalence ratio fluctuations and entropy waves, respectively. Comprehensive sweeps in parameter space were performed, including variations of the axial measurement position with respect to the reaction zone and of the fuel modulation frequency. In addition, the equivalence ratio fluctuations in the mixing section upstream of the burner were assessed by means of a tunable diode laser absorption spectroscopy. This allowed for the measurement of the transfer function between an equivalence ratio disturbance in the fuel-air mixture and the resulting entropy perturbation downstream of the flame. The investigated parameter space allowed for the validation of analytically derived models for the generation of entropy waves. A clear Strouhal number dependence of the amplitude and the phase of the cross-sectionally averaged entropy perturbation was discovered. Furthermore, the measurements of entropy waves at different axial locations in the combustor were utilized to analytically investigate the dissipation mechanisms of the advectively transported entropy spots. Based on a spatiotemporal transport model for a passive scalar, a one-dimensional transfer function for the amplitude of an entropy wave at two different axial positions in the combustion rig has been derived. Its validation with the measured transfer functions revealed a good match and showed that the model predicts the dissipation characteristic correctly, which further underlines the need of considering dispersive effects. A similar result has been found when comparing the measurement data to models from literature. In general, the models properly recover the decay of the strength of the entropy waves for increasing Strouhal numbers. In comparison with results from generic experimental approaches from literature, the more complex flow field in the present combustion chamber exhibited a stronger dissipation of the entropy waves.

This analytical study has shown that the developed measurement technique serves well for investigations of entropy waves. Two essential outcomes are the clear Strouhal number dependency of the entropy waves and the demonstration that entropy waves are convected with the bulk velocity. It has also been shown that dispersion has the most significant impact on the dissipation of entropy waves. This work allowed for the first time for a calibration of existing models with measurement data of an atmospheric combustor; this has so far not been possible. However, detailed information about the flow field in the combustor would significantly improve the validity of the analytical findings. In combination with the temperature measurement technique presented in this work, time resolved flow field data could be used to assess whether or not the entropy fluctuations can be considered as passive scalars.

In conclusion, the experimental and analytical tools derived and validated in this work show high potential to become a vital component in the undertaking of making gas

turbines sustainable for future challenges. Better understanding and monitoring of entropy waves is an important step for the development of effective countermeasures for low-frequency combustion instabilities. The high relevance of this study applies for academic research as well as for industrial concerns, where particularly a real-time high-temperature measurement technique is highly requested also for other purposes.

Bibliography

Abdel-Fattah, M. F. and Lehtonen, M. The High-Temperature Effect on the Breakdown Voltage of an Air-Gap at Atmospheric Pressure with Reference to Paschen Curve. *International Review of Electrical Engineering (IREE); Vol 8, No 6 (2013)*. Dec. 2013: –. http://www.praiseworthyprize.org/jsm/index.php?journal=iree&page=article&op=view&path%5B%5D=14441.

Alberty, R. Use of Legendre transforms in chemical thermodynamics (IUPAC Technical Report). *Pure and Applied Chemistry*. 2009, **73**: 1349–1380. issn: 00334545.

Alvarez, F. J. and Kuc, R. Dispersion relation for air via Kramers-Kronig analysis. *The Journal of the Acoustical Society of America*. 2008, **124**(2): EL57–EL61. eprint: http://dx.doi.org/10.1121/1.2947631. http://dx.doi.org/10.1121/1.2947631.

Anikin, N., Suntz, R., and Bockhorn, H. Tomographic reconstruction of the OH*-chemiluminescence distribution in premixed and diffusion flames. *Applied Physics B*. 2010, **100**(3): 675–694. issn: 1432-0649. http://dx.doi.org/10.1007/s00340-010-4051-5.

Ashraf, M. and Qayyum, H. High Accuracy Time of Flight Measurement Using Digital Signal Processing Techniques for Subsea Applications. *Journal of Signal and Information Processing*. 2011, **2**(4): 330–335.

Ayrault, C., Béquin, P., and Baudin, S. "Characteristics of a spark discharge as an adjustable acoustic source for scale model measurements". In: *Acoustics 2012*. Nantes, France, Apr. 23, 2012: 3549–3553. https://hal.archives-ouvertes.fr/hal-00810828.

Bake, F. *Schallentstehung durch Temperaturschwankungen in der Strömung einer Düse: Nachweis und Parameterstudie zum Entropieschall von Brennkammern*. PhD thesis. TU Berlin, 2008.

Bake, F., Michel, U., and Röhle, I. Investigation of Entropy Noise in Aero-Engine Combustors. *Journal of Engineering for Gas Turbines and Power*. 2007, **129**: 370–376.

Bane, S. P., Ziegler, J. L., and Shepherd, J. E. Investigation of the effect of electrode geometry on spark ignition. *Combustion and Flame*. Feb. 2015, **162**(2): 462–469. issn: 0010-2180. http://www.sciencedirect.com/science/article/pii/S0010218014002120.

Bass, H. E., Bauer, H., and Evans, L. B. Atmospheric Absorption of Sound: Analytical Expressions. *The Journal of the Acoustical Society of America*. 1972, **52**(3B): 821–825. eprint: http://dx.doi.org/10.1121/1.1913183. http://dx.doi.org/10.1121/1.1913183.

Becker, E. *Gas dynamics*. 1st. Academic Press, 1968. https://books.google.de/books?id=ehZRAAAAMAAJ.

Becker, H. A., Rosensweig, R. E., and Gwozdz, J. R. Turbulent dispersion in a pipe flow. *AIChE Journal*. 1966, **12**(5): 964–972. ISSN: 1547-5905. http://dx.doi.org/10.1002/aic.690120523.

Bernhard, F. *Handbuch der Technischen Temperaturmessung*. Springer Nature, 2014. https://doi.org/10.1007%2F978-3-642-24506-0.

Bettermann, G. *Beitrag zur Ermittlung des Messfehlers bei der Temperaturmessung mit Thermoelementen in strömenden, heißen Gasen unter besonderer Berücksichtigung der Gasstrahlung*. PhD thesis. Technische Universität Berlin, 1964.

Bjørnø, L. *Applied Underwater Acoustics*. Ed. by T. H. Neighbors and D. Bradley. Elsevier, 2017.

Blokhintzev, D. The Propagation of Sound in an Inhomogeneous and Moving Medium I. *The Journal of the Acoustical Society of America*. Oct. 1946, **18**(2): 322–328. https://doi.org/10.1121%2F1.1916368.

Blümner, R., Paschereit, C., Oberleithner, K., and Ćosić, B. "Experimental Analysis of High-Amplitude Temporal Equivalence Ratio Oscillations in the Mixing Section of a Swirl-Stabilized Burner". In: *ASME. Turbo Expo: Power for Land, Sea, and Air*. Vol. 4A. 2016.

Bobusch, B. C., Ćosić, B., Moeck, J. P., and Oliver Paschereit, C. Optical Measurement of Local and Global Transfer Functions for Equivalence Ratio Fluctuations in a Turbulent Swirl Flame. *Journal of Engineering for Gas Turbines and Power*. Nov. 2013, **136**(2): 021506–021506. ISSN: 0742-4795.

Bolaños, J. G., Pulkki, V., Karppinen, P., and Hæggström, E. An optoacoustic point source for acoustic scale model measurements. *The Journal of the Acoustical Society of America*. Apr. 2013, **133**(4): 221–227. https://doi.org/10.1121%2F1.4793566.

Borrell, P. Relaxation processes in gases. *Advances in Molecular Relaxation Processes*. 1967, **1**(1): 69–108. ISSN: 0001-8716. http://www.sciencedirect.com/science/article/pii/000187166780004X.

Bounaceur, R., Glaude, P.-A., Sirjean, B., Fournet, R., Montagne, P., Vierling, M., and Molière, M. "Prediction of Auto-Ignition Temperatures and Delays for Gas Turbine Applications". In: *ASME Turbo Expo*. June 2015: V04AT04A003–. http://dx.doi.org/10.1115/GT2015-42011.

Bradley, D. and Entwistle, A. G. Determination of the emissivity, for total radiation, of small diameter platinum-10% rhodium wires in the temperature range 600-1450 C. *British Journal of Applied Physics*. Dec. 1961, **12**(12): 708–711. https://doi.org/10.1088%2F0508-3443%2F12%2F12%2F328.

Bramanti, M., Salerno, E., Tonazzini, A., Pasini, S., and Gray, A. An acoustic pyrometer system for tomographic thermal imaging in power plant boilers. *Instrumentation and Measurement, IEEE Transactions on*. 1996, **45**(1): 159–167. ISSN: 0018-9456.

Cai, C. and Regtien, P. P. L. Accurate digital time-of-flight measurement using self-interference. *IEEE Transactions on Instrumentation and Measurement*. 1993, **42**(6): 990–994. ISSN: 0018-9456.

Cai, W. and Kaminski, C. F. Tomographic absorption spectroscopy for the study of gas dynamics and reactive flows. *Progress in Energy and Combustion Science*. Mar. 2017, **59**: 1–31. https://doi.org/10.1016%2Fj.pecs.2016.11.002.

Chessell, C. I. Three-dimensional acoustic-ray tracing in an inhomogeneous anisotropic atmosphere using Hamilton's equations. *The Journal of the Acoustical Society of America*. Jan. 1973, **53**(1): 83–87. https://doi.org/10.1121%2F1.1913331.

Chu, B.-T. On the energy transfer to small disturbances in fluid flow (Part I). *Acta Mechanica*. 1965, **1**(3): 215–234. ISSN: 1619-6937. http://dx.doi.org/10.1007/BF01387235.

Cormack, A. M. Representation of a Function by Its Line Integrals, with Some Radiological Applications. *Journal of Applied Physics*. 1963, **34**(9): 2722–2727. eprint: http://dx.doi.org/10.1063/1.1729798. http://dx.doi.org/10.1063/1.1729798.

Cornuelle, B. D., Worcester, P. F., and Dzieciuch, M. A. Ocean acoustic tomography. *Journal of Physics: Conference Series*. 2008, **118**(1): 012002. http://stacks.iop.org/1742-6596/118/i=1/a=012002.

Ćosić, B., Terhaar, S., Moeck, J. P., and Paschereit, C. O. Response of a swirl-stabilized flame to simultaneous perturbations in equivalence ratio and velocity at high oscillation amplitudes. *Combustion and Flame*. Apr. 2015, **162**(4): 1046–1062. http://www.sciencedirect.com/science/article/pii/S001021801400306X.

Ćosić, B., Wassmer, D., Terhaar, S., and Paschereit, C. Acoustic response of Helmholtz dampers in the presence of hot grazing flow. *Journal of Sound and Vibration*. Jan. 2015, **335**: 1–18. ISSN: 0022-460X. http://www.sciencedirect.com/science/article/pii/S0022460X1400697X.

Crocco, L. and Cheng, S.-I. *Theory of Combustion Instability in Liquid Propellant Rocket Motors*. Butterworth Scientific Publications, 1956.

Culick, F. E. C. and Yang, V. "Overview of Combustion Instabilities in Liquid-Propellant Rocket Engines". In: American Institute of Aeonautics and Astrophysics, 1995. Chap. 1: 3–37. http://resolver.caltech.edu/CaltechAUTHORS:20101122-074028101.

Cumpsty, N. and Marble, F. The generation of noise by the fluctuations in gas temperature into a turbine. *Report CUEDIA Turbo/TR57*. 1974: 39.

Dasch, C. J. One-dimensional tomography: a comparison of Abel, onion-peeling, and filtered backprojection methods. *Applied Optics*. Mar. 1992, **31**(8): 1146. https://doi.org/10.1364%2Fao.31.001146.

Daun, K. J., Thomson, K. A., Liu, F., and Smallwood, G. J. Deconvolution of axisymmetric flame properties using Tikhonov regularization. *Applied Optics*. July 2006, **45**(19): 4638. http://dx.doi.org/10.1364/ao.45.004638.

Daun, K., Grauer, S., and Hadwin, P. J. *Chemical species tomography of turbulent flows: Discrete ill-posed and rank deficient problems and the use of prior information*. Vol. 172. Mar. 2016: 58–74.

De Domenico, F., Rolland, E. O., and Hochgreb, S. Detection of direct and indirect noise generated by synthetic hot spots in a duct. *Journal of Sound and Vibration*. 2017, **394**: 220–236. issn: 0022-460X. http://www.sciencedirect.com/science/article/pii/S0022460X17300032.

Décamp, S., Kozack, C., and Sutherland, B. R. Three-dimensional Schlieren measurements using inverse tomography. *Experiments in Fluids*. 2008, **44**(5): 747–758. issn: 1432-1114. http://dx.doi.org/10.1007/s00348-007-0431-y.

Deduck, S. G. and Suplicki, D. *Advanced Technologies Provide New Insights for Assisting Energy from Waste (EfW) Boiler Combustion Monitoring, Operations and Maintenance*. 2008. http://dx.doi.org/10.1115/NAWTEC16-1918.

DeSilva, U., Bunce, R., and Claussen, H. "Novel Gas Turbine Exhaust Temperature Measurement System". In: *ASME Turbo Expo, San Antonio, USA*. Vol. 4. 2013.

Döbbeling, K., Hellat, J., and Koch, H. 25 Years of BBC/ABB/Alstom Lean Premix Combustion Technologies. *ASME Turbo Expo 2005: Power for Land, Sea, and Air*. 2005, **2**: 201–213. http://dx.doi.org/10.1115/GT2005-68269.

Dowling, A. The calculation of thermoacoustic oscillations. *Journal of Sound and Vibration*. 1995, **180**(4): 557–581. issn: 0022-460X. http://www.sciencedirect.com/science/article/pii/S0022460X85701009.

Dowling, A. and Williams, J. *Sound and Sources of Sound*. Ellis Horwood Limited, 1983.

Dowling, A. P. and Mahmoudi, Y. Combustion noise. *Proceedings of the Combustion Institute*. 2015, **35**(1): 65–100. issn: 1540-7489.

Dowling, A. P. and Stow, S. R. Acoustic Analysis of Gas Turbine Combustors. *Journal of Propulsion and Power*. Sept. 2003, **19**(5): 751–764. issn: 0748-4658.

Duran, I. and Moreau, S. Solution of the quasi-one-dimensional linearized Euler equations using flow invariants and the Magnus expansion. *Journal of Fluid Mechanics*. 2013, **723**: 190–231.

Eckart, C. and Young, G. The approximation of one matrix by another of lower rank. *Psychometrika*. 1936, **1**(3): 211–218. http://EconPapers.repec.org/RePEc:spr:psycho:v:1:y:1936:i:3:p:211-218.

Eckstein, J., Freitag, E., Hirsch, C., and Sattelmayer, T. "Experimental Study on the Role of Entropy Waves in Low-Frequency Oscillations for a Diffusion Burner". In: *ASME Turbo Expo 2004: Power for Land, Sea, and Air*. 41669. 2004: 743–751.

Eckstein, J. *On the Mechanisms of Combustion Driven Low-Frequency Oscillations in Aero-Engines*. PhD thesis. TU München, 2004.

Eckstein, J. and Sattelmayer, T. Low-Order Modeling of Low-Frequency Combustion Instabilities in AeroEngines. *Journal of Propulsion and Power*. Mar. 2006, **22**(2): 425–432. ISSN: 0748-4658. https://doi.org/10.2514/1.15757.

Elsinga, G. E., Wieneke, B., Scarano, F., and Schröder, A. Tomographic 3D-PIV and Applications. In: *Particle Image Velocimetry: New Developments and Recent Applications*. Berlin, Heidelberg: Springer Berlin Heidelberg, 2008: 103–125. http://dx.doi.org/10.1007/978-3-540-73528-1_6.

Ember, G., Ferron, J. R., and Wohl, K. Self-Diffusion Coefficients of Carbon Dioxide at 1180°–1680°K. *The Journal of Chemical Physics*. 1962, **37**(4): 891–897. eprint: http://dx.doi.org/10.1063/1.1733180. http://dx.doi.org/10.1063/1.1733180.

Falk, G. and Ruppel, W. *Energie und Entropie*. Springer-Verlag Berlin Heidelberg, 1976: 414.

Farag, I. "Non luminous gas radiation - Approximate emissivity models". In: *Proceedings of The Seventh International Heat Transfer Conference*. Vol. 2. 1982: 487–492.

Fattahi, A., Hosseinalipour, S. M., and Karimi, N. On the dissipation and dispersion of entropy waves in heat transferring channel flows. *Physics of Fluids*. 2017, **29**(8): 087–104. eprint: http://dx.doi.org/10.1063/1.4999046.

Fischer, J. Temperaturfühler und Strahlungsempfänger. *Zeitschrift für Technische Physik*. 1941, **22**: 316–323.

Freeman, R. A. and Cragg, J. D. Shock waves from spark discharges. *Brit. J. Appl. Phys.* 1969, **2**(2): 421–427.

Gaetani, P., Persico, G., Spinelli, A., Sandu, C., and Niculescu, F. "Entropy Wave Generator for Indirect Combustion Noise Experiments in a High-Pressure Turbine". In: *European Turbomachinery Conference*. Vol. 11. Mar. 2015.

Gelfand, I. M. and Fomin, S. V. *Calculus of Variations*. Ed. by R. A. Silverman. Prentice-Hall Inc, 1964.

Giusti, A., Worth, N. A., Mastorakos, E., and Dowling, A. P. Experimental and Numerical Investigation into the Propagation of Entropy Waves. *AIAA Journal*. Oct. 2017, **55**(2): 446–458. ISSN: 0001-1452. https://doi.org/10.2514/1.J055199.

Godin, O. A. and Voronovich, A. G. Fermat's Principle for Non-Dispersive Waves in Non-Stationary Media. 2004, **460**(2046): 1631–1647. ISSN: 13645021. http://www.jstor.org/stable/4143113.

Golub, G. and Kahan, W. Calculating the Singular Values and Pseudo-Inverse of a Matrix. *Journal of the Society for Industrial and Applied Mathematics: Series B, Numerical Analysis*. 1965, **2**(2): 205–224. ISSN: 0887459X. http://www.jstor.org/stable/2949777.

Golub, G., Hoffman, A., and Stewart, G. A generalization of the Eckart-Young-Mirsky matrix approximation theorem. *Linear Algebra and its Applications*. 1987, **88**: 317–327. ISSN: 0024-3795. http://www.sciencedirect.com/science/article/pii/0024379587901145.

Golub, G. H. and van Loan, C. F. *Matrix computations (3rd ed.)* Johns Hopkins University Press, 1996: 694.

Green, S. F. An acoustic technique for rapid temperature distribution measurement. *The Journal of the Acoustical Society of America*. 1985, **77**(2): 759–763. http://scitation.aip.org/content/asa/journal/jasa/77/2/10.1121/1.392347.

Hansen, P. C. *Rank-Deficient and Discrete Ill-Posed Problems*. Society for Industrial & Applied Mathematics (SIAM), Jan. 1998. http://dx.doi.org/10.1137/1.9780898719697.

Hansen, P. C. and O'Leary, D. P. The Use of the L-Curve in the Regularization of Discrete Ill-Posed Problems. *SIAM Journal on Scientific Computing*. 1993, **14**(6): 1487–1503. eprint: http://dx.doi.org/10.1137/0914086. http://dx.doi.org/10.1137/0914086.

Herman, G. T. *Fundamentals of Computerized Tomography*. Springer London, 2009. https://doi.org/10.1007%2F978-1-84628-723-7.

Hindasageri, V., Vedula, R. P., and Prabhu, S. V. Thermocouple error correction for measuring the flame temperature with determination of emissivity and heat transfer coefficient. *Review of Scientific Instruments*. 2013, **84**(2): 024902. http://aip.scitation.org/doi/abs/10.1063/1.4790471.

Howe, M. Indirect combustion noise. *Journal of Fluid Mechanics*. 2010, **659**: 267–288.

Hubbard, S. and Dowling, A. "Acoustic Instabilities in Premix Burners". In: *AIAA/CEAS, Aeroacoustics Conference*. 1998.

Huber, A. *Impact of fuel supply impedance and fuel staging on gas turbine combustion stability*. PhD thesis. Technische Universität München, 2009.

Huet, M. and Giauque, A. A nonlinear model for indirect combustion noise through a compact nozzle. *Journal of Fluid Mechanics*. 2013, **733**: 268–301. http://dx.doi.org/10.1017/jfm.2013.442.

Jia, R., Xiong, Q., Wang, K., Wang, L., Xu, G., and Liang, S. The study of three-dimensional temperature field distribution reconstruction using ultrasonic thermometry. *AIP Advances*. July 2016, **6**(7): 075007. https://doi.org/10.1063%2F1.4958922.

Joos, F., Brunner, P., Schulte-Werning, B., Syed, K., and Eroglu, A. Development of the Sequential Combustion System for the ABB GT24/GT26 Gas Turbine Family. 1996, (78750): 11. http://dx.doi.org/10.1115/96-GT-315.

Jovanovic, I. *Inverse problems in acoustic tomography*. eng. PhD thesis. Lausanne: IC, 2008.

Kaczmarz, S. Przyblizone rozwiazywanie ukladów równan liniowych. – Angenäherte Auflösung von Systemen linearer Gleichungen. *Classe des Sciences Mathématiques et Naturelles. Série A, Sciences Mathématiques*. 1937: 355–357.

Kak, A. C. and Slaney, M. *Principles of Computerized Tomographic Imaging*. IEEE Press, 1988.

Karimi, N., Brear, M. J., and Moase, W. H. Acoustic and disturbance energy analysis of a flow with heat communication. *Journal of Fluid Mechanics*. 2008, **597**: 67–89.

Keller, J. J. Thermoacoustic oscillations in combustion chambers of gas turbines. *AIAA Journal*. 1995, **33**(12): 2280–2287. issn: 0001-1452. http://dx.doi.org/10.2514/3.12980.

Kleppe, J. A., Maskaly, J., and Beam, G. "The application of image processing to acoustic pyrometry". In: *Proceedings of 3rd IEEE International Conference on Image Processing*. Vol. 2. 16-19 Sep 1996: 657–659.

Kleppe, J., Norris, W., McPherson, D., and Fralick, G. The Measurement of Performance of Combustors Using Passive Acoustic Methods. In: *Aerospace Sciences Meetings*. 2004-1046. American Institute of Aeronautics and Astronautics, 2004. http://dx.doi.org/10.2514/6.2004-1046.

Klinkowstein, R. E. *A Study Of Acoustic Radiation From An Electric Spark Discharge In Air*. MA thesis. Massachusetts Institute Of Technology, July 1974.

Küchler, A. *Hochspannungstechnik*. 3rd. Springer Verlag, VDI, 2009.

Küperkoch, L., Meier, T., Lee, J., Friederich, W., and Group, E. W. Automated determination of P-phase arrival times at regional and local distances using higher order statistics. *Geophysical Journal International*. 2010, **181**(2): 1159–1170. http://gji.oxfordjournals.org/content/181/2/1159.abstract.

Kuttruff, H. *Physik und Technik des Ultraschalls*. Vol. 1. Hirzel Verlag Stuttgart, 1988.

Landweber, L. An Iteration Formula for Fredholm Integral Equations of the First Kind. 1951, **73**(3): 615–624. issn: 00029327, 10806377. http://www.jstor.org/stable/2372313.

Lauer, M. *Determination of the Heat Release Distribution in Turbulent Flames by Chemiluminescence Imaging*. PhD thesis. Technische Universität München, 2011.

Lechner, C. and Bothien, M. "Measurement of the Inlet Gas Temperature of a Gas Turbine". In: *ASME Turbo Expo 2005: Power for Land, Sea, and Air*. Vol. 1. GT2005-68138. 2005: 507–515.

Lee, C. C., Lahham, M., and Martin, B. G. Experimental verification of the Kramers-Kronig relationship for acoustic waves. *IEEE Transactions on Ultrasonics, Ferroelectrics, and Frequency Control*. July 1990, **37**(4): 286–294. ISSN: 0885-3010.

Leyko, M., Nicoud, F., and Poinsot, T. Comparison of Direct and Indirect Combustion Noise Mechanisms in a Model Combustor. *AIAA Journal*. Nov. 2009, **47**(11): 2709–2716. ISSN: 0001-1452.

Li, C., Huang, L., Duric, N., Zhang, H., and Rowe, C. An improved automatic time-of-flight picker for medical ultrasound tomography. *Ultrasonics*. Jan. 2009, **49**(1): 61–72. ISSN: 0041-624X. http://www.sciencedirect.com/science/article/pii/S0041624X08000863.

Li, H., Wilhelmsen, Ã., Lv, Y., Wang, W., and Yan, J. Viscosities, thermal conductivities and diffusion coefficients of CO2 mixtures: Review of experimental data and theoretical models. *International Journal of Greenhouse Gas Control*. 2011, **5**(5): 1119–1139. ISSN: 1750-5836. http://www.sciencedirect.com/science/article/pii/S175058361100137X.

Li, H., Wehe, S. D., and McManus, K. R. Real-time equivalence ratio measurements in gas turbine combustors with a near-infrared diode laser sensor. *Proceedings of the Combustion Institute*. 2011, **33**(1): 717–724. ISSN: 1540-7489.

Li, J., Richecoeur, F., and Schuller, T. Reconstruction of heat release rate disturbances based on transmission of ultrasounds: Experiments and modeling for perturbed flames. *Combustion and Flame*. 2013, **160**(9): 1779–1788. ISSN: 0010-2180. http://www.sciencedirect.com/science/article/pii/S0010218013001028.

Li, Y.-Q. and Zhou, H.-C. Experimental study on acoustic vector tomography of2-D flow field in an experiment-scale furnace. *Flow Measurement and Instrumentation*. Apr. 2006, **17**(2): 113–122. https://doi.org/10.1016%2Fj.flowmeasinst.2005.09.001.

Lieuwen, T. C. and Yang, V. *Combustion Instabilities in Gas Turbine Engines (Progress in Astronautics and Aeronautics)*. Vol. 210. American Institute of Aeronautics and Astronautics, Inc., 2005.

Lieuwen, T., Neumeier, Y., and Zinn, B. T. The Role of Unmixedness and Chemical Kinetics in Driving Combustion Instabilities in Lean Premixed Combustors. *Combustion Science and Technology*. June 1998, **135**(1-6): 193–211. ISSN: 0010-2202.

Lieuwen, T., Torres, H., Johnson, C., and Zinn, B. T. A Mechanism of Combustion Instability in Lean Premixed Gas Turbine Combustors. *Journal of Engineering for Gas Turbines and Power*. Apr. 2000, **123**(1): 182–189. ISSN: 0742-4795. http://dx.doi.org/10.1115/1.1339002.

Lieuwen, T. and Zinn, B. "The Role of Equivalence Ratio Oscillations in Driving Combustion Instabilities in Low NOx Gas Turbines". In: *27th Symposium on Combustion/The Combustion Institute*. 1998: 1809–1816.

Loeb, A., Loebenstein, M., Ludmirsky, A., Eliezer, S., Maman, S., and Gazit, Y. Point explosion simulation by fast spark discharges. *Journal of Applied Physics*. Apr. 1985, **57**(7): 2501–2506. https://doi.org/10.1063%2F1.335435.

Lu, J., Wakai, K., Takahashi, S., and Shimizu, S. Acoustic computer tomographic pyrometry for two-dimensional measurement of gases taking into account the effect of refraction of sound wave paths. *Measurement Science and Technology*. May 2000, **11**(6): 692–697. https://doi.org/10.1088%2F0957-0233%2F11%2F6%2F312.

Marble, F. and Candel, S. Acoustic disturbance from gas non-uniformities convected through a nozzle. *Journal of Sound and Vibration*. 1977, **55**(2): 225–243. https://doi.org/10.1016/0022-460X(77)90596-X.

Marks, R. *Introduction to Shannon Sampling and Interpolation Theory*. 1431-8482 1. Springer-Verlag New York, 1991: 324.

Martinson, E. and Delsing, J. Electric spark discharge as an ultrasonic generator in flow measurement situations. *Flow Measurement and Instrumentation*. Sept. 2010, **21**(3): 394–401. issn: 0955-5986. http://www.sciencedirect.com/science/article/pii/S0955598610000579.

Mayer, A. M. On an acoustic pyrometer. *Philosophical Magazine Series 4*. 1873, **45**(297): 18–22.

McBride, B. J., Gordon, S., and Reno, M. A. *Coefficients for Calculating Thermodynamic and Transport Properties of Individual Species*. Tech. rep. NASA TM-4513. NASA, Lewis Research Center, Oct. 1993.

Morgans, A. S., Goh, C. S., and Dahan, J. A. The dissipation and shear dispersion of entropy waves in combustor thermoacoustics. *Journal of Fluid Mechanics*. 2013, **733**.

Morgans, A. S. and Duran, I. Entropy noise: A review of theory, progress and challenges. *International Journal of Spray and Combustion Dynamics*. June 2016, **8**(4): 285–298. issn: 1756-8277. https://doi.org/10.1177/1756827716651791.

Müller, I. and Müller, W. *Fundamentals of Thermodynamics and Applications*. 1st. Springer-Verlag Berlin Heidelberg, 2009: 404.

Munk, W., Worcester, P., and Wunsch, C. *Ocean acoustic tomography*. n/a. Cambridge, England: Cambridge University Press, 1995. Chap. 433.

Munk, W. and Wunsch, C. Ocean acoustic tomography: a scheme for large scale monitoring. *Deep-Sea Research*. 1979, **26A**: 123–161.

Natterer, F. *Mathematical Methods in Image Reconstruction*. Society for Industrial & Applied Mathematics (SIAM), Jan. 2001. http://dx.doi.org/10.1137/1.9780898718324.

Natterer, F. *The Mathematics Of Computerized Tomography*. Society for Industrial & Applied Mathematics (SIAM), Jan. 2001. http://dx.doi.org/10.1137/1.9780898719284.

O'Donnell, M., Jaynes, E. T., and Miller, J. G. General relationships between ultrasonic attenuation and dispersion. *The Journal of the Acoustical Society of America*. 1978, **63**(6): 1935–1937. eprint: http://dx.doi.org/10.1121/1.381902. http://dx.doi.org/10.1121/1.381902.

Oberleithner, K. and Paschereit, C. O. "Modeling Flame Describing Functions Based on Hydrodynamic Linear Stability Analysis. Turbo Expo: Power for Land, Sea, and Air". In: *ASME Turbo Expo*. Vol. GT2016-57316. 49767. 2016.

Ostashev, V. E. and Wilson, D. K. *Acoustics in Moving Inhomogeneous Media*. 2nd ed. CRC Press, Taylor & Francis Group, 2016.

Page, N. W. and McKelvie, P. "Shock Waves Generated by Spark Discharge". In: *6th Austalasian Hydraulics and Fluid Mechanics Conference*. Dec. 1977: 221–224.

Paschereit, C. O. and Polifke, W. Investigation of the Thermoacoustic Characteristics of a Lean Premixed Gas Turbine Burner. *ASME 1998 International Gas Turbine and Aeroengine Congress and Exhibition*. 1998, **3**. http://dx.doi.org/10.1115/98-GT-582.

Pause, F. *Tomografische Rekonstruktion instationärer Temperaturfelder in Brennkammern basierend auf akustischen Time-of-Flight Messungen*. MA thesis. ISTA, Fachgebiet für Verbrennungsdynamik, Technische Universität Berlin, May 2017.

Pennell, D. A., Bothien, M. R., Ciani, A., Granet, V., Singla, G., Thorpe, S., Wickstroem, A., Oumejjoud, K., and Yaquinto, M. *An Introduction to the Ansaldo GT36 Constant Pressure Sequential Combustor*. 2017. http://dx.doi.org/10.1115/GT2017-64790.

Peracchio, A. A. and Proscia, W. M. Nonlinear Heat-Release/Acoustic Model for Thermoacoustic Instability in Lean Premixed Combustors. *Journal of Engineering for Gas Turbines and Power*. July 1999, **121**(3): 415–421. ISSN: 0742-4795. http://dx.doi.org/10.1115/1.2818489.

Phillips, D. L. A Technique for the Numerical Solution of Certain Integral Equations of the First Kind. *Journal of the ACM*. Jan. 1962, **9**(1): 84–97. https://doi.org/10.1145%2F321105.321114.

Polifke, W., Kopitz, J., and Serbanovic, A. "Impact of the Fuel Time Lag Distribution in Elliptical Premix Nozzles on Combustion Stability". In: *7th American Institute of Aeronautics and Astronautics/CEAS Aeroacoustics Conference and Exhibit, 2001*. AIAA. Maastricht, The Netherlands, 2001.

Polifke, W., Paschereit, C. O., and Döbbeling, K. Constructive and Destructive Interference of Acoustic and Entropy Waves in a Premixed Combustor with a Choked Exit. *International Journal of Acoustics and Vibration*. 2001, **6**(3): 135–146.

Rayleigh, J. *The Theory of Sound, Volume II*. 1st ed. .b. MacMillan and Co, London, 1878.

Rienstra, S. and Hirschberg, A. *An Introduction to Acoustics*. 1st ed. .a. Eindhoven University of Technology, 2004.

Rothman, L., Gordon, I., Babikov, Y., Barbe, A., Chris Benner, D., Bernath, P., Birk, M., Bizzocchi, L., Boudon, V., Brown, L., Campargue, A., Chance, K., Cohen, E., Coudert, L., Devi, V., Drouin, B., Fayt, A., Flaud, J.-M., Gamache, R., Harrison, J., Hartmann, J.-M., Hill, C., Hodges, J., Jacquemart, D., Jolly, A., Lamouroux, J., Le Roy, R., Li, G., Long, D., Lyulin, O., Mackie, C., Massie, S., Mikhailenko, S., Müller, H., Naumenko, O., Nikitin, A., Orphal, J., Perevalov, V., Perrin, A., Polovtseva, E., Richard, C., Smith, M., Starikova, E., Sung, K., Tashkun, S., Tennyson, J., Toon, G., Tyuterev, V., and Wagner, G. The HITRAN2012 molecular spectroscopic database. *Journal of Quantitative Spectroscopy and Radiative Transfer*. Nov. 2013, **130**: 4–50. http://www.sciencedirect.com/science/article/pii/S0022407313002859.

Sattelmayer, T. Influence of the Combustor Aerodynamics on Combustion Instabilities From Equivalence Ratio Fluctuations. *Journal of Engineering for Gas Turbines and Power*. 2002, **125**(1): 11–19. issn: 0742-4795.

Schade, H. and Kunz, E. *Strömungslehre*. 1st. Vol. 1. Berlin, New York: de Gruyter, 1980. //www.degruyter.com/view/product/21445.

Schäfer, L. *Modeling and Simulation of Spark Ignition in Turbocharged Direct Injection Spark Ignition Engines*. PhD thesis. TU Bergakademie Freiberg, Apr. 2016.

Schimek, S., Moeck, J. P., and Paschereit, C. O. An Experimental Investigation of the Nonlinear Response of an Atmospheric Swirl-Stabilized Premixed Flame. *Journal of Engineering for Gas Turbines and Power*. Apr. 2011, **133**(10). issn: 0742-4795.

Schuermans, B., Bellucci, V., Guethe, F., Meili, F., Flohr, P., and Paschereit, C. A Detailed Analysis of Thermoacoustic Interaction Mechanisms in a Turbulent Premixed Flame. *Proceedings of ASME Turbo Expo 2004, Power for Land, Sea, and Air*. 2004, (GT2004-53831): 539–551.

Schuermans, B. *Modeling and Control of Thermoacoustic Instabilities*. PhD thesis. École Polytechnique Fédéral de Lausanne, 2003.

Schuermans, B., Polifke, W., and Paschereit, C. O. *Modeling Transfer Matrices of Premixed Flames and Comparison With Experimental Results*. 1999. http://dx.doi.org/10.1115/99-GT-132.

Sedov, L. I. *Similarity and Dimensional Methods in Mechanics*. Academic Press, 1959.

Shen, G. Q., An, L. S., and Jiang, G. S. "Real-time monitoring on boiler combustion based on acoustic measurement". In: *2006 IEEE Power India Conference*. 2006: 4 pp.–.

Shen, X., Xiong, Q., Shi, X., Wang, K., Liang, S., and Gao, M. Ultrasonic temperature distribution reconstruction for circular area based on Markov radial basis approximation and singular value decomposition. *Ultrasonics*. Sept. 2015, **62**: 174–185. https://doi.org/10.1016%2Fj.ultras.2015.05.014.

Shi, D., Zou, F., Zhu, Z., and Sun, J. Modeling the effect of surface oxidation on the normal spectral emissivity of steel 316L at 1.5 μm over the temperatures ranging from 800 to 1100 K in air. *Infrared Physics & Technology*. July 2015, **71**: 370–377. https://doi.org/10.1016%2Fj.infrared.2015.05.012.

Sielschott, H. and Derichs, W. Use of collocation methods under inclusion of a priori information in acoustic pyrometry. *Proc. European Concerted Action on Process Tomography*. 1995: 110–117.

Sielschott, H. and Derichs, W. Tomography with few data: Use of collocation methods in acoustic pyrometry. *ECMI Student Proceedings*. 1996.

Sili, E., Cambronne, J. P., and Koliatene, F. Temperature Dependence of Electrical Breakdown Mechanism on the Left of the Paschen Minimum. *IEEE Transactions on Plasma Science*. 2011, **39**(11): 3173–3179. ISSN: 0093-3813.

Smith, G., Golden, D., Frenklach, M., Eiteener, B., Goldenberg, M., Bowman, C., Hanson, R., Gardiner, W., Lissianski, V., and Qin, Z. *GRI-Mech 3.0*. 2000. http://www.me.berkeley.edu/gri_mech/.

Stow, S. R. and Dowling, A. P. Thermoacoustic Oscillations in an Annular Combustor. *ASME Turbo Expo 2001: Power for Land, Sea, and Air*. June 2001, **2**(78514). http://dx.doi.org/10.1115/2001-GT-0037.

Striggow, K. *Die Anwendung der Tomographie in der Ozeanographie - Literaturbericht*. Tech. rep. Institut für Meereskunde der AdW der DDR, 1985.

Strobio Chen, L., Bomberg, S., and Polifke, W. Propagation and generation of acoustic and entropy waves across a moving flame front. *Combustion and Flame*. Apr. 2016, **166**(4): 170–180. ISSN: 0010-2180.

Strohmer, T. and Vershynin, R. A Randomized Kaczmarz Algorithm with Exponential Convergence. *Journal of Fourier Analysis and Applications*. Apr. 2009, **15**(2): 262–278. https://doi.org/10.1007%2Fs00041-008-9030-4.

Taylor, G. Dispersion of soluble matter in solvent flowing slowly through a tube. *Proc R Soc Lond A Math Phys Sci*. Aug. 1953, **219**(1137): 186–203.

Taylor, G. The Dispersion of Matter in Turbulent Flow through a Pipe. *Proc R Soc Lond A Math Phys Sci*. May 1954, **223**(1155): 446–468.

Tewes, W. Temperaturmessfehler in strömenden Gasen und Dämpfen. *Zeitschrift für Technische Physik*. 1941, **22**: 160–167.

Tikhonov, A. Solution of incorrectly formulated problems and the regularization method. *Soviet Mathematics*. 1963, **4**: 1035–1038.

Tsien, H. S. The Transfer Functions of Rocket Nozzles. *Journal of the American Rocket Society*. May 1952, **22**(3): 139–143. https://doi.org/10.2514/8.4448.

Tucker, P. G. and Karabasov, S. A. Unstructured grid solution of the eikonal equation for acoustics. *International Journal of Aeroacoustics*. Aug. 2009, **8**(6): 535–553. https://doi.org/10.1260%2F147547209789141498.

Twynstra, M. G. and Daun, K. J. Laser-absorption tomography beam arrangement optimization using resolution matrices. *Appl. Opt.* 2012, **51**(29): 7059–7068. http://ao.osa.org/abstract.cfm?URI=ao-51-29-7059.

VDI. *VDI-Wärmeatlas*. Ed. by V. e.V. Vol. 11. Springer Vieweg, 2013.

Vecherin, S. N., Ostashev, V. E., Wilson, D. K., and Ziemann, A. Time-dependent stochastic inversion in acoustic tomography of the atmosphere with reciprocal sound transmission. *Measurement Science and Technology*. 2008, **19**(12). http://stacks.iop.org/0957-0233/19/i=12/a=125501.

Verhoeven, D. Limited-data computed tomography algorithms for the physical sciences. *Applied Optics*. July 1993, **32**(20): 3736. https://doi.org/10.1364%2Fao.32.003736.

Waheed, U. bin, Alkhalifah, T., and Wang, H. Efficient traveltime solutions of the acoustic TI eikonal equation. *Journal of Computational Physics*. Feb. 2015, **282**: 62–76. https://doi.org/10.1016%2Fj.jcp.2014.11.006.

Walker, R. E. and Westenberg, A. A. Molecular Diffusion Studies in Gases at High Temperature. II. Interpretation of Results on the He-N2 and CO2-N2 Systems. *The Journal of Chemical Physics*. 1958, **29**(5): 1147–1153. eprint: http://dx.doi.org/10.1063/1.1744669. http://dx.doi.org/10.1063/1.1744669.

Warnatz, J., Maas, U., and Dibbel, R. *Combustion*. 4th. .a. Springer Verlag, Heidelberg - New York, 2009.

Wassmer, D., Schuermans, B., Paschereit, C. O., and Moeck, J. P. An Acoustic Time-of-Flight Approach for Unsteady Temperature Measurements: Characterization of Entropy Waves in a Model Gas Turbine Combustor. *Journal of Engineering for Gas Turbines and Power*. 2016, **139**(4). http://dx.doi.org/10.1115/1.4034542.

Wassmer, D., Schuermans, B., Paschereit, C. O., and Moeck, J. P. Measurement and Modeling of the Generation and the Transport of Entropy Waves in a Model Gas Turbine Combustor. *International Journal of Spray and Combustion Dynamics*. 2017, **9**(4): 299–309. https://doi.org/10.1177/1756827717696326.

Wassmer, D., Pause, F., Schuermans, B., Paschereit, C. O., and Moeck, J. P. "An Onion Peeling Reconstruction of the Spatial Characteristics of Entropy Waves in a Model Gas Turbine Combustor. Turbo Expo: Power for Land, Sea, and Air". In: *ASME Turbo Expo*. 2017: V04BT04A037. http://dx.doi.org/10.1115/GT2017-64717.

Wiley, W. and McLaren, I. Time-of-Flight Mass Spectrometer with Improved Resolution. *The Review of Scientific Instruments*. Dec. 1955, **26**(12): 1150–1157.

Wilson, D. and Thomson, D. Acoustic tomographic monitoring of the atmospheric surface layer. *Journal of Atmospheric and Oceanic Technology*. 1994, **11**: 751–769.

Wright, W. M. Propagation in air of N waves produced by sparks. *The Journal of the Acoustical Society of America*. June 1983, **73**(6): 1948–1955. https://doi.org/10.1121%2F1.389585.

Wyber, R. The design of a spark discharge acoustic impulse generator. *Acoustics, Speech and Signal Processing, IEEE Transactions on*. 1975, **23**(2): 157–162. ISSN: 0096-3518.

Xia, Y., Duran, I., Morgans, A., and Han, X. "Dispersion Of Entropy Waves Advecting Through Combustor Chambers". In: *International Congress on Sound and Vibration*. Vol. 23. Athens, July 2016.

Yuldashev, P., Ollivier, S., Averiyanov, M., Sapozhnikov, O., Khokhlova, V., and Blanc-Benon, P. Nonlinear propagation of spark-generated N-waves in air: Modeling and measurements using acoustical and optical methods. *The Journal of the Acoustical Society of America*. Dec. 2010, **128**(6): 3321–3333. https://doi.org/10.1121%2F1.3505106.

Zhang, S., Shen, G., An, L., and Niu, Y. Online monitoring of the two-dimensional temperature field in a boiler furnace based on acoustic computed tomography. *Applied Thermal Engineering*. Jan. 2015, **75**: 958–966. https://doi.org/10.1016%2Fj.applthermaleng.2014.10.085.

Zhong, S., Miao, N., Yu, Q., and Cao, W. Energy measurement of spark discharge using different triggering methods and inductance loads. *Journal of Electrostatics*. feb 2015, **73**: 97–102. https://doi.org/10.1016%2Fj.elstat.2014.10.014.

Ziemann, A., Arnold, K., and Raabe, A. Acoustic tomography in the atmospheric surface layer. *Annales Geophysicae*. 1999, **17**(1): 139–148. https://doi.org/10.1007%2Fs00585-999-0139-9.

A Appendix

A.1 Phantom study: SVD approach applied to alternative emitter/receiver arrangements

Based on the investigations in Section 3, a similar study applied to two different arrangements of the acoustic emitter and the microphones is presented in the following. Goal is to investigate the sensitivity of the SVD approach introduced in Section 2.3.1 towards the spatial distribution of the acoustic paths. The two setups stem from the original setup shown in Fig. 4.23, a circular duct of radius $R = 0.1\,\mathrm{m}$ and seven acoustic receivers are considered in the phantom study. To account for the uncertainties of the location of the sound emitter and for the temperature noise that exists under measurement conditions, noise of $3\,\mu\mathrm{s}$ is added to the arrival time obtained from the phantom study. This is the same level of noise as applied to $\boldsymbol{\tau}_p$ in the investigation in Section 3.1.2.

In Fig. A.1, the acosutic paths of the two different setups are plotted on a contour plot of the axissymmetric radial temperature field. In Fig. A.1a, the microphone locations are not altered compared to the original setup, but the location of the acoustic source

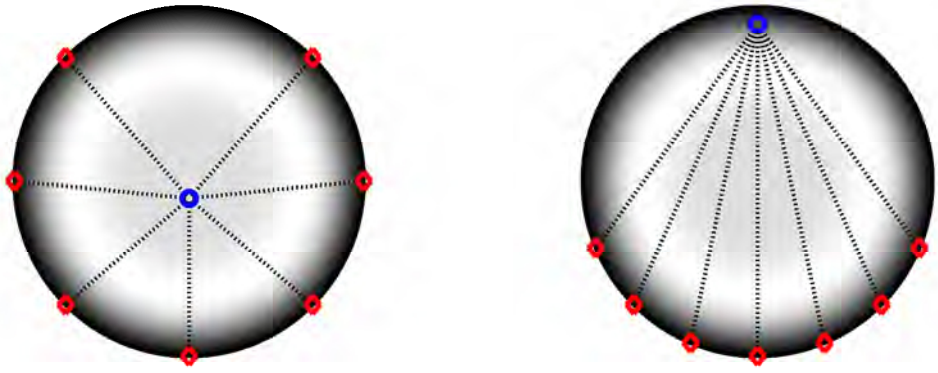

(a) Setup A **(b)** Setup B

Figure A.1: **(a)**: Setup A: acoustic emitter located close to the center of the duct, microphones distributed evenly along the circumference. **(b)**: Setup B: acoustic emitter located close to the wall, microphones placed at the opposite side of the ducts circumference.

is shifted close to the center of the duct. The second arrangement in Fig. A.1b provides the same penetration depth of the acoustic emitter as in the original setup, though the microphones are shifted towards the opposite side of the ducts circumference. Both arrangements keep symmetry with respect to the vertical axis.

Setup A

For setup A, the length of all acosutic paths is almost the same and due to the rotational symmetry, the information provided by each path is almost equal. Hence, the probability densities of the paths are approximately constant for a wide range of radii. This can be seen in Fig. A.2a, where the acoustic paths are plotted in polar coordinates for a penetration depth of $s = 1.1\mathrm{R}$ (s is defined as the distance between the emitter and the top end of a radial cross section of the circular duct). Apart from the area very close to the acoustic emitter, the paths run parallel to each other and impinge perpendicularly at the wall, which means that they "cover" the outer area of the measurement plane as sparse as possible. This is reflected in Fig. A.2b. The sum of the probability density estimates (black curve) does not correspond to the weight of the radius as it contributes to the surface area average (red dashed curve).

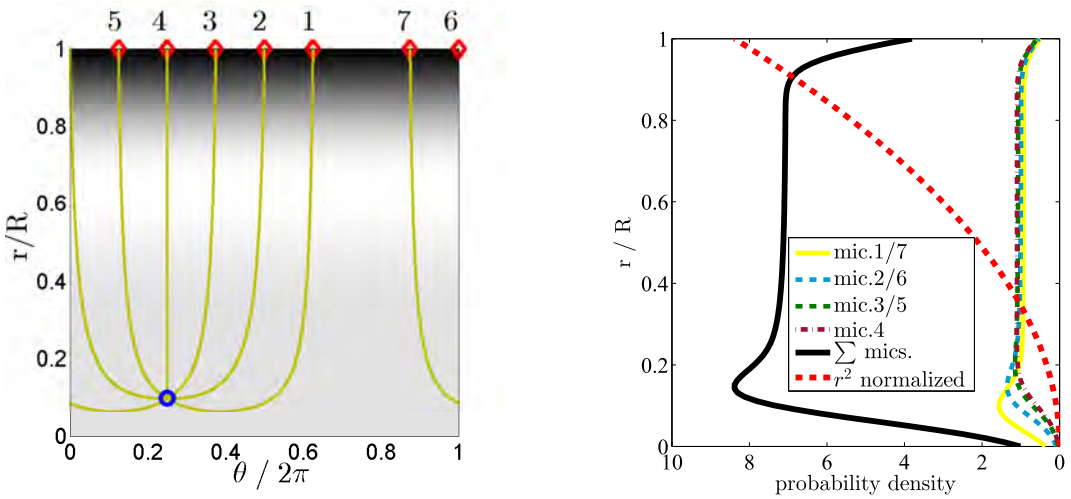

(a) **(b)**

Figure A.2: **(a)**: Acoustic paths in polar coordinates for setup A with $s = 1.1\mathrm{R}$. **(b)**: Probability density estimation of the acoustic paths as function of the radius for setup A with $s = 1.1\mathrm{R}$.

The change of the spatial acoustic emitter/receiver arrangement affects the quality of the SVD approach only weakly. The single-rank approximated arrival time matrix $\tilde{\boldsymbol{\tau}}_p$ deviates from the output matrix $\boldsymbol{\tau}_p$ by 1 %, which is almost the same level as observed for the original setup in Fig. 3.5b. With respect to the amplitude of the cross-sectionally surface averaged temperature, however, the amplitudes extracted via the SVD method for setup A deviate stronger from the input amplitude than observed for the original case in Fig. 3.6a. For all penetration depths of the acoustic emitter, the relative errors tend to be within a range of $10 - 20\,\%$. So the SVD approach overestimates the amplitude of the cross-sectionally surface averaged temperature oscillation. This is expectable, as for this arrangement, the inner region of the duct, where the temperature amplitude is

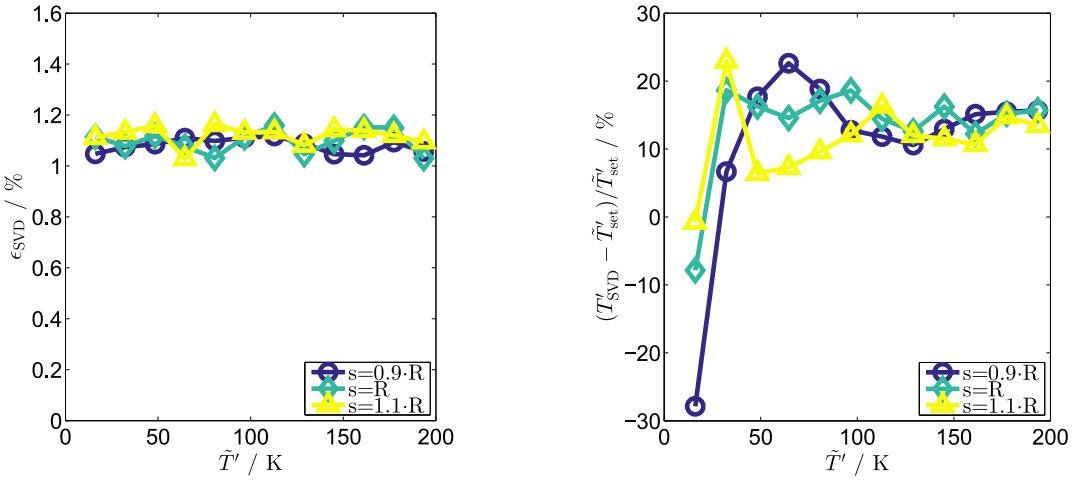

(a) **(b)**

Figure A.3: **(a)**: ϵ_{SVD} for three different penetration depths (setup A). **(b)**: Relative error between the reconstructed temperature amplitude T'_{SVD} and the defined amplitude $\tilde{T}_{set}$ for setup A.

larger than in regions closer to the wall, is weighted equally to the higher radius region. The latter, however, has a stronger influence on the cross-sectionally surface average.

Setup B

In setup B, the microphones are not evenly distributed along the circumference any more but are accumulated at the opposite side of the acoustic emitter, which is at the same position as in the original setup (see Fig. 4.23). The density of the acoustic paths with respect to the radius is not as uniform as for setup B (see Fig. A.2b) but exhibits a maximum at approximately $r = 0.6R$. This is depicted in Fig. A.4b. Although this peak is rather in the middle of the duct's radius, a favourable characteristic is found in the slightly stronger weight of regions closer to the wall compared to the radial center of the duct.

Additionally, the single-rank approximated arrival time matrix $\tilde{\boldsymbol{\tau}}_p$ matches better with the input arrival time matrix $\boldsymbol{\tau}_p$. This is shown in Fig. A.5a, where the error ϵ_{SVD} is plotted for various amplitudes of the cross-sectionally surface averaged temperature fluctuation and five different penetration depths of the acoustic source. With approximately 0.7 %, the error is about 30 % smaller than observed for setup A. This does not provide information about how well the cross-sectionally surface averaged temperature amplitude is reproduced, but it gives hint on how well conditioned the input matrix is composed. The error in the reproduction of the amplitude of the cross-sectionally surface averaged temperature fluctuation is smaller than for setup A, but it is clearly larger compared to the original setup. Apart from the low amplitude region, where the induced temperature noise (due to the noise on the arrival times) is of the order of the actual temperature amplitude, the SVD method overestimates the amplitude of the cross-sectionally surface averaged temperature fluctuations. This is depicted in Fig. A.5b. The overestimation has already been observed for setup A and can again be explained by the too low weight-

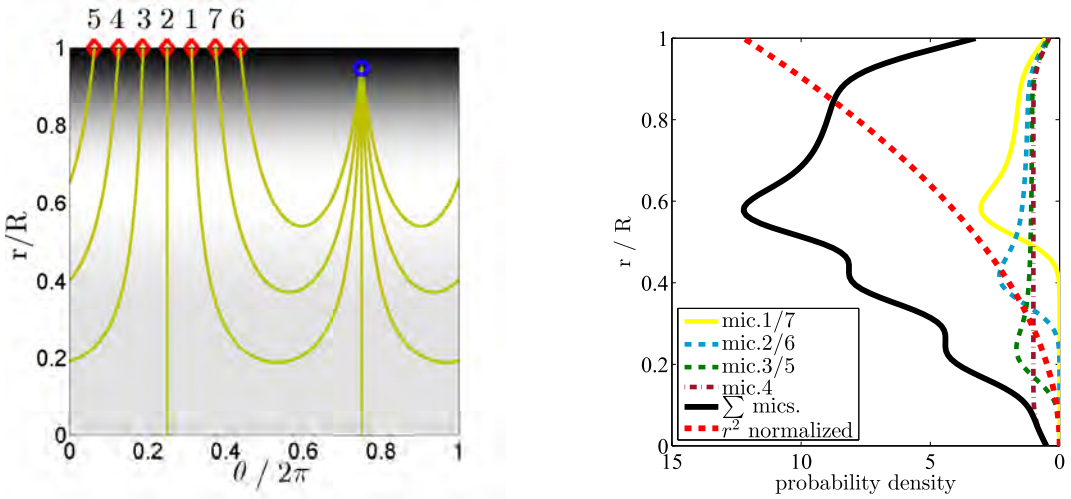

(a) **(b)**

Figure A.4: **(a)**: Acoustic paths in cartesian coordinates for setup B with $s = 0.05$R. **(b)**: Probability density estimation of the acoustic paths as function of the radius for setup B with $s = 0.05$R.

ing of the outer radius and a too strong weighting of the inner region, respectively (see Fig. A.4b).

It is worth noting that the prediction of the cross-sectionally surface averaged temperature amplitude becomes distinctively worse for increasing penetration depths of the acoustic emitter. For larger penetration depths, the outer radii are even less covered by acoustic paths. This trend has not been observed for the original emitter/microphone arrangement due to the inclusion of short acoustic paths that mainly cover the area at large radii.

The general conclusion of this appendix to Section 3.1 is that the arrangement of the acoustic source and the acoustic receivers employed in the measurements provides the best estimate of the SVD approach to reproduce the cross-sectionally surface averaged temperature amplitude. The comparison with alternative setups by means of a phantom study confirms, however, that a careful positioning of the acoustic paths is of high importance. Note that the results presented in this appendix depend quantitatively on the characteristic of the temperature fluctuation induced in the phantom study. The definition of the amplitude dependence on the radius affects the results notably.

A.2 Estimation of the bulk flow velocity

There are two possibilities to assess the bulk advection velocity in the combustor. One way is derived via mass conservation. This allows for the calculation of an overall net flow velocity by

$$u_\mathrm{h} = \frac{\dot{m}}{\rho \pi R^2}, \tag{A.1}$$

where the mass flow $\dot{m}$ refers to the total gas mass flow (air + fuel) and R denotes the radius of the circular combustion chamber. The gas density is a function of the gas temperature, which is in turn a function of the radius as well as of the axial location.

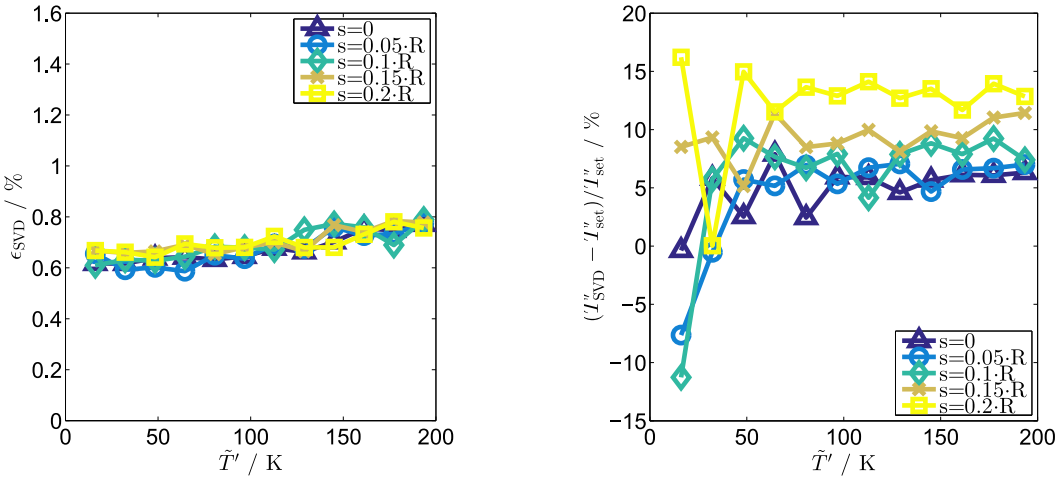

(a) **(b)**

Figure A.5: **(a)**: ϵ_{SVD} for three different penetration depths as function of the amplitude of the aurface averaged temperature fluctuation (setup B). **(b)**: Relative error between the reconstructed temperature amplitude T'_{SVD} and the defined amplitude $\tilde{T}_{set}$ for setup B.

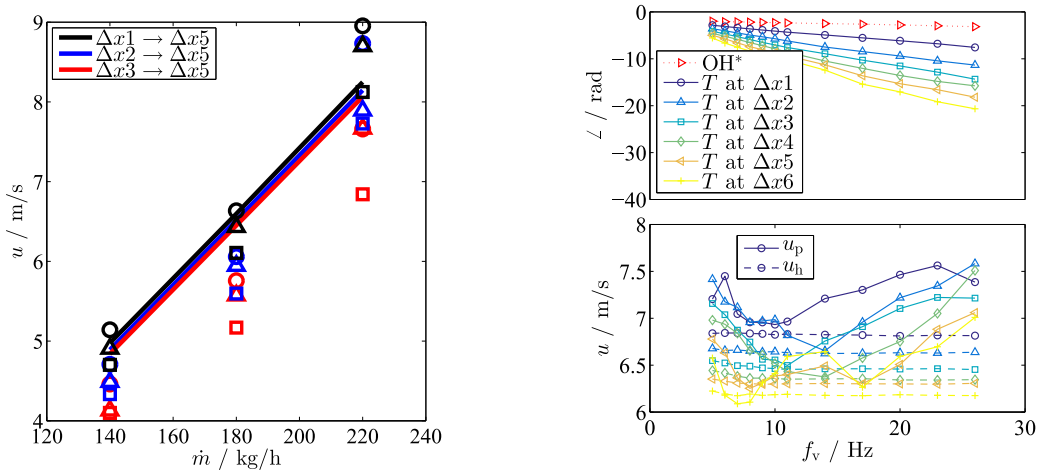

(a) **(b)**

Figure A.6: **(a)**: Integral bulk flow velocities between different axial locations: (solid lines): velocity u_h according to Eq. A.1. (markers): phase velocities u_p between two measurements of the temperature fluctuation according to Eq. A.2; (◯): $f_v = 5\,\text{Hz}$, (△): $f_v = 6\,\text{Hz}$, , (□): $f_v = 7\,\text{Hz}$. **(b)**: **Top**: Phases of the OH*-chemiluminescence intensity measurement and of the reconstructed temperature fluctuations obtained from the SVD-reconstruction at different axial positions of the measurement plane, the phases are related to the square wave sent to the fuel modulation valve; here: $\overline{\phi} = 0.6$, $g = 25\,\%$, $\dot{m} = 180\,\text{kg/h}$. **Bottom**: Bulk flow velocities evaluated from the phase measure (see plot above) u_p and obtained from Eq. A.1 for different axial positions of the measurement plane; the colors correspond to various axial measurement locations.

Therefore, an estimate of a single bulk flow velocity is not trivial and subject to assumptions. In this study, the density is evaluated based on the temperature measured with a type-S thermocouple at $r/R = 0.5$.

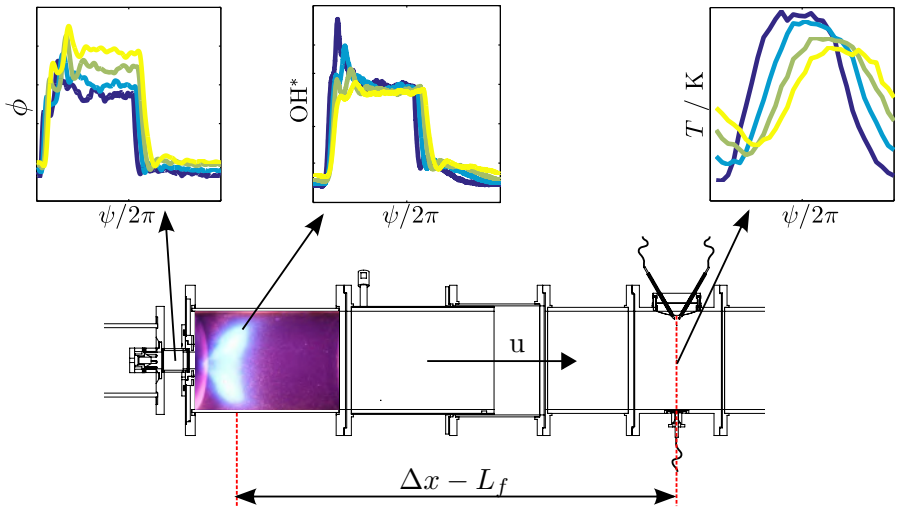

Figure A.7: Sketch of the quantities measured at different locations at the combustion test rig; the flame length L_f has to be guessed and should correspond to the axial location of the highest heat release fluctuations, where the photomultiplier for the OH*-chemiluminescence is focused on.

The second method of assessing the bulk flow velocity makes use of the phase measurements of the OH*-chemiluminescence intensity fluctuations and the temperature fluctuations depicted in Fig. 5.37a. From the phase difference of fluctuations measured at two different axial locations x_1 and x_2, the following expression for the volume-integrated net flow velocity in the combustor section between the two axial positions is derived as:

$$u_\mathrm{p} = \frac{(x_2 - x_1) f_\mathrm{v}}{\angle T'(x_2) - \angle T'(x_1)}. \tag{A.2}$$

A comparison of u_h and u_p is given in Fig. A.6a for three different axial distances in the combustion rig. The phase information is extracted from measurements of the temperature fluctuations. A good agreement is observed between the two methods of estimating the bulk velocity. The scattering of the velocity estimation via the phase measurements is due to the uncertainty of the phase extraction based on a Fourier transform. This error increases for higher fuel modulation frequencies as simultaneously the amplitude of the temperature fluctuation drops significantly. The latter hampers the amplitude and phase extraction of the temperature fluctuation.

If the measurement of the temperature fluctuation is only possible at one axial location in the combustor, the velocity u_p may be estimated based on an additional measurement of the OH*-chemiluminescence intensity. The definition of the axial distance between the TOF measurement plane and the reaction zone, where the OH*-chemiluminescence intensity fluctuations are measured, is not straight forward. A well defined assessment of the flame length L_f is difficult and has to be approximated.

The phases of the measured temperature fluctuations are plotted together with the associated phases of the OH*-chemiluminescence intensity fluctuations in the upper plot in Fig. A.6b as functions of the fuel modulation frequency f_v. All phases shown here are related to the phase of the square wave sent to the fuel modulation valve. For a fixed flame length estimation $L_f = 0.2\,\mathrm{m}$, the corresponding resulting velocities u_p are presented in the bottom plot of Fig. A.6b as solid lines. The phase-based velocities u_p are

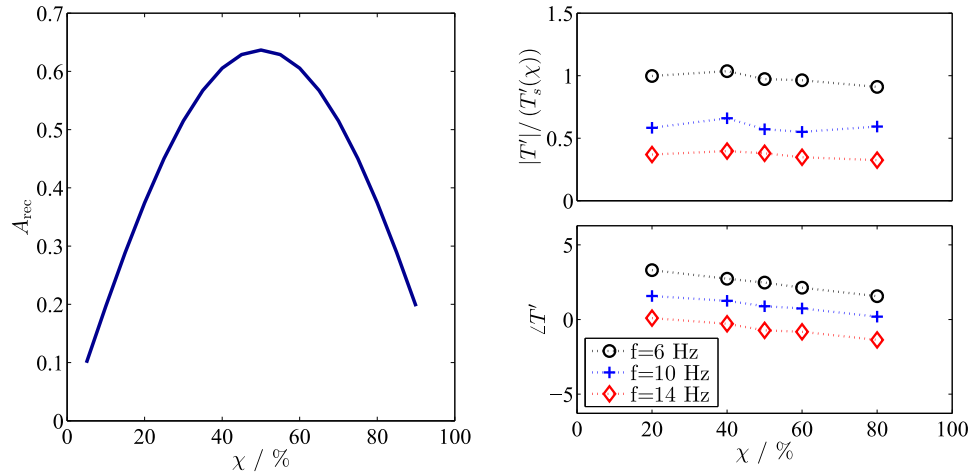

(a) **(b)**

Figure A.8: **(a)**: Amplitude A_{rec} reconstructed from a Fourier transformation of a rectangular pulse signal of amplitude 1 for different duty cycles χ. **(b)**: Ratio between the measured temperature amplitude and the temperature amplitude obtained from Eq. A.3 for three different frequencies $f_{\mathrm{v}} = 6\,\mathrm{Hz}$ (solid), $f_{\mathrm{v}} = 10\,\mathrm{Hz}$ (dashed), and $f_{\mathrm{v}} = 14\,\mathrm{Hz}$ (dotted); $\overline{\phi}_{\mathrm{set}} = 0.7$; $g = 20\,\%$; $\dot{m}_{\mathrm{air}} = 180\,\mathrm{kg/h}$; $dT/d\phi = 900\,\mathrm{K}$; measurement plane $x2$.

compared to the bulk flow velocities u_{h} (dashed lines) for the different axial measurement locations (Eq. A.2). The order of magnitude of the velocities estimated with both methods is very similar. The drop of the velocities for axial positions further downstream is due to the significant decrease of the steady-state temperature caused by the wall cooling. This trend is also well recovered by u_{p}. The significant frequency dependence of u_{p} stems from the characteristic frequency response of the OH*-chemiluminescence intensity fluctuation related to the combustor residence times (see Sec. 5.4.1.2)

Both bulk flow velocity measurement methods are comprised by assumptions, the flame length in case of u_{p} and the density measure in case of u_{h}. This allows only for a rough comparison. However, it is shown that the phase measurement of the temperature fluctuations can be used as good estimation of the bulk velocity. In turn, this means that the propagation velocity of entropy waves can well be approximated with the bulk flow velocity.

A.3 Duty cycle variation

In general, all periodic fluctuations in this study are considered as harmonic perturbations. In this section, the response of the OH*-chemiluminescence intensity in the reaction zone and the temperature at the axial location $\Delta x2$ to equivalence ratio fluctuations of various duty cycles is investigated. Therefore, the excitation can not be considered as harmonic anymore.

The time signals of the square waves sent to the fuel modulation valve and the corresponding phase averaged OH*-chemiluminescence intensity signals are plotted in Figs. A.9a and A.9b for five different duty cycles. The OH*-chemiluminescence intensity signal is

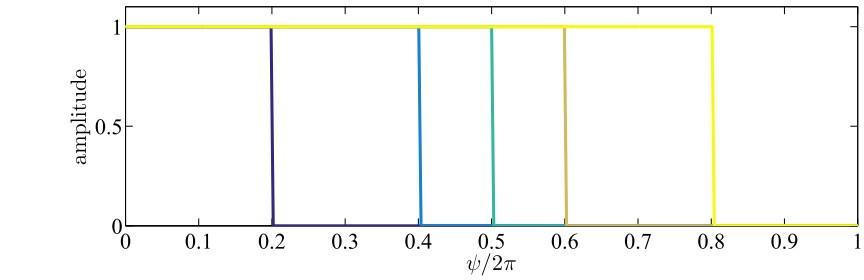

(a)

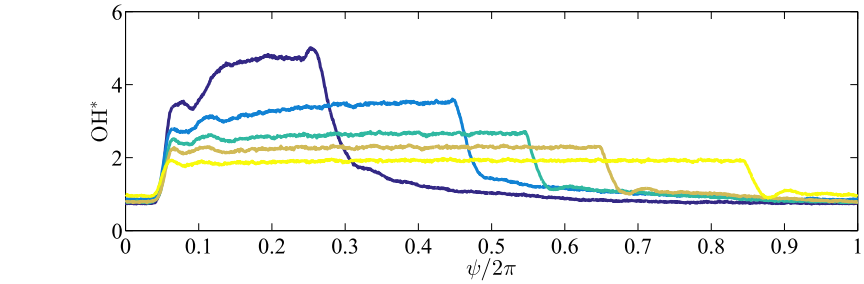

(b)

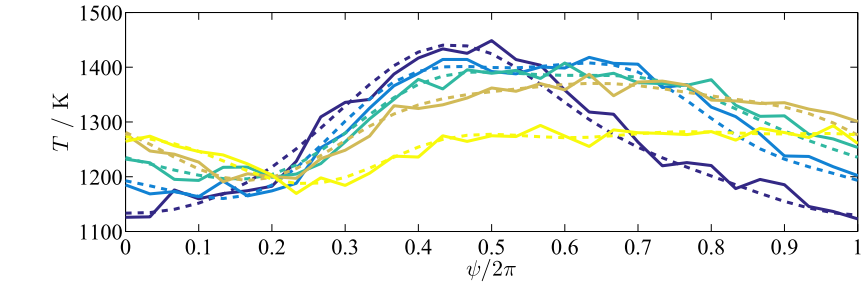

(c)

Figure A.9: **(a)**: Control signal for the valve excitation for different duty cycles $\chi = 20$ %, $\chi = 40$ %, $\chi = 50$ %, $\chi = 60$ %, and $\chi = 80$ %. **(b)**: Corresponding phase averaged global OH*-chemiluminescence intensity measurement at the reaction zone with a valve frequency $f_v = 6$ Hz; $g = 20$ %; $\dot{m}_{air} = 180$ kg/h; $\overline{\phi}_{set} = 0.7$. **(c)**: Corresponding phase averaged temperature measurement by means of the SVD method (solid) and the reconstructed signal via the Fourier coefficient associated to the excitation signal (dashed).

clearly governed by the square wave generated by the valve. For all measurements shown in Fig. A.9, the part of the mass flow sent through the modulated fuel line is the same ($g = 25$ %), however, in Fig. A.9b it is clearly shown that the amplitude of the signals strongly depends on the duty cycle. This can partly be explained by the duty cycle dependence of ϕ_{max} shown in Fig. 5.25a, it leads to a strong increase of the amplitude for smaller duty cycles. In addition to this effect, the pulse characteristic plays an important role.

The amplitude extracted from a rectangular pulse signal by a Fourier transform (as shown in Eq. 5.12) depends on the duty cycle. The amplitudes A_{rec} obtained from a Fourier transform of a square signal of amplitude 1 is shown in Fig. A.8a as a function of the duty cycle χ. For a duty cycle of $\chi = 50$ %, the highest response is obtained, whereas for smaller and larger duty cycles the amplitude response decreases. Hence, the

expected temperature amplitude, which can be estimated from the steady-state relation between equivalence ratio and temperature based on Eq. 5.3, becomes a function of the amplitude A_{rec}:

$$T_s'(\chi) = A_{\mathrm{rec}}(\chi)\frac{\phi_{\max}(\chi) - \phi_{\min}}{2}\frac{dT}{d\phi}. \tag{A.3}$$

The measured temperature fluctuations for various duty cycles are shown in Fig. A.9c. The dashed lines represent the reconstructed harmonic signals based on the Fourier transform. Their amplitudes are considered as the measured temperature amplitude in the following. A comparison between these measured temperature fluctuations T' and the calculated temperature amplitude based on Eq. A.3 is shown in Fig. A.8b. The ratios between the measured and the calculated temperature amplitudes are approximately constant for different duty cycles. The values for $\phi_{\max}$ and $\phi_{\min}$ have been evaluated according to Eqs. 5.8 and 5.9 and $dT/d\phi$ has been approximated based on Fig. 5.12 to $dT/d\phi = 900\,\mathrm{K}$.

The significant difference between the measurements at different frequencies is caused by dissipative effects that cause the temperature amplitude to decrease while being convected from the reaction zone to the measurement plane (see Sec. 6.2).

The purpose of this Appendix section was to demonstrate the plausibility of the excitation characteristics of the fuel modulation. The amplitude characteristics of the temperature fluctuations for variations of the duty cycle agree well with theoretical considerations.

Publications

Related to thesis:

Wassmer, D., Pause, F., Schuermans, B., Paschereit, C.O., and Moeck J.P.
An Onion Peeling Reconstruction of the Spatial Characteristics of Entropy Waves in a Model Gas Turbine Combustor,
Proceedings of the ASME Turbo Expo 2017: Turbomachinery Technical Conference and Exposition, Charlotte, North Carolina, USA, June 2017
DOI: 10.1115/GT2017-64717

Wassmer, D., Schuermans, B., Paschereit, C.O., and Moeck, J.P.
Measurement and Modeling of the Generation and the Transport of Entropy Waves in a Model Gas Turbine Combustor,
International Journal of Spray and Combustion Dynamics, Vol. 9(4), April 2017
DOI: 10.1177/1756827717696326

Wassmer, D., Schuermans, B., Paschereit, C.O., and Moeck, J.P.
An Acoustic Time-of-Flight Approach for Unsteady Temperature Measurements: Characterization of Entropy Waves in a Model Gas Turbine Combustor,
Journal of Engineering for Gas Turbine and Power, Vol. 139(4), July 2016
DOI: 10.1115/1.4034542

Unrelated to thesis:

Bothien, M.R. and Wassmer, D.
Impact of Density Discontinuities on the Resonance Frequency of Helmholtz Resonators,
AIAA Journal, Vol. 53(4), January 2015
DOI: 10.2514/1.J053227

Ćosić, B., Wassmer, D., Terhaar, S., and Paschereit, C.O.
Acoustic response of Helmholtz dampers in the presence of hot grazing flow,
Journal of Sound and Vibration, Vol. 335, October 2014
DOI: 10.1016/j.jsv.2014.08.025